SAVING THE JOINT: NEW METHODS FOR EARLY DIAGNOSIS AND TREATMENT

JAN HENDRIKS

Osteoarthritis is a debilitating disease affecting a large and increasing part of the population. Currently the disease is diagnosed at a late stage and no curative treatment yet exists. This results in prolonged pain and eventual joint replacement. In this thesis, we developed new methods for the early specific diagnosis of osteoarthritis. We achieved this through a new assay to sensitively measure multiple biomarkers locally in the joint fluid. This can improve prediction of disease progression and improve the efficacy of current treatments. In addition we developed new treatments for early developing joint diseases. Specifically, a cell spray treatment for cartilage defects was explored, optimized and the deposited biomaterial was improved. This expands the early treatments available and could improve the regeneration of the joint. The combination of new methods for both early diagnosis and treatment is a step forward in preventing disease progression and towards saving the joint.

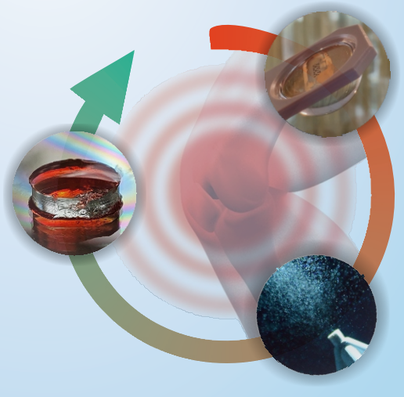

ISBN 978-90-365-4872-4

UNIVERSITY OF TWENTE.

Saving the joint: New methods for early diagnosis and treatment Jan Hendriks

SAVING THE JOINT

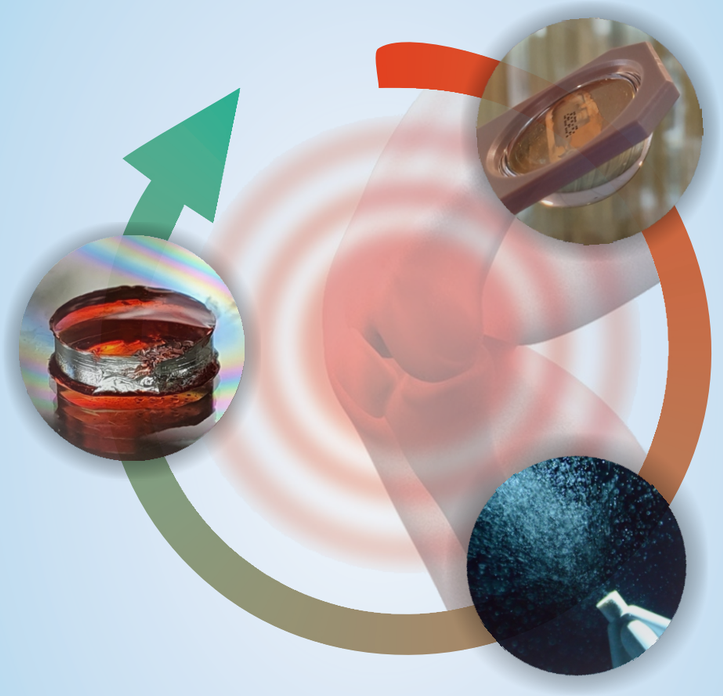

NEW METHODS FOR EARLY DIAGNOSIS AND TREATMENT

Jan Hendriks

Invitation

To attend the public defense of my dissertation

SAVING THE JOINT: NEW METHODS FOR EARLY DIAGNOSIS AND TREATMENT

On Wednesday, October 16th 2019, at 14.45

In the prof. dr. G. Berkhoff zaal (collegezaal 4), building De Waaier, University of Twente, Drienerlolaan 5, Enschede, The Netherlands

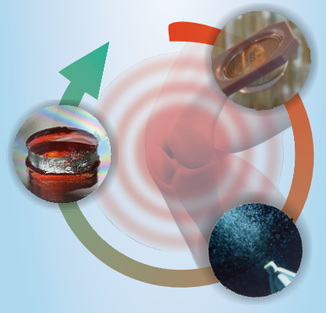

Paranymphs:

Lisanne Karbaat
Hanneke Hendriks

SAVING THE JOINT:

NEW METHODS FOR EARLY DIAGNOSIS AND TREATMENT

Jan Hendriks

2019

Graduation Committee

prof. dr. J.L. Herek (chairman)	University of Twente
prof. dr. H.B.J. Karperien (supervisor)	University of Twente
prof. dr. D.B.F. Saris (supervisor)	Mayo Clinic – Rochester, US
prof. dr. ir. J. Huskens	University of Twente
prof. dr. S.M. Garcia Blanco	University of Twente
Dr. M. Sharif	University of Bristol, UK
prof. dr. ir. J. Malda	UMCU/UU Utrecht
prof. dr. ir. J. de Boer	Eindhoven University of Technology

Saving the joint: New methods for early diagnosis and treatment

Jan Hendriks, 2019

The work in this PhD thesis was performed in the department of Developmental BioEngineering within the Technical Medical Centre, and the Faculty of Science and Technology of the University of Twente, Enschede, The Netherlands

The research was funded by the Dutch Arthritis Foundation.

Cover design: Cycle that demonstrates the process of saving an affected joint via the diagnostic and treatment options described in this thesis.

Printed by Gildeprint, Enschede, The Netherlands

ISBN: 978-90-365-4872-4

DOI: 10.3990/1.9789036548724

SAVING THE JOINT:

NEW METHODS FOR EARLY DIAGNOSIS AND TREATMENT

DISSERTATION

to obtain
the degree of doctor at the University of Twente,
on the authority of the rector magnificus,
prof. dr. T.T.M. Palstra
on account of the decision of the doctorate board,
to be publicly defended
on Wednesday, October 16th 2019, at 14.45

by

Jan Hendriks

Born on June 18th, 1989
in Goor, The Netherlands

This dissertation has been approved by:

prof. dr. H.B.J. Karperien (supervisor)
prof. dr. D.B.F. Saris (supervisor)

Summary

Osteoarthritis (OA) is a debilitating joint disease affecting millions of patients worldwide, with the prevalence set to increase further due to an aging population. Despite high morbidity and associated health costs, no curative treatment yet exists. This is caused in part by the highly complex nature of the disease, with multiple phenotypes, and by late diagnosis reducing efficacy of therapies. This results in the reality that most patients experience severe joint pain for multiple years before they inevitably undergo total joint replacement. The goal of this thesis is to make steps to upend this status quo through saving the joint by applying new methods for early diagnosis and treatment of osteoarthritis.

As mentioned, the disease is highly complex and is only diagnosed at a late stage. In the current situation, osteoarthritis is diagnosed via X-Ray many years after disease onset and limited information can be obtained on the specific subtype experienced by the patient. This demands for new diagnostic tools that can identify the multiple phenotypes of the disease at an early stage, to allow for effective personalized treatments. A promising approach is to measure biomarkers that present information on disease progression, locally in the effected joints. This requires a tool that can measure multiple biomarkers simultaneously, to detect the different phenotypes, with large sensitivity, for early diagnosis, in small volumes of joint fluids. Currently, no diagnostic tool exists that can meet these requirements.

In this work, we have developed a diagnostic method based on surface plasmon resonance array imaging (SPRi) which allows us to measure the desired biomarkers in multiplex. To achieve the required sensitivity for early diagnosis we applied a signal enhancement cascade using gold nanoparticles. In a proof of concept study, we showed we could measure relevant OA biomarkers below physiological limits with broad dynamic range in multiplex in small volumes of joint fluids. To improve the applicability of this method in a clinical setting, we developed a toolbox for extensive quality control, calibration free measurements and simple assay optimization. This was achieved by kinetically defining the SPRi enhancement cascade, allowing for prediction of the signal at any biomarker concentration. This diagnostic tool has large potential in the early specific diagnosis of OA and can therefore help improve the efficacy of existing treatment options.

However, in order to save the joint new improved early treatment options are required. Early treatment of articular cartilage defects has shown potential in this respect. Promising results have been shown by injecting a combination of cells and biomaterials at a defect site in the affected joint. While injection is suitable for small defects, larger irregular defects could benefit from spraying the cell-biomaterial combination. In this work, we looked at the effect of spraying on the viability of the cells after impact. We developed a validated analytical model that can predict cell survival based on spraying parameters. We showed that the viability is dependent on the air pressure applied to the nozzle, impact distance, viscosity and surface stiffness and that our model accurately

recapitulates these processes. Subsequently, we expanded this model by determining the effect of cell type and cellular properties on the survival. We showed that the cell type has a large influence on survival, captured by the cellular properties in our model. Furthermore, we demonstrated that changing these cellular properties could improve the survival in the spraying. Finally, we applied a custom controllable droplet impact set-up to validate our model in a large parameter space. This resulted in further improvements in our model and expanded its use to other biofrabrication methods. To further improve this treatment, we developed a toolbox for optimal biomaterials for joint repair. We demonstrated an injectable hydrogel with tuneable mechanical and biological properties that can be tailored to obtain an optimal cell response. Together, this work can result in the effective application of optimal cell/biomaterial combinations to the joint with an increased cell survival leading to a promising early treatment.

With the combination of new methods for early diagnosis and early treatment we have made steps to address the main challenges facing our joints. While no single step is ever large enough, we believe this work is a significant leap in saving the joint.

Samenvatting

Artrose is een zwaar belemmerende ziekte waar wereldwijd miljoenen patiënten aan lijden. Door de vergrijzing zal dit aantal alleen maar verder toenemen. Ondanks de schadelijke effecten en de hoge zorgkosten die ermee gepaard gaan, is er nog altijd geen genezende behandeling beschikbaar. Dit wordt deels veroorzaakt door de zeer complexe aard van de ziekte, met verschillende fenotypes, en door de late diagnose, wat leidt tot een lagere behandelingseffectiviteit. Het resultaat hiervan is de realiteit dat patiënten vele jaren leiden aan zware gewrichtspijn voordat ze overgaan tot een onvermijdelijke gewrichtstransplantatie. Het doel van dit werk is het zetten van stappen om de status quo te doorbreken. Dit door het redden van het gewricht met behulp van nieuwe methoden voor vroege diagnose en behandeling van artrose.

Zoals genoemd is de ziekte zeer complex en wordt deze pas in een laat stadium gediagnostiseerd. In de huidige situatie vindt diagnose plaats via een röntgen foto, vaak vele jaren na de start van de ziekte, waar slechts beperkte informatie uit gehaald kan worden over de specifieke ziektevorm die aanwezig is bij de patiënt. Dit vraagt om nieuwe diagnostische middelen, die de verschillende fenotypes van de ziekte kunnen identificeren in vroeg stadium om tot betere gepersonaliseerde behandelingen te komen. Een veelbelovende aanpak is het meten van biomarkers, die informatie geven over ziekte progressie, in het vocht van de beschadigde gewrichten. Dit vereist een gereedschap die meerdere biomarkers tegelijk kan meten, voor het identificeren van de verschillende fenotypes, met een hoge sensitiviteit, voor vroege diagnose, in kleine volumes van gewrichtsvocht. Op dit moment bestaat er echter nog geen diagnostische test die aan deze vereisten kan voldoen.

In deze these hebben we een diagnostische methode ontwikkeld op basis van surface plasmon resonance array imaging (SPRi) die ons in staat stelt om de gewenste biomarkers te meten in multiplex. Om de vereiste gevoeligheid voor vroege diagnose te behalen passen we een signaal versterkingscascade toe met behulp van goud nanodeeltjes. In een proof of concept study hebben we laten zien dat we relevante markers voor artrose kunnen meten in lage concentraties met een breed dynamisch bereik in multiplex in kleine volumes van gewrichtsvocht. Om de toepasbaarheid van deze methode in klinische setting te verbeteren hebben we een set instrumenten ontwikkeld voor kwaliteitscontrole, kalibratie vrije metingen en eenvoudige assay optimalisatie. Dit hebben we bereikt door het kinetisch definiëren van de SPRi versterkingscascade. Dit stelt ons in staat om het signaal te voorspellen op elke biomarker concentratie. Deze diagnostische methode heeft een grote potentie in de vroege specifieke diagnose van artrose en kan daarom helpen de effectiviteit van bestaande behandelingen te vergroten.

Om het gewricht te kunnen redden zijn er echter ook nieuwe verbeterde behandelingen nodig. Vroege behandeling van articulaire kraakbeen defecten hebben potentie laten zien. Veelbelovende resultaten zijn behaald bij het injecteren van een combinatie van cellen en biomaterialen in de beschadiging in het gewricht.

Hoewel injectie geschikt is voor kleine defecten, kunnen grotere irreguliere defecten profijt hebben van het sprayen van de cel-biomateriaal combinatie. In dit werk hebben we gekeken naar het effect van sprayen op de overleving van cellen na impact. We hebben een analytisch model ontwikkeld dat de cel overleving kan voorspellen op basis van spray parameters. We hebben laten zien dat de overleving afhankelijk is van de luchtdruk uitgeoefend op de spraykop, de impact afstand, viscositeit en de oppervlakte stijfheid. Bovendien laten we zien dat ons model deze processen accuraat beschrijft. Vervolgens hebben we het model uitgebreid door te bepalen wat het effect van celtype en cellulaire eigenschappen is op de overleving. Hierbij hebben we ook aangetoond dat het veranderen van de cel eigenschappen de overleving in sprayen kan helpen verbeteren. We zijn een stap verder gegaan door een controleerbare druppel impact set-up te ontwikkelen met als doel ons model extensief te valideren. Dit heeft geresulteerd in verder verbeteringen in ons model en zijn toepasbaarheid verbreed tot andere biofabricatie methoden. Om de spray behandeling verder te verbeteren hebben we ook gekeken naar het gesprayde biomateriaal. We hebben een instrumenten set ontwikkeld voor een optimaal biomateriaal voor gewricht herstel. We demonstreren een injecteerbare hydrogel met vrij kiesbare mechanische en biologische eigenschappen die aangepast kan worden om een optimale cel response te verkrijgen. Tezamen kan dit werk leiden tot het effectief toebrengen van optimale cel/biomateriaal combinaties in een gewricht met een hoge cel overleving, resulterend in een veelbelovende vroege behandeling.

Met de combinatie van nieuwe methode vroege diagnose en behandeling hebben we stappen gezet in het adresseren van de belangrijkste uitdagingen voor onze gewrichten. Hoewel geen enkele stap ooit groot genoeg is, geloven we dat dit werk een significante sprong is om het gewricht te redden.

Contents

“If we knew what we were doing, it wouldn’t be called research”

1

Introduction and motivation

1 Introduction

Osteoarthritis is a debilitating joint disease affecting an increasing part of the population. It is associated with intense pain, reduces mobility and significantly impairs quality of life. Currently over 2 million patients are diagnosed with OA in the Netherlands alone and this number is set to increase further due to an aging population. Unfortunately, the disease can only be diagnosed after significant symptoms are present. This diagnosis is acquired using X-Ray that enables only a general diagnosis of this highly heterogeneous disease.

At this late stage of diagnosis, the joint degradation has progressed for several years and effective treatment options are limited. Additionally, no effective treatment exists that can avoid or reverse the progression of the disease. Therefore, in current practice, patients enter the clinic with highly progressed disease and are dependent on physiotherapy, life-style changes and pain medication to manage symptoms until they are allegeable for total joint replacement.

Earlier specific diagnosis of the disease could not only improve the effectiveness of current standard treatments, it could also help provide targeted treatments tailored to specific patients to halt disease progression. Additionally, specific diagnosis could improve patient typing and provide a reliable clinical outcome parameter. This is essential for the development of new, drug based, treatments for OA. As mentioned above, besides early diagnosis effective treatments that can avoid or reduce the development of OA are currently lacking. Therefore the aims of this thesis are:

I. The development of a highly sensitive early detection method for the diagnosis of osteoarthritis.

II. The development of early treatments to avoid OA progression.

This chapter will provide a short introduction into the biology of the joint, the pathology of joint disease, and current practice in diagnosis and treatment. Following this a brief overview is presented of the chapters in this thesis in which the aims of this work are addressed.

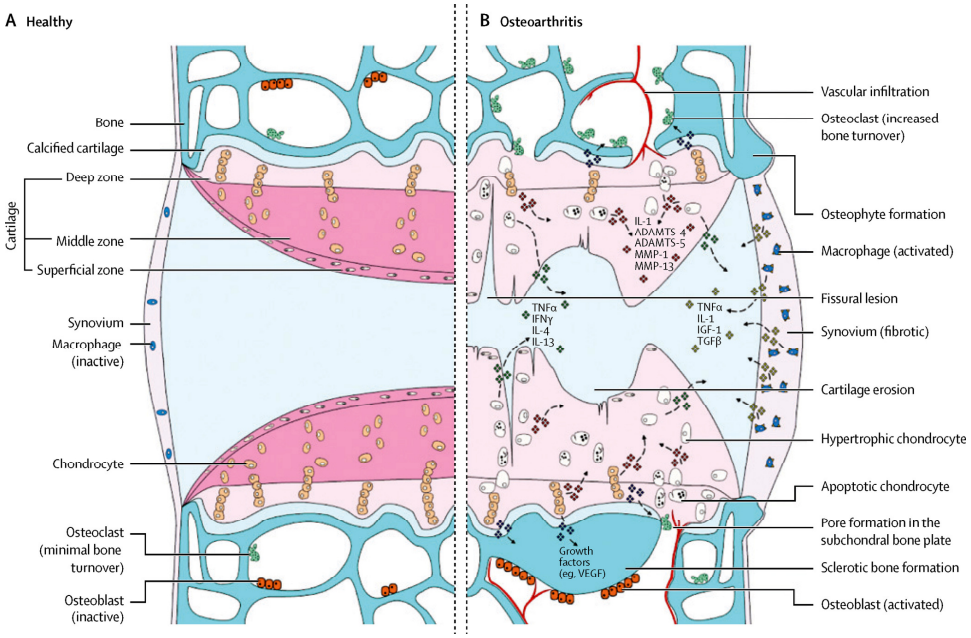

Figure 1: The biology of the joint and pathological changes that occur in osteoarthritis. reproduced with permission from [1].

The joint is an important component in our musco-skeletal system and ensures frictionless movement of connected skeletal bones. It is a complex organ consisting of many tissue types, including cartilage, subchondral bone, ligaments, synovium and synovial fluid (the knee joint is depicted in figure 1A). The hyaline cartilage is the defining tissue in joints and enables cushioning of impact and frictionless movement. This tissue is characterized by a low cell-density and is avascular and not innervated. This results in relatively limited tissue turnover and reduced repair capacity. The subchondral bone provides the connection between the cartilage and the bone parts. The ligaments ensure the joint stability and regulate freedom over movement. The synovium lines the inner surface of the capsule, produces synovial fluid that provides lubrication and nutrients to the cartilage tissue that helps maintain the integrity of the joint.

The cartilage consists mainly of ECM populated sparsely by articular chondrocytes. The ECM consists primarily of collagen type II fibres in combination with highly hydrophilic aggregan. This results in a spongy tissue with a combination of large tensile strength and cushioning capacity. When cartilage damage occurs, via acute trauma or slow progression in aging, the joint starts to slowly deteriorate. The joint starts to degrade itself by the production of proteolytic enzymes, such as MMPs (breakdown of mainly collagen) and ADAMTs (breakdown of aggregan). These enzymes are initially produced to enable remodelling and subsequent repair of the cartilage. However, due to the limited reparative capacity of the tissue, insults rapidly provide a bigger challenge than can be repaired. This results in a misbalance between anabolism and catabolism

and slowly results in joint degradation. This process is strengthened by pro-inflammatory cytokines, produced by chondrocytes and the synovium. The progression of the joint disease is associated with the development of osteophytes in the subchondral bone, which can lead to both a stabilization of the joint and to further cartilage damage. In later stages, the increased production of cytokines can result in an inflamed synovium, further increasing degradation and resulting in excessive pain. These processes finally result in an osteoarthritic joint with severely reduced cartilage content and quality reducing lubrication while increasing pain.

There are many pathways that can lead to a similar outcome: a severely degraded osteoarthritic joint. OA can be divided into four main categories that depend on the disease origin: post-traumatic, metabolic, aging and genetic. These categories are each influenced by different routes that lead to disease progression in specific magnitudes. For example, post-traumatic OA is strongly influenced by acute inflammation and mechanical instability, while aging OA is more associated with chronic inflammation, cellular senescence and reduced metabolic activity [2]. These differences have major implications for both the diagnosis and the effectiveness of subsequent treatments. In chapter 2 a literature review is presented in which the different pathways that result in OA are described. Individual processes that result in progression are highlighted and implications for treatment are stressed. This provides an overview in the state of the art of osteoarthritis research and describes the major challenges that needs to be addressed: Specific early diagnosis and directed early treatment.

In order to obtain specific early diagnosis new assays need to be developed. The most promising approach is to measure biomarkers related to individual processes implicated in the disease. Measuring these biomarkers in the synovial fluid, which is in contact with all joint tissues, could provide an early diagnosis even before symptoms are present. However, the complexity and multifactorial nature of the disease requires the detection of multiple classes of biomarkers with both high sensitivity and large dynamic range in small volumes of a complex fluid. As of yet, no biomarker assay exists that meets these challenging requirements. In chapter 3, we show the development of a biomarker assay based on surface plasmon resonance imaging (SPRi) for the early diagnosis of osteoarthritis. We demonstrate a nanoparticle signal enhancement cascade that allows us to measure biomarkers with a high sensitivity in a very broad dynamic range. Additionally, we show that we can measure four cytokines (IL-6, IL-1β, TNF-α, and IFN-γ), implicated in the disease, in multiplex with limited cross-reactivity. Finally, we show that these biomarkers can be measured with high precision even in undiluted synovial fluid. Thereby laying the groundwork for an effective early diagnostic tool for osteoarthritis diagnosis.

This diagnostic tool has significant potential for clinical application. Essential in this respect is the powerful quality control potential due to the real time measurements of antibody – biomarker interactions. In chapter 4 we demonstrate that we can fully characterize the enhancement cascade using reaction kinetics. This allows us to not only fit the cascade at any step to easily determine concentration, but also to predict the

entire cascade at any biomarker concentration. This enables the possibility to easily detect cross-reactivity, heterophilic antibodies, spotting irregularities and other confounder. This is essential for quality control in clinical application. Moreover, the predictions allow us to perform calibration free biomarkers measurements, saving time and resources. And finally, this toolbox enables simple optimization simulations that further allows for improvement of the diagnostic assay.

As mentioned above the current practice of osteoarthritis lacks both a specific early diagnosis and effective treatments to prevent or reduce disease progression. In chapter 3 and 4 we have made significant steps to address the first challenge, however it is essential that treatment options are expanded as well.

We set to explore a highly promising treatment of cartilage defects with a combination of cells and biomaterials. Promising results have already been shown by combining mesenchymal stromal cells MSCs and chondrocytes with fibrin glue in the impact trial [3]. This study demonstrates that cartilage damage can be repaired and disease progression may be delayed. These results were obtained by adding the cell/material mixture drop by drop to the defect.

In this procedure it is difficult to reach specific sites in the joint and large irregular defects are difficult to treat. Spraying the cell/material mixture allows for much better coverage of the wound and for the treatment of more advanced irregular defects often found in advanced stages of the disease. However, spraying of the cells could have a negative influence on the viability of the involved cells. In chapter 5 we demonstrate the development of an analytical model to predict cell survival during spray deposition. We subsequently validated this model using cell spray experiments. Here we show that the cell viability is dependent on the air pressure applied to the nozzle, impact distance, viscosity of the droplet and the substrate stiffness. Moreover we showed that we can accurately predict these dependencies with our model. This allows us to rationally improve our spray procedure to obtain optimal repair.

While this model has provided insight in the effect of the spray parameters on cell viability, the effect of cell type remains relatively unexplored. In chapter 6 we compared eight different cell types in spray experiments to elucidate the effect of cell type on cell survival. We showed that the cell type has indeed a large influence on the survival of the cells after spray deposition. We subsequently applied our analytical model to determine which cell property could be responsible for this large difference. Finally, we altered these cell properties in fibroblasts and showed that we can both increase and decrease the cell's resilience to the cell spray process.

These chapters provide practical insights to improve cell spraying for optimal application of cells in any treatment. However the heterogeneity of the spray which consists of relatively small and fast droplets makes it difficult to accurately determine the individual processes that are responsible for the observed cell death after impact on a surface. To further improve and validate our cell survival model and to broaden its application to other bioprinting applications, we developed a new method to investigate

survival upon impact in more detail in chapter 7. Using this set-up, we were able to create monodisperse droplets of a defined droplet size and control droplet impact at freely adjustable velocity. We showed that there is a direct influence of droplet velocity on cell viability that follows the relationship postulated by the earlier model. The relationship between the droplet size and viability however was shown to be opposite to the original model. Therefore, a new model was developed that accurately predicted cell survival in both small droplets such as used in cell spraying and in larger droplets normally used in printing, expanding its usefulness.

Besides an improvement in the application method of the cell treatment it is also important to provide biologically active and mechanically stable biomaterials. In chapter 8 we showed the versatility of polysaccharide-tyramine conjugates that crosslink in stable hydrogels using an enzymatic reaction. These hydrogels can be easily tuned in mechanical properties, crosslinking times and are highly biocompatible. However, the lack of cell attachment motives limits migration and remodelling. In this chapter we demonstrated the development of a toolbox to enhance these hydrogel with bioactive components. We showed that the addition of tyramine modified gelatin improved the attachment of cells and stimulated proliferation, migration and metabolic activity. This renders the above hydrogels highly suitable for cell therapy of cartilage defects.

In this thesis we have made steps to address the main challenges facing our joints today. The lack of early diagnosis and the lack of effective treatments. While no single step is ever large enough, we believe this work is a significant leap in saving the joint.

References

(1) Glyn-Jones, S.; Palmer, A. J. R.; Agricola, R.; Price, A. J.; Vincent, T. L.; Weinans, H.; Carr, A. J. *The Lancet* **2015**, *386*, 376-387.

(2) Loeser, R. F. *Current opinion in rheumatology* **2013**, *25*, 108-113.

(3) de Windt, T. S.; Vonk, L. A.; Slaper-Cortenbach, I. C.; Nizak, R.; van Rijen, M. H.; Saris, D. B. *Stem Cells* **2017**, *35*, 1984-1993.

1

“One may miss the (bio)mark by aiming too high as well as too low”

2

Joint Homeostasis – Implications for diagnosis and treatment

Osteoarthritis is a debilitating disease affecting increasing parts of the population. While significant improvement has been made in understanding the pathological mechanisms, no curative or disease modifying treatment are available at present. As a result, patients are still limited to symptom reducing medication and progression ultimately leads to total joint replacements. There are multiple reasons for this apparent lack of progress in effective management of OA. In this review, we have focussed on three main themes that help explain why the development of effective treatments remains extremely challenging. First, we discuss why the path to osteoarthritis matters. We describe the heterogeneity of the disease and focus on the three main phenotypes that are currently accepted: Aging OA, post-traumatic OA and metabolic OA. We provide an overview of the distinctions and describe the implications for progression and the development of potential treatments. Secondly, we focussed on the tightly controlled balance of the specific pathways that are involved in disease development. We describe the important pathways, including inflammation, WNT, TGF-beta, FGF and hypoxia. We show that the balance in the pathways is essential. Excessive, or inadequate activation can both result in disease progression. Therefore, successful application of pathway inhibitors or activators will be highly dependent on individual patients' joint homeostasis. Finally, we state the importance of the timing for treating OA. Several individual processes collectively contribute to disease progression, but occur at temporally separated time points. We provide examples showing that the correct timing is key for effective treatments. The described factors provide insight into why the development of treatments remain challenging, but they also have significant implications for how the disease should be

Jan Hendriks, Daniël B.F. Saris, Marcel Karperien

Manuscript in preparation

diagnosed. The large difference between phenotypes, the delicate balance between pathways and the importance of the timing require a highly specific and sensitively diagnosis of the disease. We therefore press the importance of developing reliable diagnostics assays, based on biomarkers measurements that provide detailed essential information on the joint homeostasis. This information is not only essential for early diagnosis and monitoring progression, but also for the highly desired development of effective treatments.

2.1 Introduction

Osteoarthritis is a disease of the joint as an organ involving the cartilage, sub-chondral bone, synovium, menisci, ligaments and the synovial fluid [1]. These joint tissues closely communicate with each other which leads to feedback loops that either strengthen or dampen the progression [2]. The disease is associated with progressive loss of cartilage, inflammation, formation of osteophytes, sub-chondral bone remodelling, impaired movement and pain. Many factors contribute to the disease, including genetics, sex, aging, trauma and obesity. While significant improvement has been made in recent years in understanding the pathological mechanisms, effective curative treatments are lacking. To date no adequate disease modifying drugs (DMOD) are available and curative treatments are left wanting. Therefore, patients are limited to symptom reducing medication. As a result, the progression will ultimate lead to total joint replacements.

There are several reasons for this apparent lack of progress in clinical outcomes. In this review, we will focus on three main themes that have received increasing attention in recent years and that are important factors explaining why developing effective treatments remains extremely challenging. These themes revolve around the high complexity of the disease and the multiple routes that ultimately lead to osteoarthritis. We will first focus on the heterogeneity of the disease. It has become increasingly clear that there is in fact no one type of osteoarthritis and therefore a universal medication is probably unrealistic. Secondly, we will focus on tightly controlled balance of specific pathways. This entails that certain medication, such as inflammatory mediators or Wnt-inhibitors can be beneficial for some, but harmful for others, and therefore require patient-specific dosing. Finally, we will focus on the importance of the right timing for specific treatments. There seems to be a specific window in which certain medication can be beneficial. If the window is missed, other treatments might be required. These three themes together can provide a framework to take into account when developing new treatments or to decide which existing treatments could be most beneficial for specific patients.

The importance of these factors in the disease progression suggests it is essential to accurately and more specifically asses the homeostasis of the joint. This can enable the delivery of effective treatment for a specific patient, but can also improve patient stratification in clinical trials. Moreover, the timing of this diagnosis is key due to the specific window in which treatments are most effective.

These findings also have significant implications for treatments that have been developed or are in development. The specific misbalance in homeostasis of the joint will determine whether treatments will be effective or fail. This results in challenges, but also provides great opportunities. For example, drugs that have failed in population wide clinical trials could very well be successful in specific patients with specific imbalance in joint homeostasis at a specific timing.

2.2 The path to osteoarthritis matters

Osteoarthritis is a heterogeneic disease with multiple risks factors and multiple pathways that eventually results in a relatively similar disease end-stage. This can be seen by the many methods to induce the disease in animal models, but is also clear in clinical practice. In recent years increasing attention has been given to this attribute of the disease, partially because of failure to develop effective treatments. Three main phenotypes have emerged: Aging OA, Post-traumatic OA and Metabolic OA [3]. These will by no means be all important phenotypes of OA, but can provide a good starting point to better understand why some treatments may work in some phenotypes and not in others.

2.2.1 Aging-OA

Aging represents a collection of processes leading to progressive deterioration of an organism's health and function. Remarkable progress has been made in the aging research field, which has given us a much better understanding of the processes involved. Nine main hallmarks of aging have been proposed: genomic instability, telomere attrition, epigenetic alterations, loss of proteostasis, deregulated nutrient sensing, mitochondrial dysfunction, cellular senescence, stem cell exhaustion, and altered intercellular communication [4]. Many of these processes have been shown to be involved in the development of osteoarthritis. In addition, together several of these processes lead to an increasingly stressed immune system and chronic inflammation, coined inflamm-aging by Franceschi et al. [5]. The influence of these processes on inflammation and OA progression is summarized in figure 1.

Inflamm-aging

Inflammation in arthritis is receiving a great deal of attention, both in basic research as well as in treatment development. It has been shown by many papers that inflammation markers, such as IL-1β, IL-6 and TNF-α, lead to the upregulation of matrix degradation enzymes and the downregulation of matrix proteins such as aggrecan and collagen II, often in a self-amplifying feedback loop [6]. Moreover, they are involved in disrupting mechanical properties of chondrocytes [7], de-regulating circadian rhythm [8] and can lead to cellular senescence [9]. It is therefore not surprising that higher levels of these markers are suspected to be involved in osteoarthritis development, and indeed many such correlations have been found [10, 11]. Considering this, it is highly relevant that these markers are increasing with age, partly due to accumulated antigenic stress [5]. This can be seen by a doubling in IL-6 and high sensitivity – CRP (HS-CRP) serum values in older individuals. However this increase is apparent in the entire older population, in both healthy and chronically ill individuals. This indicates that this chronic inflammation plays part in increasing susceptibility of older people for developing OA, but does not guarantee it.

Cellular Senescence

Another important hallmark of aging implicated in arthritis is cellular senescence. This process was initially discovered in fibroblasts after repeated cell divisions. The shortening of the telomeres leads to genomic instability and mitotic risks. In a tumour defence mechanism, cellular senescence pathways are activated leading to growth cycle arrest and the expression of a large variety of cytokines. This results in a specific phenotype called the secretory associated phenotype (SASP) [12]. This phenotype is believed to result in the activation of the immune system which subsequently leads to the removal of the senescent cells [4]. During aging however, the number of senescent cells starts to accumulate. This is possibly caused by a combination of increased genomic stress and a less efficient immune system. This increased number of cells with the SASP leads to an aggregate increase in cytokine concentration and therefore larger inflammation, possibly reducing regenerative capacity of tissue. It was thought that the low mitotic capacity of chondrocytes protects them from senescence and indeed only small amounts of senescent cells are found in healthy joints of old patients [13]. However, joints of OA patients do contain significant amounts of senescent cells, even though telomere length was not significantly different than in normal cartilage [14]. This indicates that other processes have resulted in the cellular senescence. Possibly due to stresses caused by inflammation [9], oxidation , and excessive loading [13]. This increase in senescent cells in the osteoarthritic joint can further increase the local inflammation and accelerate disease progression.

Proteostasis

The proteostasis encompasses the processes involved in the production, modification and recycling of proteins [15]. In normal conditions proteostasis maintains the health of cells in a range of stresses and protects against diseases mediated by excessive misfolding, aggregation, or degradation [16]. In aging however the stresses increase and the capacity to cope with these stresses diminishes. One example is the unfolded protein response (UPR). This response protects the endoplasmic reticulum (ER) from excessive stress by limiting protein production and by catalysing protein-folding [16]. Increasing activity of the UPR has been seen in OA chondrocytes, which may have been caused by, among others, biomechanical injury, IL-1β and nitric oxide (NO) [17]. Unsuccessful reduction of ER-stress by the UPR leads to increased inflammation, oxidative stress and apoptosis and could in turn contribute to OA pathogenesis. Another important proteostasis tool that could contribute to OA in aging is autophagy. Autophagy is an important process in which damaged organelles of cells are recycled and it has considerable chondroprotective effects [18]. However, it has been shown that the number of autophagosomes diminishes with age and that their size becomes smaller in mouse model [19]. In addition, the major autophagy control genes Atg5 and Lc3 are drastically reduced with age in cartilage in mice [20]. This reduction in effective autophagy with age could lead to increased inflammation [18] and apoptosis and therefore also contribute to disease development [20]. Interestingly, an increase in the autophagy repressor activity has been shown in both aging OA and post-traumatic OA [21] and reduction of this

repressor was protective in both phenotypes. Yet, the knock-out of the autophagy control genes only increased aging OA, with no effect on the MMT model. This suggest a different role for autophagy in these distinct phenotypes.

Mechanical stress in aging

The aging process has significant effect on the mechanical properties of the ECM in the cartilage and on the ability of chondrocytes to deal with these mechanical stresses. During aging the properties of the main components of the ECM, aggrecan and collagen II, are changing. The average core length and side chain length of the aggrecan protein is decreasing leading to reduced water retention [22]. Additionally adult aggrecan is significantly weaker in compression. This could lead to an altered loading profile and reduced nutrient supply. The collagen II network itself becomes increasingly crosslinked [23] due to the action of advanced glycation end products (AGEs) whereby the nanoelasticity of the fibres increases [24]. Together this results in a more stiff and brittle ECM. Besides this increased risk of damage to this ECM itself [25], the higher stiffness also results in an altered response of the chondrocytes which respond with the production of matrix degradation enzymes [23]. This in turn leads to the disruption of the peri-cellular matrix which results in closer contact of the chondrocytes to the interstitial cartilage matrix and further increase in matrix degradation. The stiffer matrix could also lead to dedifferentiation of chondrocytes resulting in hypertrophy [26]. In addition to changes to the ECM, the aging processes also influences the mechanical properties of the chondrocytes and their ability to respond to mechanical loading. For example, the stiffness of chondrocytes from older humans (>55 years old) is higher than from younger individuals (18-35 years old) [27]. Also, the chronic inflammatory state of the aging cartilage leads to a disruption of, and increase in, F-actin and to a more contractive state of the chondrocytes [28]. This together reduces their capacity to respond to loading. In addition, chondrocytes with an OA phenotype respond differently to loading. For example, dynamic compression induced a pro-anabolic response in healthy chondrocytes, but results in a pro-catabolic response in OA chondrocytes, indicated by upregulation of IL-1β and IL-6[29]. Therefore, loads that might be beneficial in healthy joints, could very well increase inflammation in aging joints. Together these processes lead to chondrocyte apoptosis, senescence and to a higher level of inflammation.

Implications

In the previous paragraphs we have described several processes that occur during aging that separately or in combination lead to an increased disbalance in the homeostasis of the joint. These processes are potentially damaging on their own, but also contribute to inflammation adding to the inflamm-aging phenotype. Consequently, homeostasis is disturbed by increasing susceptibility for degradation and decreasing regenerative capacity.

This however remains a delicate balance and is influenced by many factors. In addition, the ability of an individual to cope with these aggregate higher levels of inflammation is dependent on their genetic susceptibility and lifestyle [5]. Therefore by

no means all old people develop osteoarthritis, but their risk is considerably increased [30].

Higher levels of inflammation have inspired many researchers to develop anti-inflammatory drugs as treatments for OA, for example IL-1RA [31] and non-steroidal anti-inflammatory drugs (NSAIDS) [32, 33]. Partially encouraged by promising results of inflammation blockers in animal models and in vitro [34]. However, none of these blockers have proven successful in clinical trials [35] and NSAIDS have even shown to be detrimental to cartilage health [33]. The latter resulted in a 2% reduction in cartilage volume per year, leading to a 20% increased risk of joint replacement [36]. The lack of success of these drugs demonstrate several aspects of the disease. The success of drugs in post-traumatic animal OA models, normally performed in young animals, do not mean that these are effective in aging OA. Thus, the phenotype of the disease determines the effectivity of the treatment. Secondly, inflammation in aging comes from many sources and might in part be more a messenger than an active contributor. In addition, while there is a strong increase in aging of pro-inflammatory markers, there is also a strong increase in anti-inflammatory markers [37]. In a very interesting study by Morrisette-Thomas et al., elderly from the InCHIANTI cohort were followed and inflammatory markers in serum were correlated to mortality and chronic diseases [38]. The authors performed a principal component analysis to 19 inflammatory markers. They found two axes that correlated with mortality and chronic diseases, but in opposite direction. The first axis contained both pro and anti-inflammatory markers and was strongly predictive for mortality and multiple chronic diseases. They found that the variation between the pro vs. anti-inflammatory balance in individuals was relatively small, but that mainly the total amount of markers is predictive. This indicates that primarily the total level of activity of the immune system is of importance and can explain why anti-inflammatory drugs do not add much to the already high levels of natural inhibitors. The second axis that they found contained markers of the innate immune system (MCP, IL-12 and IL-8). Interestingly these markers were found to be protective for chronic diseases and mortality. Clearly suggesting not all inflammation is bad and provides an interesting avenue for further research.

The fact that so many processes during aging create a disbalance in joint homeostasis on their own, makes it very likely that no treatment targeting a single process will be fully effective in all patients. It is therefore very important that the disease state is carefully diagnosed, and that the dominant damaging process in a specific patient is recognised. Subsequently, drugs should be developed targeting some or all of these aging processes. We will focus on these subjects in more detail later in this review.

2.2.2 Post-Traumatic OA

A second major phenotype is OA that develops after major injuries to the joint. Well known examples are anterior crucial ligament rupture, meniscus tear or focal defects in the cartilage. These injuries often occur in young patients and lead to a major risk of developing OA in a relatively short time. As these patients are often too young for joint

replacements, delaying the disease progression or alleviating symptoms are major clinical priorities. While the end-stage disease of post-traumatic OA and aging OA is relatively similar, the path towards this end-stage is markedly different. This is important to recognise and has significant implications for the effectivity of treatments. The main contributors of trauma on OA progression is summarized in figure 1.

Post-traumatic OA is the most studied phenotype of OA in animal models. Well known examples are the destabilization of medial meniscus model (DMM) and the anterior cruciate ligament transection (ACLT) [39].

A major trauma to the joint results in an acute and intense inflammation. This inflammation is partially caused by the release of damage associated molecular patterns (DAMPs) [40] and is more intense in young than in old patients, yet results in better recovery in young patients [41, 42]. The inflammatory response attracts immune cells and leads to the initiation of repair [42]. However, the immune response also leads to the increase in matrix degradation enzymes and to a generally catabolic environment [6]. Additionally the continued mechanical stress and inflammatory environment leads to the accumulation of cells with the SASP, further increasing inflammation [43]. While this is required for tissue remodelling, there might be a delicate balance to take into account. Successful repair can lead to a reduction of inflammation and limited subsequent degeneration. In a majority of patients however, repair of the tissue is not possible leading to altered biomechanics and continued chronic inflammation. While surgical procedures can help improve the biomechanics and reduce mechanical stress, they often do not result in a complete resolve of the inflammatory homeostasis [44]. This increased inflammatory state and mechanical damage eventually results in the development of post-traumatic OA.

Despite the similarities between end-stage post-traumatic OA and aging-OA, the pathways to these phenotypes are considerably differentand lead to different responses to treatments. For example inflammation mediators show significant promise of protecting the joint from OA development in several animal models[31, 43]. In addition, treatments with specific exercise could potentially be highly beneficial [45]. We will focus on these treatments in more detail in the final paragraph.

2.2.3 Metabolic OA

A third important phenotype of OA results from the metabolic syndrome and is associated with obesity. This phenotype often co-exist with Aging OA, but has several specific pathways that increase the pathological risk (summarized in figure 1).

It has been shown that the systemic level of adipokines and inflammatory markers is increased in patients with metabolic syndrome [46]. These adipokines could also leak from the infra-patellar fat pad into the joint and disturb homeostasis. It has been demonstrated that several of these adipokines, for example leptin [47], result in a pro-catabolic response in chondrocytes. Moreover, the metabolic syndrome is associated with hypercholesterolemia. This condition results in mitochondrial dysfunction [48] and

could further promote inflammation [49]. In addition obesity results in increased and abnormal loading. This in combination with an inflammatory environment could lead to failure of chondrocytes to adequately adapt and result in apoptosis or senescence [50].

The combination of these factors creates risk for developing OA. This process is often synergetic with aging, as fat tissue increases with aging [46], and leads to 20% higher chance of developing OA than in aging individuals who are not obese [30]

Treatments for this phenotype could focus on the same processes that are associated with the aging phenotype, since they are often intertwined. However, specific treatments for this phenotype could provide additional benefit. An obvious treatment is weight loss through diet and or exercise. This can reduce loading, metabolic syndrome and systemic inflammation [51]. Additional treatments that have shown potential are the application of statins and mitochondrial protectants [48]. We will focus on this in more detail later.

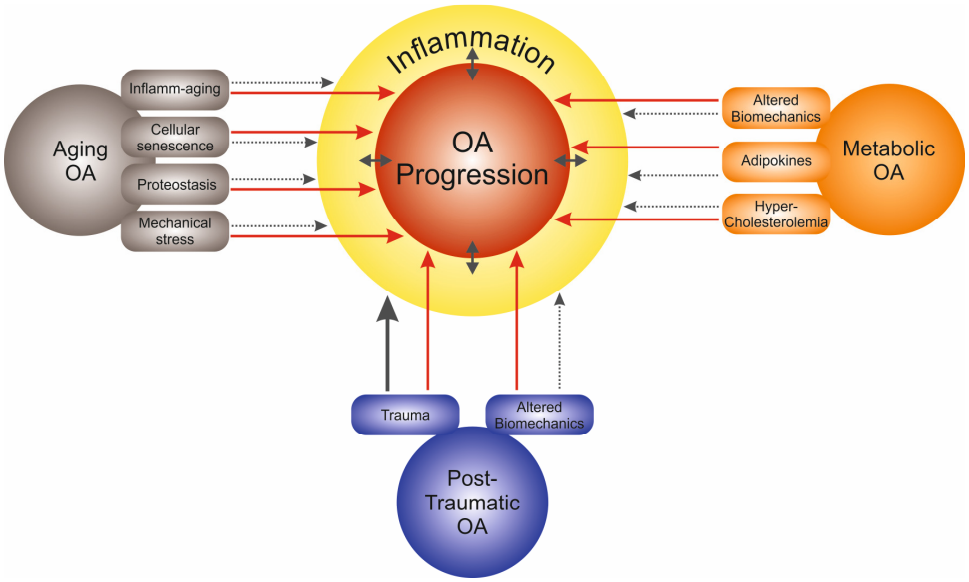

Figure 1. Major specific processes that drive OA progression in the different phenotypes. The influence of individual processes on OA progression is shown with red arrows and their contribution to the inflammatory state is depicted in grey. The truncated arrows indicate a transient increase, while the fixed arrows describe more acute interactions. We have chosen to show the interaction between the individual processes and inflammation and the interplay between inflammation and OA progression in grey, to demonstrate the controversy in cause and effect.

2.3 It all about the balance

It is clear that the phenotype of OA is important for diagnosis, but also for effective treatment. However, within these phenotypes several pathways contribute to the disease and these pathways are not active to the same extend in all patients. Moreover, it has become increasingly clear that while over-activity of specific pathways can be detrimental, underactivity can be destructive as well. Therefore, it really is all about the

balance. This further complicates giving the most beneficial treatment to a specific patient and could in part explain why some treatments fail in a subset of patients, even from the same major phenotype. In this section we will focus on some pathways important in the development of OA and provide examples of this often delicate balance.

2.3.1 Inflammation

In the previous section we have shown that many processes in the pathophysiology of osteoarthritis lead to the increase in inflammatory markers. These markers can result in increased matrix catabolism and therefore are often considered as bad. However, the reality is a bit more complex. In a mouse study, De Hooge et al. knocked-out IL-6 to determine the effect on spontaneous aging OA and collagenase induced post-traumatic OA [52]. They found that spontaneous aging OA was more severe in IL-6 knock-out male mice, but not in female, than in wild type specimens. This indicates that a certain level of IL-6 is necessary and can help reduce OA progression. Interestingly, there was no marked difference in the post-traumatic OA development, again demonstrating the importance to differentiate between phenotypes. Additionally, the difference between male and female mice indicates further complexity. The rela protein is a key subunit required in NF-κB signalling and is therefore associated with inflammation [53]. Knock-out of Rela was therefore expected to result in less severe OA development. However, homozygous deletion of Rela resulted in more severe OA, mediated by increased chondrocyte apoptosis, despite dramatic reduction in inflammation. In contrast, haploinsufficiency protected against DMM induced post-traumatic OA development. Similar results were obtained with a low dose of an IKK small molecule inhibitor (BMS-345541) to partially reduce this signalling [3]. This confirms that some inflammation is required for healthy tissue homeostasis.

Even in the process of cell senescence and in other cell damage, the inflammatory response serves to recruit the immune system to clear the non-functioning cells. This results in a reduction of damaged cells and therefore a healthier joint. It only becomes problematic if the damage to cells outpaces the ability of the immune system to clear them and inflammation increases. However, even in these situations blocking the low grade inflammatory response to a too large extent might do more harm than good. Therefore, anti-inflammatory treatments should be carefully designed and preferably adapted to the disbalance in homeostasis of a specific patient.

2.3.2 WNT

The Wnt pathway is extremely important in the development of organisms, in tissue homeostasis and is a major player in disease in adult life [54]. A certain level of Wnt activation is required to maintain the articular phenotype of chondrocytes and an over stimulation results in hypertrophic differentiation which is detrimental for articular cartilage health [55]. For this reason Wnt has been implicated in OA development and has received considerable attention.

The main Wnt pathway involved in OA pathophysiology is the canonical pathway in which upon activation, β-catenin is translocated to the nucleus. This results in activation of downstream transcription activity and finally to a switch from SOX-9 dominated transcription towards RUNX-2 dominant transcription and thus in increased hypertrophy [56].

The Wnt signalling pathway can be activated by 19 members of the Wnt family of secreted glycoproteins and is regulated on several levels [54]. It is regulated by direct inhibitors to Wnts, binders to co-receptors, competition for receptors by other types of Wnts of different potencies, it is regulated on transcriptional levels and has significant epigenetic control [57]. It has been shown that several regulation mechanisms of Wnt are reduced in aging and OA development. As an example the secreted Wnt antagonists DKK1 and sFRP3 (FRZB) are suggested to function as natural breaks on hypertrophic differentiation. In addition they can prevent catabolic degradation of cartilage caused by IL-1β stimulation [58] and protect subchondral bone [59]. However, they are significantly downregulated in OA cartilage [56] and lower concentrations are measured in synovial fluid of OA patients [60]. Interestingly, while these markers are reduced with age, no difference was seen between healthy and acute post-traumatic patients [61]. Indicating the Wnt pathway might be implicated in a later stage in the post-traumatic phenotype. In addition, it has been shown that loss of another antagonist sclerostin also promotes osteoarthritis [62]. Similarly, enhancer of zeste homolog 2 (EZH2) which can inhibit gene expression through methylation of histone H33 lysine 27 (H3K27) is increased in chondrocytes with OA compared with healthy controls. This results in reduced sFRP1 expression and increased Wnt activation [63].

Since Wnts are implicated in OA development it is again reasonable to assume that blocking Wnt/β-catenin pathway can result in reduced progression. However, the delicate balance of Wnt activation creates complications for simple Wnt-blockers. Two studies have demonstrated this delicate balance by either activating or blocking the β-catenin signalling in animal models. They showed that both activation [55] and blocking [64] Wnt signalling resulted in cartilage breakdown and OA. Moreover, not all Wnt activators are bad for cartilage. As an example, Wnt-16 is most strongly associated with post-traumatic OA development. Upon trauma this Wnt is strongly activated and therefore was assumed to be involved in disease development. However, blocking of this Wnt resulted in a more severe OA phenotype in a DMM model, presumably caused by lack of lubricin (proteoglycan 4) upregulation [65]. Apparently Wnt-16 is required for the phenotype of superficial zone (SZ) chondrocytes, the production of lubricin and is upregulated in response to tissue damage. This Wnt-16 can compete with Wnt-3a and reduce canonical signalling [57].

It is therefore important that if Wnts are blocked to block the right ones and only to a certain extent. Evidence for this delicate balance is demonstrated in the promising clinical randomized, controlled, phase I trial for Wnt-blocker SM04690 [66]. While this study was exploratory and focussed on safety, several interesting preliminary results were found. The patients who received the blockers showed improvement in all

exploratory efficacy measures. Significant improvement in joint space width was also observed, but only in the medium dosage and not in the high or low dosage. And after 24 weeks the lowest dosage started to outperform the medium and high dosage in cartilage turnover markers. This possibly confirms the importance of delicately balancing the Wnt activation and also demonstrates the importance of timing. It is therefore reasonable that the effect of promising drugs like Wnt blockers can be highly beneficial for some patients and possible detrimental for others. A careful assessment of the disbalance in joint homeostasis of a specific patient is therefore important.

2.3.3 FGF, TGF-beta and hypoxia

Other pathways similarly show this delicate balance in anabolic or catabolic potential for OA development. In the fibroblast growth factor (FGF) pathway it was shown that the knock-out of FGF receptor FGFR1 resulted in less severe proteoglycan loss at 12 months of age and reduced cartilage lesion in the DMM model [67]. In contrast, knock-out of FGFR3 resulted in more severe OA with age [68]. This indicates a protective function for FGFR3 and a destructive function for FGFR1 [69] and demonstrate the paradoxical role of bFGF. Similarly, the transforming growth factor (TGF) alpha and beta has been implicated in OA development. However, the role of TGFs is relatively complex and dependent on phenotype and possibly timing. For example, TGF-α knock-out was protective against post-traumatic OA in young mice (10 weeks old), but not in middle aged mice (6 months old). Also, no protective effect was seen in the aging model, again showing the differences in response between phenotypes. Blocking of TGF-β by systemic injection of a neutralizing antibody (1D11) resulted in reduced ACTL-induced post-traumatic OA in mice. However, high dose of this antibody resulted in thinner hyaline cartilage and proteoglycan loss, suggesting that a certain level of TGF-β is required for bone and cartilage integrity [70]. Similar pro- [71] and anti-catabolic [16] effects were also shown at the level of transcription factors for the hypoxia inducible transcription factor HIF-2α.

This provides further evidence that special care should be taken when developing therapies for OA to restore the balance of specific pathways. These pathways are not on-off switches and might be more active in some patients than in others. Careful diagnosis of the activity of specific pathways can provide the basis for the most effective rebalancing medication for a specific patient. How the pathways described above influence OA progression is illustrated in figure 2.

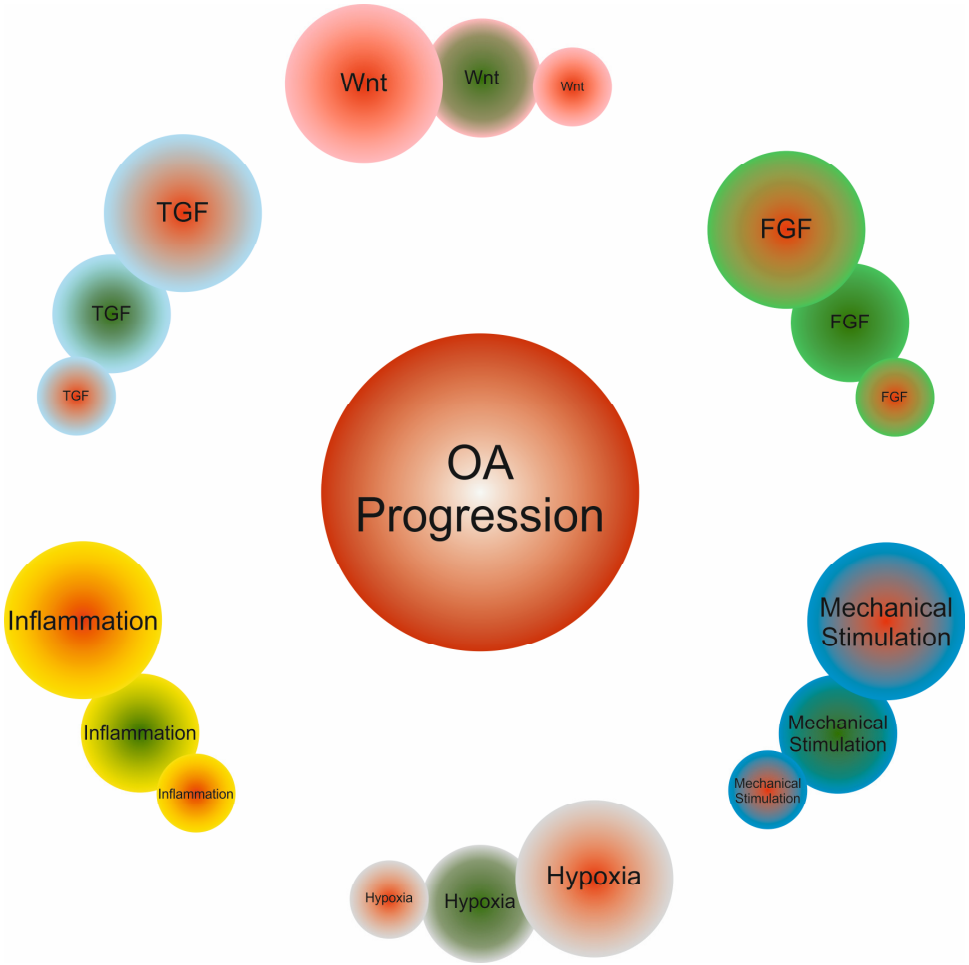

Figure 2. Illustrates how the balance of specific pathways influences OA progression. For each of these pathways too much or too little activity results in aggravating OA progression. Over-activity is illustrated with large circles, while under-activity is illustrated with small circles. A red inner centre indicates a pathway is aggravating OA, while a green inner centre indicates that a pathway is protective against OA.

2.4 Timing is key

Next to the importance of the correct phenotype and the delicate balance of specific pathways, the timing of events in the pathophysiology of OA could have significant impact on the effectivity of treatments. In the subsequent paragraph, we will provide several examples which demonstrate the importance of applying the correct timing for a specific treatment.

In post-traumatic OA the importance of timing has been shown in several animal studies. In a study by Longobardi et al., the CCL2 chemokine receptor CCR2 was inhibited transiently by a small molecule RS504393. The inhibition was timed together

with post-traumatic OA induction surgery, 4 weeks after surgery of 8 weeks after surgery [72]. Here they showed that treatment was only effective and resulted in joint protection if started together with surgery or 4 weeks after surgery. When the treatment was started 8 weeks after surgery there was a reduced protective effect. Interestingly sustained therapy for at least 8 weeks also resulted in a reduced protective effect. This indicates that a transient reduction of the inflammatory response upon trauma could be protective when applied immediately or shortly after injury and can help reduce the intensity of the acute inflammatory response. But sustained reduction of this inflammatory response could prevent adequate healing response. In different studies, inflammatory mediators were applied immediately after post-traumatic OA induction surgery and were shown to be protective [31, 34]. It would be interesting to see if these therapies are also as dependent on timing or could result in beneficial effects when applied at later stages. In a study investigating the effect of exercise on rats that underwent DMM surgery, Lijima et al. assigned rats to either a sedentary or walking group that had access to a treadmill [45]. The walking rats showed improvement on all outcomes in comparison with the sedentary group, with lower OARSI score, more toluidine blue staining and more collage type II staining. The group that had access during the last 4 weeks of the total 8 weeks performed slightly better than the other groups. Together this indicates that immediate treatment with anti-inflammatory drugs combined with delayed treatment with exercise could probably be beneficial for improved outcomes.

In aging and metabolic OA the pathway to OA occurs in the space of years and therefore the importance of acute timing is reduced. Yet, also in these phenotypes the chances of successful recovery or even prevention of the disease greatly diminish with time. Besides continued reduced capacity of repair in aging cartilage, changes during OA lead to a reduced ability of the chondrocytes to respond to therapy. As mentioned before, OA chondrocytes react with a catabolic response to a level mechanical stimulation that is anabolic in healthy chondrocytes. Yet mouse studies have shown that exercise can be protective against age related OA, partially by upregulating lubricin [73]. Therefore early exercise in patients that are on the path to developing OA could prevent further degradation, while the same exercise in progressed patients could further deteriorate the joint. Similarly, our group has shown that certain blockers of IL-1β and Wnt are protective in healthy chondrocytes, but result in no effect in OA chondrocytes (unpublished data). It is therefore possible that treatments of end-stage OA with these agents is ineffective, but could save the joint when applied on time. In metabolic OA similar reasoning applies. The earlier we can reduce the metabolic stress on the joint, the lower the risk of developing pathological OA develops.

Therefore, the timing in which we treatments are applied could be of significant importance for successful protection from OA and correct timing could potentially lead to an adequate recovery. However, in aging- or metabolic OA patients are often first diagnosed after they complained of pain symptoms and when the disease has progressed to Kellgren and Lawrence scale (K&L) grade 2-3. In this stage the disease is fully mature and key windows for protective treatments may have been missed. To better treat these

patients we need earlier and more specific diagnostic tools. How timing can influence the key window for specific treatments is shown in figure 3.

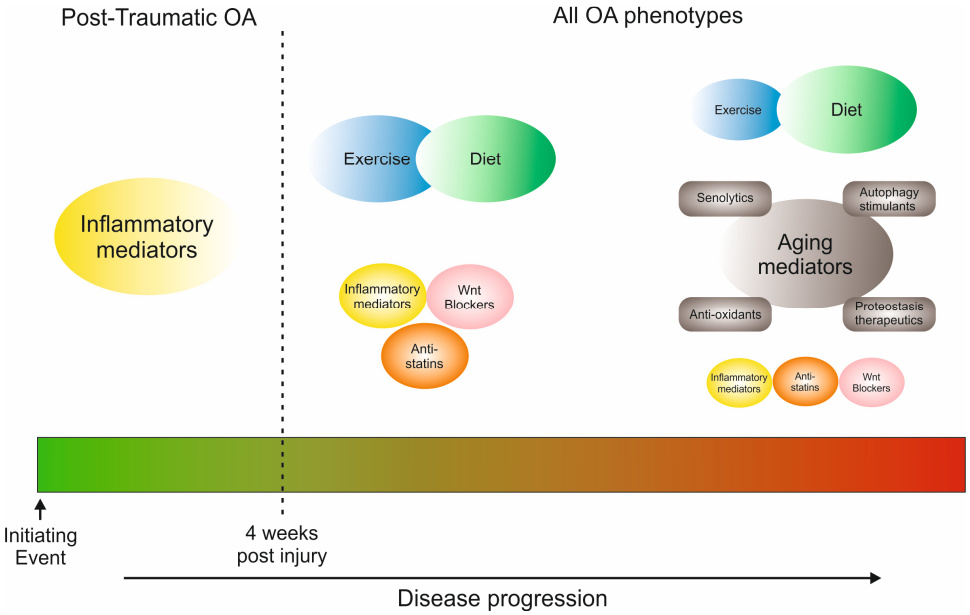

Figure 3. Timing is key: implication of timing for effectivity of OA treatments. From left to right the progression of the disease is illustrated on a non-linear scale. From onset of disease, mainly of relevance for post-traumatic OA, there is a short time span of ~4 weeks in which inflammatory mediators can be protective for OA development. In early OA progression, there is a strong case for applying a combination of exercise and diet. Additionally, inflammatory mediators, Wnt blockers and statins (metabolic OA) could be beneficial. In late stage OA, exercise should be more carefully applied and likely aging mediators are required. This could be combined with inflammatory mediators, Wnt blockers and anti-statins.

2.5 Implications for diagnosis

The previous paragraphs have described some of the factors that are involved in the large challenge of developing effective treatments for OA, but they also have significant implications for how we should diagnose the disease. Clearly there are large differences between the different phenotypes, of which we have only described three, there is a large influence of the activity level of specific pathways and the timing of diagnosis is important. However, in the clinical situation the gold standard for the diagnosis of OA is still an x-ray and subsequent K&L scoring [74]. This makes early diagnosis highly challenging [75], and provides little information on the specific phenotype of OA. Additionally, information on the activity of specific pathways is missed. When applying therapies to patients based on x-ray, only treatments can be given that are beneficial for all phenotypes. Regrettably, the complexity of the disease makes it highly unlikely that these therapies will be found. Targeted therapies optimized to improve the specific homeostasis of a specific patient could have large potential to modify or even prevent

the development of osteoarthritis. However, this requires more sophisticated diagnostic tools.

In order to receive a comprehensive overview of processes that contribute to the development of OA in a specific patient it is important to measure relevant biomarkers [76]. As most processes are a result of delicate balances it is likely that biochemical biomarkers will be most accurate and that multiple biomarkers should be measured. For example for aging OA it will probably be necessary to measure biomarkers from the processes that result from the hallmarks of aging as described before, to determine the dominant process that contributes most to the disease development in this patient. This process can subsequently be targeted. Biomarkers for many of these processes exist and can provide information on successful or unsuccessful aging [77]. Similarly, biomarkers from the Wnt, FGF and TGF-β pathways should be measured. For example, the levels of antagonists, DKK1 and FRZB in case of Wnt, could indicate whether patients would benefit from specific blockers or whether they would do harm. Additionally, highly validated biomarkers for cartilage turnover such as COMP and uCTX-II [78] could provide information on progression and whether treatments are effective, yet are less informative about phenotype or treatment directive. The same is probably true for inflammation markers, both pro and anti-inflammatory. While they are both increased in OA joints, it is possible they are the aggregate result of many damaging processes and are more a measure of stress, than a highly active contributor. Therefore, they can serve as a benchmark to determine health state of a joint and possibly provide some information on progression, but care should be taken in deducing underlying pathologies from these markers. The interesting result from Morrisette-Thomas et al. [38] showed that inflammation markers associated with innate immunity could be protective from OA and could be a measure for coping capacity of individuals. In post-traumatic OA, the importance of especially the inflammatory markers is likely higher. The concentrations of these markers after acute injury reaches high levels that can seriously damage the cartilage in the short term. Over-activity of these markers could therefore be a reason to start anti-inflammatory treatment. The other markers mentioned for aging OA will probably also be of importance after the acute phase. Even the markers for aging processes, as the degenerative environment will lead to accelerated local aging. In metabolic OA, markers of oxidative stress, cholesterol levels and adipokines could be additionally measured to provide information on disease development and on treatment success. A summary of important biomarkers for each of the processes is depicted in figure 4.

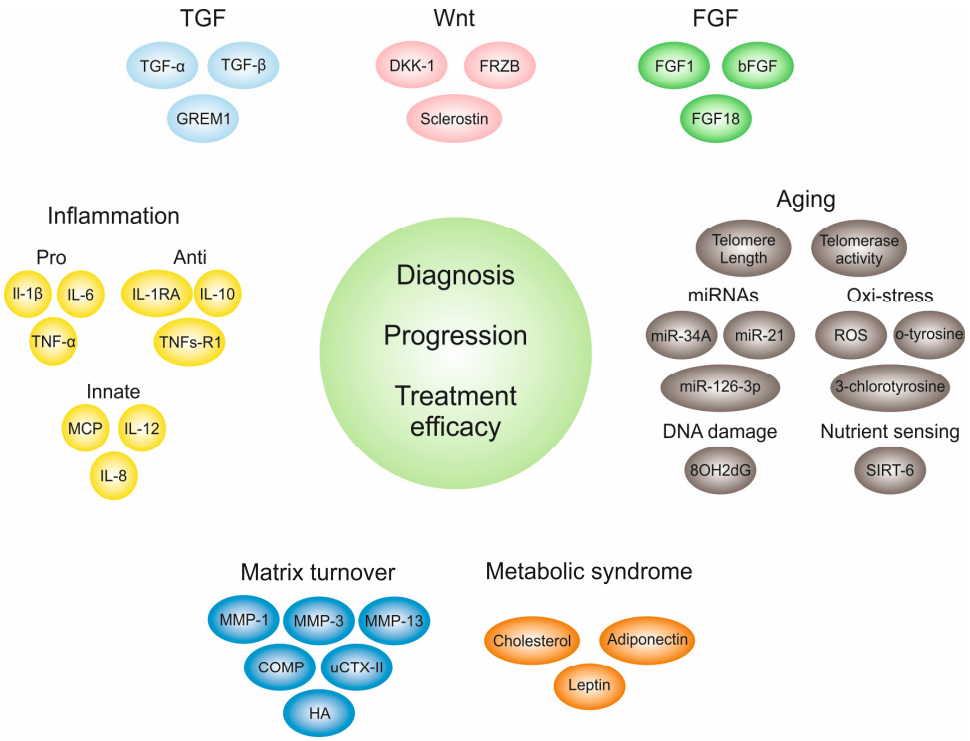

Figure 4. Overview of some of the biomarkers that are involved in the processes leading to OA. This figure demonstrates many of the processes that should be measured to gain meaningful insight in the joint homeostasis.

It is not only important to measure a broad spectrum of markers simultaneously, but also to measure them in an early disease stage. This is because the timing of treatment is very important in the success rate. However, this poses several challenges. First the concentration of some of the markers associated with disease development will likely be relatively low, or the relative change will be small, in an early stage. This is especially true if those markers are measured in the serum. This could be improved by more sensitive immunoassays, but also by measuring closer to the action, e.g. by measuring in the synovial fluid. A second challenge is that most patients do not know that they have early OA until the disease has progressed to a stage where pain becomes an issue. Why would we measure biomarker concentrations in healthy people with no symptoms? This is an important question to be addressed. A logical answer would be: because they have a high risk of developing the disease. Screening elderly, people with history of joint injury or individuals with metabolic syndrome could help identify disease progression in an early stage when any treatments are likely to be more effective.

2.6 Perspectives for translation

We have described the importance of an accurate and early assessment of the homeostasis of the joint in order to improve treatments. We have shown that several treatments that were considered promising in animal models failed in specific phenotypes or in subset of patients. In order to improve the efficacy of treatments, the pathophysiology that resulted in OA in specific patients should be taken into account. Therefore, the phenotype of OA, the activity specific pathways and timing should be considered. In this section, we describe several recent promising treatments for OA and indicate how patient selection and targeted treatment would improve the effectiveness of these treatments.

2.6.1 Inflammation mediators

As mentioned previously inflammation is receiving a lot of attention in the OA field and several treatments based on inflammation mediators are being proposed. In 2017 two randomized trials were reported on non-steroidal anti-inflammatory drugs (NSAIDS) Zilretta and Triamcinolone in aging OA patients. As the retention time of NSAIDs in the joint is relatively short, a sustained drug delivery system based on poly(lactic-co-glycolic acid) (PLGA) microbeads was developed and was approved by the FDA [32]. While this could in potential be interesting for sustained release of drugs, the long term efficacy of Zilretta was not significantly improved vs free injection. Additionally, while the main rational for injecting NSAIDs, pain relieve, was, the drugs may have caused considerable damage to the cartilage [33]. This was demonstrated in a clinical trial involving Triamcinolone injections. Here they showed that sustained injections in a period of two years resulted in 2% extra cartilage degradation per year. This could be caused by side effects of the drugs or by disrupting the balance of inflammation in a negative way. It is however also possible that the pain relieve allowed the patients to overload the OA joint leading to catabolic responses. The exact mechanism is of interest to improve treatments, but it shows that these types of drugs are not ideal to treat aging OA patients. Other inflammatory mediators have also been combined with drug delivery systems to increase retention in the joint. For example IL-1RA was combined with PLGA microspheres [31] and dexamethasone was attached to positively charged avidin to achieve electrostatic retention in the cartilage [79]. These treatments might result in longer reduction of inflammation in the joint, however as shown with the NSAIDs this might not help the aging OA joint in the long term. Therefore, these treatments are likely to be most promising for mediating the acute inflammatory response in post-traumatic patients. As it has been shown that immediate (<4 weeks post injury) anti-inflammatory treatment can be protective for post-traumatic OA. However, because continues injections were not protective, the sustained release might become a disadvantage if not carefully orchestrated.

Other cell based approaches to mediate inflammation have emerged in recent years. They either involve the injection of mesenchymal stromal cells (MSCs), which act as trophic mediators, or extracellular vesicles originating from these cells [80]. These vesicles

can contain cytokines, growth factors and other proteins, mRNAs and micro RNAs and can modulate the joint homeostasis [81]. Additionally, these vesicles can be loaded with specific drugs to further improve their potential. This might be an interesting therapeutic in especially early treatments, but could also be useful in late stage disease.

2.6.2 Addressing aging

To effectively treat aging OA it is likely that more targeted treatments are required than only reducing inflammation. As mentioned before many processes are involved in aging that contribute to OA and could be a target for therapy. Of these processes, cellular senescence has received most attention recently.

2.6.3 Senolytic agents

In aging tissue and in tissues developing OA, there is an accumulation of cells with the SASP that could lead to a catabolic local environment. This seems to be a major player in aging and in several chronic diseases. Therefore many group have started developing agents to specifically target and kill these cells, called senolytics. The agent ABT263 (Navitoclax) could selectively kill senescent cells in mice and resulted in rejuvenation of aged hematopoietic and muscle stems cells [82]. Similarly, the small molecule ABT-737 resulted in apoptosis of senescent cells and improved hair-follicle stem cell proliferation. In a different approach Baar et al. [83] designed a small peptide that binds to p53, also resulting in initiation of apoptosis of senescent cells. Specifically, this resulted in effective clearance of these cells in mice and rejuvenation, shown by regrowth of hairs, improved activity and renal function. Senolytic agents have also found their way to osteoarthritis. In very promising study Jeon et al. used senolytic agents ganciclovir and UBX0101 to selectively target senescent cells in the joint [43]. They used three OA mouse models. An aging OA model, post-traumatic OA model and a combination of both. They found that the number of senescent cells increased in all models of OA. Removing the senescent cells with senolytic treatment resulted in anabolic gene expression profiles and reduced joint damage scores in both aging OA and post-traumatic OA. However, the beneficial effects were smaller in the combination of post-traumatic and aging OA. These results are very promising and could aid in an effective treatment of several phenotypes of OA by providing a durable improvement of the homeostasis of the joint.

2.6.4 Targeting other factors of aging

Other processes of aging that could be targeted in OA are oxidative stress, autophagy and ER stress. Some promising results in these area have already been shown. Farnaghi et al. applied a mitochondria specific anti-oxidant (Mito-Tempo) and demonstrated positive effects on cartilage damage [48]. To study the effect of autophagy, OA was induced in rabbits with collagenase treatment either with autophagy inhibitor (3-MA) or activator (Torin-1) [84]. It was shown that inhibition of autophagy aggravated OA development, while activation reduced severity. This demonstrates that autophagy activators could have potential for attenuating OA. The therapeutic potential in reducing ER stress has been recognised [85]. However few studies are performed applying

therapeutics in this direction in OA. Possible avenues exist and could involve inhibiting ER stress responses (with small molecule inhibitors of eIF2a [86], PERK [87, 88], or IRE [89], stimulating chaperone-assisted protein folding (by pharmacological treatment with BiPX, a BiP protein inducer or with chemical chaperone 4-phenyl-butyrate, PBA [90]), and/or enhancing degradation of misfolded protein [85]. In a rat study, Chen et al. reduced ER stress by adding liraglutide, an activator of glucagon-like peptide-1 receptor (GLP-1R) [91]. They showed that this treatment significantly reduced the severity of cartilage degeneration and therefore provided evidence of the potential of this approach.

It is likely that activity of specific aging processes is more pronounced in different subpopulations of patients. Therefore, careful diagnosis of patients could help in determining which targeted treatment might have most potential. Additionally, it is likely that a combination of aging processes should be targeted to deliver the switch to an anabolic joint homeostasis.

2.6.5 Wnt treatment

Targeting specific treatments involved in OA could be promising in specific patients with increased pathway activity. Last year a promising phase I clinical trial was performed testing the safety of Wnt blocker SM04690 [66]. In this trial they compared injection of 0.03 mg, 0.07 mg and 0.23 mg of Wnt blocker with placebo. They showed beneficial effect of this blocker, but only at lower concentrations. We await the results of a phase II trial, but when applied to patients with for example reduced Wnt antagonists, this could be a very promising disease modifying treatment.

2.6.6 Systemic treatments

While our understanding of the pathological mechanisms of OA and aging is improving, resulting in new and better targets for medication, systemic approaches for improving the joint environment are still not used to its full potential [92].

Exercise has shown to lead to increase lubricin expression [45], reduced systemic inflammation markers [51, 93], and results in anabolic response of chondrocytes when applied in an early stage of OA [29]. Moreover, it has been shown that exercise can improve several markers associated with aging [93, 94], such as increased telomerase activity, reduced oxidative stress, reduced DNA damage, lower cortisol levels and reduced inflamm-aging [93], and can prevent the accumulation of senescent cells [95]. It increases muscle strength, improves stability of the joint and increases GAG [96] content. Additionally, it results in weight loss, and therefore improves healthy loading, and reduces metabolic syndrome related pathology [51]. Together this can result in patients being protected from all phenotypes of OA by improving all pathways that are involved. However, it is likely that the story becomes more complicated in more advanced OA. The OA joint is less responsive to the beneficial effect of mechanical stimulation and chondrocytes might show a catabolic response. Therefore, the intensity of the exercise should be carefully balanced and adjusted to the situation of a specific patient. The pain associated with OA might also result in less compliance of patients with exercise therapy.

It is therefore important to realise that many of the beneficial effects of exercise are systemic and do not necessary need to involve the affected joint [97]. Exercises can therefore focus on other body parts and slowly work towards the joint as pain levels improve.

Diet is an excellent synergic treatment together with exercise for many patients with risk of developing OA. It can help in achieving weight loss and reducing adipose tissue levels [98]. It improves cholesterol levels [99] and reduces level of adipokines and systemic inflammation [100]. Therefore it can protect from the development of metabolic OA, but also aging OA.

A third systemic approach in improving treatment for OA is by considering mental health. Mental health has been associated pain levels [101] and quality of sleep. Additionally close feedbacks loops exist between psychological stress and systemic inflammation [102]. As pain [103-105], circadian rhythm [8] and inflammation are directly involved in osteoarthritis pathophysiology, this makes mental health an important parameter to consider when treating patients. Therefore, it is clear that reduced mental health is not only a result of pain and inflammation in OA, but also actively contributes to the disease development. Adequate psychological treatment could improve pain levels [106], sleeping quality and reduce systemic inflammation providing a protective role against OA.

2.7 Conclusion

Despite large progress in understanding the pathophysiology of osteoarthritis, effective treatments remain elusive. In this review we have focused on the importance of the joint homeostasis and focussed on three key elements in the disease that contribute to the lack of successful treatments. We have described why the phenotype of OA is an essential parameter to recognise when treating patients. We have currently described three phenotypes, but more will emerge and should be considered. Additionally, we have shown there is a delicate balance involved in many of the processes that drive OA. Therefore, a simple block of a pathway without knowing the current homeostasis might do more harm than good. Finally, we have discussed the importance of the correct timing and suggest that most OA treatments could have specific windows in which they would be effective. The importance of determining the disbalance in joint homeostasis, demands for accurate and early diagnostic tools. These tools should subsequently be applied in an early stage to maximize potential for effective treatments. Finally, we have focussed on recent progress in treatments for OA and discussed how knowledge of joint homeostasis can help improve efficacy of treatments.

References

1. Loeser, R.F., et al., *Osteoarthritis: A disease of the joint as an organ.* Arthritis & Rheumatism, 2012. **64**(6): p. 1697-1707.
2. Goldring, S.R. and M.B. Goldring, *Changes in the osteochondral unit during osteoarthritis: structure, function and cartilage-bone crosstalk.* Nature reviews. Rheumatology, 2016. **12**(11): p. 632-644.
3. Appleton, C.T., *Osteoarthritis year in review 2017: biology.* Osteoarthritis and Cartilage, 2017.
4. López-Otín, C., et al., *The Hallmarks of Aging.* Cell, 2013. **153**(6): p. 1194-1217.
5. Franceschi, C., et al., *Inflamm-aging: An Evolutionary Perspective on Immunosenescence.* Annals of the New York Academy of Sciences, 2000. **908**(1): p. 244-254.
6. Lieberthal, J., N. Sambamurthy, and C.R. Scanzello, *Inflammation in Joint Injury and Post-Traumatic Osteoarthritis.* Osteoarthritis and cartilage / OARS, Osteoarthritis Research Society, 2015. **23**(11): p. 1825-1834.
7. Pritchard, S. and F. Guilak, *Effects of interleukin-1 on calcium signaling and the increase of filamentous actin in isolated and in situ articular chondrocytes.* Arthritis & Rheumatism, 2006. **54**(7): p. 2164-2174.
8. Dudek, M., et al., *The chondrocyte clock gene Bmal1 controls cartilage homeostasis and integrity.* The Journal of Clinical Investigation, 2016. **126**(1): p. 365-376.
9. Nagai, K., et al., *Depletion of SIRT6 causes cellular senescence, DNA damage, and telomere dysfunction in human chondrocytes.* Osteoarthritis and Cartilage, 2015. **23**(8): p. 1412-1420.
10. Livshits, G., et al., *Interleukin-6 is a significant predictor of radiographic knee osteoarthritis: The Chingford study.* Arthritis & Rheumatism, 2009. **60**(7): p. 2037-2045.
11. Stannus, O.P., et al., *Associations between serum levels of inflammatory markers and change in knee pain over 5 years in older adults: a prospective cohort study.* Annals of the Rheumatic Diseases, 2013. **72**(4): p. 535.
12. Freund, A., et al., *Inflammatory networks during cellular senescence: causes and consequences.* Trends in Molecular Medicine, 2010. **16**(5): p. 238-246.
13. Price, J.S., et al., *The role of chondrocyte senescence in osteoarthritis.* Aging Cell, 2002. **1**(1): p. 57-65.
14. Rose, J., et al., *DNA damage, discoordinated gene expression and cellular senescence in osteoarthritic chondrocytes.* Osteoarthritis and Cartilage, 2012. **20**(9): p. 1020-1028.
15. Balch, W.E., et al., *Adapting Proteostasis for Disease Intervention.* Science, 2008. **319**(5865): p. 916-919.
16. Liu-Bryan, R. and R. Terkeltaub, *Emerging regulators of the inflammatory process in osteoarthritis.* Nature reviews. Rheumatology, 2015. **11**(1): p. 35-44.
17. Husa, M., et al., *C/EBP homologous protein drives pro-catabolic responses in chondrocytes.* Arthritis Research & Therapy, 2013. **15**(6): p. R218-R218.
18. Lotz, M. and B. Caramés, *Autophagy: a new therapeutic target in cartilage injury and osteoarthritis.* The Journal of the American Academy of Orthopaedic Surgeons, 2012. **20**(4): p. 261-262.
19. Caramés, B., et al., *The Relationship of Autophagy Defects to Cartilage Damage During Joint Aging in a Mouse Model.* Arthritis & Rheumatology, 2015. **67**(6): p. 1568-1576.
20. Bouderlique, T., et al., *Targeted deletion of Atg5 in chondrocytes promotes age-related osteoarthritis.* Annals of the Rheumatic Diseases, 2016. **75**(3): p. 627-631.
21. Zhang, Y., et al., *Cartilage-specific deletion of mTOR upregulates autophagy and protects mice from osteoarthritis.* Annals of the Rheumatic Diseases, 2014.
22. Lee, H.-Y., et al., *Age-related nanostructural and nanomechanical changes of individual human cartilage aggrecan monomers and their glycosaminoglycan side chains.* Journal of Structural Biology, 2013. **181**(3): p. 264-273.
23. Kim, J.-H., et al., *Matrix cross-linking–mediated mechanotransduction promotes posttraumatic osteoarthritis.* Proceedings of the National Academy of Sciences, 2015. **112**(30): p. 9424-9429.
24. Verzijl, N., et al., *Crosslinking by advanced glycation end products increases the stiffness of the collagen network in human articular cartilage: A possible mechanism through which age is a risk factor for osteoarthritis.* Arthritis & Rheumatism, 2002. **46**(1): p. 114-123.
25. Wong, B.L., et al., *Biomechanics of cartilage articulation: Effects of lubrication and degeneration on shear deformation.* Arthritis & Rheumatism, 2008. **58**(7): p. 2065-2074.

26. Zhong, W., et al., *YAP-mediated regulation of the chondrogenic phenotype in response to matrix elasticity.* Journal of Molecular Histology, 2013. **44**(5): p. 587-595.
27. Steklov, N., et al., *Aging-related differences in chondrocyte viscoelastic properties.* Molecular & cellular biomechanics : MCB, 2009. **6**(2): p. 113-119.
28. Chen, C., et al., *Interleukin-1β and tumor necrosis factor-α increase stiffness and impair contractile function of articular chondrocytes.* Acta Biochimica et Biophysica Sinica, 2015. **47**(2): p. 121-129.
29. Salter, D.M., et al., *Differential responses of chondrocytes from normal and osteoarthritic human articular cartilage to mechanical stimulation.* Biorheology, 2002. **39**(1-2): p. 97-108.
30. Leyland, K.M., et al., *The natural history of radiographic knee osteoarthritis: A fourteen-year population-based cohort study.* Arthritis & Rheumatism, 2012. **64**(7): p. 2243-2251.
31. Elsaid, K.A., et al., *Intra-articular interleukin-1 receptor antagonist (IL1-ra) microspheres for posttraumatic osteoarthritis: in vitro biological activity and in vivo disease modifying effect.* Journal of Experimental Orthopaedics, 2016. **3**: p. 18.
32. Inc., F.T. *Zilretta (triamcinolone acetonide extended-release injectable suspension), for intra-articular use*. Available from: https://www.accessdata.fda.gov/drugsatfda_docs/label/2017/208845s000lbl.pdf.
33. McAlindon, T.E., et al., *Effect of intra-articular triamcinolone vs saline on knee cartilage volume and pain in patients with knee osteoarthritis: A randomized clinical trial.* JAMA, 2017. **317**(19): p. 1967-1975.
34. Latourte, A., et al., *Systemic inhibition of IL-6/Stat3 signalling protects against experimental osteoarthritis.* Annals of the Rheumatic Diseases, 2016.
35. Chevalier, X., F. Eymard, and P. Richette, *Biologic agents in osteoarthritis: hopes and disappointments.* Nature Reviews Rheumatology, 2013. **9**: p. 400.
36. Cicuttini, F., et al., *Rate of cartilage loss at two years predicts subsequent total knee arthroplasty: a prospective study.* Annals of the Rheumatic Diseases, 2004. **63**(9): p. 1124-1127.
37. Penninx, B.W.J.H., et al., *Inflammatory markers and physical function among older adults with knee osteoarthritis.* The Journal of Rheumatology, 2004. **31**(10): p. 2027-2031.
38. Morrisette-Thomas, V., et al., *Inflamm-aging does not simply reflect increases in pro-inflammatory markers.* Mechanisms of Ageing and Development, 2014. **139**: p. 49-57.
39. Kuyinu, E.L., et al., *Animal models of osteoarthritis: classification, update, and measurement of outcomes.* Journal of Orthopaedic Surgery and Research, 2016. **11**: p. 19.
40. Liu-Bryan, R. and R. Terkeltaub, *The Growing Array of Innate Inflammatory Ignition Switches in Osteoarthritis.* Arthritis and rheumatism, 2012. **64**(7): p. 2055-2058.
41. Loeser, R.F., et al., *Microarray analysis reveals age-related differences in gene expression during the development of osteoarthritis in mice.* Arthritis & Rheumatism, 2012. **64**(3): p. 705-717.
42. Brophy, R.H., et al., *Molecular Analysis of Age and Sex-Related Gene Expression in Meniscal Tears with and without a Concomitant Anterior Cruciate Ligament Tear.* The Journal of Bone and Joint Surgery. American volume., 2012. **94**(5): p. 385-393.
43. Jeon, O.H., et al., *Local clearance of senescent cells attenuates the development of post-traumatic osteoarthritis and creates a pro-regenerative environment.* Nature Medicine, 2017. **23**: p. 775.
44. Swärd, P., et al., *Cartilage and bone markers and inflammatory cytokines are increased in synovial fluid in the acute phase of knee injury (hemarthrosis) – a cross-sectional analysis.* Osteoarthritis and Cartilage, 2012. **20**(11): p. 1302-1308.
45. Iijima, H., et al., *Exercise intervention increases expression of bone morphogenetic proteins and prevents the progression of cartilage-subchondral bone lesions in a post-traumatic rat knee model.* Osteoarthritis and Cartilage, 2016. **24**(6): p. 1092-1102.
46. *Longitudinal study of muscle strength, quality, and adipose tissue infiltration.* The American Journal of Clinical Nutrition, 2009. **90**(6): p. 1579-1585.
47. Hui, W., et al., *Leptin produced by joint white adipose tissue induces cartilage degradation via upregulation and activation of matrix metalloproteinases.* Annals of the Rheumatic Diseases, 2012. **71**(3): p. 455.
48. Farnaghi, S., et al., *Protective effects of mitochondria-targeted antioxidants and statins on cholesterol-induced osteoarthritis.* The FASEB Journal, 2016. **31**(1): p. 356-367.
49. Vaamonde-García, C., et al., *Mitochondrial dysfunction increases inflammatory responsiveness to cytokines in normal human chondrocytes.* Arthritis & Rheumatism, 2012. **64**(9): p. 2927-2936.
50. Blanco, F.J., I. Rego, and C. Ruiz-Romero, *The role of mitochondria in osteoarthritis.* Nature reviews. Rheumatology, 2011. **7**(3): p. 161-169.

51. Messier, S.P., et al., *Effects of Intensive Diet and Exercise on Knee Joint Loads, Inflammation, and Clinical Outcomes Among Overweight and Obese Adults With Knee Osteoarthritis: The IDEA Randomized Clinical Trial.* JAMA, 2013. **310**(12): p. 1263-1273.
52. de Hooge, A.S.K., et al., *Male IL-6 gene knock out mice developed more advanced osteoarthritis upon aging.* Osteoarthritis and Cartilage, 2005. **13**(1): p. 66-73.
53. Kobayashi, H., et al., *Biphasic regulation of chondrocytes by Rela through induction of anti-apoptotic and catabolic target genes.* Nature Communications, 2016. **7**: p. 13336.
54. Nusse, R. and H. Clevers, *Wnt/β-Catenin Signaling, Disease, and Emerging Therapeutic Modalities.* Cell, 2017. **169**(6): p. 985-999.
55. Zhu, M., et al., *Activation of β-Catenin Signaling in Articular Chondrocytes Leads to Osteoarthritis-Like Phenotype in Adult β-Catenin Conditional Activation Mice.* Journal of Bone and Mineral Research, 2009. **24**(1): p. 12-21.
56. Leijten, J.C.H., et al., *GREM1, FRZB and DKK1 mRNA levels correlate with osteoarthritis and are regulated by osteoarthritis-associated factors.* Arthritis Research & Therapy, 2013. **15**(5): p. R126-R126.
57. Monteagudo, S. and R.J. Lories, *Cushioning the cartilage: a canonical Wnt restricting matter.* Nature Reviews Rheumatology, 2017. **13**: p. 670.
58. Zhong, L., M. Karperien, and J.N. Post, *DKK1, FRZB, GREM1 prevent IL1B induced articular cartilage degradation.* Osteoarthritis and Cartilage. **22**: p. S156-S157.
59. Funck-Brentano, T., et al., *Dkk-1–Mediated Inhibition of Wnt Signaling in Bone Ameliorates Osteoarthritis in Mice.* Arthritis & Rheumatology, 2014. **66**(11): p. 3028-3039.
60. Honsawek, S., et al., *Dickkopf-1 (Dkk-1) in plasma and synovial fluid is inversely correlated with radiographic severity of knee osteoarthritis patients.* BMC Musculoskeletal Disorders, 2010. **11**: p. 257-257.
61. Zhong, L., et al., *Synovial fluid concentration of gremlin1 but not frizzled-related protein is increased in patients after acute knee injury.* Osteoarthritis and Cartilage. **23**: p. A39-A40.
62. Bouaziz, W., et al., *Loss of sclerostin promotes osteoarthritis in mice via β-catenin-dependent and -independent Wnt pathways.* Arthritis Research & Therapy, 2015. **17**(1): p. 24.
63. Chen, L., et al., *The inhibition of EZH2 ameliorates osteoarthritis development through the Wnt/β-catenin pathway.* Scientific Reports, 2016. **6**: p. 29176.
64. Zhu, M., et al., *Inhibition of β-catenin signaling in articular chondrocytes results in articular cartilage destruction.* Arthritis & Rheumatism, 2008. **58**(7): p. 2053-2064.
65. Nalesso, G., et al., *WNT16 antagonises excessive canonical WNT activation and protects cartilage in osteoarthritis.* Annals of the Rheumatic Diseases, 2016.
66. Yazici, Y., et al., *A novel Wnt pathway inhibitor, SM04690, for the treatment of moderate to severe osteoarthritis of the knee: results of a 24-week, randomized, controlled, phase 1 study.* Osteoarthritis and Cartilage, 2017. **25**(10): p. 1598-1606.
67. Weng, T., et al., *Genetic Inhibition of Fibroblast Growth Factor Receptor 1 in Knee Cartilage Attenuates the Degeneration of Articular Cartilage in Adult Mice.* Arthritis and rheumatism, 2012. **64**(12): p. 3982-3992.
68. Valverde-Franco, G., et al., *Defects in articular cartilage metabolism and early arthritis in fibroblast growth factor receptor 3 deficient mice.* Human Molecular Genetics, 2006. **15**(11): p. 1783-1792.
69. Loeser, R.F., *Aging Processes and the Development of Osteoarthritis.* Current opinion in rheumatology, 2013. **25**(1): p. 108-113.
70. Blaney Davidson, E.N., A.P.M. van Caam, and P.M. van der Kraan, *Osteoarthritis year in review 2016: biology.* Osteoarthritis and Cartilage, 2017. **25**(2): p. 175-180.
71. Yang, S., et al., *Hypoxia-inducible factor-2alpha is a catabolic regulator of osteoarthritic cartilage destruction.* Nature medicine, 2010. **16**(6): p. 687-693.
72. Longobardi, L., et al., *Role of the C-C chemokine receptor-2 in a murine model of injury-induced osteoarthritis.* Osteoarthritis and Cartilage. **25**(6): p. 914-925.
73. Musumeci, G., et al., *Physical activity ameliorates cartilage degeneration in a rat model of aging: A study on lubricin expression.* Scandinavian Journal of Medicine & Science in Sports, 2015. **25**(2): p. e222-e230.
74. Kellgren, J.H. and J.S. Lawrence, *Radiological Assessment of Osteo-Arthrosis.* Annals of the Rheumatic Diseases, 1957. **16**(4): p. 494-502.

75. Harada, Y., et al., *Relationship Between Cartilage Volume Using MRI and Kellgren-Lawrence Radiographic Score in Knee Osteoarthritis With and Without Meniscal Tears.* American Journal of Roentgenology, 2011. **196**(3): p. W298-W304.
76. Kraus, V.B., et al., *OARSI Clinical Trials Recommendations: Soluble biomarker assessments in clinical trials in osteoarthritis.* Osteoarthritis and Cartilage. **23**(5): p. 686-697.
77. Xia, X., et al., *Molecular and phenotypic biomarkers of aging.* F1000Research, 2017. **6**: p. 860.
78. Mobasheri, A., et al., *Osteoarthritis Year in Review 2016: biomarkers (biochemical markers).* Osteoarthritis and Cartilage, 2017. **25**(2): p. 199-208.
79. Bajpayee, A.G., et al., *Charge based intra-cartilage delivery of single dose dexamethasone using Avidin nano-carriers suppresses cytokine-induced catabolism long term.* Osteoarthritis and Cartilage. **24**(1): p. 71-81.
80. Miyaki, S. and M.K. Lotz, *Extracellular vesicles in cartilage homeostasis and osteoarthritis.* Current Opinion in Rheumatology, 2018. **30**(1): p. 129-135.
81. Malda, J., et al., *Extracellular vesicles — new tool for joint repair and regeneration.* Nature Reviews Rheumatology, 2016. **12**: p. 243.
82. Chang, J., et al., *Clearance of senescent cells by ABT263 rejuvenates aged hematopoietic stem cells in mice.* Nature Medicine, 2015. **22**: p. 78.
83. Baar, M.P., et al., *Targeted Apoptosis of Senescent Cells Restores Tissue Homeostasis in Response to Chemotoxicity and Aging.* Cell. **169**(1): p. 132-147.e16.
84. Cheng, N.-T., A. Guo, and H. Meng, *The protective role of autophagy in experimental osteoarthritis, and the therapeutic effects of Torin 1 on osteoarthritis by activating autophagy.* BMC Musculoskeletal Disorders, 2016. **17**: p. 150.
85. Patterson, S.E. and C.N. Dealy, *Mechanisms and models of endoplasmic reticulum stress in chondrodysplasia.* Developmental Dynamics, 2014. **243**(7): p. 875-893.
86. Joshi, M., A. Kulkarni, and J.K. Pal, *Small molecule modulators of eukaryotic initiation factor 2α kinases, the key regulators of protein synthesis.* Biochimie, 2013. **95**(11): p. 1980-1990.
87. Moreno, J.A., et al., *Oral Treatment Targeting the Unfolded Protein Response Prevents Neurodegeneration and Clinical Disease in Prion-Infected Mice.* Science Translational Medicine, 2013. **5**(206): p. 206ra138-206ra138.
88. Li, Y.-H., et al., *The unfolded protein response genes in human osteoarthritic chondrocytes: PERK emerges as a potential therapeutic target.* Arthritis Research & Therapy, 2016. **18**: p. 172.
89. Tomasio, S.M., et al., *Selective inhibition of the unfolded protein response: targeting catalytic sites for Schiff base modification.* Molecular BioSystems, 2013. **9**(10): p. 2408-2416.
90. Gorbatyuk, M.S. and O.S. Gorbatyuk, *The Molecular Chaperone GRP78/BiP as a Therapeutic Target for Neurodegenerative Disorders: A Mini Review.* Journal of genetic syndromes & gene therapy, 2013. **4**(2).
91. Chen, J., et al., *Glucagon-like peptide-1 receptor regulates endoplasmic reticulum stress-induced apoptosis and the associated inflammatory response in chondrocytes and the progression of osteoarthritis in rat.* Cell Death & Disease, 2018. **9**(2): p. 212.
92. Bosomworth, N.J., *Exercise and knee osteoarthritis: benefit or hazard?* Canadian Family Physician, 2009. **55**(9): p. 871-878.
93. Tolahunase, M., R. Sagar, and R. Dada, *Impact of Yoga and Meditation on Cellular Aging in Apparently Healthy Individuals: A Prospective, Open-Label Single-Arm Exploratory Study.* Oxidative Medicine and Cellular Longevity, 2017. **2017**: p. 9.
94. Tucker, L.A., *Physical activity and telomere length in U.S. men and women: An NHANES investigation.* Preventive Medicine, 2017. **100**: p. 145-151.
95. Schafer, M.J., et al., *Exercise Prevents Diet-Induced Cellular Senescence in Adipose Tissue.* Diabetes, 2016. **65**(6): p. 1606-1615.
96. Roos, E.M. and L. Dahlberg, *Positive effects of moderate exercise on glycosaminoglycan content in knee cartilage: A four-month, randomized, controlled trial in patients at risk of osteoarthritis.* Arthritis & Rheumatism, 2005. **52**(11): p. 3507-3514.
97. Beavers, K.M., T.E. Brinkley, and B.J. Nicklas, *Effect of exercise training on chronic inflammation.* Clinica chimica acta; international journal of clinical chemistry, 2010. **411**(0): p. 785-793.
98. Ross, R., et al., *Reduction in obesity and related comorbid conditions after diet-induced weight loss or exercise-induced weight loss in men: A randomized, controlled trial.* Annals of Internal Medicine, 2000. **133**(2): p. 92-103.

99. Varady, K.A. and P.J.H. Jones, *Combination Diet and Exercise Interventions for the Treatment of Dyslipidemia: an Effective Preliminary Strategy to Lower Cholesterol Levels?* The Journal of Nutrition, 2005. **135**(8): p. 1829-1835.
100. Stefanyk, L.E. and D.J. Dyck, *The interaction between adipokines, diet and exercise on muscle insulin sensitivity.* Current Opinion in Clinical Nutrition & Metabolic Care, 2010. **13**(3): p. 255-259.
101. Wise, B., et al., *Psychological factors and their relation to osteoarthritis pain.* Osteoarthritis and cartilage / OARS, Osteoarthritis Research Society, 2010. **18**(7): p. 883-887.
102. Slavich, G.M. and M.R. Irwin, *From Stress to Inflammation and Major Depressive Disorder: A Social Signal Transduction Theory of Depression.* Psychological bulletin, 2014. **140**(3): p. 774-815.
103. Malfait, A.-M. and T.J. Schnitzer, *Towards a mechanism-based approach to pain management in osteoarthritis.* Nature reviews. Rheumatology, 2013. **9**(11): p. 654-664.
104. Miller, R.E., et al., *CCR2 chemokine receptor signaling mediates pain in experimental osteoarthritis.* Proceedings of the National Academy of Sciences, 2012. **109**(50): p. 20602.
105. Bonnet, C.S., et al., *AMPA/kainate glutamate receptors contribute to inflammation, degeneration and pain related behaviour in inflammatory stages of arthritis.* Annals of the Rheumatic Diseases, 2015. **74**(1): p. 242.
106. Solowiej, K., V. Mason, and D. Upton, *Psychological stress and pain in wound care, part 3: management.* Journal of Wound Care, 2010. **19**(4): p. 153-155.

2

"The cool thing about this enhancement cascade is that together it is more than the sum of its parts. Each element is crucial and contributes in its own way to the success of the system. This technique mimics the complex interaction cascades of biology on a small scale."

"60 percent of the time, it works all the time"

3

A nanoparticle enhancement cascade for sensitive multiplex measurements of biomarkers in complex fluids with SPRi

There is large unmet need for reliable biomarker measurement systems for clinical application. Such systems should meet challenging requirements for large scale use, including large dynamic detection range, multiplexing capacity and both high specificity and sensitivity. More importantly, these requirements need to apply to complex biological samples, which require extensive quality control. In this paper, we present the development of an enhancement detection cascade for surface plasmon resonance array imaging (SPRi). The cascade applies an antibody sandwich assay, followed by neutravidin and a gold nanoparticle enhancement for quantitative biomarker measurements in small volumes of complex fluids. We present a feasibility study both in simple buffers and in spiked equine synovial fluid with four cytokines, IL1β, IL-6, IFNγ and TNF-α. Our enhancement cascade leads to an antibody dependent improvement in sensitivity up to 40000 times, resulting in a limit of detection as low as 50 fg/ml and a dynamic detection range of more than 7 logs. Additionally, measurements at these low concentrations are highly reliable with intra- and inter-assay CVs between 2 - 20%. We subsequently showed this assay is suitable for multiplex measurements with good specificity and limited cross-reactivity. Moreover,

---

Jan Hendriks†, Ivan Stojanovic‡, Richard B.M. Schasfoort‡, Daniël B.F. Saris§,#, Marcel Karperien,†*

† Department of Developmental BioEngineering, TechMed institute, University of Twente, The Netherlands.

‡ Medical Cell Biophysics, TechMed institute, University of Twente, The Netherlands.

§ Department of Orthopedics, UMC Utrecht, The Netherlands.

 # Department of Reconstructive Medicine, TechMed institute, Faculty of Science and Technology, University of Twente, The Netherlands.

Published in Anal. Chem. 2018, DOI: 10.1021/acs.analchem.8b00260.

we demonstrated robust detection of IL-6 and IL-1β in spiked undiluted equine synovial fluid with small variation compared to buffer controls. In addition, the availability of real time measurements provides extensive quality control opportunities, essential for clinical applications. Therefore, we consider this method is suitable for broad application in SPR(i) for multiplex biomarker detection in both research and clinical settings.

3.1 Introduction

The complexity and multifactorial nature of chronic diseases requires the measurement of multiple biomarkers to provide robust information for both diagnosis and prognosis [1]. For this reason, there is a large interest in developing reliable biomarker detection systems suitable for clinical use. These systems should preferably combine high sensitivity, wide dynamic detection range and multiplexing capacity in complex fluids with robust quality control opportunities. To our knowledge, considering the challenging demands, presently no system adequately meets these requirements.

Traditionally, biomarker measurements are performed using the ELISA format in both research and clinical settings. Although its benefits are clinically proven, the ELISA assay comes with a number of disadvantages: it requires relatively large sample volumes, has a small dynamic detection range necessitating the use of dilution series and has only limited multiplexing capabilities. Furthermore, the need for expensive kits and bulky automation limits its usefulness for point-of-care applications [2]. Therefore, many alternative biomarker assays have been developed [3]. These can be separated into 2D planar assays and bead suspension assays. The 2D planar assays, such as Mesoscale Discovery and Searchlight, use a similar approach to the standard ELISA, with variation in the detection method (electro-chemiluminescent, chemiluminescent, fluorescent or colorimetric). They apply a microarray format, allowing for multiplex measurements in small sample volumes. Despite the frequent use and the improvement over standard ELISAs, reports show a high inter-assay variability [4, 5], unreliability [4, 6, 7] and lack of quality control opportunities [5, 7]. Bead suspension assays are also often used for multiplex applications, especially in research settings. Of these, Flow cytometry bead arrays and Luminex™ are the most common. These assays show excellent sensitivity over an acceptable dynamic detection range [8]; however reports show a high inter-assay CV at low concentrations, resulting in unreliable results [9]. Also, the inherent increase in non-specific interactions in suspension places a restraint on the multiplexing capacity [10].

To overcome these limitations, new platforms are being developed that combine advanced surface chemistry and nanotechnology to create sophisticated sensing platforms [11]. In the literature, many elegant approaches are proposed that provide exceptional sensitivity [12], an acceptable dynamic detection range [13] and good multiplexing potential [14, 15]. However most of the aforementioned approaches are complex and are often end-point measurements. Due to the inherent variability in sensors and their 'black box' nature, this leaves a large challenge for adequate and real-time quality control in clinical applications unaddressed [16].

Surface Plasmon Resonance (SPR) is widely used in biomolecular interaction research applications for its sensitivity and real-time measurements. This technique evolved with SPR imaging (SPRi) to allow for simultaneous multiplex detection. More recently, its potential for biomarker detection has been explored. However, due to the small refractive index changes following interaction between a ligand and analyte, the signal-

to-noise ratio is inadequate at low concentrations. Therefore, many attempts have been made to improve the sensitivity of measuring biomarkers. Nathan's group was the first to show improved sensitivity using nanoparticle tags [17]. Following this, several approaches using various nanoparticles were explored for their suitability in taking low concentration measurements [18, 19] and more recently the chemical conjugation of these nanoparticles was optimized [20]. However, little work has focussed on the detection of biomarkers at high sensitivity and over a wide dynamic detection range in a multiplex setting. More particularly, ease of use and applicability in a future clinical setting is not often considered.

In this paper, we propose a method to improve both the sensitivity and the dynamic detection range in a multiplex setting with SPRi. We apply an antibody sandwich cascade using the biotin-neutravidin system in combination with commercially available biotinylated gold nanoparticles to sequentially increase the signal (Schematically shown in figure 1). We present a feasibility study both in clean buffers and in spiked equine synovial fluid with four cytokines, IL1β, IL-6, IFNɣ and TNF-α. These cytokines are implicated in many diseases and can provide information on diagnosis and prognosis. However, they are present in pg/ml (low fM) in bodily fluids, therefore requiring high sensitivity. In addition, they can vary dramatically in concentration between disease states, requiring a large dynamic detection range [21]. We show that our method leads to a large improvement of both the sensitivity and the dynamic detection range and provides extensive quality control opportunities. Therefore, we feel that this approach is an important step forward for the broader application of the SPR(i) technique for multiplex biomarker detection. This can eventually lead to exciting applications in both research and clinical setting.

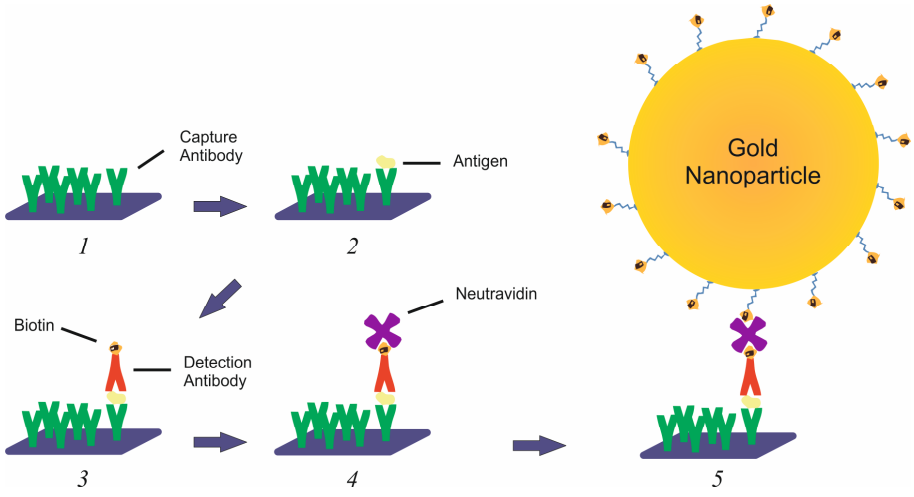

Figure 1. SPRi signal enhancement cascade using biotinylated gold nanoparticles. In this cascade, there is a sequential build-up of the complex, and thus in SPRi signal. Initially a specific capture antibody (1) interacts with the antigen (2); this is followed by a specific detection antibody towards that antigen in a sandwich format (3). Subsequently, neutravidin binds to the complex (4) followed by a commercially available biotinylated gold nanoparticle for large signal improvement (5).

3.2 Materials and Methods

3.2.1 Chemicals, immunological reagents and equipment

Acetic Acid, Sodium Acetate, Phosphorous Acid, Phosphate buffered saline, Magnesium Chloride, Tween 20, Tween 80 and Bovine serum Albumin (BSA) were obtained from Sigma Aldrich (Zwijndrecht, the Netherlands). The capture antibodies (cAb) and biotinylated detection antibodies (dAb) for IL-6 (cAb clone MQ2-13A5, dAb clone MQ2-39C3), IL-1β (cAb clone JK1B1, dAb clone JK1B2) and TNF-α (cAb clone Mab1, dAb clone Mab11), as well as the recombinant proteins IL-6, IL-1β, TNF-α and IFN-γ were purchased from Biolegend (San Diego, USA). The capture antibodies and biotinylated detection antibodies for IFN-γ (cAb clone A35, dAb clone B27) were obtained from Mybiosource (San Diego, USA). Neutravidin was obtained from Thermo Fisher (Waltham, USA). 40 nm biotinylated gold nanoparticles were purchased from Cytodiagnostics (Burlington, Ontario, Canada). Pre-activated sensors for amine coupling (G-type easy2spot) were purchased from Ssens bv (Hengelo, The Netherlands).

3.2.2 Sensor preparation

Antibodies were immobilized on G-type easy2spot sensors via reaction to free amines using the Wasatch microfluidics continuous flow spotter (Wasatch Microfluidics, Salt Lake City, UT, US) for 30 min. Gel-type sensors were used for their increased binding capacity and more efficient use of the evanescent field, compared to a planar surface sensor. The immobilization reaction was performed in 50 mM acetic acid buffer (150 µl per spot) with antibody concentrations specified in the respective experiments. An immobilization buffer of pH4.6 provided antibody coupling with the highest retained activity and was therefore used for all experiments. At this pH the antibodies are concentrated to the negatively charged hydrogel. Additionally, the low pH reduces the reactivity of lysines, leading to more directed coupling to primary amines. To reduce non-specific interactions, the sensor was deactivated by 1% BSA in 50 mM acetate buffer at pH4.6 for 7 min and subsequently with 0.2 M ethanolamine at pH8.5 for an additional 7 min.

3.2.3 SPRi measurements

The IBIS MX96™ (IBIS Technologies, Enschede, The Netherlands) was used for the SPRi measurements. It applies an angle-scanning method with automatic fitting to determine SPR shifts. It has an automatic fluid-handling system and utilizes back-and-forth flow through a microfluidic flow cell that fits the array to enable minimal sample use. It is capable of measuring 96 spots simultaneously and is therefore highly suitable for our desired multiplex measurements. Measurements were programmed using SUIT software (IBIS Technologies, Enschede, the Netherlands). In this program, the type of interaction, interaction times, samples and regions of interest (ROIs) for the antibodies were set. Subsequently, a template was created and loaded into the IBIS data acquisition software. Before each experiment an angle offset was applied to ensure a wide dynamic detection range. After programming, the machine provides automatic liquid handling

and SPR angle measurements. For each experiment, 48 sensor spots were used. Back-and-forth flow was set to 10 µl/min in a flow cell containing 12 µl of sample. Sprint software was used for data collection and referencing. Data was subsequently exported to Matlab R2015a for further analysis and quality control through the use of custom scripts (available upon request).

3.2.4 Antibody affinity measurements

The affinity between the capture antibodies and cytokines was characterized by applying the kinetic titration method proposed by Schasfoort et al. [22] to avoid possible reduction in binding capacity under regeneration conditions. Sensors were prepared as explained above. Antibodies were spotted at 5 µg/ml, 2.5 µg/ml, 1.25 µg/ml, 0.625 µg/ml at eight spots per concentration leading to average RU of 2000 ± 250, 1500 ± 225, 900 ± 250 and 300 ± 50 respectively. Cytokines were dissolved in system buffer, containing PBS with 0.075% Tween80, at a concentration of (1, 2, 4, 8, 16, 32, and 64 nM).

The kinetic titration was performed as follows: first two blanks were injected followed by the respective cytokine at 1 nM and successive injections of two times increased concentrations up to 64 nM. The association time of each interaction was 10 minutes followed by 12 minutes' dissociation. Between each injection the sensor was washed with system buffer.

Scrubber2 software was used to analyze the affinity data as described previously [22]. The blanks were subtracted and the signal was zeroed to the first interaction. To determine the affinity of a specific spot, first the k_{off} rate was determined in the dissociation phase. Subsequently the k_{on} rate was determined using a fixed k_{off} and a floating start point, to compensate for the titration set-up. The affinity was determined for the antibodies at four spot densities leading to binding capacities (R_{max}) and an affinity curve of K_D to R_{max}. The reported affinity for each antibody was calculated by extrapolating R_{max} to 100 (Capture antibody affinities can be found in figure S1-4).

3.2.5 SPRi enhancement cascade

A SPRi signal enhancement cascade measurement was performed with the cytokines IL-6, IL-1β, TNF-α, and IFN-γ in a broad dynamic detection range. Cytokine specific sensors were prepared as explained above. Antibodies were spotted at 5 µg/ml, 2.5 µg/ml, 1.25 µg/ml, 0.625 µg/ml, 0.3125 µg/ml and 0.15625 µg/ml with eight spots per concentration. Samples were dissolved in system buffer, containing PBS with 0.075% Tween80 and 0.5% BSA. Cytokines were measured at a concentration ranging from 100 fg/ml (~5 fM) to 1 µg/ml (~50 nM), spanning a dynamic detection range of 7 logarithms. A baseline of 5 min was used and an association time of 120 min. The detection antibody concentration was optimized for each cytokine, leading to 2.5 µg/ml (16.5 nM) for IL-6, 5 µg/ml (33 nM) for IL-1β and TNF-α, and 10 µg/ml (66 nM) for IFN-γ respectively. Interaction with the detection antibody was performed with a baseline of 2 min and 30 min association time. Neutravidin was used at concentration of 1.5 µg/ml (25 nM), 2 min baseline and 15 min association (optimization shown in figure S5-6), and the gold

nanoparticle concentration was 77.69 mg/ml (0.2 nM), 2 min baseline and 15 min association (optimization shown in figure S7). After each cascade, the sensor was regenerated using a double regeneration pulse for 30s. Optimal regeneration conditions were antibody dependent and were determined according to the protocol adapted from Anderson et al. [23]. The first regeneration pulse consisted of 200 mM phosphoric acid at pH 2.5, which was sufficient to remove IL-1β, TNF-α, and IFN-γ. The second pulse consisted of 66 mM phosphoric acid, 333 mM $MgCl_2$ and 6.66 mM EDTA, and was required to regenerate IL-6 binding antibodies. Reproducibility of interaction after multiple regenerations is demonstrated in figure S8.

The cascade interaction was performed as follows: First a cytokine was injected, followed by a specific biotinylated detection antibody, neutravidin and a biotinylated gold nanoparticle (40nm diameter, which has optimal absorption vs scattering properties [24]). After each interaction, the sensor was washed to reduce the non-specific signal. Each step in the cascade will increase the interaction signal proportionally and thus the sensitivity of the assay.

A typical experiment started with two full cascades with system buffer in each step to remove unbound antibody and to create a stable baseline. Subsequently, three blank cascades were measured, with system buffer in the cytokine interaction step, followed by the biotinylated detection antibody, neutravidin and the biotinylated gold nanoparticle. These blanks were used to determine non-specific interactions and provide the background correction. Finally the cytokine cascades were performed starting from the lowest concentration.

Data was collected using Sprint software, referenced and exported to Matlab. A custom Matlab script (available upon request) was used to determine the R_{max} of each antibody spot, by 1-1 Langmuir fitting to at least three cytokine concentrations. Signals were extra- or interpolated to R_{max} 100 to correct for spotting irregularities. Subsequently, the signal from eight antibody spots of similar spotting density was combined to average the noise and to increase the robustness of signal. The Limit of Blank (LoB) and Lower Limit of Detection (LLoD) were calculated as described by Armbruster et al. [25] using the following equations: $LoB = mean_{blank} + 1.645\ (SD_{blank})$ and $LLoD = LoB + 1.645\ (SD_{low\ concentration\ sample})$. The dynamic detection range was then calculated as the log10 of the Upper Limit of Detection (ULoD) divided by the LLoD.

3.2.6 Multiplex cytokine measurement

In the multiplex experiments, sensors with antibodies for IL-6, IL-1β, TNF-α and IFN-γ were spotted at a concentration of 5 µg/ml with 10 spots per cytokine. As a control, 5 µg/ml BSA was immobilized on eight spots. Samples were dissolved in system buffer, containing PBS with 0.075% Tween80 and 0.5% BSA. Five mixtures of cytokines were measured. The first mixture contained the cytokines at a concentration in the lower region of the dynamic detection range determined previously. The concentrations chosen were 10 pg/ml, 33 pg/ml, 333 pg/ml and 333 pg/ml for IL-6, IL-1β, TNF-α and IFN-γ respectively. In mixtures 2 to 5, the concentration of a single cytokine was increased to

a level higher in its dynamic detection range, while the other remained at the concentration of mixture 1. This leads to 333 pg/ml for IL-6 (mixture 2), and 1 ng/ml for IL-1β (mixture 3), TNF-α (mixture 4) and IFN-γ (mixture 5). The detection antibodies were used in a mix in their optimal concentrations (2.5 µg/ml (16.5 nM) for IL-6, 5 µg/ml (33 nM) for IL-1β and TNF-α, and 10 µg/ml (66 nM) for IFN-γ respectively). Neutravidin was used at a concentration of 1.5 µg/ml (25 nM), and the gold nanoparticle concentration was 77.69 mg/ml (0.2 nM).

The multiplex experiment was performed as follows. Two cascades with system buffer were performed in each step to remove unbound antibody and to create a stable baseline. Next, three blank cascades were measured with system buffer in the cytokine interaction step, followed by the biotinylated detection antibody mix, neutravidin and the biotinylated gold nanoparticle. These blanks were used to determine non-specific interactions and provide the background correction. Finally the cytokine mixtures were measured starting from 1 to 5. At the end of the measurement a calibration with 2% Glycerol was performed.

In addition, we performed an experiment to determine the specificity of the capture and the detection antibodies. In this experiment we used the same sensor as described in the standard multiplex experiment. Instead of mixtures, we injected single cytokines at 100 ng/ml with an association time of 120 min, followed by detection antibodies for 30 min. The detection antibodies were used in a mix in their optimal concentrations (2.5 µg/ml (16.5 nM) for IL-6, 5 µg/ml (33 nM) for IL-1β and TNF-α, and 10 µg/ml (66 nM) for IFN-γ respectively). Neutravidin was used at a concentration of 1.5 µg/ml (25 nM), and the gold nanoparticle concentration was 77.69 mg/ml (0.2 nM).

3.2.7 Cytokine measurement in spiked synovial fluid

To determine the feasibility of our approach with complex fluids, a spiking experiment was performed using equine synovial fluid. Sensors were prepared as explained above. A system buffer, containing 1M NaCl, 2% tween20 and 0.5% BSA (adapted from [19]), was used to reduce non-specific binding. The detection antibody mix, containing optimal concentrations, neutravidin and the gold nanoparticles were dissolved in this buffer. Cytokines were measured at a concentration at the higher end of their dynamic detection range, namely 333 pg/ml for IL-6 and 1 ng/ml for IL-1β respectively. They were dissolved in either pure synovial fluid, half system buffer half synovial fluid, or only system buffer as control.

The spiking experiment was performed as follows. Two cascades with system buffer in each step were performed to remove unbound antibody and to create a stable baseline. Subsequently, two blank cascades were measured with system buffer in the cytokine interaction step, followed by the biotinylated detection antibody mix, neutravidin and the biotinylated gold nanoparticle. These blanks were used to determine non-specific interactions and provide the background correction. Then, alternating a blank and a spike in buffer, half synovial fluid or synovial fluid was measured. At the end of the measurement, a calibration with 2% Glycerol was performed.

3.3 Results and Discussion

3.3.1 SPRi enhancement cascade

The signal enhancement of the SPRi measurement of cytokines using our sequential cascade is shown in figure 2. Here, the response over time is shown after interaction with IL-6 at 10 ng/ml (~500 pM).

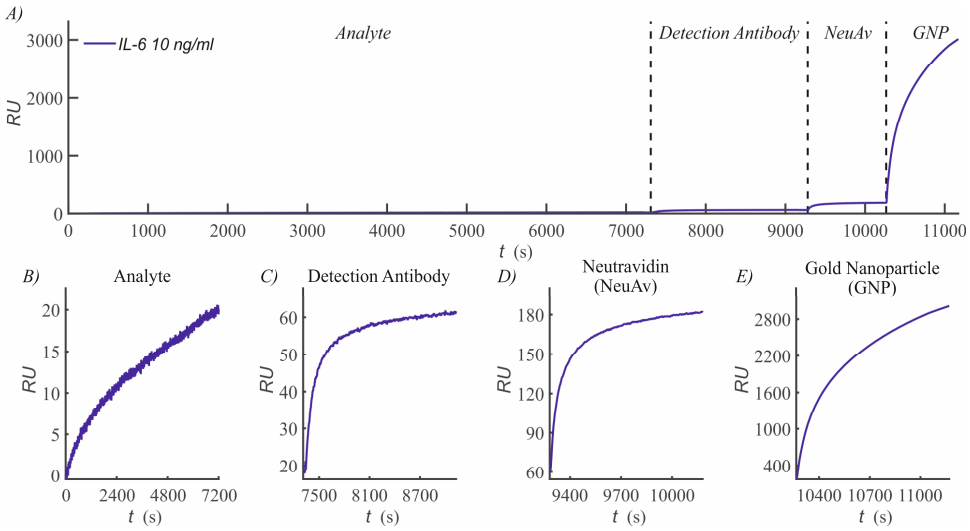

Figure 2. SPRi enhancement cascade response over time. The interaction with IL-6 is shown, followed by specific detection antibody, neutravidin and gold nanoparticle. The graph (A) shows the average signal, in refractive index units (RU), combined from eight unique antibody spots with a uniform spotting density, corrected as described to Rmax = 100 RU. The subplots (B-E) show the individual autoscaled graphs for each step in the signal enhancement cascade.

The graph shows association with IL-6 leads to a small signal of 20 RU. After the subsequent addition of biotinylated IL-6 antibody, this signal increases to 60 RU within 30 minutes. Association with neutravidin increases the signal further to 180 RU in 15 minutes. Finally, the biotinylated gold nanoparticle dramatically increases the signal to approximately 3000 RU. In combination, the three consecutive enhancement steps lead to a signal increase of 3, 9 and 150 times respectively compared to the IL-6 signal alone. Moreover, the use of a detection antibody increases not only the sensitivity, but also the specificity for the respective cytokine leading to increased reliability of the measurement.

3.3.2 Dynamic detection range measurements

The signal enhancement cascade was used to measure the cytokines IL-6, IL-1β, TNF-α and IFN-γ over a broad concentration range from 100 fg/ml (~5 fM) up to 1 µg/ml (~50 nM) spanning a dynamic detection range of 7 logs. The resulting signal increase after each step in the enhancement cascade is shown in log-log plots in figure 3.

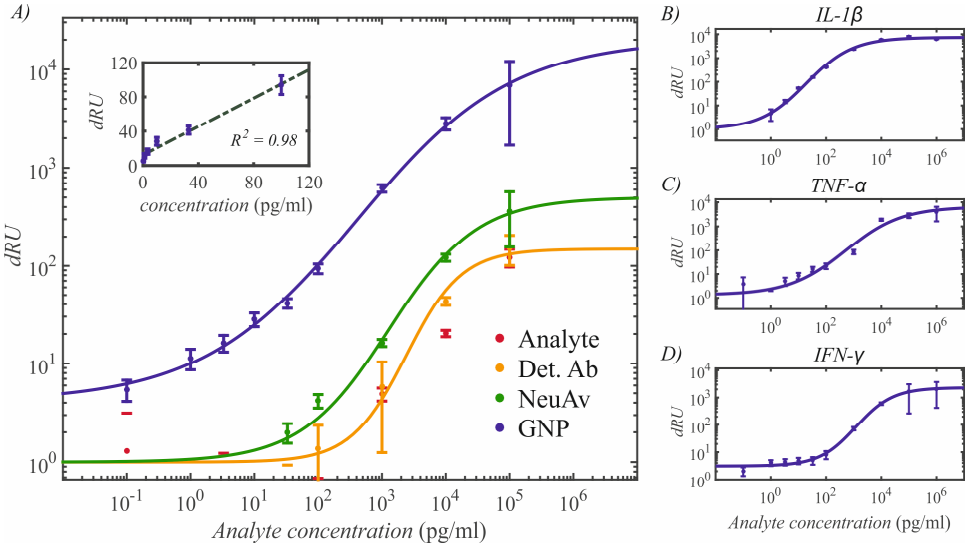

Figure 3. The enhancement cascade leads to sequential improvement in sensitivity and dynamic detection range. A) The signal increase (dRU) after association with analyte, detection antibody (Det. Ab), neutravidin (NeuAv) and gold nanoparticle (GNP) is shown for IL-6 over a concentration range from 100 fg/ml to 100 ng/ml (1 µg/ml is omitted due clipping of too high signal). The insert shows the linear signal increase between 0.1 and 100 pg/ml (R2=0.98), data for other cytokines are shown in figure S9. The signals represent the average of eight spots, corrected to Rmax = 100 RU. Error bars depicts standard deviations. Four-parameter logistic regression was used to fit the data points. B-D) depict the signal after gold nanoparticle enhancement for IL-1β, IFN-γ and TNF-α over a concentration range from 100 fg/ml to 1 µg/ml.

Figure 3a shows the signal increase after each enhancement step using IL-6 as the analyte. The lower limit of detection improves from 2 ng/ml after analyte association, to 300 pg/ml after detection antibody, to 20 pg/ml after neutravidin and finally to 50 fg/ml after the gold nanoparticle enhancement. This leads to an improvement in the limit of detection of 40000 times. Additionally, the dynamic detection range increases from 3 logarithms to at least 7 logs. Moreover, the intra-assay precision is high (table S5 for more details), especially in the linear range (CV<10%), but also at low concentrations (CV<20%). This allows for excellent concentration measurements, especially in the challenging lower portion of the dynamic detection range. We subsequently determined inter-assay precision (table S6). This resulted in good precision at higher concentrations after analyte and antibody interaction, and at lower concentration after neutravidin and gold nanoparticle interaction (CVs 2-20%). Thus depending on the analyte concentration one can select the best step in the amplification cascade for concentration measurement.

Figures 3b-d shows the signal increase over the dynamic detection range for IL-1β, IFN-γ and TNF-α after the gold nanoparticle signal enhancement. Similar increase in signal in each enhancement step was achieved as depicted with IL-6 (data shown over a range of spot densities in figure S10). The figures show a good logistic regression fit and a broad dynamic detection range for the measured cytokines.

Figure 4 shows a plot for the limit of detection versus the capture antibody affinity.

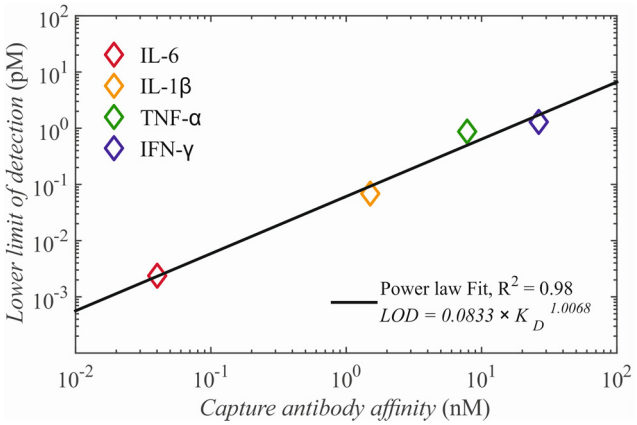

Figure 4. The lower limit of detection is plotted against the affinity of the capture antibody for the four cytokines measured. The figure shows good correlation between the capture antibody affinity and the LLOD in a power law function (R2 = 0.98). This indicates that the capture antibody affinity is the main predictor for the sensitivity of the assay. Variations in detection antibody affinity and biotin availability for neutravidin potentially play a less pronounced role.

The data shows the detection limit and dynamic detection range are dependent on the individual cytokine, and thus on the antibody pair used in the sandwich assay (more details in table S7). This is shown by an increasing LOD of 1.2, 15, and 22 pg/ml for IL-1β, TNF-α and IFN-γ respectively compared to IL-6 and a decreasing dynamic detection range of 5 logs. This follows the trend in the affinity of the capture antibodies with a KD of 43 pM for IL-6, 1.5 nM for IL-1β, 7.8 nM for TNF-α and 26.3 nM for IFN-γ respectively (affinity measurements are shown in figure S1-4). Although the affinities of the detection antibodies were not measured, the table shows the capture antibody affinity is a good predictor for the sensitivity (R2 = 0.98, figure 4).

3.3.3 Multiplex cytokine measurement

The cytokines were measured in mixtures of both low and high concentrations to show the multiplexing potential of the enhancement cascade. The results are shown in figure 5.

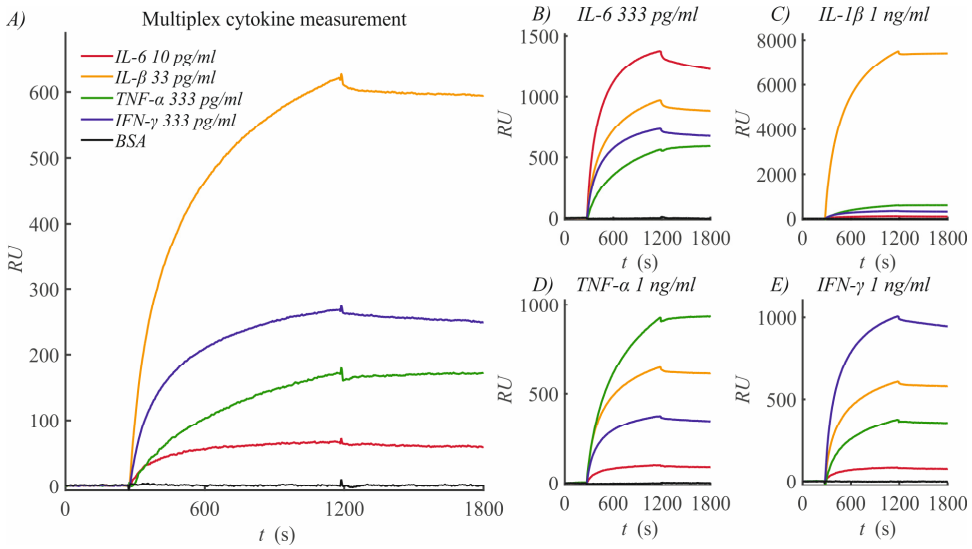

Figure 5. Cytokines were measured specifically in multiplex. A) The RU signal during gold nanoparticle association after interaction with a mixture of cytokines in the lower region of the dynamic detection range, followed by the detection antibody and neutravidin cascade. The graph shows the baseline, followed by 15 minutes of association and 10 min of dissociation. The signals shown are an average of 10 spots. B-E). Similar measurement as in (A) were performed; however, the concentration of a single cytokine is increased to the higher region in their dynamic detection range, without changing other concentrations in the mixture. In this way, the specificity and cross-reactivity of the cytokine detection was assessed.

Figure 5a shows the signal during the injection of the biotinylated gold nanoparticle as the last step in the signal enhancement cascade after incubation with a mixture of cytokines in the lower part of their respective dynamic detection range. The signals in the detection antibody and neutravidin steps were similar to those measured in earlier singleplex experiments at these concentrations, indicating specific interactions (data not shown). In figures 5 b-e, the concentration of one of the cytokines was increased by 3 times for IL-6 and IL-1β, or 30 times for TNF-α and IFN-γ, depending on the size of the dynamic detection range. As shown in figure 5b-e, increasing the concentrations of individual cytokines leads to no (in case of IL-6), minor (in case of IL-1β and TNF-α) or moderate (in case of IFN-γ) non-specific signal and to a large specific signal increase (Further clarified in figure S11). In figure S12, the specificity is further assessed with injections of single cytokines and detection antibodies. Here we show there is very limited non-specificity with both analyte and detection antibody. This indicates that the signal amplification method is suited to for multiplex measurements.

3.3.4 Cytokine measurement in spiked synovial fluid

For clinical biomarker assays, reliable measurements in complex fluids are essential. These complex fluids can range from serum- to urine to synovial fluid; of which synovial fluid is considered the most challenging due to its high viscosity, particle contaminants and limitations of small volumes. Here, we demonstrate a spike and recovery experiment of IL-6 and IL-1β in equine synovial fluid. The cytokines were either spiked in synovial fluid, in synovial fluid diluted with buffer, or in pure buffer. In figure 6, we show the results after gold nanoparticle association for IL-6 and IL-1β.

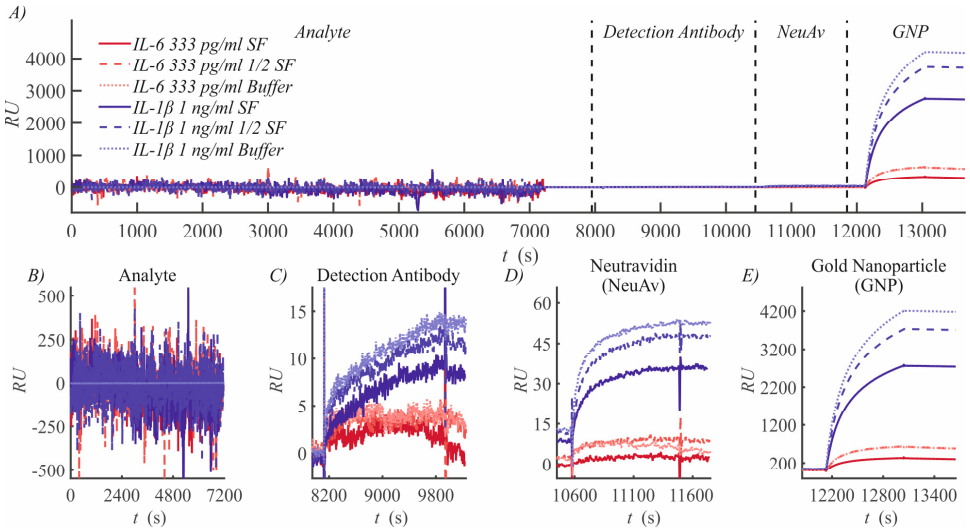

Figure 6. Spikes in synovial fluid can be measured with only minor variation compared to buffer controls. A) The graph shows RU signal after interaction with a mixture of cytokines in the higher region of the dynamic detection range, followed by the detection antibody, neutravidin and gold nanoparticle cascade. The cytokines were spiked in either synovial fluid, half synovial fluid and half buffer or in pure buffer. The signals shown represent the average of 10 measurement spots. B-E) Subplots are shown for each step in the enhancement cascade. The graphs show the baseline, followed by association and dissociation.

Figure 6 shows that direct measurements of cytokines in synovial fluid are impossible due to the large RU shifts caused by refractive index inhomogeneities in the synovial fluid. After incubation with synovial fluid, the sensor is washed and all subsequent measurement steps are performed in clean buffers resulting in stable base line RUs allowing for reliable measurements (background signal shown in figure S13). Consequently, after the enhancement cascade both IL-6 and IL-1β can be measured in spiked diluted synovial fluid with no to very small variation compared to buffer controls (recovery 98% and 89% for IL-6 and IL-1β respectively). Considering the challenging nature of synovial fluid, this is excellent accuracy. In pure synovial fluid, the signal decreases to roughly half that of buffer controls, but can still be readily measured with precision (recovery 53% and 67% for IL-6 and IL-1β respectively). The lower recovery in pure synovial fluid may be accounted for by its electrolyte composition which may influence the binding equilibrium. Together, this indicates that, while refractive index

inhomogeneities in synovial fluid have effect on the cytokine measurements, this effect is minimal in the enhancement cascade and can be easily corrected.

Biomarker detection systems for chronic diseases in both research and clinical settings require high sensitivity, wide dynamic detection range and multiplexing capability in complex fluids with robust quality control opportunities. A system combining these demanding requirements does not yet exist.

In this study we have implemented an enhancement cascade for SPRi that shows significant improvement in signal with only minor non-specific background interactions. We have shown that the combination of the large signal increase, with the reduction in standard deviation, through correction for ligand density variation, leads to very high sensitivity and a LLoD as low as 50 fg/ml (2 fM), depending on the capture antibody. Additionally, as the upper limit of detection is not reduced in the enhancement cascade, we obtained an extremely high dynamic detection range of 7 logarithms for quantitative measurements. This is comparable to, if not more sensitive than, the most sensitive commercial planar (Mesoscale discovery™: average LLoD = 500 fg/ml, dynamic detection range = 3.5 logs) and bead suspension (Luminex™: average LLoD = 2 pg/ml, dynamic detection range = 4 logs) assays available today [26]. When comparing our method to other experimental assays we demonstrate similar (low fg/ml [15, 18]) or better (low pg/ml [13, 19]) sensitivity. Yet, our dynamic detection range is much wider than most reported, which is often no more than 3-4 logs [13, 15, 19]. This wide dynamic detection range is highly relevant considering the large difference between base level concentrations of different biomarkers and the large variation in individual biomarker concentrations between the healthy population and sick individuals, but also between individual patients. Additionally, the large dynamic detection range can avoid the need for dilution series. The sensitivity we have achieved is essential in the measurement of biomarkers, in particularly for cytokines. The concentration of IL-6, TNF-α and IFN-γ is in the low pg/ml range in healthy subjects and will often not increase above 100 pg/ml in patients [27, 28]. This already poses a large challenge in clinical diagnostics for these markers with non-detectable values in a substantial subset of patients. For example, IL-1β is a highly interesting potent marker, associated with many inflammatory diseases and could have diagnostic potential. However, its concentration in serum never exceeds 10 pg/ml, even in patients [29], and can therefore not be reliably measured with most current clinical tools. The high sensitivity of our method does allow for measuring these challenging biomarkers, opening new opportunities for clinical diagnostics.

We have demonstrated the multiplexing potential of our method by specifically measuring the cytokines in mixtures compared to single controls. We show there is only minor cross-reactivity, especially with IL-6 and IL-1β. Moderate but larger cross reactivity was shown with TNF-α and IFN-γ. Furthermore, we have demonstrated the potential of our method to measure biomarkers in complex fluids simultaneously in multiplex. To achieve this, we have used a single sensor to measure IL-6 and IL-1β spiked in equine synovial fluid, either pure or diluted with buffer. We have shown that only

minor signal variations occur in half diluted synovial fluid compared to buffer controls. Considering the highly viscous nature of the synovial fluid with major impurities and the large non-specific signal during the cytokine association phase, this represents remarkable accuracy. Association in pure synovial fluid leads to a small signal reduction of roughly half compared to that achieved in buffer controls. This reduction can potentially be attributed to the salt concentration, pH and viscosity of the synovial fluid which can exert a specific effect on the antibodies and their binding characteristics. While this reduction might slightly decrease the sensitivity, it is probable that a small dilution in concentrated buffer can help diminish these effects. Therefore, we are confident that our method can be applied to measure simultaneously various cytokines sensitively and specifically in complex fluids.

The availability of real time measurements allow us to measure the signal at any given moment in the cascade. This provides extensive quality control opportunities, essential for clinical applications. For example, the evaluation of binding curves can provide more quantitative data and help detect and eliminate non-specific signals. In addition it can provide actual binding capacities of spots allowing for a correction for spotting irregularities, which we have applied. As a results we have achieved small intra-assay CVs with eight individual spots of no more than 10% in the linear range and less than 20% at the lowest concentrations, leading to excellent reproducibility. These are major advantages compared to standard assays, which show problems with spotting irregularities, assay reproducibility [30] and large CVs in the low concentration range [31], making them unsuitable for large scale clinical implementation [7].

Our enhancement cascade leads to excellent sensitivity, dynamic detection range, works in multiplex and we have shown feasibility for measuring in complex fluids. However, although our method works reliably for all cytokines tested, there is a large influence of the quality of the antibody pair on the outcome of the assay. For example when comparing our best antibody pair (IL-6) to our worst (IFN-γ) the LLoD worsens from 50 fg/ml to 22 pg/ml, leading to an almost 1000 times lower sensitivity. In fact, we showed that there is a strong direct correlation between the affinity of the capture antibody and the sensitivity. Furthermore, we have shown larger non-specific interactions in multiplex with our weakest antibody pairs. It is striking that the antibodies with the lowest affinity, highest limit of detection and smallest dynamic detection range, also show the highest cross-reactivity. This importance of the capture antibody is well known and received extra attention due to the reproducibility crisis [32], but is still not often considered in detail. It is notoriously difficult to find high affinity antibody pairs [33] without ranking various antibodies from different suppliers and specific information of antibody affinity is not known or is not given by suppliers [34].

The SPRi technology specifically is well positioned to determine the antibody quality considering its long history in assessing molecular interactions. Therefore, this technique should be used to select good antibody pairs with high affinity and low cross-reactivity for clinical assay development. Considering our antibody panel, it becomes

apparent that only the antibodies for IL-6 and IL-1β are suitable for clinical application. For the other cytokines, higher affinity antibody pairs should be found.

While the SPRi technology is highly suitable for multiplex measurements in small volumes and provides excellent quality control, it also has some limitations which are important to consider for large scale use. Signal fluctuations that occur with this technology require user experience and advanced software to deal with appropriately. In addition, the technology is still costly, with machines costing over 100k. This limits the availability of the technology. Smaller point of care devices that are under development could potentially address this issue.

We have demonstrated the feasibility of our enhancement cascade to measure biomarkers in multiplex in complex fluids. However, for clinical application it is desired to further validate our method in human or equine samples. It is recommended to measure recovery and precision of spikes, potential interferences, and to perform comparative measurements with standard methods in the field. This will be part of future work in which we will apply our method to measure cytokines in equine and human cohorts.

3.4 Conclusion

In this paper, we present the development of an enhancement cascade for SPRi based on a sandwich assay and nanoparticle amplification. This method can not only measure at high sensitivity, and over a large dynamic detection range, but it achieves this in multiplex, requiring small volumes and still is very accurate even in synovial fluid, one of the most demanding complex bodily fluids. In addition, our method shows good reproducibility and allows for extensive quality control, essential for clinical application. In future work, we will further validate our method in equine and human patient cohorts to allow for both research and clinical diagnostic applications.

3.5 Supplementary Information

3.5.1 Affinity measurement for the capture antibody to IL-6

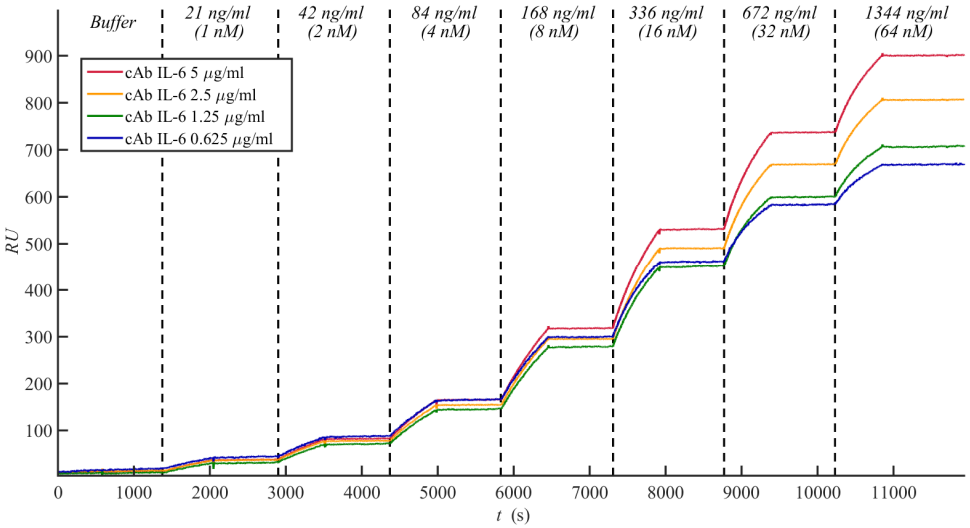

Figure S1: Kinetic titration of IL-6. The graph shows the specific interaction of IL-6 with the capture antibody spot density (5 µg/ml to 0.625 µg/ml). A buffer injection was followed by IL-6 at 1 nM and subsequent injections of increasing concentrations with multiples of two. The association time per injection was 10 minutes, followed by 12 minutes dissociation.

	k_{on} (M^{-1} s^{-1})	k_{off} (s^{-1})	R_{max} (RU)	K_D (M)	Res sd
IL-6 5 µg/ml	4.4 x 10^4	4.5 x 10^{-6}	830	1.0 x 10^{-10}	4.25
IL-6 2.5 µg/ml	4.8 x 10^4	5.5 x 10^{-6}	770	1.1 x 10^{-10}	3.56
IL-6 1.25 µg/ml	5.4 x 10^4	2.5 x 10^{-6}	670	4.6 x 10^{-11}	3.19
IL-6 0.625 µg/ml	6.1 x 10^4	5.5 x 10^{-6}	625	9.1 x 10^{-11}	2.61
Extrapolation R_{max} = 100	7.5 x 10^4	3.2 x 10^{-6}	100	4.3 x 10^{-11}	-

Table S1: Kinetic fits evaluated by the Scrubber2 program with the kinetic titration as input. First the k_{off} was fitted in the dissociation phase, followed by fits of k_{on} and R_{max} in the association phase, with a floating start point. Table entries are the averages for the 4 spots densities and a linear extrapolation to R_{max} = 100.

3.5.2 Affinity measurement for the capture antibody to IL-1β

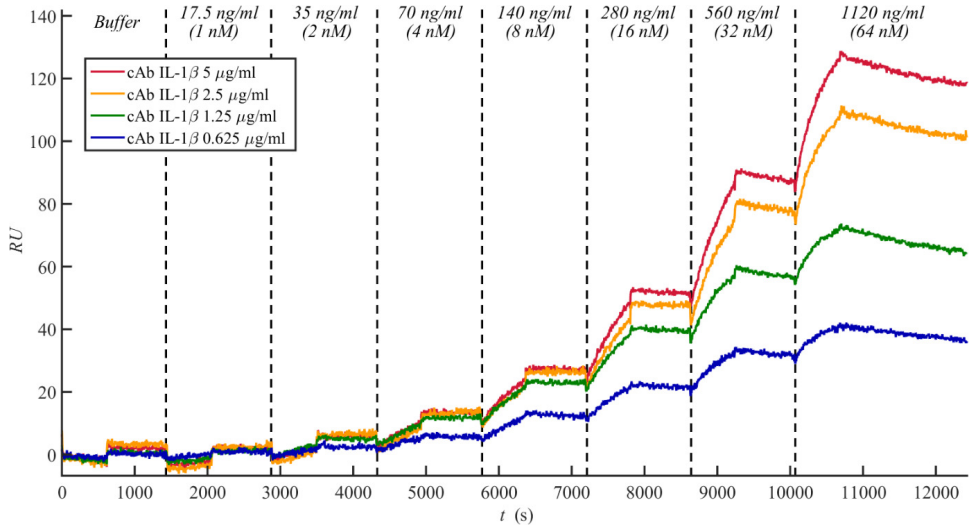

Figure S2: Kinetic titration of IL-1β. The graph shows the specific interaction of IL-1β with the capture antibody spot (density 5 µg/ml to 0.625 µg/ml). A buffer injection was followed by IL-1β at 1 nM and subsequent injections of increasing concentrations with multiples of two. The association time per injection was 10 minutes, followed by 12 minutes dissociation.

	k_{on} (M^{-1} s^{-1})	k_{off} (s^{-1})	R_{max} (RU)	K_D (M)	Res sd
IL-1β 5 µg/ml	2.7 x 10^4	4.7 x 10^{-5}	300	1.7 x 10^{-9}	2.00
IL-1β 2.5 µg/ml	3.2 x 10^4	4.8 x 10^{-5}	245	1.5 x 10^{-9}	2.27
IL-1β 1.25 µg/ml	4.8 x 10^4	6.6 x 10^{-5}	155	1.4 x 10^{-9}	1.40
IL-1β 0.625 µg/ml	4.6 x 10^4	6.5 x 10^{-5}	90	1.4 x 10^{-9}	1.30
Extrapolation R_{max} = 100	4.8 x 10^4	7 x 10^{-5}	100	1.5 x 10^{-9}	-

Table S2: Kinetic fits evaluated by the Scrubber2 program with the kinetic titration as input. First the k_{off} was fitted in the dissociation phase, followed by fits of k_{on} and R_{max} in the association phase, with a floating start point. Table entries are the averages for the 4 spots densities and a linear extrapolation to R_{max} = 100.

3.5.3 Affinity measurement for the capture antibody to TNF-α

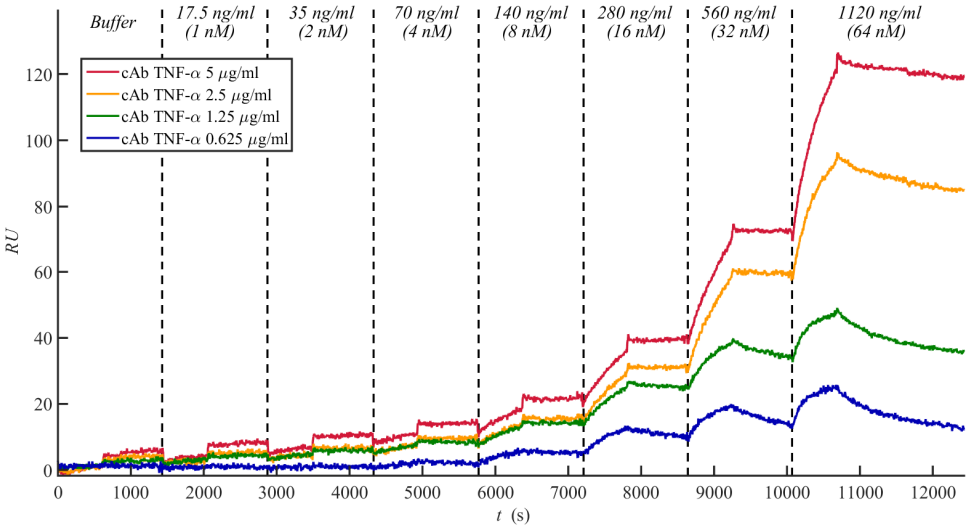

Figure S3: Kinetic titration of TNF-α. The graph shows the specific interaction of TNF-α with the capture antibody spot (density 5 µg/ml to 0.625 µg/ml). A buffer injection was followed by TNF-α at 1 nM and subsequent injections of increasing concentrations with multiples of two. The association time per injection was 10 minutes, followed by 12 minutes dissociation.

	k_{on} (M^{-1} s^{-1})	k_{off} (s^{-1})	R_{max} (RU)	K_D (M)	Res sd
TNF-α 5 µg/ml	1.1 x 10^4	2.2 x 10^{-5}	575	2.1 x 10^{-9}	1.99
TNF-α 2.5 µg/ml	1.9 x 10^4	6.4 x 10^{-5}	245	3.4 x 10^{-9}	2.00
TNF-α 1.25 µg/ml	5.2 x 10^4	2.2 x 10^{-5}	90	4.3 x 10^{-9}	1.48
TNF-α 0.625 µg/ml	5.6 x 10^4	5.6 x 10^{-5}	50	1.0 x 10^{-8}	1.31
Extrapolation R_{max} = 100	4.3 x 10^4	3.4 x 10^{-5}	100	7.8 x 10^{-9}	-

Table S3: Kinetic fits evaluated by the Scrubber2 program with the kinetic titration as input. First the k_{off} was fitted in the dissociation phase, followed by fits of k_{on} and R_{max} in the association phase, with a floating start point. Table entries are the averages for the 4 spots densities and a linear extrapolation to R_{max} = 100.

3.5.4 Affinity measurement for the capture antibody to IFN-γ

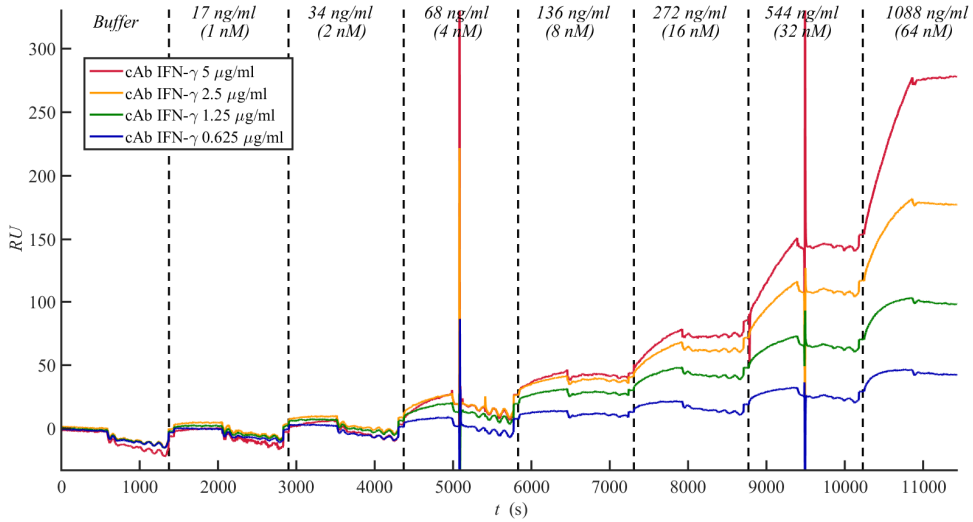

Figure S4: Kinetic titration of IFN-γ. The graph shows the specific interaction of IFN-γ with the capture antibody spot (density 5 µg/ml to 0.625 µg/ml). A buffer injection was followed by IFN-γ at 1 nM and subsequent injections of increasing concentrations with multiples of two. The association time per injection was 10 minutes, followed by 12 minutes dissociation.

	k_{on} (M^{-1} s^{-1})	k_{off} (s^{-1})	R_{max} (RU)	K_D (M)	Res sd
IFN-γ 5 µg/ml	1.1 x 10^4	5.8 x 10^{-4}	670	5.3 x 10^{-8}	21.58
IFN-γ 2.5 µg/ml	1.6 x 10^4	5.3 x 10^{-4}	270	3.4 x 10^{-8}	33.67
IFN-γ 1.25 µg/ml	6.1 x 10^4	1.3 x 10^{-4}	190	2.1 x 10^{-8}	19.06
IFN-γ 0.625 µg/ml	1.5 x 10^4	5.2 x 10^{-4}	90	3.4 x 10^{-8}	17.70
Extrapolation R_{max} = 100	4.3 x 10^4	3.3 x 10^{-4}	100	2.6 x 10^{-8}	-

Table S4: Kinetic fits evaluated by the Scrubber2 program with the kinetic titration as input. First the koff was fitted in the dissociation phase, followed by fits of kon and Rmax in the association phase, with a floating start point. Table entries are the averages for the 4 spots densities and a linear extrapolation to Rmax = 100.

3.5.5 Concentration dependent comparison between Avidin and neutravidin

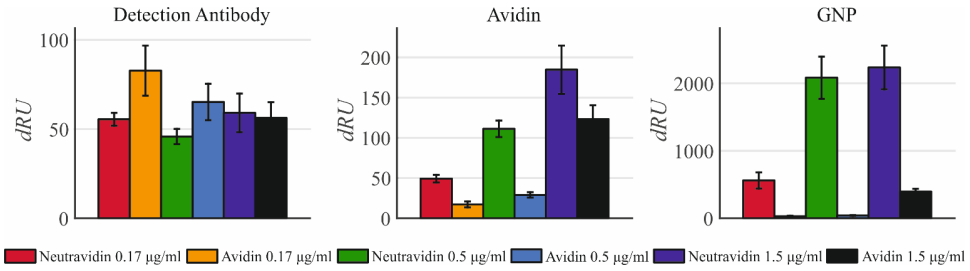

Figure S5: Difference in RU post cytokine association (IL-1β 10 ng/ml 30 min) after detection antibody, avidin/neutravidin and gold nanoparticle enhancement. The results indicate an avidin/neutravidin concentration dependent increase in both avidin and gold nanoparticle enhancement. In addition neutravidin was superior to avidin in this enhancement cascade at all concentrations tested.

3.5.6 Optimization of neutravidin concentration

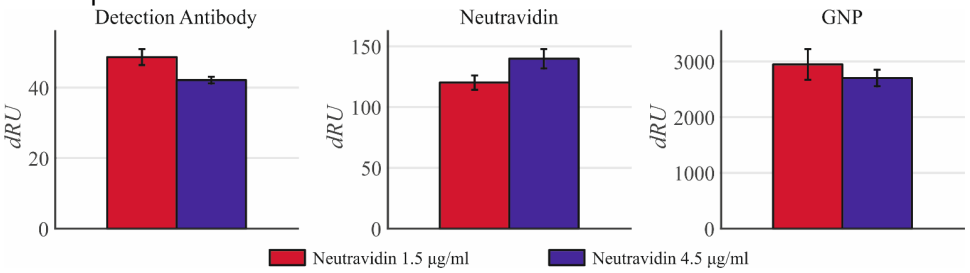

Figure S6: Difference in RU post cytokine association (IL-1β 10 ng/ml 30 min) after detection antibody, neutravidin and gold nanoparticle enhancement. The results indicate that higher neutravidin concentrations than 1.5 µg/ml provide no further benefit in the cascade.

3.5.7 Optimization of Gold nanoparticle concentration

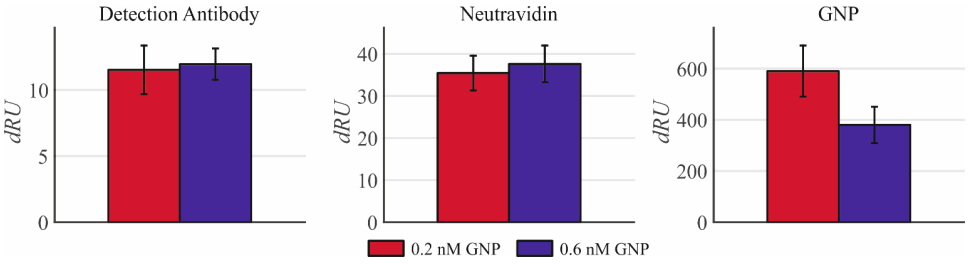

Figure S7: Difference in RU post cytokine association (IL-1β 3 ng/ml 30 min) after detection antibody, neutravidin and gold nanoparticle enhancement. The results indicate that higher concentrations than 0.2 nM provide no improvement in nanoparticle signal.

3.5.8 Antibody spot interactions are reproducible after multiple regenerations

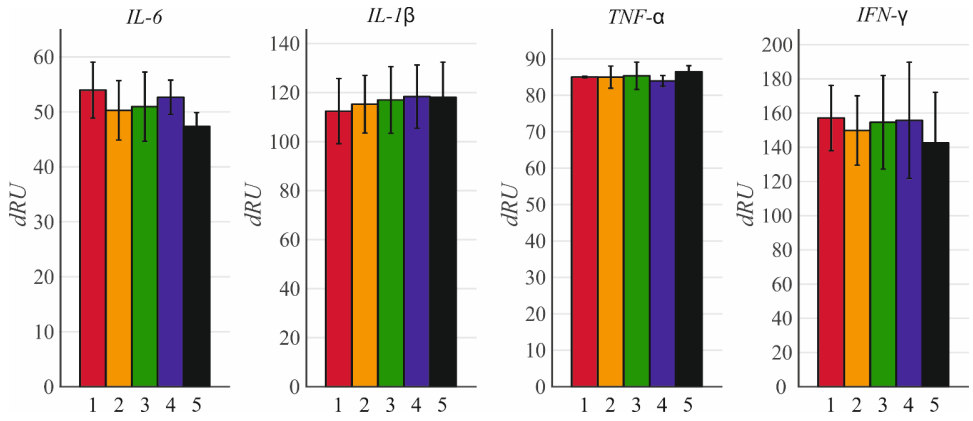

Figure S8: Difference in RU post cytokine association (100 ng/ml 30 min) after repeated regenerations (5 times shown). The figure shows that our regeneration conditions allow for multiple reproducible measurements using a single sensor.

3.5.9 Signal is linearly dependent on concentration in SPRi Cascade

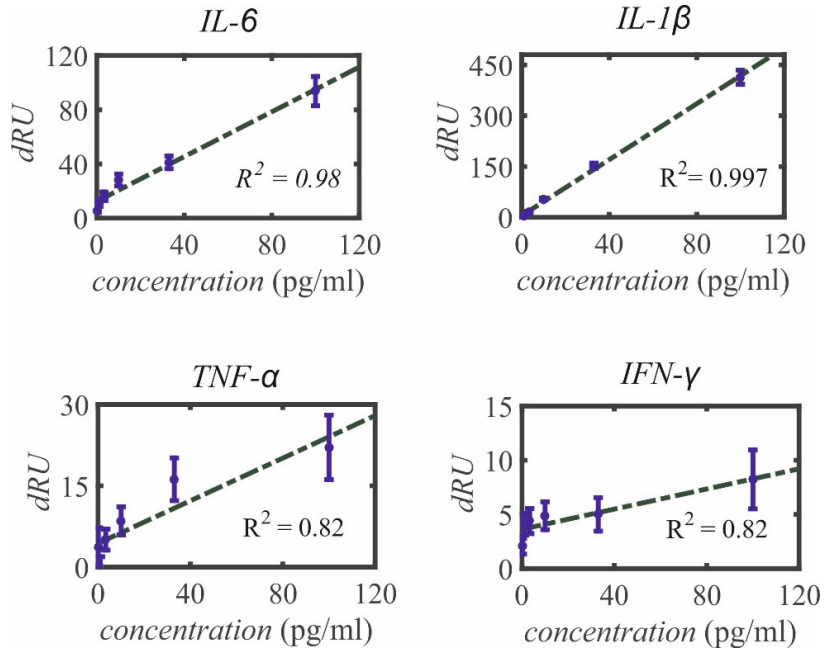

Figure S9: Linear signal increase depending on cytokine concentration. The figure shows the signal increase after GNP interaction at 6 concentrations (100 fg/ml, 1 pg/ml, 3.3 pg/ml, 10 pg/ml, 33 pg/ml and 100 pg/ml). There is a good linear dependency of the signal to the concentration for the high affinity antibodies at these concentrations (IL-6 R2=0.98, IL-1β R2=0.997). The linear dependency lower affinity antibodies is reduced at these concentrations (TNF-α R2=0.82, IFN-γ R2=0.82). This can be explained by their higher LLoD.

3.5.10 Intra-Assay precision

IL-6	Analyte	Det. Ab.	NeuAv	GNP
100 fg/ml	N.D.	N.D.	N.D.	24.3
1 pg/ml	N.D.	N.D.	N.D.	23.7
3.3 pg/ml	N.D.	N.D.	N.D.	19.2
10 pg/ml	N.D.	N.D.	N.D.	15.9
33 pg/ml	N.D.	N.D.	22.5	11.4
100 pg/ml	N.D.	71.1	15.8	11.6
1 ng/ml	15.2	78.6	8.3	8.9
10 ng/ml	7.5	9.5	8.4	14.5
100 ng/ml	20.9	34.2	56.9	75.3
1 ug/ml	N.D.	N.D.	N.D.	N.D.

IL-1β	Analyte	Det. Ab.	NeuAv	GNP
100 fg/ml	N.D.	N.D.	N.D.	N.D.
1 pg/ml	N.D.	N.D.	N.D.	22.9
3.3 pg/ml	N.D.	N.D.	N.D.	11.4
10 pg/ml	N.D.	N.D.	17.9	4.7
33 pg/ml	N.D.	N.D.	8.7	5.2
100 pg/ml	N.D.	25.1	9.4	5.2
1 ng/ml	N.D.	13.0	2.9	5.0
10 ng/ml	42.8	4.3	3.6	2.8
100 ng/ml	5.6	6.3	6.1	6.5
1 ug/ml	8.7	6.8	2.4	3.2

TNF-α	Analyte	Det. Ab.	NeuAv	GNP
100 fg/ml	N.D.	N.D.	N.D.	N.D.
1 pg/ml	N.D.	N.D.	N.D.	N.D.
3.3 pg/ml	N.D.	N.D.	N.D.	N.D.
10 pg/ml	N.D.	N.D.	N.D.	19.5
33 pg/ml	N.D.	N.D.	14.0	17.4
100 pg/ml	N.D.	N.D.	42.1	22.5
1 ng/ml	N.D.	33.1	23.2	17.4
10 ng/ml	22.7	12.2	12.4	10.0
100 ng/ml	16.2	12.2	8.3	7.4
1 ug/ml	4.5	10.9	31.0	59.0

IFN-γ	Analyte	Det. Ab.	NeuAv	GNP
100 fg/ml	N.D.	N.D.	N.D.	N.D.
1 pg/ml	N.D.	N.D.	N.D.	N.D.
3.3 pg/ml	N.D.	N.D.	N.D.	N.D.
10 pg/ml	N.D.	N.D.	N.D.	N.D.
33 pg/ml	N.D.	N.D.	N.D.	31.9
100 pg/ml	N.D.	N.D.	22.3	24.0
1 ng/ml	N.D.	16.3	34.0	16.4
10 ng/ml	N.D.	17.1	15.2	11.4
100 ng/ml	45.7	14.2	11.5	65.4
1 ug/ml	17.2	22.3	41.4	77.3

Table S5: The table shows the intra-assay precision for IL-6, IL-1β, TNF-α and IFN-γ over a dynamic range between 100 fg/ml and 1 ug/ml over 8 antibody spots. The intra-assay precision is generally excellent with CVs ranging from 2-20%. There is a clear relation between the concentration and the CV at specific steps in the enhancement cascade. Lower concentrations decreases the CVs at early steps in the cascade due to the low signal to noise ratio. At higher concentration the CVs can decrease at the neutravidin or gold nanoparticle step due to saturation or clipping of signal. This indicates that depending on the analyte concentration one can select the best step in the amplification cascade for concentration measurement. The table also clearly shows the relation between the quality of the antibody and the precision. The high affinity antibodies IL-6 and IL-1β generally show better precision than the low affinity antibodies TNF-α and IFN-γ.

3.5.11 Inter-Assay precision

Concentration	Analyte	Det. Ab.	NeuAv	GNP
100 pg/ml	21.3	30.5	14.9	19.7
1 ng/ml	27.0	1.4	1.7	21.3
10 ng/ml	18.7	5.6	7.7	20.0
100 ng/ml	18.2	10.4	80.5	112.1
1 µg/ml	18.1	12.4	89.2	116.9

Table S6: The table shows the inter-assay precision for IL-1β between 3 individual experimental days over 8 antibody spots. The inter-assay precision is generally excellent with CV<20%. Again there is a clear relation between the concentration and the CV at specific steps in the enhancement cascade. At lower concentration the CV decreases at the Analyte and Detection antibody step due to low signal to noise ratio. At higher concentration the CV decreases at the neutravidin and gold nanoparticle step due to saturation and clipping of signal. Thus depending on the analyte concentration one can select the best step in the amplification cascade for concentration measurement.

3.5.12 Influence of antibody spotting density on SPRi cascade

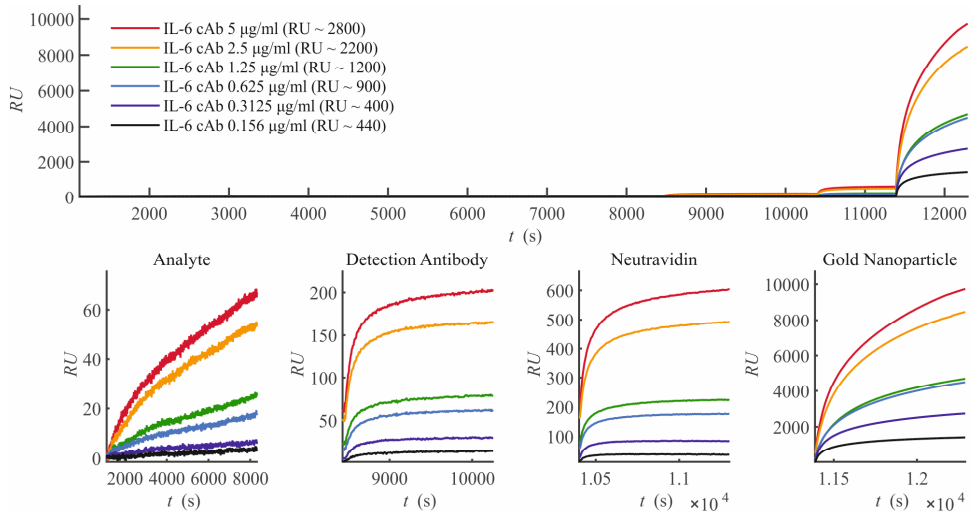

Figure S10.1: Influence of antibody density on IL-6 SPRi enhancement cascade. The association with IL-6 (10 ng/ml) and enhancement cascade is shown for 6 antibody spotting densities (5 µg/ml to 0.156 µg/ml). Average RLL values corresponding to these densities were calculated with the Sprint software from the manufacturer and are shown in the legend.

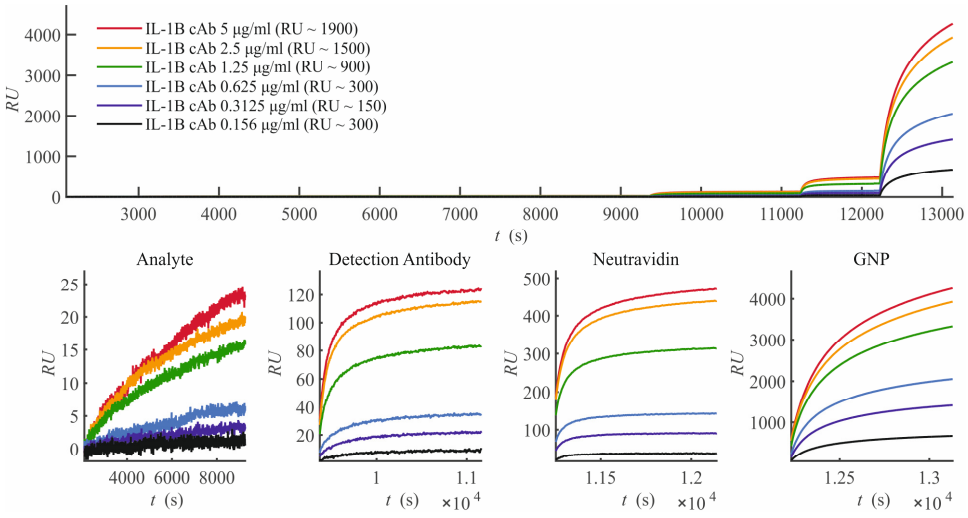

Figure S10.2: Influence of antibody density on IL-1β SPRi enhancement cascade. The association with IL-1β (10 ng/ml) and enhancement cascade is shown for 6 antibody spotting densities (5 µg/ml to 0.156 µg/ml). Average RLL values corresponding to these densities were calculated with the Sprint software from the manufacturer and are shown in the legend.

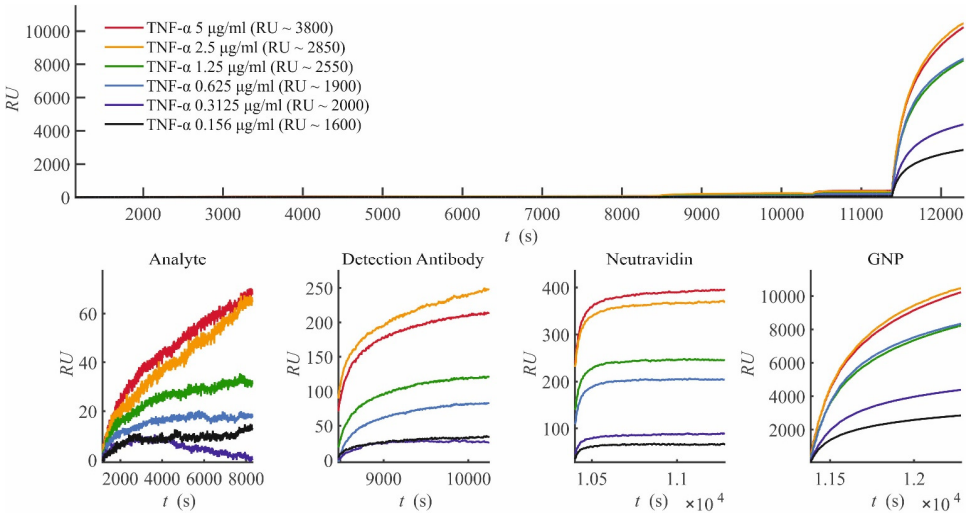

Figure S10.3: Influence of antibody density on TNF-α SPRi enhancement cascade. The association with TNF-α (10 ng/ml) and enhancement cascade is shown for 6 antibody spotting densities (5 µg/ml to 0.156 µg/ml). Average RLL values corresponding to these densities were calculated with the Sprint software from the manufacturer and are shown in the legend.

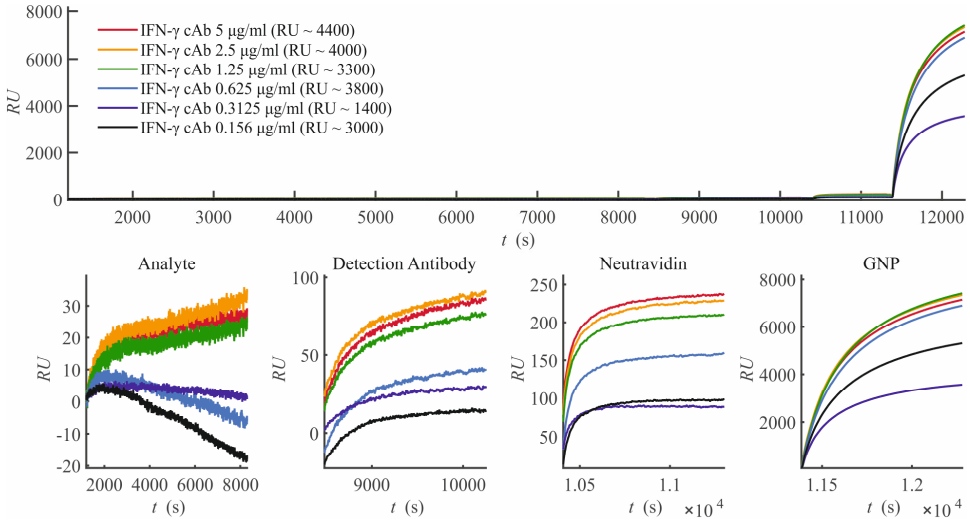

Figure S10.4: Influence of antibody density on IFN-γ SPRi enhancement cascade. The association with IFN-γ (10 ng/ml) and enhancement cascade is shown for 6 antibody spotting densities (5 µg/ml to 0.156 µg/ml). Average RLL values corresponding to these densities were calculated with the Sprint software from the manufacturer and are shown in the legend.

3.5.12 Enhanced SPRi cascade enables high sensitivity and broad dynamic detection range.

Cytokine	K_D (nM)	SPRi			Enhanced SPRi		
		LLOD (pg/ml)	ULOD (pg/ml)	DDR (log)	LLOD (pg/ml)	ULOD (pg/ml)	DDR (log)
IL-6	0.04	2000	10^6	2.7	0.05	10^6	7.3
IL-1β	1.5	4800	10^6	2.3	1.2	10^6	5.9
TNF-α	7.8	380	10^6	3.4	15	10^6	4.8
IFN-γ	26.3	6000	10^6	2.2	22	10^6	4.7

Table S7: The table shows an overview of the results of the SPRi versus enhanced SPRi method. K_D = Affinity of capture antibody (nM), LLOD= Lower Limit of Detection (pg/ml), ULOD = Upper Limit of Detection (pg/ml), DDR= Dynamin Detection Range (log).

3.5.13 Multiplex cytokine measurement: Differential increase in signal

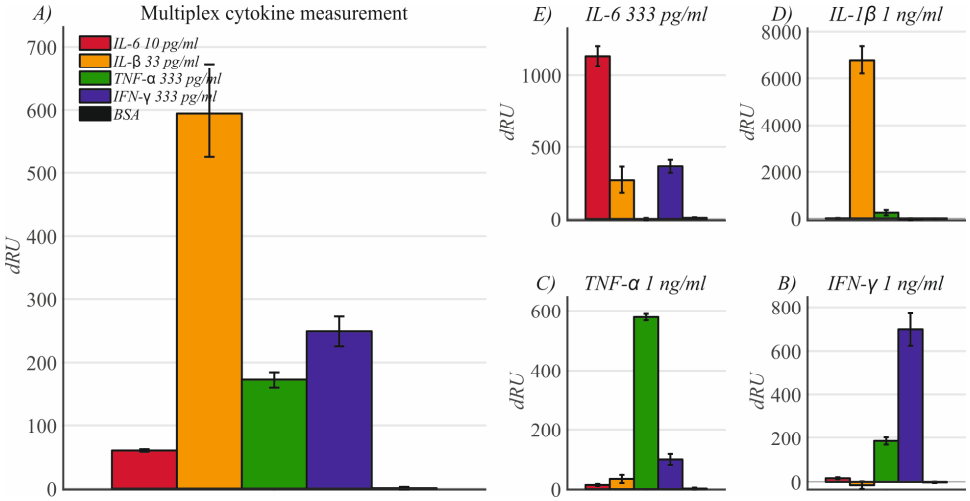

Figure S11. Cytokines were measured specifically in multiplex. A) The dRU signal after gold nanoparticle association after interaction with a mixture of cytokines in the lower region of the dynamic detection range, followed by the detection antibody and neutravidin cascade. The signals shown are an average of 10 spots. B-E). Similar measurement as in (A) were performed; however, the concentration of a single cytokine is increased to the higher region in their dynamic detection range, without changing other concentrations in the mixture. In this way, the specificity and cross-reactivity of the cytokine detection was assessed. In these figures the difference between the resulting signal and the standard mixture is shown. This provides a clear quantitative picture of the cross-reactivity in the experiment. This picture shows the moderate cross-reactivity for the weak IFN-γ antibody, minor cross-reactivity for TNF-α and IL-1β and no cross-reactivity for IL-6.

3.5.14 Cross-reactivity of Capture- and detection antibodies

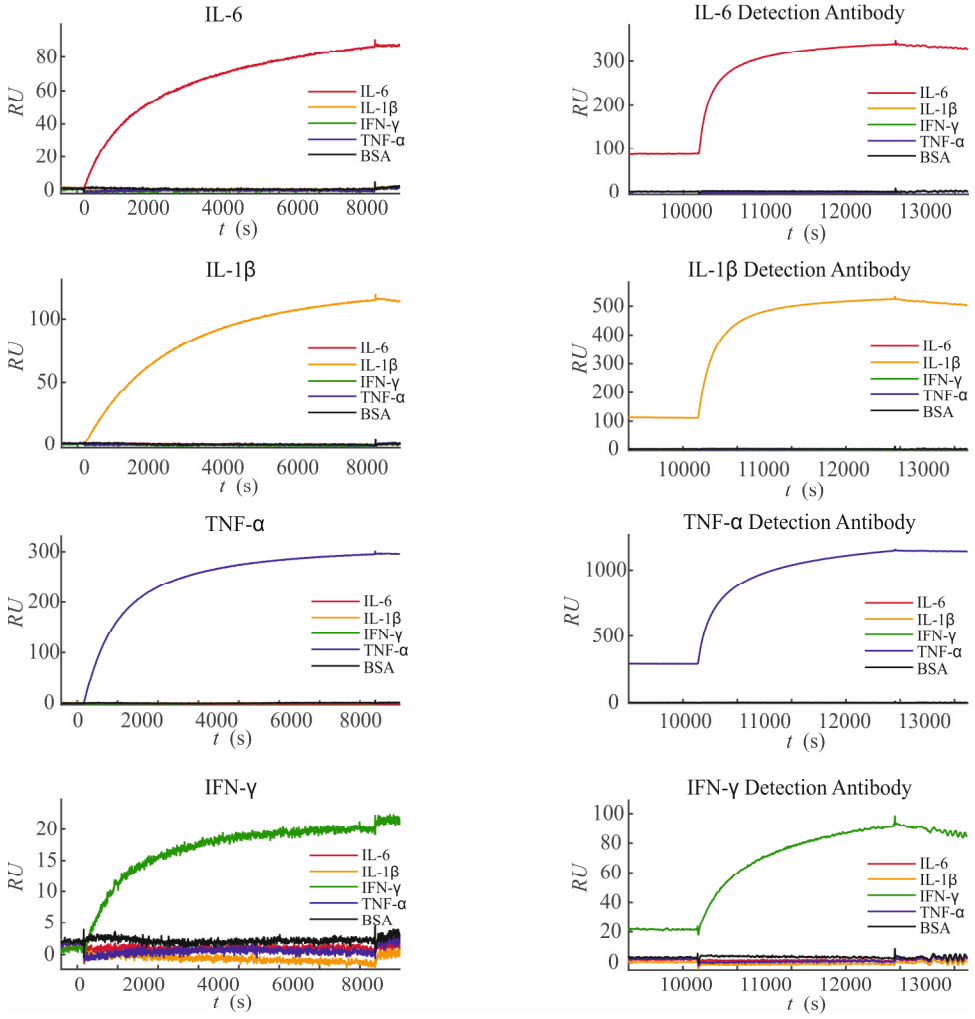

Figure S12: Cross-reactivity of capture- and detection antibodies. Figures 8 A-D depict the interaction with IL-6, IL-1μ, TNF-α and IFN-γ respectively at 100 ng/ml. In each figure the signal is shown for the capture antibody spots of IL-6, IL-1β, TNF-α and IFN-γ with BSA as a control. It can be seen that the capture antibodies only respond to the specific cytokines with negligible cross-reactivity. In figure 6 E-H the subsequent interaction with the specific detection antibodies are depicted. These interactions are additionally shown to be specific with no measurable cross-reactivity.

3.5.15 Synovial fluid spiking experiment background signal

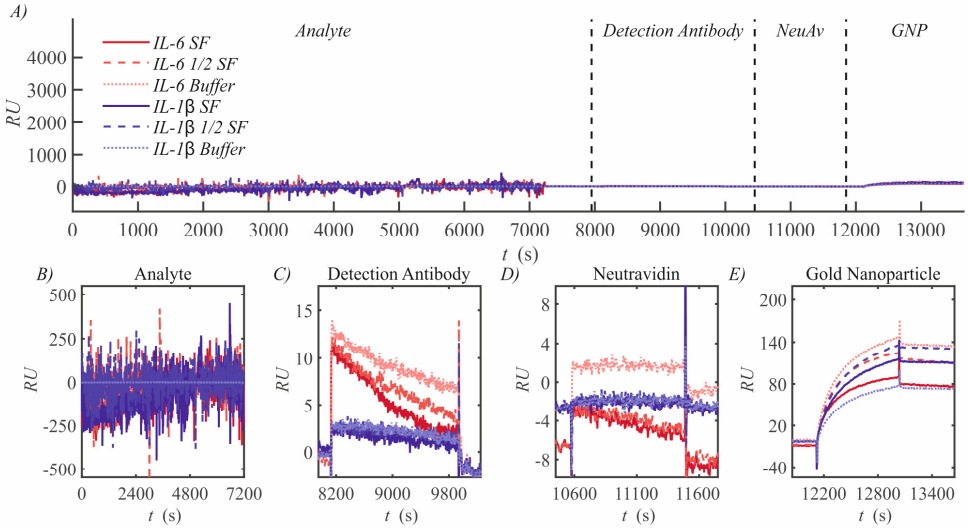

Figure S13: The background signal for IL-6 and IL-1β antibody spots after interaction with SF, half diluted synovial fluid and buffer controls. 9A) The figure shows the enhancement cascade during the blank measurements before interaction with IL-6 and IL-1β. 9B-E) the subplots show the individual stages of the enhancement cascade, the association with the analyte (b), detection antibody (c), neutravidin (d) and gold nanoparticle (e).

References

1. Frampton, J.P., et al., *Aqueous two-phase system patterning of detection antibody solutions for cross-reaction-free multiplex ELISA.* Sci Rep, 2014. **4**: p. 4878.
2. Chikkaveeraiah, B.V., et al., *Electrochemical Immunosensors for Detection of Cancer Protein Biomarkers.* ACS Nano, 2012. **6**(8): p. 6546-6561.
3. Tighe, P.J., et al., *ELISA in the multiplex era: Potentials and pitfalls.* Proteomics Clin Appl., 2015. **9**(3-4): p. 406-422.
4. Bastarache, J.A., et al., *Accuracy and Reproducibility of a Multiplex Immunoassay Platform: A Validation Study.* J Immunol Methods, 2011. **367**(1-2): p. 33-39.
5. Ellington, A.A., et al., *Antibody-Based Protein Multiplex Platforms: Technical and Operational Challenges.* Clin Chem, 2010. **56**(2): p. 186-193.
6. Backen, A.C., et al., *'Fit-for-purpose' validation of SearchLight multiplex ELISAs of angiogenesis for clinical trial use.* J Immunol Methods, 2009. **342**(1–2): p. 106-114.
7. Cretich, M., F. Damin, and M. Chiari, *Protein microarray technology: how far off is routine diagnostics?* The Analyst, 2014. **139**(3): p. 528-542.
8. Moncunill, G., et al., *Performance of multiplex commercial kits to quantify cytokine and chemokine responses in culture supernatants from Plasmodium falciparum stimulations.* PloS one, 2013. **8**(1).
9. Tighe, P., et al., *Utility, reliability and reproducibility of immunoassay multiplex kits.* Methods, 2013. **61**(1): p. 23-29.
10. Juncker, D., et al., *Cross-reactivity in antibody microarrays and multiplexed sandwich assays: shedding light on the dark side of multiplexing.* Curr Opin Chem Biol, 2014. **18**: p. 29-37.
11. Lei, J. and H. Ju, *Signal amplification using functional nanomaterials for biosensing.* Chem Soc Rev, 2012. **41**(6): p. 2122-2134.
12. Munge, B.S., et al., *Nanostructured Immunosensor for Attomolar Detection of Cancer Biomarker Interleukin-8 Using Massively Labeled Superparamagnetic Particles.* Angew. Chem. Int. Ed., 2011. **50**(34): p. 7915-7918.
13. Jo, H., et al., *A highly sensitive and selective impedimetric aptasensor for interleukin-17 receptor A.* Biosens Bioelectron, 2016. **81**: p. 80-86.
14. Osterfeld, S.J., et al., *Multiplex protein assays based on real-time magnetic nanotag sensing.* PNAS, 2008. **105**(52): p. 20637-20640.
15. Lai, G., et al., *Streptavidin-Functionalized Silver-Nanoparticle-Enriched Carbon Nanotube Tag for Ultrasensitive Multiplexed Detection of Tumor Markers.* Adv. Funct. Mater., 2011. **21**(15): p. 2938-2943.
16. Master, S.R., C. Bierl, and L.J. Kricka, *Diagnostic challenges for multiplexed protein microarrays.* Drug Discov Today, 2006. **11**(21–22): p. 1007-1011.
17. Lyon, L.A., M.D. Musick, and M.J. Natan, *Colloidal Au-Enhanced Surface Plasmon Resonance Immunosensing.* Anal. Chem., 1998. **70**(24): p. 5177-5183.
18. Krishnan, S., et al., *Attomolar Detection of a Cancer Biomarker Protein in Serum by Surface Plasmon Resonance Using Superparamagnetic Particle Labels.* Angew. Chem. Int. Ed., 2011. **50**(5): p. 1175-1178.
19. Martinez-Perdiguero, J., et al., *Surface plasmon resonance immunoassay for the detection of the TNFα biomarker in human serum.* Talanta, 2014. **119**(0): p. 492-497.
20. Špringer, T., et al., *Functional gold nanoparticles for optical affinity biosensing.* Anal Bioanal Chem, 2017. **409**(16): p. 4087-4097.
21. Damas, P., et al., *Cytokine serum level during severe sepsis in human IL-6 as a marker of severity.* Ann Surg, 1992. **215**(4): p. 356-362.
22. Schasfoort, R.B.M., et al., *Interpolation method for accurate affinity ranking of arrayed ligand–analyte interactions.* Anal Biochem, 2016. **500**: p. 21-23.
23. Andersson, K., M. Hämäläinen, and M. Malmqvist, *Identification and Optimization of Regeneration Conditions for Affinity-Based Biosensor Assays. A Multivariate Cocktail Approach.* Anal. Chem. , 1999. **71**(13): p. 2475-2481.
24. Zeng, S., et al., *Size dependence of Au NP-enhanced surface plasmon resonance based on differential phase measurement.* Sens Actuators B Chem., 2013. **176**: p. 1128-1133.
25. Armbruster, D.A. and T. Pry, *Limit of Blank, Limit of Detection and Limit of Quantitation.* Clin Biochem Rev, 2008. **29**(Suppl 1): p. S49-S52.

26. Fu, Q., J. Zhu, and J.E. Van Eyk, *Comparison of Multiplex Immunoassay Platforms.* Clin Chem, 2010. **56**(2): p. 314-318.
27. Chung, S.-J., et al., *The Correlation between Increased Serum Concentrations of Interleukin-6 Family Cytokines and Disease Activity in Rheumatoid Arthritis Patients.* Yonsei Med J, 2011. **52**(1): p. 113-120.
28. Arican, O., et al., *Serum Levels of TNF-α, IFN-γ, IL-6, IL-8.* Mediators Inflamm, 2005. **2005**(5): p. 273-279.
29. Di Iorio, A., et al., *Serum IL-1β levels in health and disease: a population-based study. 'The InCHIANTI study'.* Cytokine, 2003. **22**(6): p. 198-205.
30. Berthoud, T.K., et al., *Comparison of commercial kits to measure cytokine responses to Plasmodium falciparum by multiplex microsphere suspension array technology.* Malar J, 2011. **10**(1): p. 1-9.
31. Chowdhury, F., A. Williams, and P. Johnson, *Validation and comparison of two multiplex technologies, Luminex® and Mesoscale Discovery, for human cytokine profiling.* J Immunol Methods, 2009. **340**(1): p. 55-64.
32. Bake, M., *Reproducibility crisis: Blame it on the antibodies*, in *Nature*. 2015, Nature. p. 274-276.
33. Marx, V., *Finding the right antibody for the job.* Nat Meth, 2013. **10**(8): p. 703-707.
34. Schonbrunn, A., *Editorial: Antibody can get it right: confronting problems of antibody specificity and irreproducibility.* J Mol Endocrinol, 2014. **28**(9): p. 1403-1407.

“It would be so nice if something made sense for a change.”

4

Kinetic characterization of SPRi-based biomarker assays enables quality control, calibration free measurements and robust optimization for clinical application

Biomarker measurements are essential for the early diagnosis of complex diseases. However, many current biomarker assays often lack sensitivity and multiplexing capacity, work in a narrow detection range and importantly lack real time quality control opportunities. We have previously demonstrated the development of a SPRi based biomarker assay that addresses the challenges of sensitivity, dynamic range and multiplexing by the sequential application of an enhancement cascade involving biotinylated gold nanoparticles. In this paper, we now complement this essay with a toolbox to kinetically characterize biomarker measurements with ample opportunities for real time quality control by exploiting quantitative descriptions of the physical interactions underlying SPRi measurements.

To achieve this characterization, we have performed three steps. 1) Kinetically defining the individual cascade steps using a heterogeneity of binding sites model, 2) Defining the correlation of ligand binding species to interaction signal and 3) determining the relationship between cascade steps. Combined this resulted in an accurate prediction of SPRi measurements at both low and high concentrations of analytes with deviations <5% between actual measurements and predicted measurement.

Jan Hendriks†, Richard B.M. Schasfoort‡, Daniël B.F. Saris§,#, Marcel Karperien,†*

† Department of Developmental BioEngineering, TechMed institute, University of Twente, The Netherlands.

‡ Medical Cell Biophysics, TechMed institute, University of Twente, The Netherlands.

§ Department of Orthopedics, UMC Utrecht, The Netherlands.

 # Department of Reconstructive Medicine, TechMed institute, Faculty of Science and Technology, University of Twente, The Netherlands.

Manuscript in preparation

Deviation between prediction and real time measurements could point to cross-reactivity, heterophilic antibodies, spotting irregularities and/or other confounders, enabling unmatched quality control opportunities lacking in end point measurements. The toolbox can also be used to create a (simulated) calibration curve, enabling calibration free measurements with good recovery (108 % vs 94% in standard curve). Finally, we show in a proof of concept that these simulations can be used to easily optimize signal (25% increase) while reducing essay time (>50% reduction), compared to the original assay, without requiring extensive experimental work.

The theoretical framework of our essay can be applied to any real time biomarker assay relying on molecular interactions. It can also be used to optimize standard end-point assays. Therefore, this toolbox could help bridge the gap to bring new biomarker assays to the clinic.

4.1 Introduction

Early diagnosis of diseases can avoid progression, improve clinical outcomes and reduce healthcare costs [1]. However, in the onset of diseases changes between healthy subjects and patients are often minor and difficult to detect. Disease specific proteins, in this paper referred to as biomarkers, can give vital information on the disease progression from an early stage. Yet, the concentration of these biomarkers is often low, requiring highly sensitive assays. In addition, the complexity of many diseases, and the heterogeneity of the patient populations, requires the measurement of several biomarkers simultaneous in order to acquire the desired differentiating capacity [2]. Therefore, early disease diagnosis would benefit from highly sensitive, multiplex biomarkers assays.

The most important biomarker assay currently used in both research and clinic relies on the ELISA format or variations thereof. This tool has proven clinical effectivity and has shown to be reliable for over 30 years. However, it can measure only one biomarker at a time and has a relatively small dynamic range, often requiring multiple dilution series [3]. To be able to diagnose more complex diseases, several multiplex assays have been developed [2]. These assays can be subdivided into 2D planar and bead suspension assays. Planar assays function similarly to ELISAs, with a sequential build up in complexity relying on one end point measurement. The final read-out can be colorimetric, fluorescent, chemiluminescent or electro-chemiluminescent, with Searchlight (chemiluminescent) and Mesoscale Discovery (electro-chemiluminescent) as examples. Sensitivity of these assays is generally high, but dynamic range is still limited. This is especially important for multiplex assays, as different biomarkers often exist in a wide variety of concentrations. Furthermore, these assays are shown to experience difficulty from spotting irregularities and unreliability [4], low precision [5, 6], and lack of quality control opportunities [6, 7]. Suspension assays are other multiplex alternatives to the standard ELISA. These assays combine all reagents in suspension and therefore avoid the need for washing steps. Well known examples are the flow cytometry bead arrays and the Luminex™ assay. These assays show acceptable sensitivity and dynamic range [8]. However, they suffer from large inter-assay variation at low concentrations [9] and inherent increase in cross-reactivity due to the suspension format [10].

Despite the development of several multiplex platforms, currently no platform is routinely used in a clinical setting [7]. The main reason for this is the increasing complexity of the measurements as the number of biomarkers increases. For each biomarker added additional cross-reactivity can occur, leading both to more difficult assay development and to more complex quality control [10]. In addition, confounders in the sample matrix, for example heterophilic antibodies, can interfere in the interaction with any of the individual biomarkers [11]. The black-box nature of the current multiplex assays based on end point measurements only makes it extremely difficult to detect these confounders and hampers quality control, seriously limiting clinical use.

In order to advance the use of multiplex assays in clinical settings, more advanced methods for quality control than is possible with end-point assays are needed. We have recently described the development of a multiplex biomarker measurement system based on the real time surface plasmon resonance array imaging (SPRi) system. We have applied a sandwich antibody system followed with a neutravidin and biotinylated gold nanoparticle cascade to sequentially improve the detection signal (ref [12]). With this platform we have shown that we can quantitatively measure biomarkers in low fM (~fg/ml) concentration up to 1 µg/ml in one assay depending on the quality of the capture antibody. In addition, this method proofed suited for multiplex measurements in highly challenging complex sample matrix such as serum and synovial fluid. This assay measures biomarker interactions in real-time allowing for extensive quality control and optimization opportunities for multiplex measurements.

In this paper, we describe the development of a simulation toolbox incorporating these opportunities. The method consists of a complete kinetic characterization of the biomarker cascade and the individual steps. First, we have fitted the individual cascade steps for test biomarker IL-1β by applying both a simple 1:1 Langmuir kinetics model and a model for heterogeneity of binding sites. We subsequently determined the relationship between the interaction steps over a concentration between 10 pg/ml and 10 ng/ml. This allowed us to fit the entire cascade and extrapolate the results accurately for all concentrations tested. This provided us with several interesting opportunities. We can avoid the need for extensive calibration series, as we only need one single measurement to determine the spot density. In addition, the complete characterization of the biomarker assay makes it possible to detect potential confounders and be highly useful for quality control. For example, cross-reactivity and heterophilic antibodies can be easily detected as deviations from the kinetics of the specific antibody and changes to the predicted cascade. Furthermore, the toolbox we have developed can used to simulate optimization experiments to minimize time of maximize signal, without the need for extensive experimentation. This can save time, effort and costs.

4.2 Materials and Methods

4.2.1 Chemicals, immunological reagents and equipment

Acetic Acid, Sodium Acetate, Phosphorous Acid, Phosphate buffered saline, Tween 20, Tween 80 and Bovine serum Albumin (BSA) were obtained from Sigma Aldrich (Zwijndrecht, the Netherlands). The capture antibodies (cAb) and biotinylated detection antibodies (dAb) for IL-1β (cAb clone JK1B1, dAb clone JK1B2), as well as the recombinant proteins IL-1β were purchased from Biolegend (San Diego, USA). Neutravidin was obtained from Thermo Fisher (Waltham, USA). 40 nm biotinylated gold nanoparticles were purchased from Cytodiagnostics (Burlington, Ontario, Canada). Pre-activated sensors for amine coupling (G-type easy2spot) were purchased from Ssens bv (Hengelo, The Netherlands).

4.2.2 Sensor preparation

Il-1β antibodies were immobilized on G-Type easy2spot sensors by reaction to free amines using the Wasatch microfluidics continuous flow spotter (Wasatch Microfluidics, Salt Lake City, UT, US) for 30 min. We have used a Gel-type sensor for the efficient use of the evanescent field and large binding capacity. The antibodies were prepared in a reaction buffer of 50 nM acetic acid (150 µl per spot). Optimal reaction pH was 4.6 and assured concentration to negatively charged sensor and favoured coupling to primary amines. After successful spotting, the sensor was deactivated with 1% BSA in reaction buffer for 7 min and with 0.2M ethanolamine at pH8.5 for another 7 min to reduce non-specific interactions.

4.2.3 Instrumentation

The SPRi measurements were performed on the IBIS MX96™ (IBIS Technologies, Enschede, the Netherlands). The instruments applies an angle-scanning method with automatic fitting to determine SPR shift with 1Hz frequency. An automatic fluid-handling system controls a back and forth flow through a microfluidic flow cell to ensure minimal sample use. It can measure up to 96 spots simultaneously making it highly suitable for multiplex experiments. The measurements were programmed using SUIT software (IBIS Technologies, Enschede, the Netherlands). The type of interaction, interaction times, samples and regions of interest (ROIs) for the antibodies were set and a template was created that was loaded into IBIS data acquisition software. Before each experiment the angle offset was calibrated to ensure wide dynamic detection range. After programming the machine ensures automatic liquid handling and SPR angle measurements. In each experiment 48 spots were used. A back-and-forth flow rate of 10 µl/ml was applied through a flow cell with 12 µl sample volume. Sprint software was used for data collection and referencing. Data was subsequently exported to Matlab R2015A for evaluation through the use of custom scripts.

4.2.4 SPRi enhancement cascade

A SPRi signal enhancement cascade measurement was performed with IL-1β in a broad dynamic detection range. The sensors were prepared as explained above. Antibodies (cAb) were spotted at 5 µg/ml, 2.5 µg/ml, 1.25 µg/ml, 0.625 µg/ml, 0.3125 µg/ml and 0.15625 µg/ml, to achieve multiple ligand densities, with eight spots per concentration. Samples were dissolved in system buffer, containing PBS with 0.075% Tween80 and 0.5% BSA. Cytokines were measured at a concentration ranging from 100 fg/ml (~5 fM) to 1 µg/ml (~50 nM), spanning a dynamic detection range of 7 logarithms. A baseline of 5 minutes was used and an association time of 120 min. The detection antibody concentration was 5 µg/ml (33 nM) and the interaction was performed with a baseline of 2 min and 30 min association time. Neutravidin was used at concentration of 1.5 µg/ml (25 nM), 2 min baseline and 15 min association, and the gold nanoparticle concentration was 77.69 mg/ml (0.2 nM), 2 min baseline and 15 min association. After each cascade, the sensor was regenerated using a double regeneration pulse for 30s, consisting of 200 mM phosphoric acid at pH 2.5.

The cascade interaction was performed as follows: First a cytokine (Cyt) was injected, followed by a specific biotinylated detection antibody (dAb), neutravidin (NeuAv) and a biotinylated gold nanoparticle (GNP) (40nm diameter). After each interaction, the sensor was washed to reduce the non-specific signal. Each step in the cascade will increase the interaction signal proportionally and thus the sensitivity of the assay. For more details, we kindly refer the reader to the extensive characterization in ref [12].

In each step of the cascade the complex grows sequentially. In the first step the capture antibody is the ligand and the cytokine is the analyte. In the second step the capture antibody – cytokine complex is the ligand and the detection antibody can be considered as the analyte. In the third step the capture antibody – cytokine – detection antibody complex is the ligand and neutravidin is the analyte. In the final step the capture antibody – cytokine – detection antibody – neutravidin complex is the ligand and the gold nanoparticle is the analyte. This is summarized in table S1.

A typical experiment started with two full cascades with system buffer in each step to remove unbound antibody and to create a stable baseline. Subsequently, three blank cascades were measured, with system buffer in the cytokine interaction step, followed by the biotinylated detection antibody, neutravidin and the biotinylated gold nanoparticle. These blanks were used to determine non-specific interactions and provide the background correction. Finally the cytokine cascades were performed starting from the lowest concentration.

Data was collected using Sprint software, referenced and exported to Matlab.

4.2.5 Fitting of cascade steps

In order to kinetically characterize the enhancement cascade, first the kinetic parameters of the individual cascade steps were determined. We applied three different models to fit these steps. The first model describes a simple 1:1 Langmuir interaction that can be captured with exponential equation 1.

$$RU(t) = \frac{R_{max}}{1+\frac{k_{off}}{k_{on}c}} * \left(1 - e^{\left(-\left(k_{on}c+k_{off}\right)*t\right)}\right) \quad (1)$$

In this equation Rmax is the binding capacity of the ligand (RU), kon the rate of association (M^{-1} s^{-1}), koff the rate of dissociation (s^{-1}), c is the analyte concentration (M) and t is time from start of the interaction (s).

In many interactions, including antibody-antigen, a simple 1:1 interaction model cannot explain all curvature in the data. Therefore often more complex interaction models are required [13]. There can be several reasons for the deviation from the 1:1 interaction. The most common ones are a heterogeneity of binding sites, mass transport limitations or a combination of both [14].

Therefore, we applied a second model accounting for the heterogeneity of binding sites. We chose to use the simplest version of this model accounting for two ligand

species, one with relatively high and one with relatively low affinity. This lead to exponential equation 2.

$$RU(t) = \frac{R_{max1}}{1+\frac{k_{off1}}{k_{on1}c}} * \left(1 - e^{(-(k_{on1}c+k_{off1})*t)}\right) + \frac{R_{max2}}{1+\frac{k_{off2}}{k_{on2}c}} * \left(1 - e^{(-(k_{on2}c+k_{off2})*t)}\right) \quad (2)$$

In this equation Rmax1 and Rmax2 are the binding capacities (RU), kon1 and kon2 the rate of association (M-1 s-1), and koff1 and koff2 the rate of dissociation (s-1) of the ligand species 1 and 2 respectively, c is the analyte concentration (M) and t is time from start of the interaction (s).

As a third model, we corrected for mass transport limitations according to [14]. Here, they describe the following differential equation 3.

$$\frac{dRU}{dt} = k_{on}^{(app)} c_0 (R_{max} - RU(t)) - k_{off}^{(app)} \quad (3)$$

$$\frac{k_{on}^{(app)}}{k_{on}} = \frac{k_{off}^{(app)}}{k_{off}} = \frac{1}{1+\frac{k_{on}(R_{max}-RU(t))}{k_{tr}}} \quad (4)$$

In these equations Rmax is the binding capacity of the ligand (RU), and kon(app) and koff(app) are the apparent kon and koff rates which are reduced by ligand capacity divided by the mass transport rate (ktr) (equation 4). This rate is dependent on the specific analyte, the SPR machine and the flow chamber, and can range between 107 and 1013 s-1. The model predicts a large influence of mass transport with small mass transport rate, large kon and large ligand binding capacity.

We have used custom Matlab scripts to fit the different models. For the 1:1 and heterogeneity model, we have used the lsqcurvefit function embedded in Matlab. As input we have provided time, RU signal, and concentrations. Additionally we applied upper and lower limits to the fits, determined by initial guess and physiological feasibility. We applied different fitting strategies for the analyte interaction step and the cascade enhancement steps. We fitted the antibody-analyte kinetics globally over the concentrations 1 ng/ml, 10 ng/ml and 100 ng/ml and spotting densities 5 µg/ml, 2.5 µg/ml, 1.25 µg/ml, 0.625 µg/ml, 0.3125 µg/ml and 0.15625 µg/ml simultaneously. Kon (1,2) and koff (1,2) were shared variables, c a concentration dependent input, and Rmax (1,2) was allowed to vary between the different ligand densities.

The enhancement cascade steps interact with the previously captured ligand – analyte complex. This complex can be considered the ligand with a specific binding capacity. The ligands and analytes at each step in the cascade are defined in table S1. The variable in these interactions is now not the 'analyte' concentration, but the ligand density. For these steps we applied global fitting over all signals from the concentrations [10 pg/ml, 33 pg/ml, 100 pg/ml, 1 ng/ml and 10 ng/ml] and spotting densities 5 µg/ml, 2.5 µg/ml, 1.25 µg/ml, 0.625 µg/ml, 0.3125 µg/ml and 0.15625 µg/ml simultaneously (30 signals in total per step). Kon (1,2) and koff (1,2) were shared variables, c a cascade step dependent input, and Rmax (1,2) was allowed to vary between the different ligand densities.

The differential equations to describe mass transport limitations were solved numerically using the Matlab function dsolve, with starting condition s(0)=0. Using the equation we have performed fits on especially the neutravidin and gold nanoparticle steps at high ligand density. This according to the expectation that the high affinity of neutravidin and high mass of the gold nanoparticle could result in significant mass transport limitations. No significant mass transport limitations were observed in both neutravidin and in the gold nanoparticle steps (Figure S1). Therefore, we decided not to use this relatively complex model.

4.2.6 Correlation of ligand binding species to interaction signal

The simple 1:1 fits and more complex fits accounting for heterogeneity of binding sites resulted in a large number of Rmax(1,2) values for each cascade step depending on the ligand density. It is important to know how these values relate to the maximum RU values after saturation (dRU). If the 1:1 fit is good over the entire concentration range tested, we can expect a linear correlation of Rmax to the dRU value. This is however not by definition true for the fits accounting for multiple ligand affinities. It is likely that binding is dominated by high affinity spots at low ligand densities leading to a high Rmax1/Rmax2 ratio [13]. This would resemble a simple 1:1 fit. At higher binding capacities the number of lower affinity spots could increase, partially due to steric effects, and could lead to a low Rmax1/Rmax2 ratio. The Rmax(1,2) could grow with dRU in linear fashion, but it also possible that it follows a non-linear relationship. Therefore, we plotted dRU vs Rmax(1,2) and applied 3 fitting models. The first model is a simple linear fit with slope a, with a constraining condition (dRU=0, Rmax(1,2)=0) ensuring the fit intersects the origin (equation 5).

$$R_{\max(1,2)} = a_{1,2} * dRU \tag{5}$$

The other two models are non-linear. The second model describes a 4-parameter logistic fit, often applied in biomarker assays and is shown in equation 6.

$$R_{\max(1,2)} = D_{1,2} + \frac{(A_{1,2} - D_{1,2})}{(1+(\frac{dRU}{C_{1,2}})^{B_{1,2}}} \tag{6}$$

In which A is the minimum asymptote, B is the Hill's slope, C is the inflection point and D is the maximum asymptote.

As we expect a maximum in high affinity binding spots as ligand density increases, we tested a third model based on a simple exponential equation 7.

$$R_{\max(1,2)} = I_{1,2} * (1 - e^{-S_{1,2} * t}) \tag{7}$$

In which I is the maximum asymptote and S is the slope.

4.2.7 Relationship between cascade steps

After the thorough characterization of the individual cascade steps it is necessary to determine the relationship between the different cascade steps. To achieve this, the difference in signal from the end of an interaction with the beginning of interaction at a

specific cascade step was determined (dRU). This was performed for the concentrations [1pg/ml, 3.33 pg/ml, 10 pg/ml, 33 pg/ml, 100 pg/ml, 1 ng/ml and 10 ng/ml] and spotting densities [5 µg/ml, 2.5 µg/ml, 1.25 µg/ml, 0.625 µg/ml, 0.3125 µg/ml and 0.15625 µg/ml] for the detection antibody (dAb), neutravidin (NeuAv) and gold nanoparticle (GNP) steps. This resulted in 42 individual dRU values per cascade step. We subsequently determined the relationship between the detection antibody and neutravidin, and neutravidin and gold nanoparticle steps according to the three fitting models described above.

For the relationship between the analyte and detection antibody step a slightly different approach was taken. The analyte step resulted in dRU values below the measurable threshold from a concentration of 1 ng/ml (meaning that 1pg/ml, 3.33 pg/ml, 10 pg/ml, 33 pg/ml and 100 pg/ml were not measurable). This would make it impossible to create meaningful fits between dRUs for this important step. To overcome this we have used the simulated dRU values for analyte step at the relevant concentrations based on the kinetic data acquired via the 1:1 Langmuir or heterogeneity of binding sites models. The relationship between these dRU and the dRU values of antibodies step were subsequently determined as described above.

4.2.8 Prediction of enhancement cascade

We applied the information on the kinetics of the individual cascade steps, the correlation between Rmax and dRU and the relationship between the cascade steps to simulate the enhancement cascade. To achieve this we first simulate the analyte step for three low [1pg/ml, 3.33 pg/ml, 10 pg/ml] and three high [100 pg/ml, 1 ng/ml and 10 ng/ml] IL-1β concentrations at a spotting density of 5 µg/ml by either the 1:1 model or the heterogeneity model. The resulting dRUanalyte is used to calculate dRUdAb by fitting model 1, 2 or 3. Rmax,dAb(1,2) is derived from the dRUdAb by fitting model 1, 2 or 3 and the detection antibody step can be simulated. dRUdAb is subsequently used to calculate dRUNeuAv, which is used to derive RmaxNeuAv(1,2). The same steps are again used to calculate the parameters for the GNP step. This leads to the complete simulation of the enhancement cascade for the concentrations tested.

4.2.9 Calibration free measurements

The accurate prediction of the enhancement cascade allows for calibration free measurements. In principle only knowledge of the Rmax of the analyte spot is required to predict the entire cascade. To demonstrate the potential, we have fitted the curves at a specific step in the enhancement cascade (Cyt, dAb, NeuAv or GNP) and reverse calculated the concentration. We have performed this for the concentrations [1pg/ml, 3.33 pg/ml, 10 pg/ml, 33 pg/ml, 100 pg/ml, 1 ng/ml and 10 ng/ml] and spotting density 5 µg/ml by either the 1:1 model or the heterogeneity model. The procedure is as follows: For example, a fit is performed at the GNP step resulting in Rmax (1,2), this can be recalculated to dRUGNP, which can be recalculated to dRUNeuAv, to dRUdAb and to dRUanalyte. From this dRUanalyte the concentration of the analyte can be calculated based on the kinetics data. Using this method we have created a simulated calibration

curve. We have compared the simulated calibration curve to the concentrations calculated from calibration curve derived via the standard method in biomarker assays (fit according to equation 6) and to the actual concentrations.

4.2.10 Assay optimization

The kinetic characterization of the enhancement cascade allows for optimization experiments using simulations. We have demonstrated this by adjusting the concentrations of the individual cascade steps and their association times. This results in enhancement cascades with different timings and signals. We have subsequently optimized the cascade to obtain maximal signal (by adjusting concentration) and optimized for both time and signal (by adjusting concentration and association times).

4.3 Results

4.3.1 SPRi enhancement cascade

We have used the SPRi enhancement cascade that was described before [12], as a model biomarker assay that can be fully kinetically characterized. The SPRi enhancement cascade first measures the interaction with a biomarker and subsequently enhances the signal with a biotinylated detection antibody, neutravidin and in the last step with a biotinylated gold nanoparticle. For our model reactions we have measured IL-1β in a concentration range between 100 fg/ml and 1 µg/ml over six spot densities. A representative measurement at 10 ng/ml at a spotting density of 5 µg/ml is shown in figure 1.

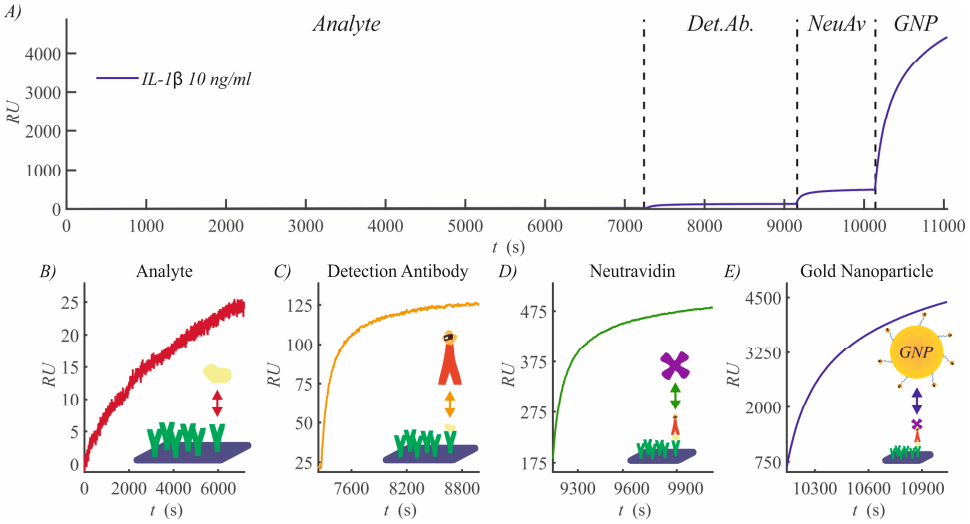

Figure 1: SPRi enhancement cascade for IL-1β. The signals are based on the average of 8 individual spots at spotting density of 5 µg/ml. A) The sequential build up in SPRi signal is shown. Det.Ab = Detection antibody, NeuAv = Neutravidin, GNP = Gold nanoparticle. B-E) in the subplots the signals for the individual cascade steps are shown magnified. The figure inserts schematically depict each interaction.

The figure shows the sequential increase in SPRi signal in the enhancement cascade. The signal increases from 25 RU after analyte interaction to 125 RU after detection antibody, 475 RU after neutravidin and to 4500 RU after gold nanoparticle interaction. This results in a total signal increase of 5, 15 and 180 times respectively. This large signal increase allowed us to measure biomarkers in a concentration as low as 50 fg/ml and in a dynamic range of more than 7 logarithms. In total 480 individual cascade signals served as input for our simulation model, which were based on measurements of IL1β in a concentration range from 100 fg/ml to 1 µg/ml at 6 different spotting densities of the capture antibody.

4.3.2 Fitting of cascade steps

Each step of the enhancement cascade is governed by specific kinetics and can as such be kinetically characterized. We applied two different models to fit each step in the cascade, the simple 1:1 Langmuir interaction model and the more complex heterogeneity of binding sites model. First we applied both models to fit the antibody – analyte interaction step over the concentrations 1 ng/ml, 10 ng/ml and 100 ng/ml. The 1:1 interaction model resulted in relatively good fits at low concentrations, but started to deviate from the signal at higher concentrations (results in figure S2). The results for the heterogeneity of binding sites model is shown in figure 2.

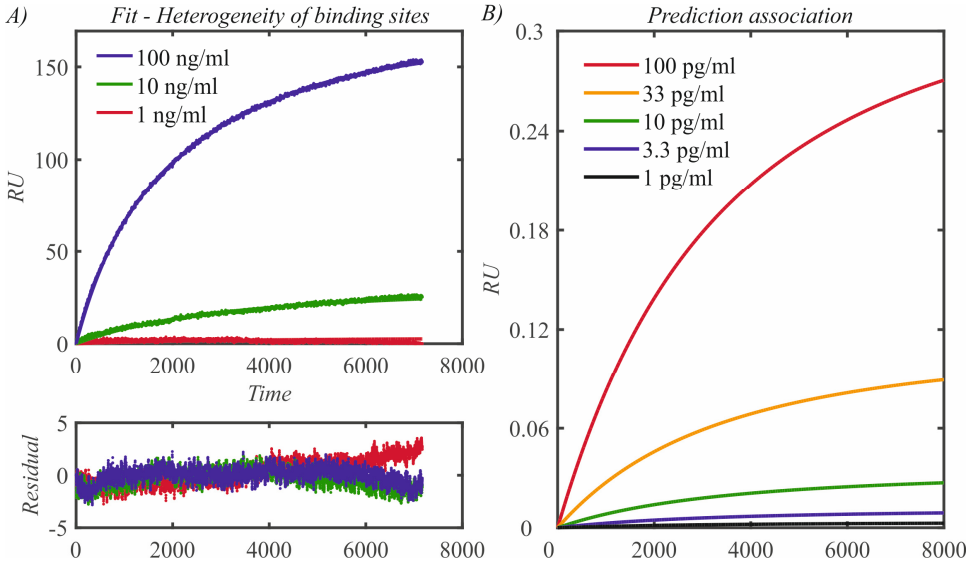

Figure 2. Fits and simulations of the antibody – analyte interaction. A) The fits using the heterogeneity of binding sites model is shown over the concentrations 1, 10 and 100 ng/ml at a spot density of 5 µg/ml (~ 1900 RU). The residuals, i.e. the difference between fit and actual measurements are shown in the subplot (mean residuals are 0.75 RU) below. Fitted parameters were: R_{max1} = 66 RU and R_{max2} = 286 RU. k_{on1} = 1.6x10^5 M^{-1} s^{-1} and k_{off1} = 5.7x10^{-4} s^{-1} resulting in K_{D1} = 3.7 nM, k_{on2} = 2.5x10^4 M^{-1} s^{-1} and k_{off2} = 1.9x10^{-4} resulting in K_{D2} = 7.6 nM. B) The simulations using the kinetic model for the lower concentrations are shown.

Figure 2A clearly shows that this antibody can be fitted with small residuals defined as the difference between the fit and actual measurement using the heterogeneity of binding sites fit. This resulted in a K_{D_1} of 3.7 nM and a K_{D_2} of 7.6 nM. The average K_D was 6.9 nM which closely resembles the K_D of the 1:1 fit (K_D = 5.1 nM) and the 1:1 fit K_D determined with extensive single cycle kinetics (SCK) experiment (K_D = 1.7 nM). In the supplemental figure S3, the fits for the other spot densities are shown. Figure 2B shows the simulations for the antibody – analyte signal for the lower concentrations. These signals are all lower than the noise of the system (~1 RU) and could never be measured with accuracy. However, these simulations allow for a more accurate estimate of RU values, which are essential for complete characterization of the cascade.

The enhancement steps of the cascade were fitted globally with both the 1:1 Langmuir and heterogeneity of binding sites model over six ligand densities. The fits for the 1:1 model were accurate at low IL-1β concentrations, and thus 'ligand' densities, but started to deviate strongly at higher concentrations (more detail in figure S4). For this reason, we have decided to continue with the heterogeneity of binding sites model. We have first determined the kinetic parameters by global fit at a specific IL-1β concentration at the six spot densities (1-10 ng/ml for dAb and 100 pg/ml for NeuAv and GNP respectively). We subsequently assessed the correctness of these parameters for all IL-1β concentrations. The results for relatively low and high IL-1β concentrations over the spot densities 5 µg/ml, 2.5 µg/ml and 1.25 µg/ml are depicted in figure 3.

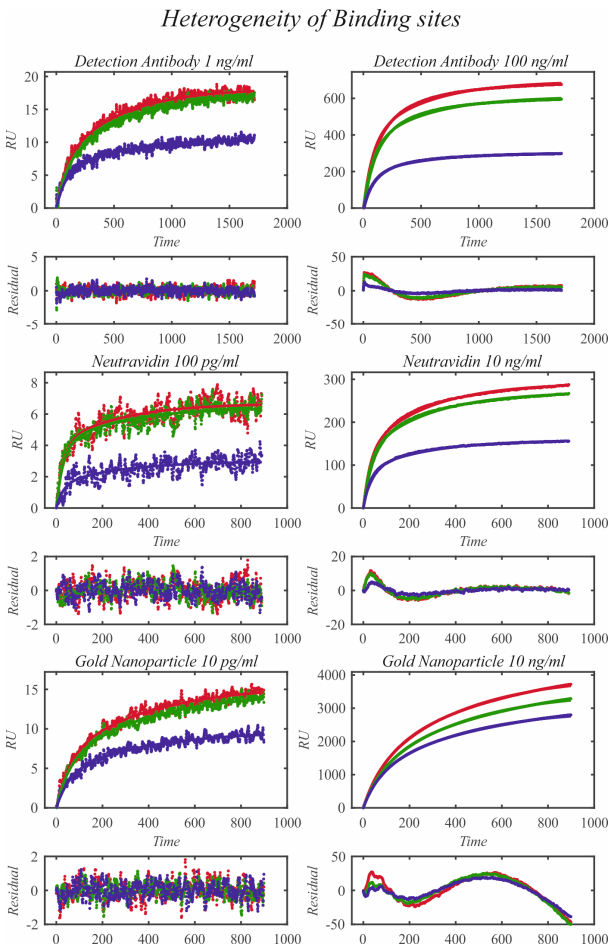

Figure 3. Fits of enhancement cascade steps using heterogeneity of binding sites model. In this figure the left graphs show signal and fit overlay at relatively low IL-1β concentration and the right graphs at high concentration. The subplots show the residuals of the fits. Fitting parameters were as follows. Detection antibody: K_{on1} = 2.5x10^5 M^{-1} s^{-1} and K_{off1} = 4.6x10^{-3} s^{-1} leading to K_{D1} = 18 nM, K_{on2} = 5.7x10^4 M^{-1} s^{-1} and K_{off2} = 6.9x10^{-5} s^{-1} leading to KD2 = 1.2 nM. Neutravidin: K_{on1} = 1.4x10^6 M^{-1} s^{-1} and K_{off1} = 8.4x10^{-6} s^{-1} leading to KD1 = 6.1 pM, K_{on2} = 1.5x10^5 M^{-1} s^{-1} and K_{off2} = 6.3x10^{-8} s^{-1} leading to K_{D2} = 0.42 pM. Gold nanoparticle: K_{on1} = 9.3x10^7 M^{-1} s^{-1} and K_{off1} = 2.1x10^{-6} s^{-1} leading to KD1 = 22 fM, K_{on2} = 1.3x10^7 M^{-1} s^{-1} and K_{off2} = 2.3x10^{-8} s^{-1} leading to K_{D2} = 1.7 fM.

It can be seen from figure 3 that the enhancement steps can be fitted with small residuals at both low and high IL-1β concentrations using the heterogeneity of binding sites model (although residuals do increase slightly at higher concentrations from 0.36, 0.38 and 0.37 to 5.26, 1.98 and 14.19 RU for detection antibody, neutravidin and gold nanoparticle respectively). We have tested a more complex model with three ligand species, but this did not result in further reduced residuals (data not shown). Therefore, we suggested that these residuals might have a different origin. When we compare R_{max1}/R_{max2} at low concentrations (Average = 0.93) vs R_{max1}/R_{max2} at high concentrations

(Average = 0.84), we can see that the ligand binding sites with slower association kinetics become more dominant at higher concentrations. Which is in line with the results for the antibody-analyte interaction. The K_D's for the detection antibody are close to the KDs for the primary capture antibody, although the ligand sub-species seems to be more separated. The K_D for detection antibody neutravidin step is extremely high ($6.1x10^{-12}$ - $4.2x10^{-13}$ M), which is expected from a biotin – avidin interaction (K_D 10^{-15}). The KD from the neutravidin – gold nanoparticle interaction is even closer to the expected values ($2.2x10^{-14}$ – $1.7x10^{-15}$). This is caused by the higher k_{on} rates, which could be a result of the steric freedom of the biotins though the PEG linker, in contrast with direct biotin coupling on the antibody.

4.3.3 Correlation of ligand binding species to interaction signal

The enhancement cascade steps could only be successfully kinetically characterized over the entire concentration range using the heterogeneity of binding sites model. This indicates that there are multiple species of ligands with different k_{ons}, k_{offs} and thus affinities. In the model that we have tested, this means there are two distinct species: one with faster association and one with slower association kinetics. It is expected from literature and seen in our data that there is a relationship between both analyte concentration and ligand density with the occupation of the specific ligand species. As the analyte concentration in the enhancement steps is fixed (e.g. the concentration of the detection antibody, neutravidin and the gold nanoparticle), only the ligand density varies between the experiments and is determine by both the capture antibody spot density and the IL-1β concentration. We have assessed the correlation between the R_{max} (1, 2) of the ligand species and the ligand density over the IL-1β concentrations [10 pg/ml, 33 pg/ml, 100 pg/ml, 1 ng/ml and 10 ng/ml] and the spot densities [5 µg/ml, 2.5 µg/ml, 1.25 µg/ml, 0.625 µg/ml, 0.3125 µg/ml and 0.15625] with three fitting models. The linear fitting model was unable to capture the dynamics, especially at higher ligand densities (Figure S5 for 1:1 model, Figure S6 for heterogeneity of binding sites model). The non-linear models (equation 6 and 7) in combination could explain the curvature in the data, which is shown in figure 4.

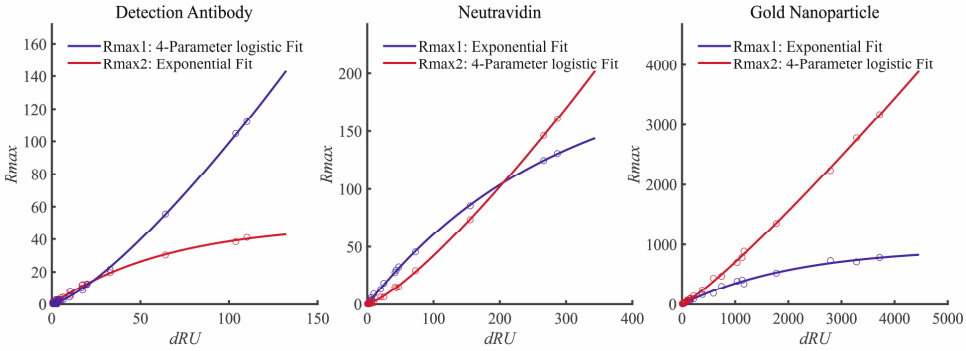

Figure 4. Correlation between dRU and R_{max} (1, 2) of ligand species. In this figure R_{max} (1, 2) is plotted against dRU for the detection antibody, neutravidin or gold nanoparticle step and either an exponential fit or 4-parameter logistic fit is applied.

It can be seen from figure 4 that there is a clear non-linear relationship between the dRU signal (and thus ligand density) and the Rmax of the ligand species. In all three cascade steps one ligand species can be characterized by an exponential fit. This ligand species is dominant at lower densities, but becomes less dominant at higher densities. Interestingly, the higher affinity species becomes less dominant in the antibody step as expected, but the lower affinity species become less dominant in the neutravidin and gold nanoparticle steps indicating different behaviour. The other species can be characterized with a 4 parameter logistic fit. This species is less dominant at lower densities, but slowly becomes more important as the ligand density increases.

4.3.4 Relationship between cascade steps

After the characterization of the individual cascade steps, it is important to determine the relationship between these steps. We have assessed the relationship using the same three fitting models as described above: Linear model, Exponential model and 4-parameter logistic model. The relationship between the cascade steps was assessed over the IL-1β concentrations [1 pg/ml, 3.3 pg/ml, 10 pg/ml, 33 pg/ml, 100 pg/ml, 1 ng/ml and 10 ng/ml] and the spot densities [5 µg/ml, 2.5 µg/ml, 1.25 µg/ml, 0.625 µg/ml, 0.3125 µg/ml and 0.15625]. The linear model was unable to capture the curvature at higher IL-1β concentrations and the exponential model under-predicted the curvature at the lower concentrations (Figure S7 and S8). Therefore, we have used the 4-parameter logistic model to describe the relationship between the interaction steps. The results are shown in figure 5.

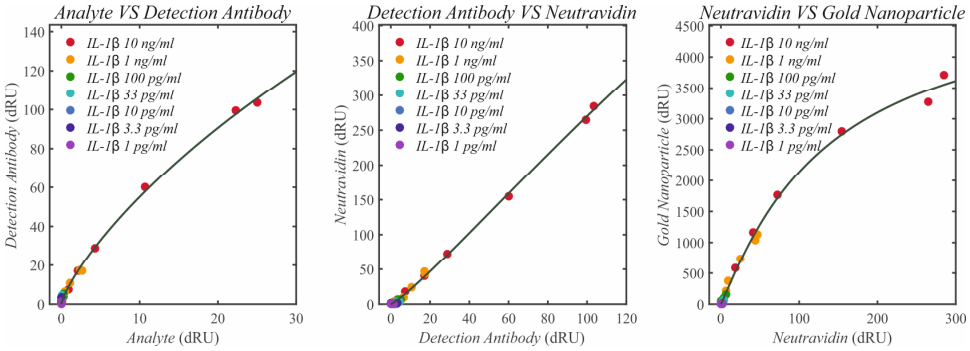

Figure 5. Relation between the enhancement cascade steps. From left to right the relationship between analyte vs detection antibody, detection antibody vs neutravidin and neutravidin vs gold nanoparticle is shown. The signals for specific IL-1β concentration over the six spot densities is grouped by colour. The fits depict the results from the 4-parameter logistic model.

It can be seen from figure 5 that there is clear curvature in the relationship between the different enhancement cascade steps. This curvature is especially prominent in the relationship between analyte vs detection antibody and neutravidin vs gold nanoparticle and is characterized by a declining slope, indicating a certain saturation. The curvature in the relationships is captured accurately with the 4-parameter logistic model.

4.3.5 Prediction of enhancement cascade

The characterization of the individual enhancement steps and their inter relationships allows us to predict the enhancement cascade at a specific concentration and spot density. To demonstrate this we have predicted the cascade at three high (100 pg/ml, 1 ng/ml and 10 ng/ml) and three low (1 pg/ml, 3.3 pg/ml and 10 pg/ml) IL-1β concentrations at a spot density of 5 µg/ml and compared this to the actual measured data. The results are shown in figure 6. Additionally, we have performed the same predictions using the 1:1 model, which can be seen in Figure S9.

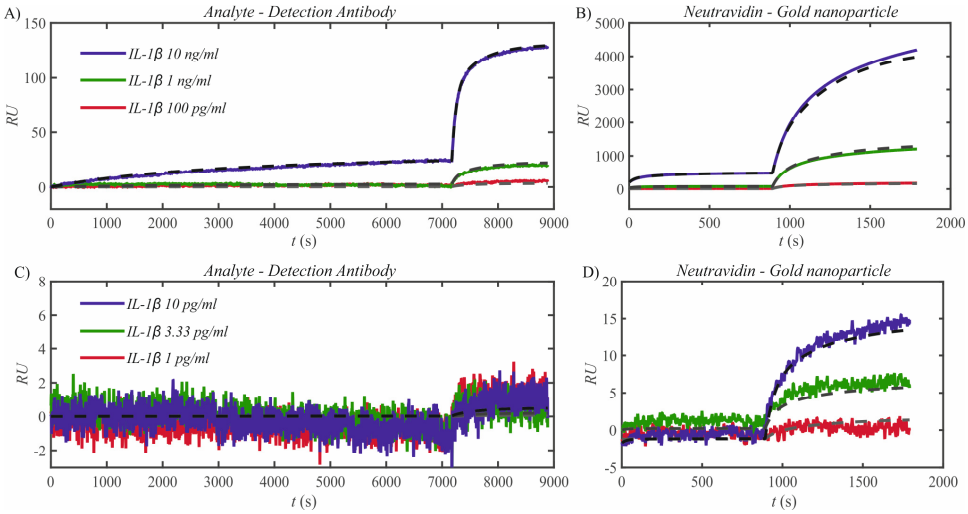

Figure 6: prediction of the enhancement cascade. The predictions of the enhancement cascade (dashed lines) are shown in comparison with the SPRi signals (solid lines) for three high (A-B) and three low (C-D) IL-1β concentrations. The analyte – detection antibody step (A and C) and neutravidin – gold nanoparticle step (B and D) are shown separately to increase clarity.

Figure 6 shows that the enhancement cascade can be predicted with good accuracy for both very low (deviation 2.9%) and high (deviation 4.3%) concentrations by applying the parameters from the heterogeneity of binding sites model, the correlation between dRU and Rmax(1,2) and relationship between the cascade steps. This is in contrast with the 1:1 model that could only predict the correct curvature for the low concentrations (Figure S9). These accurate predictions allows for extensive quality control opportunities. A deviation from the predicted curvature and thus kinetics can be easily detected. This enables the detection of spotting irregularities, cross-reactivity and heterophilic antibodies, which are easily missed in assays based on end-point measurements.

4.3.6 Calibration free measurements

In addition to extensive quality control, the accurate prediction of the enhancement cascade also allows for calibration free measurements. This can be achieved by reversing the steps required to predict the cascade at a specific IL-1β concentration. A fit at any step in the cascade can then be used to acquire the IL-1β concentration. We have applied

these fits and the reverse prediction at the IL-1β concentrations [1 pg/ml, 3.3 pg/ml, 10 pg/ml, 33 pg/ml, 100 pg/ml, 1 ng/ml and 10 ng/ml] and spot density of 5 µg/ml at all 4 steps of the enhancement cascade. We compared this to a standard calibration curve calculated with the 4 parameter logistics model. The results are shown in figure 7 (results for 1:1 fit in figure S10).

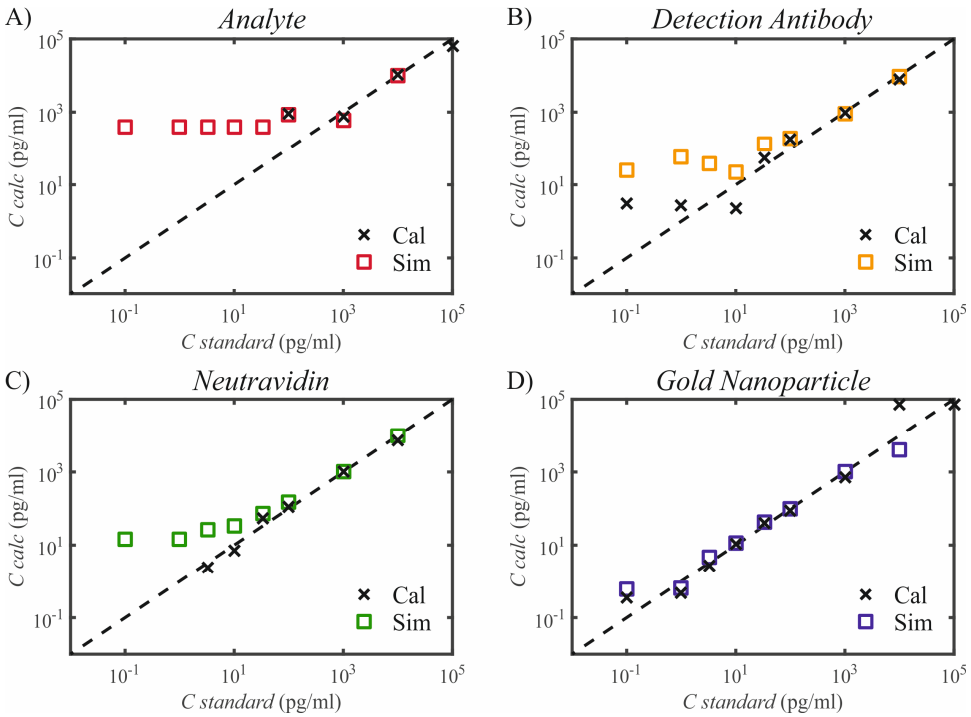

Figure 7: Predictions of enhancement cascade can be used for calibration free measurements. A-D) IL-1β calculated concentration is plotted against the standard in the biomarker, detection antibody, neutravidin and gold nanoparticle step respectively. The dashed line shows the actual concentration, x shows calculated concentration based on the standard calibration curve and the squares the calculated concentration based on the simulations.

Figure 7 shows that the IL-1β concentration can be calculated from the simulations in all steps of the enhancement cascade. These calculations are accurate until a lower limit of detection (LLoD) that is dependent on the step in the enhancement cascade. Based on the simulated calibration curve these LLoD are 600 pg/ml, 200 pg/ml, 75 pg/ml and 1 pg/ml for analyte, detection antibody, neutravidin and gold nanoparticle step respectively. It can be seen that that the simulated calibration curve is as good as the normal calibration curve to determine concentrations (mean recovery in linear range for gold nanoparticle 108 % vs 94 % for standard curve). This avoids the need for extensive calibration measurements, saving time and money.

4.3.7 Assay optimization

The kinetic characterization of the enhancement cascade allows us to easily optimize the biomarker assay without requiring large number of experiments. We can simply adjust concentrations and times of individual steps and simulate the cascade. As a proof of concept, we have performed two assay optimizations, one optimizing the signal and one optimizing both time and signal. The result is shown in figure 8.

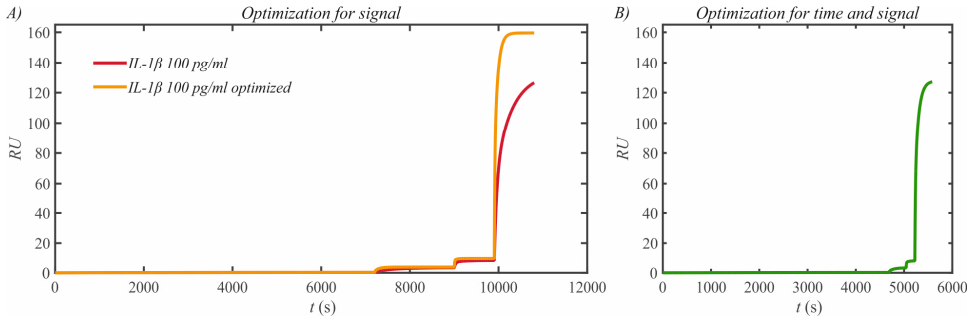

Figure 8: Optimization simulations for the enhancement cascade. A) The optimization for signal is shown compared to the standard cascade at an IL-1β concentration of 100 pg/ml. B) At the same IL-1β concentration the optimization for both time and signal is shown.

In figure 8A the optimization for the total signal in the enhancement cascade is shown. This optimization is achieved by increasing the concentration of each component of the enhancement cascade by 5 times (detection antibody, neutravidin and gold nanoparticle). This leads to an improvement in signal by 25% and thus a higher sensitivity. Similarly, we optimized the enhancement cascade for both time and signal (figure 8B). When a 5 times higher concentration was used, this resulted in a reduction of assay time by 50% with no signal decrease, improving the applicability for point of care applications. This proof of concept demonstrates that optimizations for biomarker assays can be easily designed using our method which can then be subsequently experimentally validated.

4.4 Discussion

Biomarker assays are essential for early diagnosis of complex diseases. However, current biomarker assays lack the required sensitivity, dynamic range and multiplexing capacity [2]. In addition, most assays are end-point measurements and therefore lack essential quality control making them unsuitable for large scale clinical application [7]. We have previously developed a biomarker assay based on SPRi by applying an enhancement cascade [12]. This has allowed us to measure biomarkers in multiplex with both high sensitivity and specificity in a broad dynamic detection range. In this paper, we have we have fully kinetically characterized this biomarker assay as a proof of concept. This enables extensive quality control, calibration free measurements and allows for simple optimizations. The same steps can be applied to any biomarker assays

using real time technologies, both label free and with enhancement tags. This can help bridge the gap and finally bring these technologies to the clinic.

To kinetically characterize our biomarker assay we first modelled our interactions using the simple 1:1 Langmuir model. This model describes the interaction between a monodisperse ligand and analyte species. We demonstrated that this model describes the interaction well at low analyte (cytokine) concentrations and with small ligand (cascade complexes) densities. However, the curvatures deviates from this model at higher concentrations and at larger densities in all steps of the enhancement cascade. This indicates that this model is insufficient to describe our interactions. A model accounting for mass transport could not improve the fits and was therefore not used. A model accounting for a heterogeneity of binding sites using two binding species was able to account for almost all variation in the data. This indicates that there are distinct binding species in all steps of the enhancement cascade. The behaviour that the heterogeneity was more apparent at higher concentration and ligand densities is well known [13]. This can be explained by a high and low affinity species. At low concentration only the high affinity species will be occupied and therefore a 1:1 behaviour can be observed. At higher concentrations both high and low affinity species will become occupied leading to a two-phasic curvature. The heterogeneity in the enhancement cascade can be caused by several processes. The capture antibody in the first step is covalently immobilized to the hydrogel matrix on the sensor. This immobilization process is random and can lead to differences in orientation and steric freedom leading to different affinities. A subset of affinities and orientation in the capture antibody step could in theory work through the entire cascade and explain the heterogeneity of subsequent steps. However, other unique factors could play a role in the enhancement steps. The biotinylation of the detection antibody is achieved by similar random chemistry as the immobilisation of the capture antibody. This could lead to different species of detection antibodies with different affinities. Moreover, this could lead to differences in the steric availability of the biotin groups leading to multiple affinities in the detection antibody – neutravidin interaction. In addition, more than one biotin is available per detection antibody which further increases heterogeneity. Finally, the interaction between the neutravidin and the gold nanoparticle in not only influenced by the heterogeneity of the preceding steps, but also limited by steric effects, especially at high concentrations. The number of possible causes for heterogeneity would suggest a continuum of binding affinities instead of just two, as was described by [14]. However, tests using three or four distinct species did not result in better fits for any of the steps. Therefore, because of the good fits and by applying Occam's razor, we decided to continue to use the heterogeneity of binding models with two binding species.

By comparing R_{max} of both binding species to the resulting maximum signal (which is related to the total binding capacity) in the enhancement steps, we showed that there is a clear relationship between the binding on a specific ligand species and the total ligand capacity. It is shown that high affinity binding species are dominant at lower ligand densities and reach a maximum occupation at higher densities. Low affinity binding

species are not occupied or available at lower ligand densities and become more prominent in the compound binding curves at higher densities. This leads to binding curves demonstrating slower kinetics at higher ligand capacities. This behaviour is as expected according to Luo et al. [13] as explained. However, it remains unclear whether steric effects at higher ligand densities might additionally play a role.

We showed that the relationship between the enhancement cascade steps could be captured with good fits by applying a 4 parameter logistic model and moderately with an exponential model. This indicates that there is a linear relationship between the cascade steps at relatively low concentrations that reaches a saturation at higher concentrations. This saturation might be related to the saturation of the higher affinity binding spots, resulting in the increased prominence of the lower affinity binding spots leading to altered kinetics. Despite this, the good fits demonstrate that the cascade was well defined over the entire concentration range that was tested.

Based on the characterization data we simulated the enhancement cascade at both low and high IL-1β concentrations and showed that we could accurately predict the entire cascade with average deviations of less than 5%. This enables extensive quality control opportunities. A very important limitation in all multiplex assays is cross-reactivity of the antibodies. This cross-reactivity can come in many forms. The capture and detection antibodies can cross-react to different biomarkers themselves or other components of the sample matrix. In standard end-point assays these interactions will result in a lower or higher signal, which will be interpreted as a lower or higher biomarker concentration. This is notoriously difficult to detect [15] and can lead to false positives or negatives that can be devastating in a clinical setting [10]. Using our method, we can detect this cross-reactivity through knowledge of the kinetics. When a capture antibody non-specifically cross-reacts with a biomarker, this will impact the different binding curves of both the capture antibody – biomarker and the biomarker – detection antibody interactions. In addition, the relationship between the enhancement cascade steps will start to deviate from expectation. When the detection antibody non-specifically cross-reacts to a biomarker, it will also lead to different binding kinetics. Similarly, common confounders such as heterophilic antibodies and spotting irregularities will translate into experimentally determined binding curves which deviate from predicted curves. These deviations can be automatically detected leading to highly accurate quality control both for assay development and clinical application.

The simulation of the enhancement cascade can additionally be used to calculate biomarker concentrations by fitting at a specific step in the cascade. We demonstrated that we could create a simulated calibration curve by which we could measure concentrations with a recovery of 108 % (when measured in linear range) compared to a recovery of 94 % with a standard calibration curve. This indicates that the kinetic characterization of the biomarker assays allows for calibration free measurements. The only requirement is knowledge of the binding capacity of the capture antibody spot. This knowledge can be gained by a simple triple biomarker injection requiring very limited time. According to Mehand et al. [16] it might even be possible to achieve calibration free

measurements with this method, without sensor specific knowledge on the ligand density, by determining this density in real time. This reduced need for calibrators can save time and reagents and can be very useful, especially in point of care applications.

Finally, we showed a proof of concept of the possibility to optimize the biomarker assay offline when all parameters of the binding kinetics are known. We showed we could optimize for signal with an improvement of 25% or for time and signal by reducing assay time by 50% while maintaining a 100% signal. These simulations need to be tested in real experiments, but show a proof of concept that simple changes in concentration or assay time can be easily simulated when kinetic characteristics are known enabling educated essay optimization rather than trial and error. This can save a lot of time, reagents and money in optimizing biomarker assays, especially when multiple markers are added and assays become more complex.

We have demonstrated that the kinetic characterization of a biomarker assay can lead to extensive quality control opportunities, can lead to calibration free measurements and can help in assay optimization. We have shown this for the enhancement cascade that we have developed, but the principles are applicable to all real-time assay technologies. The method works well for complex kinetics with a wide range of affinities (nM for antibodies and fM for neutravidin/GNP) and can be applied in label free and other nanoparticle tags assays. In addition, when knowledge on the specific kinetics of antibody – biomarker pairs is gathered using a real time technology, this can also easily be applied to optimize traditional end-point assays, such as the standard ELISA and multiplex assay. Therefore, our method can be highly beneficial for any biomarker assay and can hopefully lead to widespread use of these assays in a clinical setting were they are desperately needed.

4.5 Conclusion

Biomarker assays are essential for the early diagnosis of diseases, but are currently lacking for clinical application. In this paper, we have developed a toolbox to kinetically define the biomarker assay and show that this has large potential for quality control, calibration free measurements and assay optimizations. This method is applicable to all real-time assay technologies and can also be applied to optimize standard end-points assays. Therefore, this could be a useful tool to bring the desired biomarker assays for early diagnosis one step closer to the clinic.

4.6 Supplementary information

Cascade Step	Ligand	Analyte
1	Capture antibody	Cytokine
2	Capture antibody – Cytokine	Detection antibody
3	Capture antibody – Cytokine – Detection antibody	Neutravidin
4	Capture antibody – Cytokine – Detection antibody – Neutravidin	Gold Nanoparticle

Table S1: The ligand and analyte for each of the 4 cascade steps is defined.

4.6.1 Mass transport limited fitting

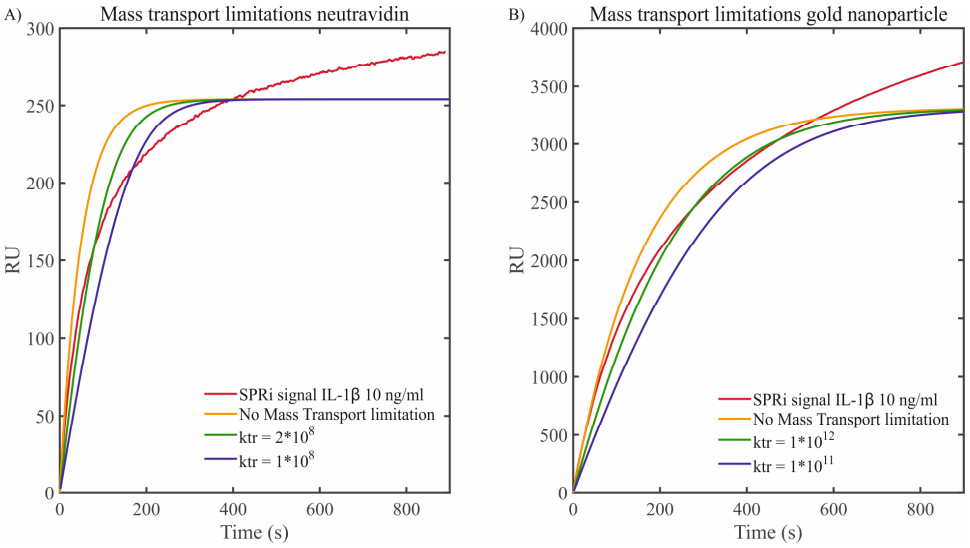

Figure S1: Transport limitations were added to the interaction model and tested for neutravidin (A) and gold nanoparticle steps (B) to see if it would increase goodness of fit. A) SPRi data at IL-1β concentration of 10 ng/ml is shown at neutravidin step. The overlays show 1:1 fits based on kon-koff data received from figure S3 with or without mass transport limitation (ktr = $2*10^8$ and ktr = $1*10^8$). It can be seen that adding mass transport limitations does not result in an accurate fit. B) SPRi data at IL-1β concentration of 10 ng/ml is shown at gold nanoparticle step. The overlays show 1:1 fits based on kon-koff data received from figure S3 with or without mass transport limitation (ktr = $2*10^{11}$ and ktr = $1*10^{11}$). Again, it can be seen that adding mass transport limitations does not result in an accurate fit.

4.6.2 Antibody – analyte interaction 1:1 Langmuir fit.

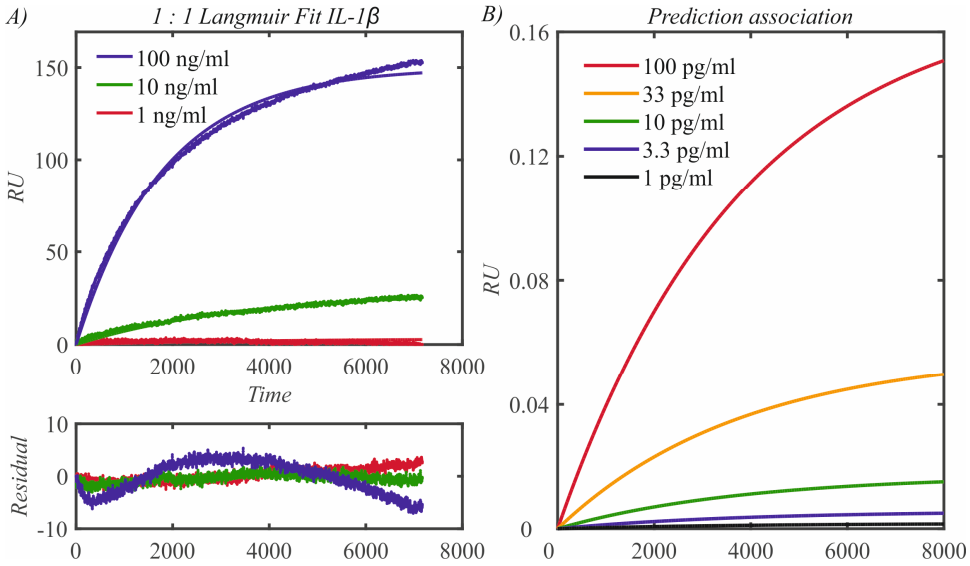

Figure S2: 1:1 Langmuir fit antibody - analyte interaction and simulations of association of lower concentrations. A) The global 1:1 fit for the antibody – analyte interaction is shown for the concentrations 1, 10 and 100 ng/ml at a spot density of 5 µg/ml. The subplot shows the residuals. It can be seen that the residuals increase at larger concentrations (mean residuals at 1 ng/ml = 1.05 RU, at 100 ng/ml = 2.6 RU and on average 1.46 RU). Fit results: Rmax = 284 RU, kon = $5.1x10^4$, koff = $2.6x10^{-4}$, leading to KD = 5.1nM. B) The simulations, based on the kinetic fit, for the lower concentrations are shown.

4.6.3 Capture antibody spot density dependent kinetics

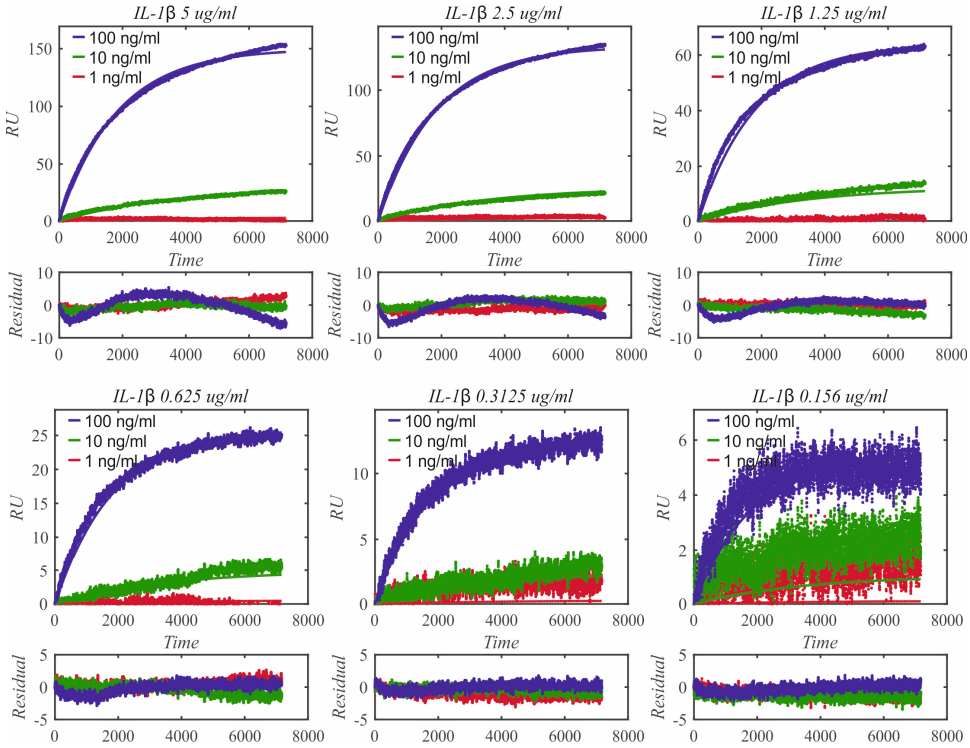

Figure S3. The 1:1 fits are shown over the spot densities ranging from 5 µg/ml to 0.156 µg/ml. Global fitting was applied resulting in a single Kon and Koff, described in figure S2. Rmax was the fitting variable and was 284 RU, 252 RU, 121 RU, 49 RU, 24 RU and 10 RU for 5 µg/ml, 2.5 µg/ml, 1.25 µg/ml, 0.625 µg/ml, 0.3125 µg/ml and 0.15625 µg/ml spot densities respectively. It can be seen that the 1:1 fit is generally good with small residuals at smaller spotting densities and at lower concentrations, but becomes worse at higher densities and concentration. This behavior points to a heterogeneity of binding sites, since lower affinity sites become occupied only at larger ligand densities and higher concentrations.

4.6.4 Enhancement Cascade 1:1 Langmuir fits

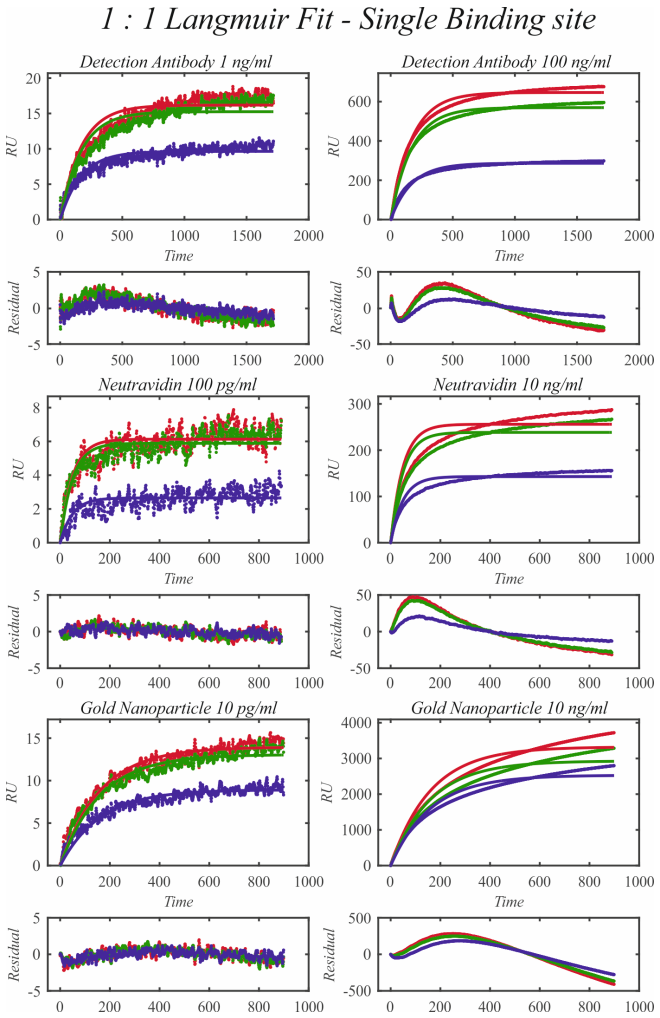

Figure S4. Fits of enhancement cascade steps using 1:1 Langmuir interaction model. In this figure the left graphs show signal and fit overlay at relatively low IL-1β concentration and the right graphs at high concentration. The subplots show the residuals of the fits. It can be seen that the simple 1:1 fits are generally good with small residuals at low concentrations (mean residuals 0.95, 0.49 and 0.55 RU for detection antibody, neutravidin and gold nanoparticle respectively), but deviate significantly at higher concentrations (mean residuals 13.67, 16.55 and 155.69 RU). This indicates that this model is not suitable for all IL-1β concentrations and thus ligand densities and that a more complex model is required. The fitting parameters were as follows. Detection antibody: Kon = $1.7x10^5$ M^{-1} s^{-1} and Koff = $1.8x10^{-4}$ s^{-1} leading to KD = 1 nM. Neutravidin: Kon = $8.2x10^5$ M^{-1} s^{-1} and Koff = $1x10^{-9}$ s^{-1} leading to KD = 1.2 fM. Gold nanoparticle: Kon = $3.1x10^7$ M^{-1} s^{-1} and Koff =$1x10^{-8}$ s^{-1} leading to KD = 0.32 fM.

4.6.5 Enhancement cascade 1:1 Langmuir model: correlation Rmax to dRU

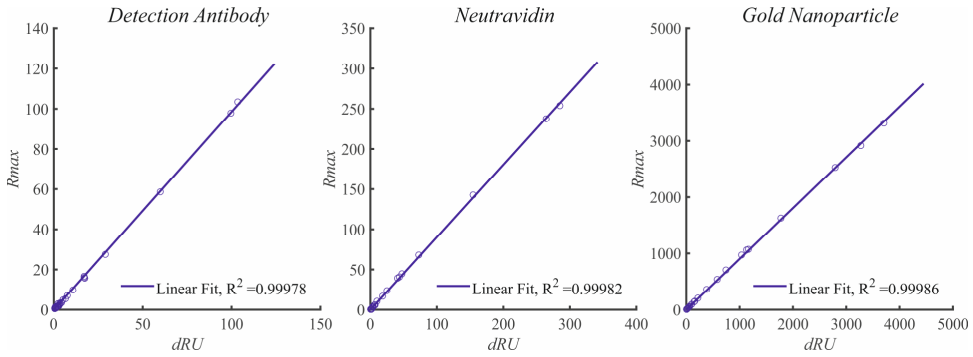

Figure S5. The correlation between dRU and the fitted Rmax for the 1:1 model is shown. It can be seen that there is an excellent correlation (R^2>0.999) between dRU and Rmax for all ligand densities in the three cascade steps. This includes the fitted Rmax from higher ligand densities, where residuals were generally high, indicating that even though the curvature could not be accurately characterized, the fitted Rmax is still of value.

4.6.6 Enhancement cascade heterogeneity of binding sites model: correlation Rmax to dRU

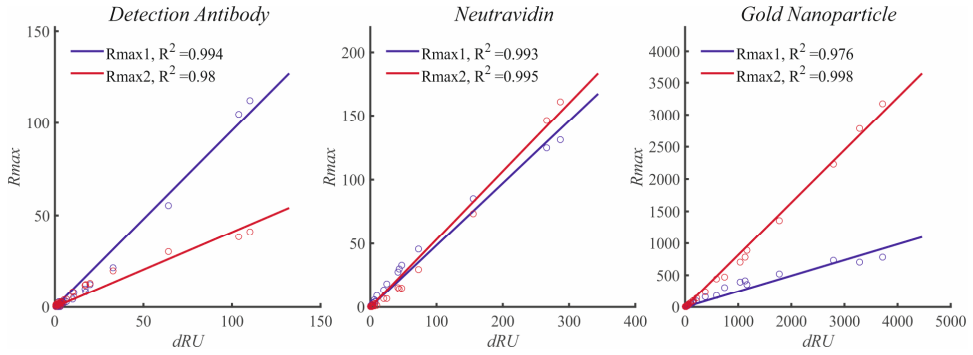

Figure S6. The correlation between dRU and the fitted Rmax(1,2) for the heterogeneity of binding sites model is shown. It can be seen that there is a good linear fit (R^2>0.97) between the ligand density and the Rmax of the ligand species, however individual data points do seem to deviate from the fits. In addition, important curvature seems to be missed. This is especially true for the Rmax2 of detection antibody, and Rmax1 for Neutravidin and Gold nanoparticle steps. The data seems to show a clearly declining slope with dRU, which is not captured in the linear fit.

4.6.6 Relationship between cascade steps: Linear Fit

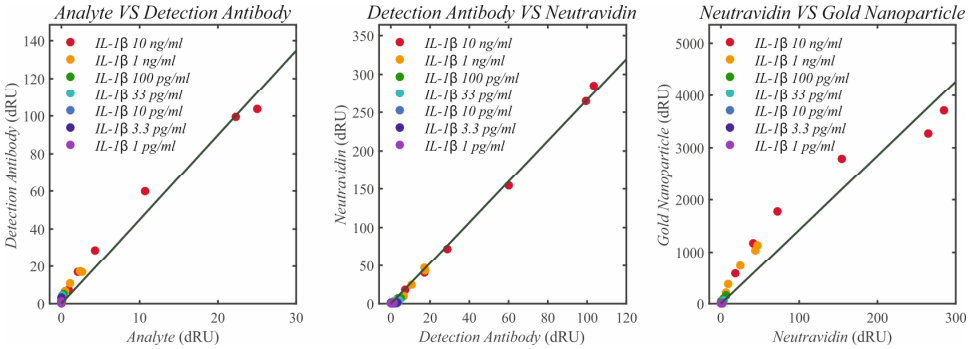

Figure S7: The relationship between the cascade steps. From left to right: Analyte vs detection antibody, detection antibody vs neutravidin and neutravidin vs gold nanoparticle. The data points per IL-1β concentration are grouped by colour. It can be seen that the linear fit is only accurate for the detection antibody vs neutravidin relationship, but fails to capture the curvature in the other two relationships.

4.6.7 Relationship between cascade steps: Exponential Fit

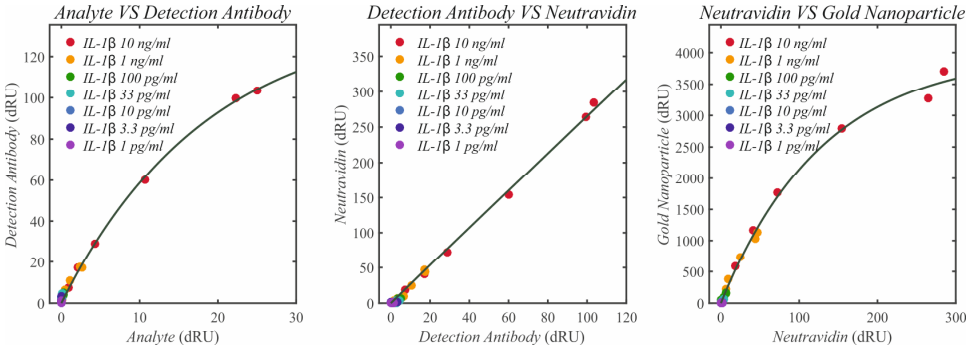

Figure S8: The relationship between the cascade steps. From left to right: Analyte vs detection antibody, detection antibody vs neutravidin and neutravidin vs gold nanoparticle. The data points per IL-1β concentration are grouped by colour. It can be seen that the exponential fit is only accurate for the neutravidin vs gold nanoparticle relationship, but fails to capture the curvature, at low dRU, in the other two relationships.

4.6.8 Prediction of enhancement cascade

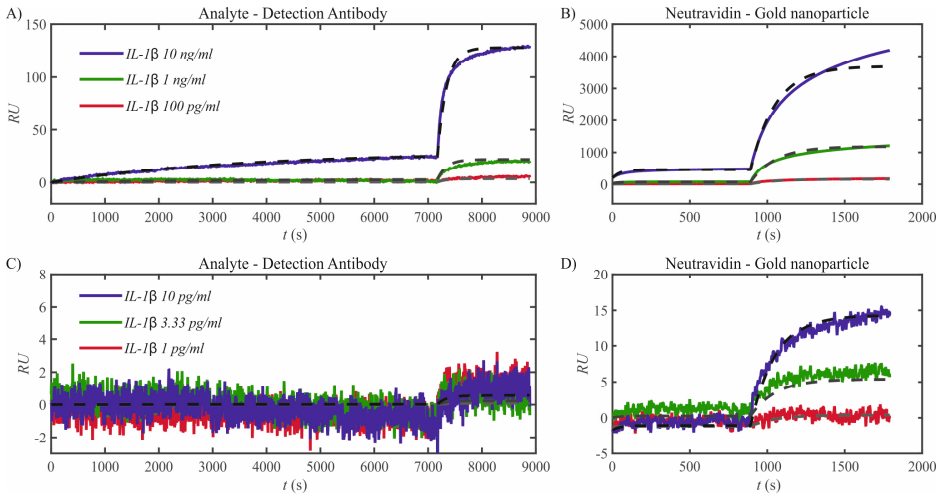

Figure S9: The predictions for the enhancement cascade using 1:1 Langmuir model at three high (A-B) and three low (C-D) IL-1β concentrations is shown in comparison to SPRi signal. The predictions seem generally accurate at low concentrations, but curvature starts to deviate significantly at higher concentrations. This makes it not possible to apply these fits for quality control at higher concentrations. As the total signals are predicted with relatively high accuracy (Deviation 12% at highest concentration), this 1:1 fit can be used to determine concentrations.

4.6.9 Calibration Free measurements 1:1 Langmuir model

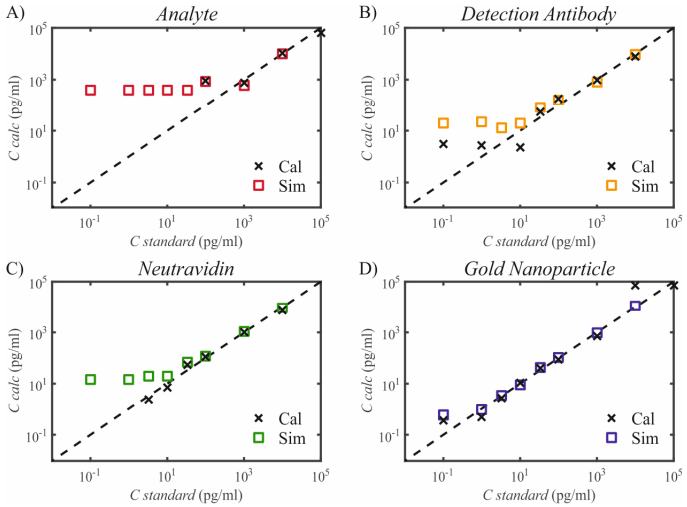

Figure S10: The predictions of the enhancement cascade allow for calibration free measurements. A-D) the calculated concentration of IL-1β versus the actual concentration is plotted in the four steps of the enhancement cascade. The calculations using a simulated calibration curve based on the 1:1 Langmuir model (squares) is compared to the calculated values using a standard calibration curve (x). The results

show the simulated calibration curve is as good as the standard calibration curve to determine the concentration (Recovery in linear range for gold nanoparticle step: 102 % vs 94% in standard method.

References

1. Frampton, J.P., et al., *Aqueous two-phase system patterning of detection antibody solutions for cross-reaction-free multiplex ELISA.* Scientific Reports, 2014. **4**: p. 4878.
2. Tighe, P.J., et al., *ELISA in the multiplex era: Potentials and pitfalls.* PROTEOMICS – Clinical Applications, 2015. **9**(3-4): p. 406-422.
3. Chikkaveeraiah, B.V., et al., *Electrochemical Immunosensors for Detection of Cancer Protein Biomarkers.* ACS Nano, 2012. **6**(8): p. 6546-6561.
4. Bastarache, J. A.; Koyama, T.; Wickersham, N. L.; Mitchell, D. B.; Mernaugh, R. L.; Ware, L. B. Journal of immunological methods 2011, 367, 33-39
5. Bastarache, J.A., et al., *Accuracy and Reproducibility of a Multiplex Immunoassay Platform: A Validation Study.* Journal of immunological methods, 2011. **367**(1-2): p. 33-39.
6. Ellington, A.A., et al., *Antibody-Based Protein Multiplex Platforms: Technical and Operational Challenges.* Clinical chemistry, 2010. **56**(2): p. 186-193.
7. Cretich, M., F. Damin, and M. Chiari, *Protein microarray technology: how far off is routine diagnostics?* The Analyst, 2014. **139**(3): p. 528-542.
8. Moncunill, G., et al., *Performance of multiplex commercial kits to quantify cytokine and chemokine responses in culture supernatants from Plasmodium falciparum stimulations.* PloS one, 2013. **8**(1).
9. Tighe, P., et al., *Utility, reliability and reproducibility of immunoassay multiplex kits.* Methods, 2013. **61**(1): p. 23-29.
10. Juncker, D., et al., *Cross-reactivity in antibody microarrays and multiplexed sandwich assays: shedding light on the dark side of multiplexing.* Current Opinion in Chemical Biology, 2014. **18**: p. 29-37.
11. Bolstad, N., D.J. Warren, and K. Nustad, *Heterophilic antibody interference in immunometric assays.* Best Practice & Research Clinical Endocrinology & Metabolism, 2013. **27**(5): p. 647-661.
12. Hendriks, J., et al., *Nanoparticle Enhancement Cascade for Sensitive Multiplex Measurements of Biomarkers in Complex Fluids with Surface Plasmon Resonance Imaging.* Analytical Chemistry, 2018. **90**(11): p. 6563-6571.
13. Luo, J., et al., *Determination of Interaction Mechanism of Sensorgrams by Analysis of Binding Kinetics.* Journal of Protein Chemistry, 1999. **18**(6): p. 709-719.
14. Schuck, P. and H. Zhao, *The Role of Mass Transport Limitation and Surface Heterogeneity in the Biophysical Characterization of Macromolecular Binding Processes by SPR Biosensing.* Methods in molecular biology (Clifton, N.J.), 2010. **627**: p. 15-54.
15. Pla-Roca, M., et al., *Antibody Colocalization Microarray: A Scalable Technology for Multiplex Protein Analysis in Complex Samples.* Molecular & Cellular Proteomics : MCP, 2012. **11**(4): p. M111.011460.
16. Mehand, M.S., B. Srinivasan, and G.D. Crescenzo, *Estimation of analyte concentration by surface plasmon resonance-based biosensing using parameter identification techniques.* Analytical Biochemistry, 2011. **419**(2): p. 140-144.

“As with his beer, the author ensures with his research that not a single drop is wasted.”

“Don’t let your printer know you are in a hurry, it smells fear”

5

Optimizing cell viability in droplet based cell deposition

Biofabrication commonly involves the use of liquid droplets to transport cells to the printed structure. However, the viability of the cells after impact is poorly controlled and understood, hampering applications including cell spraying, inkjet bioprinting, and laser-assisted cell transfer. Here, we present an analytical model describing the cell viability after impact as a function of the cell-surrounding droplet characteristics. The model connects (1) the cell survival as a function of cell membrane elongation, (2) the membrane elongation as a function of the cell-containing droplet size and velocity, and (3) the substrate properties. The model is validated by cell viability measurements in cell spraying, which is a method for biofabrication and used for the treatment of burn wounds. The results allow for rational optimization of any droplet-based cell deposition technology, and we include practical suggestions to improve the cell viability in cell spraying.

Jan Hendriks[1,], Claas Willem Visser[2,*], Sieger Henke[1], Jeroen Leijten[1], Daniël B.F. Saris[3,4], Chao Sun[2], Detlef Lohse[2] & Marcel Karperien[1]*

1 Department of Developmental BioEngineering, TechMed institute, University of Twente, The Netherlands.

2 Physics of Fluids Group, TechMed institute, Faculty of Science and Technology, University of Twente, The Netherlands.

3 Department of Orthopedics, UMC Utrecht, The Netherlands.

4 Department of Reconstructive Medicine, TechMed institute, Faculty of Science and Technology, University of Twente, The Netherlands.

**These authors Contributed equally to this work.*

Published in Nature scientific reports, 2015, DOI: 10.1038/srep11304

5.1 Introduction

Droplet-based cell deposition is receiving increasing attention as a tool to construct or fill a variety of biological tissues. Striking examples are the cell spray treatment of burns[1,2] or ulcers[3], which provide faster and improved healing and are currently introduced in clinical practice. With one successful application in place, we seek to expand to other clinical areas including laparoscopic, endoscopic, and arthroscopic procedures[4]. This opens the possibility for minimally invasive cell therapy for tissue regeneration. A second example is the fabrication of functional tissue replacements in a laboratory, to enable curing non-functional tissues[5–7]. In current biofabrication technologies including ink-jet bioprinting[8–10], laser-induced forward transfer[11], valve-based bioprinting[12,13], and cell spraying[2,14–17], the cell transport from the initial cell suspension, called "bio-ink", to the manufactured tissue is achieved by liquid droplet ejection and deposition. Although these technologies allow for high-viability cell deposition, limited throughput, limited precision, and poorly optimized cell-containing bio-inks are major obstacles in the controlled deposition of cells, such as required for the fabrication of functional tissues[5,7].

To solve these issues and thereby optimize droplet-based cell deposition, knowledge of the cell viability as a function of the cell-containing droplet size and impact velocity is crucial. Ideally, single, highly reproducible impacts of droplets containing a single cell would be monitored for a large range of the impact parameters (droplet size, velocity, and material properties). Drop-on-demand systems provide such highly reproducible droplets, but usually the impact parameter space is relatively narrow for the cell-containing liquids used[18–23]. Therefore, to study post-impact cell viability, we use cell spray deposition, which allows for a much larger range of impact parameters. The substantial influence of the spray parameters on post-impact cell viability[2,15–17,24] suggests that cell viability can be controlled, providing a model system to assess cell survival after impact. Additionally, the shear stress exerted on the cell within the spray nozzle is much lower than the shear stress during impact, which allows for assessment of the impact process alone (for other technologies this is not the case, as explained in supplementary section I).

The current work aims to understand the influence of the droplet impact on cell viability, which is applicable both to drop-on-demand and spray deposition technologies. We introduce a model describing the cell viability as a function of the cell-containing droplet size, the viscosity, and the impact velocity. The model is validated by cell spray experiments, following a two-step approach. First, the droplet size and impact velocity are measured and used to obtain model predictions as described. Subsequently, the cell viability after spraying is measured as a function of the air pressure, the liquid viscosity, the nozzle-substrate distance, and the substrate stiffness. The model is shown to accurately describe the viability measurements as a function of the input parameters. These results provide a powerful tool to rationally evaluate and improve clinical spray treatments and tissue engineering applications.

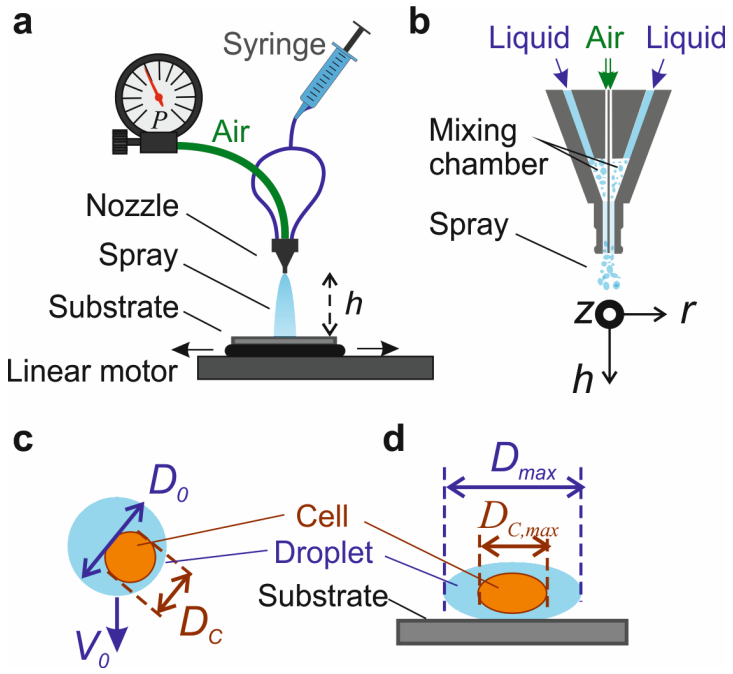

Figure 1. Overview of the experimental method and parameter definition. A two-phase spray nozzle is used to generate the spray, and placed at a distance *h* from the surface. The cell-containing liquid (with viscosity μ) is delivered to the nozzle using a syringe pump (not shown). Air at controlled pressure *P* is applied to the nozzle gas inlet. The impact substrate is moved under the spray (indicated by horizontal arrows) using a linear motor, ensuring clean and homogeneous impact. Generally, a clean glass substrate is used, but gelatin-water mixtures (with gelatin weight fractions C_g) are used to assess the influence of the surface stiffness. (**b**) Cross-section of the nozzle, illustrating the air and liquid flows, and the coordinate system used. Figures (**c**) and (**d**) illustrate key variables describing the cell-containing droplets in air (**c**) and during impact (**d**).

5.2 Materials and Methods

5.2.1 Cell culture

Neonatal rat dermal fibroblasts (ITK Diagnostics) were cultured in Minimum Essential Medium α (α -MEM) (Gibco) supplemented with 10% Fetal Bovine Serum (FBS) (Lonza), 1% L-Glutamine (Gibco) and 1% Pen/Strep (Gibco) at 37 °C and 5% CO2.

5.2.2 Cell suspension

Cells were harvested at 80% confluence by trypsinization and suspended at 1.5×10^6 cells per ml in culture medium excluding FBS for impact experiments. Optionally dextran (Sigma, 15–25 kDa) was added to the cell suspensions to increase the viscosity. The influence of the dextran concentration on the liquid viscosity was measured using a viscometer (Rheolab QC, Anton Paar). As shown in supplementary Figure 10, the measured viscosity is in agreement with literature values.

5.2.3 Cell viability measurements

Cell spray experiments were performed with the set-up shown in Fig. 1. Using a syringe pump, the cell suspension was pushed through a spray nozzle (Duploject spray system (Baxter AG). Photographs of this system, which is also known as bio-airbrush, are provided in supplementary Figure 9) at a controlled liquid flow rate of 2.4 ml per min. The impact surface consisted of a standard clean microscope slide covered with a PDMS mask to ensure a defined and reproducible impact area. These slides were optionally coated with a layer of gelatin (Type A, Sigma, d = 0.5 mm), in order to adjust the surface stiffness. A crucial aspect of the experiment is that impact occurs on a dry surface, i.e. that the cell spray does not impact onto previously sprayed droplets. To ensure this, the impact surface was reproducibly moved using a programmable linear motor. The substrate velocity was set such that 12 ± 0.5 mg of the sprayed liquid was collected for each experiment (the velocity was decreased for increasing nozzle-substrate distances since the spray density decreases for increasing distance from the nozzle). This weight corresponds to a liquid film of 18 μm (which is equivalent to ~1 cell thickness) and resulted in covering roughly half of the surface area with sprayed droplets, such that most droplets land on the dry surface. Within 10 s after each spray experiment, the surface was rinsed with FBS-free culture medium to collect the cells. The cells rinsed from three different samples (sprayed using equal parameter settings) were collected into a 12 ml centrifuge tube (Greiner). The contents of each tube were subsequently processed in a live-dead assay. For each parameter setting, three independent spray cycles were performed (i.e. 9 impact surfaces were collected in three different tubes). This approach provided three data points for each parameter setting, which were used to display the error bar in Fig. 5.

5.2.3 Live-dead assay

The collected cells were incubated in phosphate buffered saline (PBS), supplemented with 1 nM calcein AM and 6 nM ethidium homodimer, at 37 °C and 5% CO_2 for 30 minutes. Each stained cell suspension sample was transferred to a well in a 24 wells-plate and 8 random spots per well were imaged (EVOS Fl microscope), within 2 hours after each spray experiment. Live (green) and dead (red) cells were automatically counted using a home-written Matlab script (Fig. 5 shows an example), resulting in an average of 450 ± 332 (s.d.) detected cells per sample (with a minimum of 12 cells). Cells stained both live and dead were considered damaged, but viable, so counted as alive. For each sample, viability was calculated accordingly. All measurements were subsequently corrected by setting the control viability (non-impact, measured at the same time) to 100%.

5.2.4 Spray characterization

As cell survival critically depends on the characteristics of the cell-containing droplets, the spray characteristics were determined in detail. The setup used is shown in supplementary Fig. 2. All spray-generating components were equal to the components used for assessment of the cell viability (Fig. 1). A dual-pulse ND:Yag laser with a pulse duration of 6 ns was used for brightfield illumination. To prevent fringes, the coherent

laser light was diffused using a fluorescent plate placed in front of the laser. The non-coherent pulses were captured by a dual-shutter camera (Sensicam, PCO). The time delay between the illumination pulses was set to 1 μ s, which is sufficiently long to measure the translation Δ *h* of the droplets while preventing confusion between different droplets. All timings were controlled using a BNC 575 pulse-delay generator (not shown). A 10× long-distance objective was used, resulting in a field of view of 0.67 × 0.89 mm2. As the focal plane thickness of this objective is $\delta F \approx 0.1 \pm 0.03$ mm, a volume of 0.67 × 0.89 × 0.1 mm³ was visualized. As the spray is much larger than this volume, measurements were taken at different *z*- and *h*-positions to fully characterize the spray, as illustrated by the small rectangles in supplementary Figure 1(b) (the *r*-position is maintained at the nozzle axis). For each measurement, 400 image pairs were obtained. Example images are shown in Fig. 3(a,b), where the downward translation of the droplets is clearly visible. Motion blur was prevented by the short illumination pulses of 6 ns. The droplets were automatically detected using a home-written Matlab script. Droplets appearing sufficiently sharp were automatically selected, as illustrated by the red circles in Fig. 3(c,d). Here, the top-left droplet was too blurred for detection and discarded. Although the droplets in Fig. 3 are similar in size, the image processing software allowed for successful detection of droplets in the range of $1 \leq D_0 \leq 100$ μm.

5.2.5 Soft substrate preparation

Glass microscope slides were optionally coated with a layer of gelatin (Type A, Sigma) of thickness 0.5 mm, and kept in air at room temperature for 30 min prior to the experiment. The surface stiffness was adjusted by adding gelatin mass fractions of Cg = [2, 5, 10, 20]% to PBS. PBS without gelatin was used in the soft-surface limit.

5.3 Results

5.3.1 Cell viability model

In cell spraying, cell damage is primarily expected during impact of the cell-containing droplets (see supplementary section I). In particular, impact generally results in cell deformation and elongation of the cell membrane[25], as illustrated in Fig. 1(c,d). For an increase of the cell membrane area up to ~5%, the membrane is stretched, but remains intact. However, for larger extensions, rupture can be observed[26]. As rupture generally results in cell death, the probability of survival η is modelled as a function of the relative cell membrane area γ (compared to the undisturbed case) according to ref. 27:

$$\eta(\gamma) = 1 \text{ for } \gamma < \gamma_{cr} - \Delta\gamma \quad (1)$$

$$\eta(\gamma) = \frac{1}{2} - \frac{\gamma - \gamma_{cr}}{2\Delta\gamma} \text{ for } \gamma_{cr} - \Delta\gamma < \gamma < \gamma_{cr} + \Delta\gamma \quad (2)$$

$$\eta(\gamma) = 0 \text{ for } \gamma > \gamma_{cr} + \Delta\gamma \quad (3)$$

with γ_{cr} = 1.5 the critical membrane expansion as quantitatively provided in ref. 27, and $2\Delta\gamma = 1$ the range of surface expansion in which the cells partly survive. Key model conditions include an elastic cell response to stresses (which is fulfilled for shear rates τ

≤ $10^9 s^{-1}$ [26]; for the estimate of the shear stress see supplementary section I) and negligible lipid membrane replenishment during deformation (fulfilled for $\tau \geq 10^{-3}$ s^{-1} [28]), which are met in the current work.

To obtain the relative cell membrane area γ, first a "clean" cell impact on a hard substrate is considered. The cell is described as a spherical liquid droplet with diameter D_c, velocity V_c, viscosity μ_c = 12 mPa s, density ρ_c = 1015 kg/m³ and surface tension σ_c = 0.072 N/m² (key parameters are visualized in Fig. 1(c,d)). The maximal spreading diameter reached during impact $D_{c,max,0}$ is then calculated as a function of the cell Weber number, which describes the ratio between kinetic energy and surface energy[29–31]:

$$\frac{D_{c,max,0}}{D_c} = 1.25 \text{ for } We_c < 5 \quad (4)$$

$$\frac{D_{c,max,0}}{D_c} \sim We_c^{1/4} \text{ for } We_c \geq 5 \quad (5)$$

with cell Weber number $We_c \rho_c D_c V_c^2 / \sigma_c$. These equations are valid for Newtonian liquids and for $We_c < Re_c^{4/5}$ [29] (which is fulfilled for our experiments), in which the cell Reynolds number $Re_c = \rho_c V_c D_c / \mu_c$ represents the ratio between inertia and viscosity. The cell shape is defined by assuming cell deformation into an oblate spheroid and volume conservation. At the instant of reaching its maximal extension, its height equals $h_o = D_c^3 / D_{c,max,0}^2$. This provides the deformation M_0 for an impacting cell, which is defined according to ref. 25:

$$M_0 = \frac{D_{c,max,0} - h_0}{D_{c,max,0} + h_0} = \frac{D_{c,max,0}^3 - D_c^3}{D_{c,max,0}^3 + D_c^3} \quad (6)$$

i.e. M_0 = 0 for a sphere, and M_0 = 1 for a plane.

The potentially large influence of the surrounding droplet on the cell's deformation was modeled numerically by Tasoglu *et al.*[25]. Re-interpreting their results provides a quantitative expression capturing the cell deformation M as a function of M_0, the surrounding droplet's diameter D_0, and its viscosity μ_0 (for details see supplementary section III, for viscosity-dominated deformation of compound drops see ref. 32):

$$M = C_0 M_0 \cdot e^{-0.26 D_0/D_c} \left(\frac{\mu_c}{\mu_0}\right)^{-0.56} \quad (7)$$

with C_0 a fitting parameter (which is set to C_0 = 5, as discussed in supplementary section III). Subsequently, M is translated into the maximal spreading diameter of the (oblate-spheroid) cell as $\frac{D_{c,max}}{D_c} = \left(\frac{1+M}{1-M}\right)^{1/3}$, which is used below to calculate the cell surface area. Since this occasionally results in a cell diameter exceeding the droplet's diameter, we additionally implement the condition $D_{c,max} = min(D_{c,max,0}, D_{max})$. The surface area A of an oblate spheroid (the assumed shape of a single trypsinized cell) can be calculated as:

$$A = \frac{\pi D_{c,max}^2}{2} \left(1 + \frac{1-e^2}{e} tanh^{-1} e\right) \quad (8)$$

with $e^2 = 1 - h^2/D_{c,max}^2$. The relative surface area is given by $\gamma = A/\pi D_c^2$, which completes the system. Finally, the model is extended to account for the stiffness of the impact substrate. We assume impact on a liquid pool (with material properties equal to the droplet) as a soft surface limit. A droplet with diameter D_o and velocity V_o impacting on such a pool is (in first approximation) described by the impact of a droplet with diameter $2D_o$ and velocity $0.5V_o$ on a hard substrate[33]. As soft-surface droplet impact is not adequately understood even for basic model systems[34], we propose an effective droplet diameter and velocity as:

$$D_{eff} = \frac{2D_0}{1+S} \text{ and } V_{eff} = \frac{V_0(1+s)}{2} \quad (9)$$

with S an arbitrary stiffness parameter ranging from S = 0 for liquid surfaces to S = 1 for hard surfaces. A gelatin-water mixture is used to generate a substrate stiffness range corresponding to a large variety of natural tissues[35,36]. In the high-shear regime associated to fast micro-droplet impact the viscoelastic properties of these substrates cannot be measured by any standard viscometer. Therefore, the gelatin mass fraction Cg is used to define the stiffness: $S = C_1C_g$, with C_1 a fitting constant. Using $C_1 = 5$ provides reasonable agreement between the model and our soft-surface impact measurements. For $C_g > 1/C_1$ we define $S = 1$, which implies an effectively stiff surface for $C_g > 0.2$.

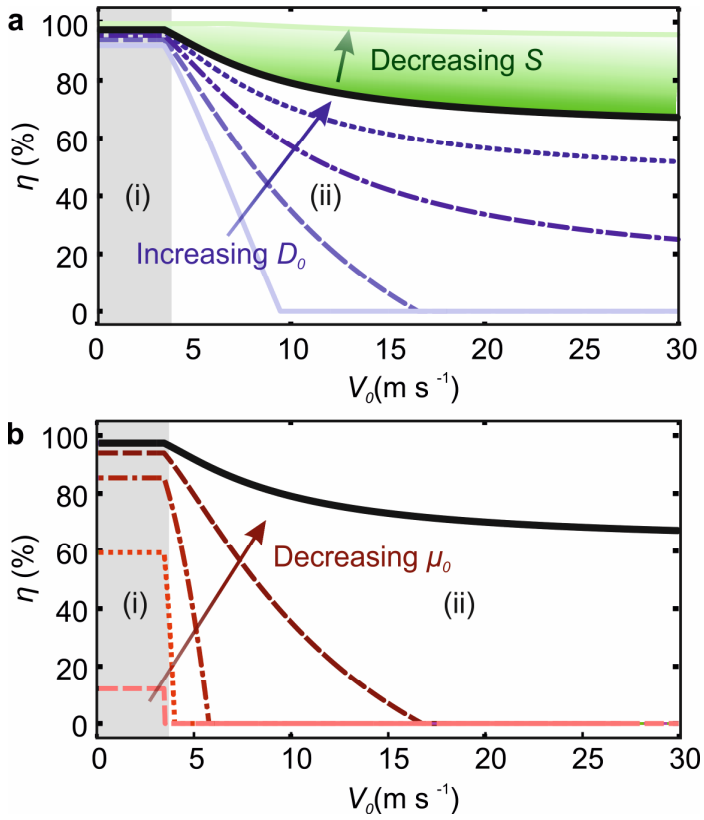

Figure 2. Model predictions of the post-impact cell survival probability η as a function of the impact velocity V_o, for a single-cell containing droplet. Figure (a) shows the influence of the droplet diameter D_o (indicated by lines representing $1 \leq D_o/D_c \leq 3$ in steps of 0.5) and the surface stiffness (indicated by the color gradient representing $S = 1$ (stiff substrate) to $S = 0$ (liquid pool)). Figure (b) shows the influence of the droplet viscosity (lines plotter for μ_o = 1, 2, 4, 8, 12 mPa s). The solid black lines indicate the viability values obtained for the reference parameters: $D_o/D_c = 3$, $\mu_c/\mu_o = 10$, and $S = 1$. Region (i) (shaded) indicates the low-Weber number regime (We < 5). Here the cell deformation is small and independent of the impact velocity. In region (ii), decreasing viability is obtained for increasing velocities, due to increasing cell deformation.

Figure 2 shows example model results. The viability probability of individual cells is shown as a function of the impact velocity, for different sizes of the surrounding droplet (Fig. 2(a)), and different relative viscosities (Fig. 2(b)). At low velocities, the cell viability is only weakly dependent on the impact parameters since a small and constant cell deformation is assumed for low Weber numbers (We < 5). For increasing velocities (corresponding to We > 5) a decrease in cell viability is observed. In this regime, the size of the surrounding droplet and its viscosity strongly affect cell viability. Larger surrounding droplets provide stronger cushioning and thereby increase the viability (Fig. 2(a)). Increasing the droplet viscosity negatively influences the cell viability, since for $\mu_c = \mu_o$ the droplet will flow around the (relatively stiff) cell, whereas for $\mu_c < \mu_o$ the cell

flows to dampen the (relatively stiff) droplet's impact, resulting in significant cell deformation and decreased viability. Finally, softer substrates provide increased cushioning as shown by the color gradient in Fig. 2(a). Here, the surface deforms such that the deformation of the droplet is reduced. Consequently, cell deformation is suppressed and a higher viability is expected. In conclusion, optimal cell viability is expected for slow, large, and low-viscosity cell-containing droplets impacting onto a soft surface.

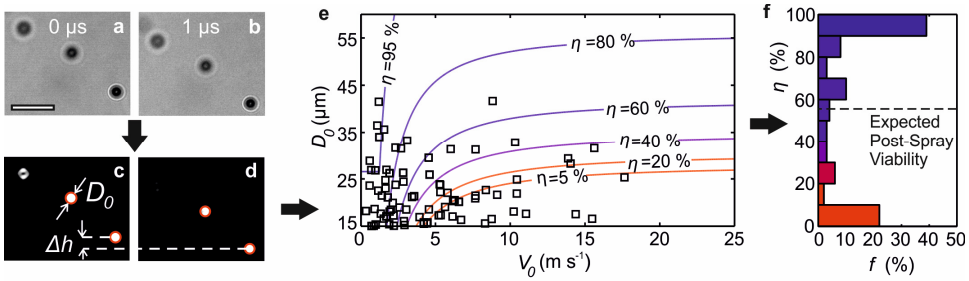

Figure 3. Characterization of the spray. An example image pair is shown before ((**a**) and (**b**)) and after image processing ((**c**) and (**d**)). As indicated by the circles in (**c**) and (**d**), two droplets are automatically detected using home-written image analysis software, which provides their diameter *D*o and translation Δ *h*. Figure (**e**) shows the droplet size- and velocity for P = 0.4 ·10^5 Pa, μ = 1 mPa s, h = 3 cm. The markers (·) show 100 statistically representative droplets constituting the spray. The contours represent predicted cell viability values (η). Figure (**f**) shows the relative incidence f of each cell survival probability η, which is binned for the sake of clarity. Averaging these probability values results in the expected post-spray cell viability (dashed line). The expected cell viability strongly depends on the spray parameters setting, as plotted in Fig. 5 (red diamond).

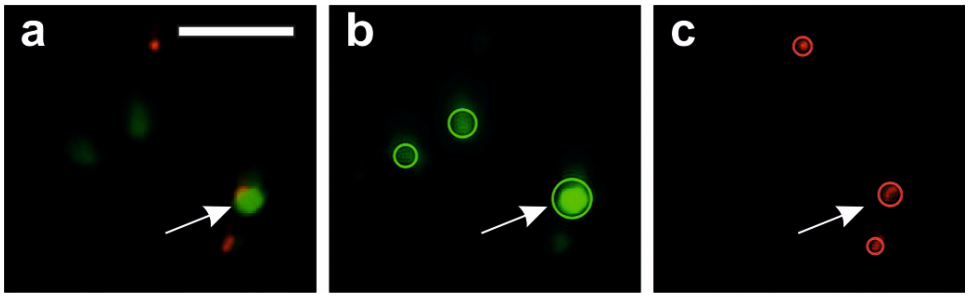

Figure 4. Example live-dead assay. Figure (**a**) shows the original image; figure (**b**) shows the calcein staining (in green), and figure (**c**) shows the EthD staining (in red). The circles in figures (**b**) and (**c**) indicate the automatically detected cells for each staining. The arrows show a cell in which both stainings are retrieved. These cells are considered damaged but viable, and therefore counted as live.

5.3.2 Spray characterization

To obtain cell viability predictions from the model, the droplet size- and velocity are required. We obtain these parameters according to Fig. 3. First, the droplets are visualized as shown in Fig. 3(a,b). Automated image analysis then provides the droplet diameter *D*o and velocity $V_0 = \Delta h/\Delta t$, as illustrated in Fig. 3(c,d). For any spray experiment, a wide range of droplet sizes and velocities is observed. A representative

sample of droplet sizes and velocities is indicated by the black markers in Fig. 3(e), which also contains indicative cell viability contours (similar graphs for different spraying parameters are included in supplementary section II). To obtain the cell viability, for each drop the cell survival probability was calculated as a function of the size, speed, viscosity, and surface stiffness. This provides a distribution of cell viability probabilities as shown in Fig. 3(f) (corresponding to the drop size and speed distributions), of which the average provides a single predicted cell viability value which is compared to experimental viability data in the following section.

5.3.3 Cell viability measurements and model validation

To measure the post-impact cell viability, spray experiments are performed using the setup displayed in Fig. 1. After spraying, the cells are collected and stained in a live-dead assay of which an example is shown in Fig. 4. Using automated image analysis, the cell viability is determined for each measurement. Figure 5 shows the measured cell viability as a function of the pressure, the nozzle-substrate distance, the viscosity, and the surface stiffness. The cell viability is also measured as a function of the time after spraying (see supplementary section V), demonstrating the long-term viability of the surviving cells.

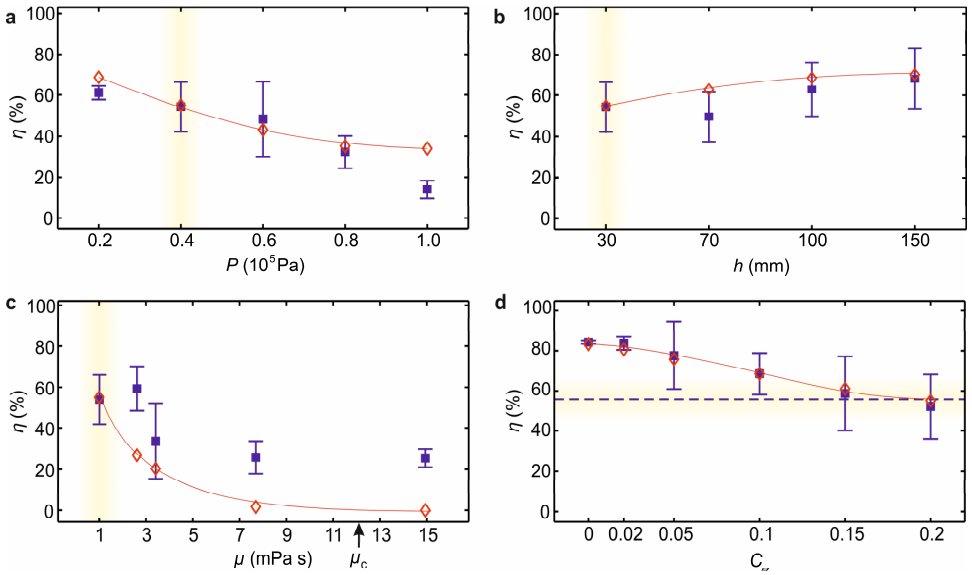

Figure 5. Cell viability η as a function of the spray control parameters. Figures (**a–d**) indicate the viability as a function of the pressure P, the nozzle-substrate distance h, the liquid viscosity μ, and the substrate gelatin percentage, respectively. Measured values are indicated as blue squares with the error bar representing the standard deviation; red diamonds indicate model predictions. The lines are a guide to the eye for the model predictions (which cannot be displayed as smooth curves as they depend on the spray distributions, as explained in supplementary section II). The reference settings are P = 0.4 .10^5 Pa, μ = 1 mPa s, h = 3 cm, and a glass impact substrate, as indicated by the yellow shade in each plot.

The model is compared to cell viability measurements in Fig. 5. Good agreement is observed for the pressure, the nozzle-substrate distance, and the surface stiffness. In particular, except for the lower and upper pressure data points, the measured data is

quantitatively described by the model, which is remarkable in view of the single fitting parameter used. Our model over-estimates the influence of increased viscosity, but still captures the trend. The origin of the lower cell viability for increasing pressure (4(a)) is that the spray consists of smaller drops impacting at increasing velocities, as shown in Fig. 6. Both factors result in stronger cell deformation and therefore cell death. Increasing the nozzle-substrate distance improves the cell viability, as shown in Fig. 5(b). Figure 6 shows that this trend is primarily caused by the decreasing droplet velocity far from the nozzle, which results in less deformation of the cell and increased viability. Higher viscosities result in a lower cell viability, as shown in Fig. 5(c). For high viscosity, the deformation of the cell-containing droplet primarily occurs within the cell. Consequently, the cell membrane is significantly stretched, and the viability decreases. Finally, decreasing the surface stiffness improves the viability (Fig. 5(d)), since the deforming surface "cushions" the impacting cell-containing droplet.

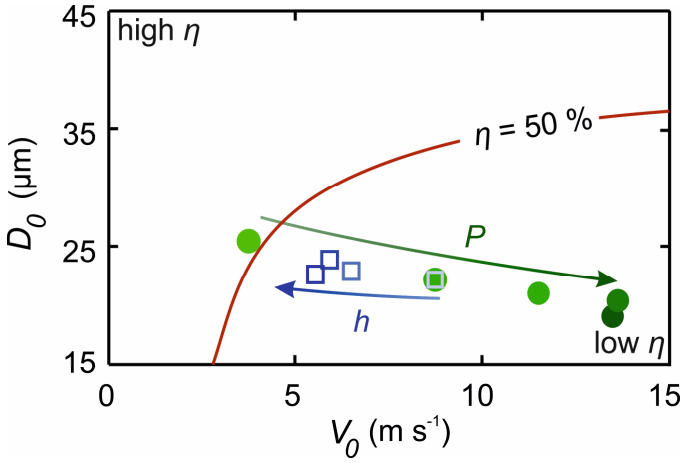

Figure 6. Viability as a function of the droplet size and speed. The line represents the 50% viability contour; additional contours are plotted in Fig. 3(e). The dots indicate the mean diameter versus the mean velocity as a function of the spray pressure (the arrow indicates increasing pressure for P = [0.2, 0.4, 0.6, 0.8, 1]·10^5 Pa). The open squares indicate the distance from the nozzle for h = [30, 50, 100, 150] mm. For increasing pressure, the droplet size decreases and the impact velocity increases, resulting in a lower viability. For a larger distance from the nozzle, the impact speed decreases, resulting in improved viability. The influence of the viscosity and the surface stiffness is displayed in Fig. 2), since these variables do not affect the droplet size and speed.

5.4 Discussion

The model assumptions affect its applicability, and therefore deserve further discussion. First, the assumption that the cells are centered in the droplet will be approximately true for drop sizes just exceeding the cell size, but for larger droplets the cells may be located at the edge of the spreading film where the shear stresses are much higher than in the center[31]. Therefore, for larger drops such as generated for low pressures (see supplementary Figure 4(a)), the cell viability may be suppressed. This

mechanism possibly explains the lower viability for $P = 0.2 \cdot 10^5$ Pa observed in Fig. 5(a). Second, following ref. 25, we assume that the cell viscosity is independent of the shear stress. As experiments reveal shear-thinning behaviour of cells[37,38], implementing shear thinning could further improve the model. Third, the influence of the droplet volume on the number of cells per drop is not yet taken into account. Finally, the influence of viscosity on cell deformation might be different from equation (7), since equation (7) is derived from numerical results for much larger cell-containing droplets (ref. 25, also see supplementary section III) whereas most of our droplets have a size just exceeding the cell size (supplementary Figure 3). Avoiding these assumptions by extending the model may result in even better agreement. Still, the agreement between our model and measurements is remarkable and provides evidence for correctly capturing the underlying physics.

Droplet impact-induced cell damage has far-reaching consequences for users as well as developers of cell spraying and other bioprinting technologies. In clinical practice, the need for adequate cell-spraying protocols[39] is even more pressing than expected. In particular, manual operation of spray devices is common practice, but associated with variations in nozzle-substrate distance, the air pressure, and the viscosity. These variables should be carefully controlled to ensure high cell viabilities. The actual values may still depend on the nozzle design and the cell type, but increasing the spray distance and using low-viscosity spray suspensions, while avoiding hard impact surfaces, will generally improve cell survival. However, harmful spraying conditions cannot always be avoided due to treatment-specific clinical requirements or constraints in biofabrication. For example, in arthroscopic procedures, the nozzle-surface distance is limited to at most 1 cm[4]. In view of our results, it is unclear whether the treatment success shown for burn treatments, where this distance usually exceeds 10 cm, can be reproduced in arthroscopic application (see Fig. 5(b)). Also, in many treatments, the impact surface is a tissue defect and therefore cannot be freely chosen or altered. Our hardest gelatin-containing surfaces result in similarly low viability as hard glass surfaces. These 20% gelatin surfaces are similar in stiffness to muscle tissue[35], which is one of the softer human tissues[36]. Thus, clinically relevant surfaces are relatively stiff, possibly affecting cell survival. To solve this problem, the spray parameters require optimization. Similarly, the deposition of viscous, cell-containing hydrogels is usually required to preserve the desired 3D tissue architecture in biofabrication[12]. However, such liquids are likely to negatively affect the cell viability (see Fig. 5(c)). Decreasing the spray pressure[2,15–17], using softer impact surfaces[24], or increasing the nozzle-substrate distance can counteract the negative influence of the increased viscosity (see Fig. 5), but, unfortunately, these parameters are sometimes also constrained.

The greatest potential to improve cell viability in cell spraying therefore seems to be optimization of spray nozzle designs. Particularly, design optimization resulting in increased and monodisperse droplet sizes and reduced impact velocities would allow for successful cell deposition in an extended viscosity range. In this study we have used the Duploject system, which is approved for clinical application of fibrin glue by spraying

and also used for cell spraying[4]. The spray produced by this nozzle is characterized by highly polydisperse droplet diameters and velocities. High-velocity impacts occur even for the most gentle spraying parameters, limiting the measured highest post-spray cell viabilities to 90%. Nozzle designs producing more monodisperse droplets may prevent these lethal events, even for high-throughput spraying of viscous liquids. Our experimental setup can be used to rationally optimize such future spray nozzles, which may substantially enhance the application window of cell-spraying.

Finally, other droplet-based cell deposition technologies may benefit from our approach. In ink-jet bioprinting, highly monodisperse cell-containing droplets40–43 are deposited. Here, typically, low-viscosity droplets of 40 µm (exceeding the cell size by a factor of 3) impact at velocities below 10 ms^{-1}. Good viability is generally measured in this range[23], in agreement with our model (Fig. 2). However, reduced cell viability is observed for neural cells[44]. Our study suggests that especially decreasing the liquid viscosity or reducing the droplet ejection velocity could improve the cell viability of such more fragile cell types. These measures reduce the expected cell damage both in the nozzle and during impact, which are both likely causes of cell damage in ink-jet printing (see supplementary section 1). Using soft impact substrates or larger nozzle-substrate distances will still reduce impact-related damage, but nozzle-induced cell damage or poration[10] cannot be suppressed in this manner.

Cell viability trends observed in laser-assisted bioprinting (LAB) are also described by our model. Here, a pulsed laser is focused onto a cell-containing liquid film, resulting in the deformation of this film and break-up into cell-containing droplets[45,46]. By placing a receiver substrate in the line-of-flight of the cell-containing droplet, deposition is achieved. Increased impact velocities result in decreased cell viability[47,48], and soft impact surfaces improve cell survival49, analogous to our model results shown in Fig. 2. Surprisingly, improved cell viability was reported for increased viscosity48, but this was explained by the reduced impact velocity due to the increased viscosity. Studying the cell viability as a function of the liquid viscosity at a controlled impact velocity would therefore be highly interesting. Such experiments may also advance the understanding of cell membrane deformation due to pulsed shear stresses[50], as occurring in cell-containing droplet impact.

5.5 Conclusion

In conclusion, we present and validate an analytical model describing the cell viability as a function of the droplet impact parameters. The model describes cell-viability trends in cell spraying, inkjet bioprinting, and laser-assisted cell transfer, confirming the general importance of droplet impact for cell survival in bioprinting. Since future biofabrication applications may involve high-throughput deposition of different, possibly more fragile, cell types contained by high-viscosity bio-inks, we expect that preventing cell damage will become even more important. In particular, post-spray cell survival will be cell-type dependent. In addition, different bio-inks may require distinct

deposition parameters in combination with dedicated nozzle designs allowing monodisperse droplet ejection while maintaining low shear rates inside the nozzle. Our study provides a framework to optimize cell survival in such future applications, contributing to reliable biofabrication of complex 3D-tissue constructs of a clinically relevant size.

5.6 Supplementary information

5.6.1 Shear rate analysis

The shear rates in the spray nozzle and during impact are estimated. The shear rate is defined as $\gamma(h) = \delta u = \delta h$, with u(r) the velocity in r-direction. The coordinate system shown in supplementary figure 1. By dimensional analysis the shear rate during impact is estimated as $\gamma \sim V_0/D_0 \approx 10^6\, s^{-1}$ for a D_o = 10 µm droplet impacting at 10 ms^{-1}. For drop-on-demand systems (i.e. ink-jet printing, valve-based deposition, and certain regimes of laser-induced forward transfer) both the velocity inside the nozzle and the diameter of the nozzle are of the same order as D_o and V_o, respectively. Therefore, distinguishing the nozzle-induced shear from the impact-induced shear is far from trivial. However, for the cell spray, the diameter of the nozzle $DN \sim 500\ \mu m$ is much larger than Do, resulting in a strongly reduced shear rate within the nozzle, which is estimated as $\gamma \sim \frac{V_0}{D_N} \approx 2 \cdot 10^4 s^{-1}$. Therefore, only the impact of cell-containing droplets is expected to have a significant shear-induced effect in cell spraying.

5.6.2 Spray characterization

As described in the Methods section, the spray is characterized using the setup shown in supplementary figure 1.

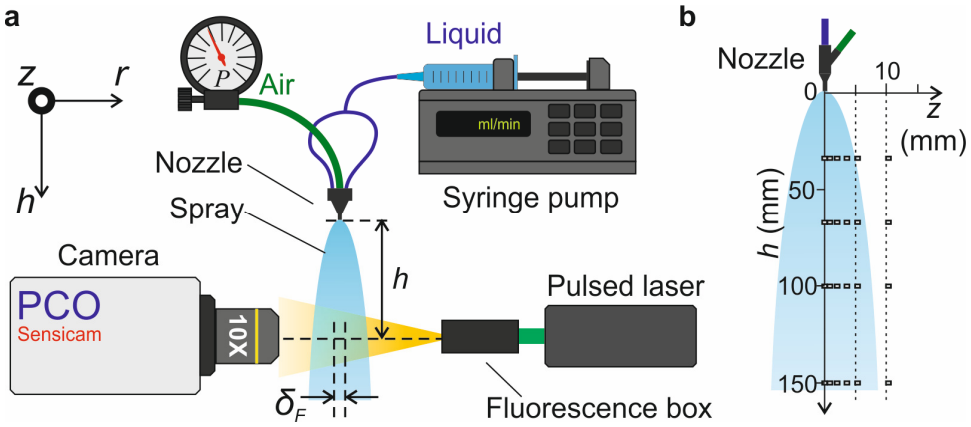

Supplementary figure 1: (a) Overview of the setup used for the spray characterization measurements. For visualization, a dual-shutter camera is used. For each image a slice of the spray is visualized, corresponding to the depth of the focal plane δF. Illumination is provided by dual-pulse ND:Yag laser combined with a fluorescence box to remove the laser coherence. The spray generation is equal to the cell spraying experiments. (b) Side-view of the spray. Each small rectangle indicates a measurement location used for spray characterization, corresponding to the field of view of the camera (drawn to scale).

Supplementary figure 2 shows images of the spray as a function of the air pressure similar to observation with the naked eye. The spray visually changes as a function of the pressure and widens with increasing distance from the nozzle. Some droplets are individually visible, but these only represent the largest and slowest droplets.

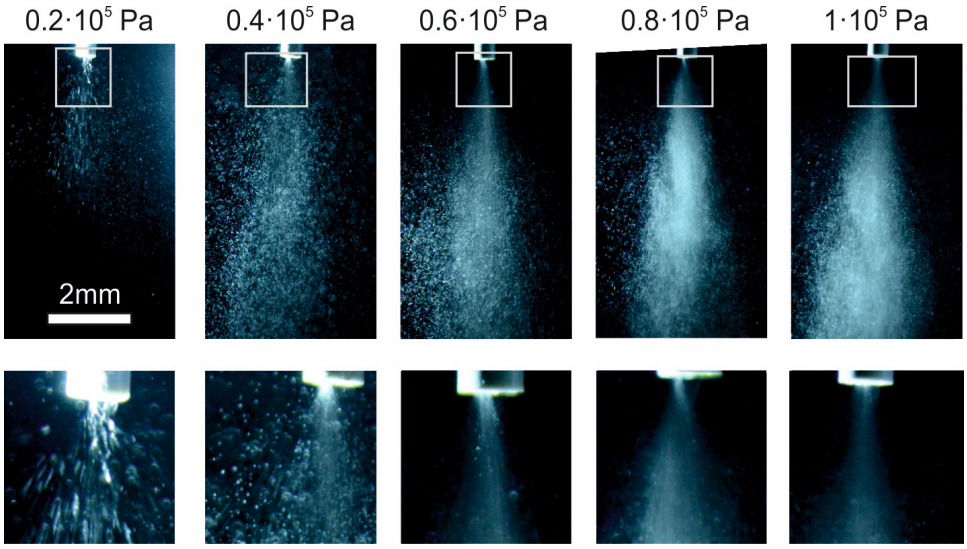

Supplementary figure 2: Low-speed images of the spray as a function of the air pressure. Each bottom images represents a magnification of the white rectangle in the top image. For P = 0.2 · 10⁵ Pa the droplets in the spray appear as stripes, due to motion blur. At higher pressures the individual droplets within the spray are no longer visible. The droplets which appear spherical fall through the surrounding air at very low velocity (i.e. they are not part of the main spray), and constitute a nebula around the spray.

Key spray characteristics are shown in supplementary figure 3. Supplementary figures 3 (a) and (b) respectively show that the droplet diameter decreases for increasing pressure, and that the droplet velocity increases for increasing pressures. Supplementary figure 3 (c) illustrates the strong influence of the nozzle-substrate distance on the spray velocity. In addition, we found that the nozzle-substrate distance hardly affects the droplet diameter, and that the viscosity neither affects the droplet diameter nor the droplet velocity (not shown).

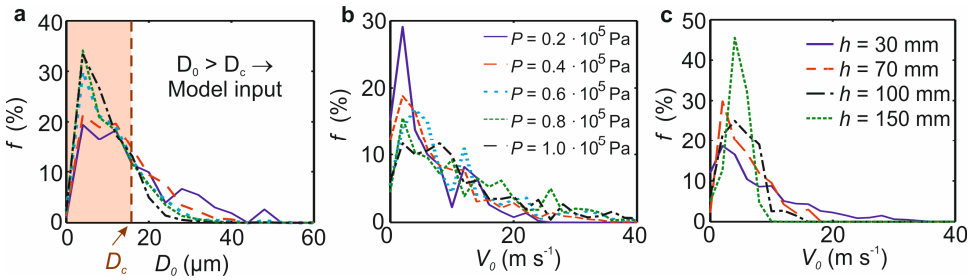

Supplementary figure 3: Figure (a) shows the spatially-averaged droplet diameter distribution for different air pressures (legend in figure (b)). The shaded area indicates droplet sizes Do smaller than the cell size *Dc* = 15μm, which are omitted in cell viability predictions. Figures (b) and (c) show the droplet velocity distributions for different air pressures (b) and distances from the nozzle (c), for droplets diameters exceeding the cell size. Unless specified in the legend, $P = 0.4 \cdot 10^5$ Pa, $\mu = 1$ mPa s, $h = 30$ mm, and $z = 0$ mm.

The influence of the spray characteristics on the cell viability is shown in supplementary figures 4 to 7. Here, the droplet size- and velocity distributions are plotted for a range of spraying parameters (left figures). In each plot, the corresponding viability probability contours are also plotted. For increasing pressure, the droplet size decreases and the droplet velocity strongly increases, which results in more low-viability impacts as observed by comparing supplementary figure 4 (a) and (c). This trend is reflected in supplementary figure 4 (d), where almost half of the cells will certainly not survive the impact. Increasing the distance from the nozzle primarily decreases the impact velocity, as shown in supplementary figure 5 (a) and (c). Consequently, the viability increases as shown in supplementary figure 5 (d).

Increasing the viscosity hardly affects the droplet size- and velocity-distributions. However, for a given droplet size and velocity, the viability dramatically decreases, resulting in a strong shift of the viability contours shown in supplementary figure 6. Similarly, the viability contours change as a function of the substrate stiffness, resulting in increased viability for softer surfaces as shown in supplementary figure 7.

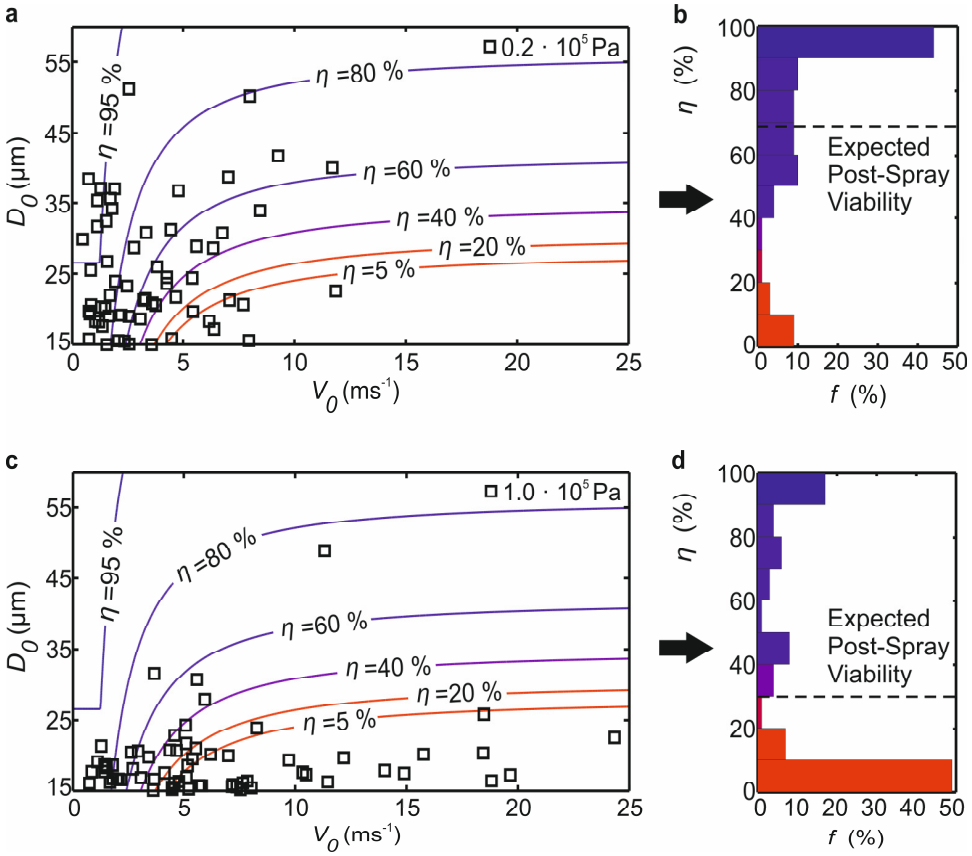

Supplementary figure 4: Droplet size- and velocity for a pressure $P = 0.2 \cdot 10^5$ Pa (a) and $P = 1 \cdot 10^5$ Pa (c). Representative cell viability contours are plotted in both figures. For $P = 1 \cdot 10^5$ Pa, more small and fast droplets are observed, which corresponds to low-viability regions of the diagram, and a lower predicted cell viability. Cell viability distributions are shown in figures (b) and (d), for pressure $P = 0.2 \cdot 10^5$ Pa (c) and $P = 1 \cdot 10^5$ Pa (d). The graphs are obtained analogous to figure 3(f) in the main text. The other control parameters are maintained constant at nozzle-substrate distance h = 30 mm, viscosity $\mu = 1$ mPa s, and a glass impact surface for which stiffness $S = 1$.

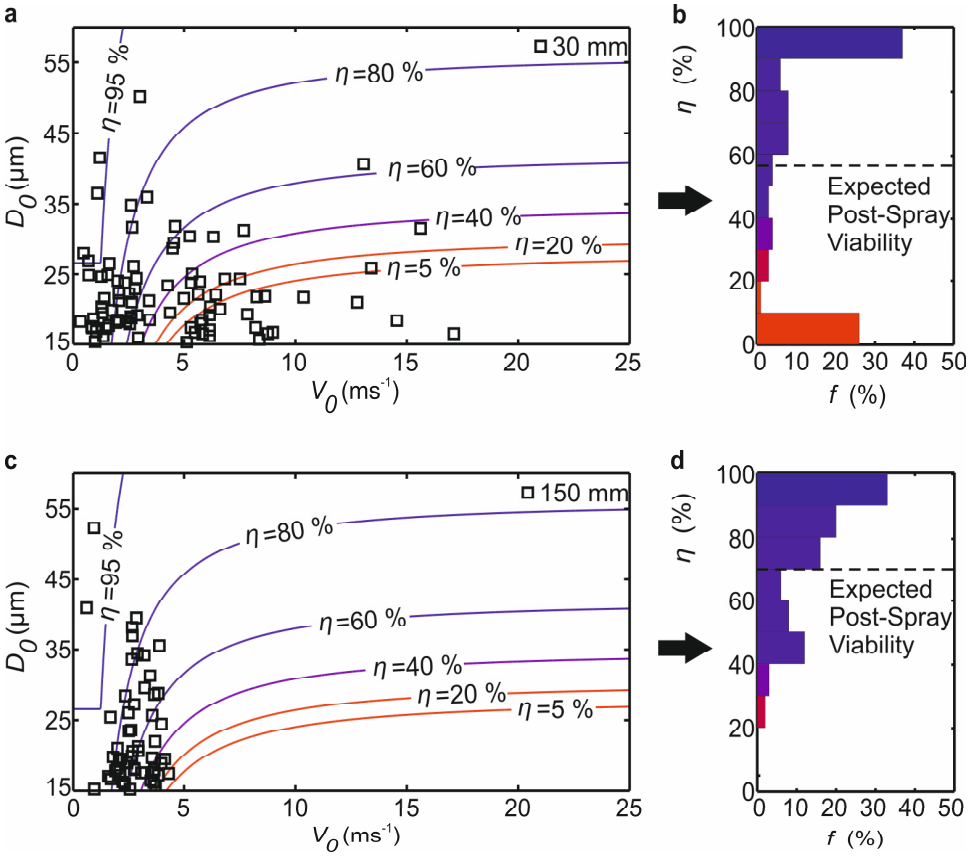

Supplementary figure 5: Droplet size- and velocity for a nozzle-substrate distance h = 30 mm (a) and h = 150 mm (c). For increasing distance, primarily the droplet velocity is decreased and the distribution corresponds to a high-viability region of the diagram. The increased viability is reflected in the cell viability distributions as shown in figures (b) and (d), respectively. The other control parameters are maintained constant at $P = 0.4 \cdot 10^5$ Pa, viscosity μ = 1 mPa s, and a glass impact surface for which stiffness S = 1.

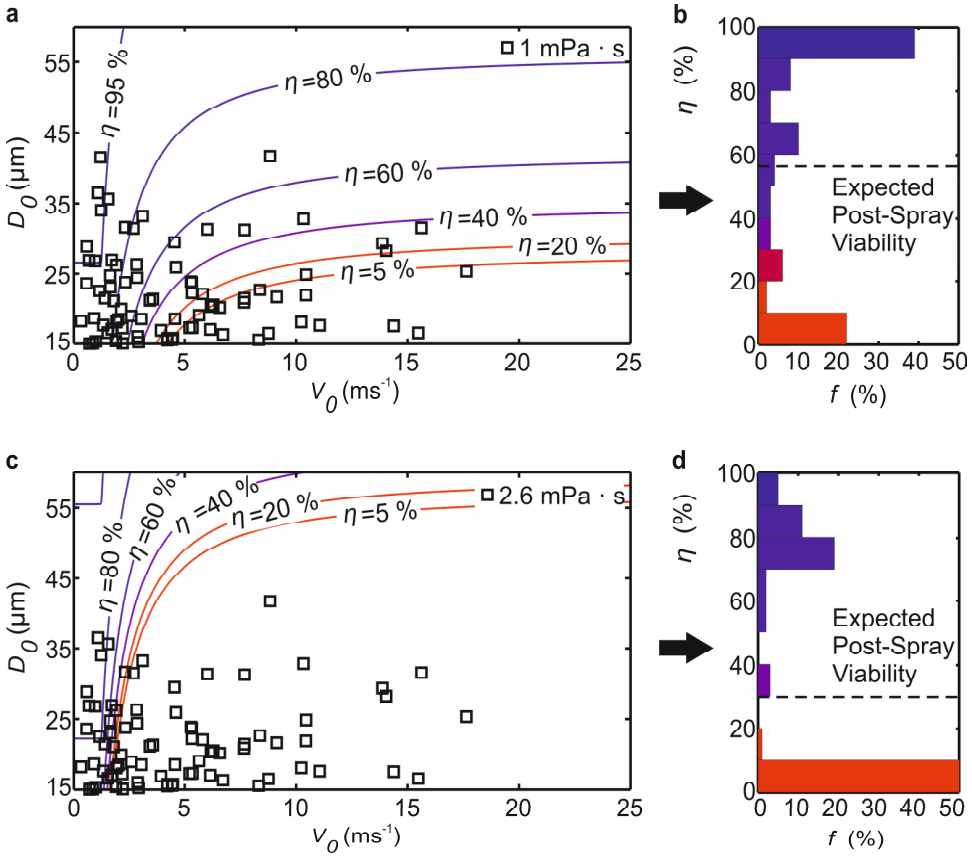

Supplementary figure 6: Droplet size- and velocity for a liquid viscosity μ = 1 mPa s (a) and μ = 2.6 mPa s (c). The increasing viscosity hardly affects the droplet size and velocity distribution. However, the expected viability sharply drops for a constant droplet size and speed, which is reflected by a change in the viability contours in figure (c) as compared to (a). The reduced viability is reflected in the cell viability distributions as shown in figures (b) and (d), respectively. The other control parameters are maintained constant at pressure $P = 0.4 \cdot 10^5$ Pa, nozzle-substrate distance h = 30 mm, and a glass impact surface for which stiffness S = 1.

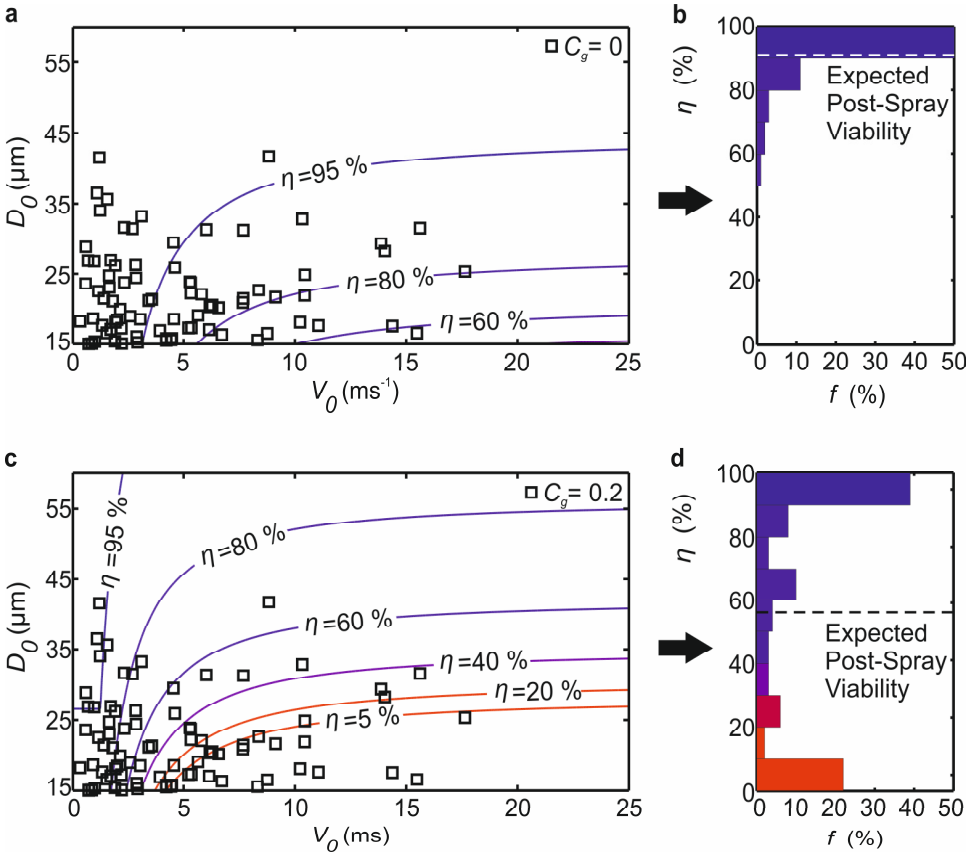

Supplementary figure 7: Influence of the substrate gelatin percentace: C_g = 0% in figure (a) (water surface, corresponding to stiffness S = 0) and C_g = 20% in figure (c) (corresponding to stiffness S = 1). The expected viability increases for a constant droplet size and speed, which is reflected by the difference between the viability contours in figure (c) as compared to (a). The increased viability is reflected in the cell viability distributions as shown in figures (b) and (d), respectively. The other control parameters are maintained constant at pressure $P = 0.4 \cdot 10^5$ Pa, nozzle-substrate distance h = 30 mm, and viscosity μ = 1 mPa s.

5.6.3 Influence of the surrounding droplet on cell deformation

The influence of the cell diameter and impact velocity on cell deformation (equations (4) and (5) of the main text) are obtained from basic models describing droplet impact [29]. The influence of the surrounding droplet's diameter D_o and viscosity μ on the cell deformation are obtained from the numerical results in ref. [25], as incorporated in equation (7) of the main text (the procedure is discussed below).

To obtain the influence of the surrounding droplet's diameter D_o and viscosity μ on the cell deformation, the maximal cell deformation values provided in figures 15 and 19 in ref. [25] are extracted and plotted in supplementary figure 8 (a) and (b). A priori, the scaling of M as a function of these parameters is unknown. Therefore, different fit functions were tested and the best results are indicated by the dashed lines within these plots (the functional form is provided by the equations). Supplementary figure 8 (c) shows M as a function of both control parameters. Finally, supplementary figure 8 (d) shows the predicted increase in surface area as a function of the surrounding droplet's diameter D_o and viscosity μ, using γ and equation (8) from the main text.

In our work, other relevant control parameters (e.g. surface tension and contact angle [25]) are not varied, and therefore captured by a constant prefactor C_o in equation (7) of the main text. Fitting C_o to our reference measurement (for which $P = 0.4 \cdot 10^5$ Pa, $\mu = 1$ mPa s, $h = 30$ mm, and a glass impact substrate) provides $C_o = 5$. Importantly, even if the contact angle would be varied (for example by spraying onto a hydrophobic substrate), we would not expect a significant influence of this parameter, since the contact angle does not affect the spreading behavior of the drop for high Weber number impact [31]. Therefore, the influence of the contact angle on the outer drops spreading (and therefore cell deformation) is expected to be negligible. For low velocity impact ($V \leq 1$ m/s) the Weber number becomes of order 1. In this case, the contact angle drives the drops spreading, and is therefore expected to affect cell deformation resulting in a change of C_o.

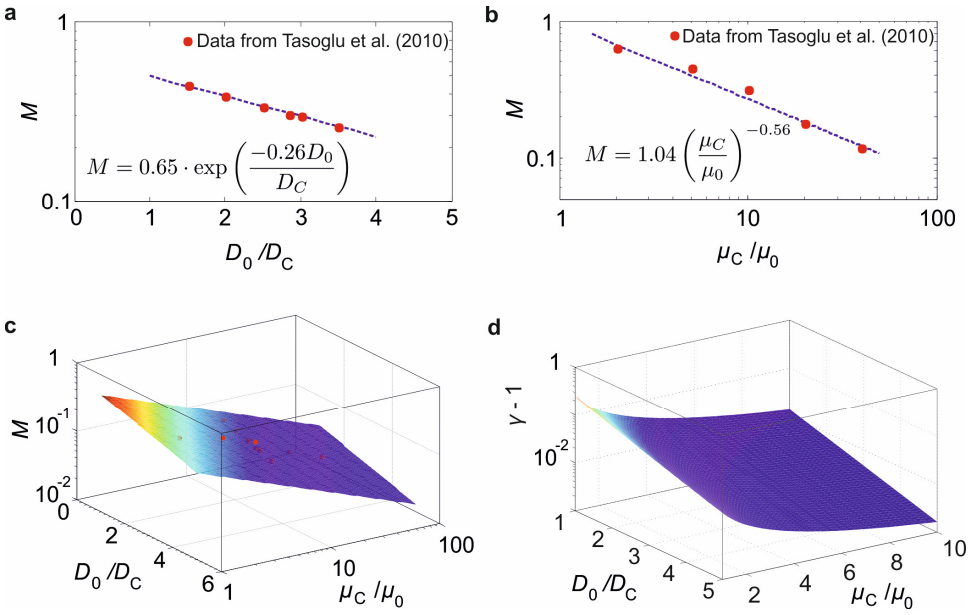

Supplementary figure 8: Cell deformation as a function of (a) the relative droplet diameter D_o/D_C and (b) the relative viscosity μ_C/μ_o. The dashed lines indicate our fit, as indicated by the equations within the plots. The data in figures (a) and (b) are the maximal values of the curves in figures 15 and 19 in Tasoglu et al., respectively. (c) The cell deformation M and (d) the change in relative surface area $\boldsymbol{\gamma - 1 = A/\pi D_c - 1}$ as a function of the droplet diameter and viscosity.

5.6.4 Material characterization

See supplementary figure 9 for images of the spray nozzle, and supplementary figure 10 for the measured dextran viscosity.

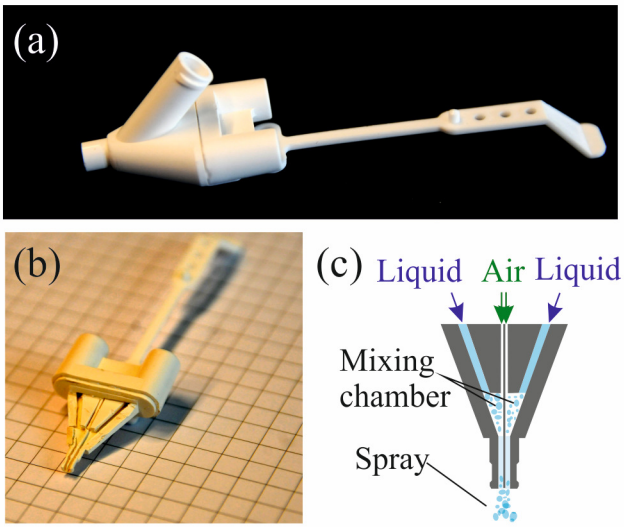

Supplementary figure 9: Images of the DuploJect nozzle used. (a) Overview image. The air enters through the top inlet, the liquid enters through the side inlets. (b) Nozzle that is cut to reveal the internal structure (the air inlet is also removed). (c) Top-view of the cut nozzle.

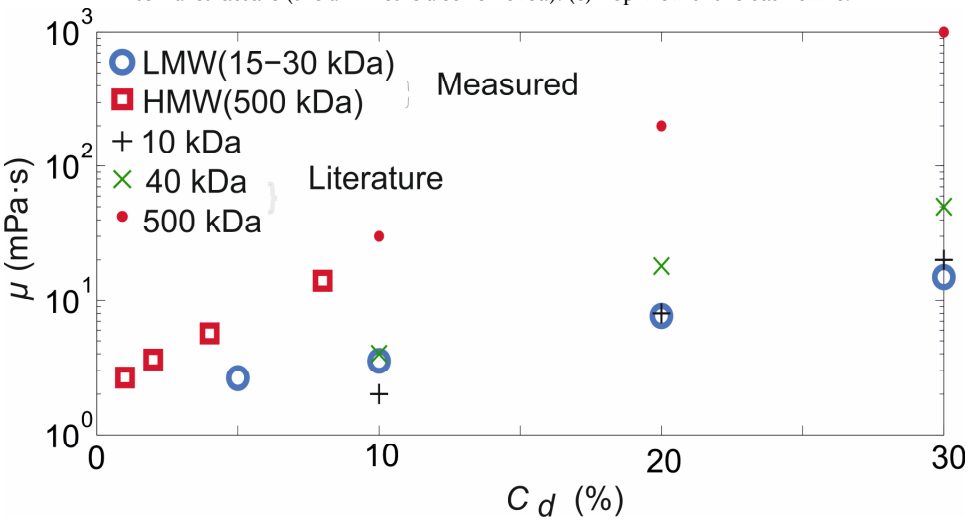

Supplementary figure 10: Measured viscosity as a function of the dextran concentration (mass %). Literature values [51] are shown for reference, indicating reasonable agreement.

5.6.5 Cell survival in time

The long-term viability of the cells is crucial both for clinical and laboratory application of cell spraying, and is plotted in supplementary figure 11a. All measurements are corrected by setting the control viability (non-impact, measured at the same time point) to 100%. Initially, after 2 hours, the control-corrected viability of 65% is comparable to the reference measurement. After 96 hours, the viability increases to around 90%. Although this shows that the cell population recovers after spraying, a considerable time is required before a high viability is reached. Spraying with high-viability parameters will prevent this problem, and may also reduce the potential influence of dead cells on the sprayed cell structure.

The absolute cell counts (normalized by the value after 2 hours) are plotted in supplementary figure 11b. The number of viable cells increases considerably in time, due to proliferation of surviving cells resulting in small cell clusters around these cells. This confirms the long-term viability and health of the surviving cells.

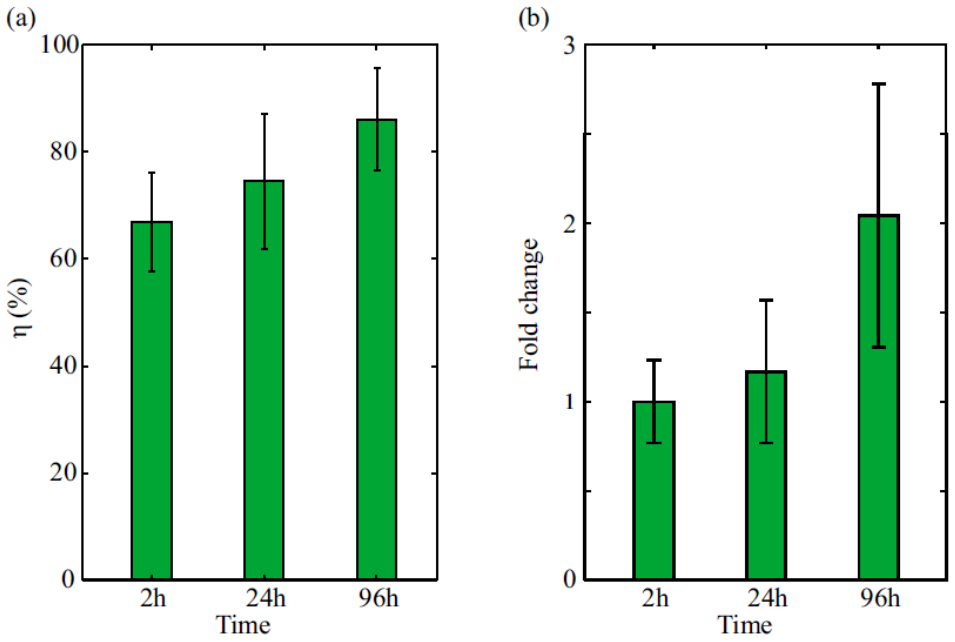

Supplementary figure 11: Cell survival and proliferation in time, for the standard experimental parameters (P = 0.4 · 10^5 Pa, viscosity μ = 1 mPa s, h = 30 mm, and a glass impact surface for which stiffness S = 1). Figure (a) shows that the initial viability of 65% steadily increases in time, to reach around 90% after a four-day period. Figure (b) shows the number of surviving cells in time, normalized by the initial measurement after two hours. For both sub-figures, the error bars indicate the standard deviations of cell counts from different areas in the same well.

References

1. Navarro, F. A. *et al.* Sprayed keratinocyte suspensions accelerate epidermal coverage in a porcine microwound model. *J. Burn. Care Rehabil.* **21,** 513–8 (2000).

2. Harkin, D. G., Dawson, R. A. & Upton, Z. Optimized delivery of skin keratinocytes by aerosolization and suspension in fibrin tissue adhesive. *Wound Repair Regen.* **14,** 354–63 (2006).

3. Kirsner, R. S. *et al.* Spray-applied cell therapy with human allogeneic fibroblasts and keratinocytes for the treatment of chronic venous leg ulcers: a phase 2, multicentre, double-blind, randomised, placebo-controlled trial. *Lancet* **380,** 977–85 (2012).

4. De Windt, T. S. *et al.* Arthroscopic airbrush assisted cell implantation for cartilage repair in the knee: a controlled laboratory and human cadaveric study. *Osteoarthr. Cartilage* 1–8 (2014).

5. Murphy, S. V. & Atala, A. 3D bioprinting of tissues and organs. *Nat. Biotechnol.* **32,** 773–785 (2014).

6. Mota, C., Puppi, D., Chiellini, F. & Chiellini, E. Additive manufacturing techniques for the production of tissue engineering constructs. *J. Tissue Eng. Regen. Med.* (2012).

7. Malda, J. *et al.* 25th anniversary article: Engineering hydrogels for biofabrication. *Adv. Mat.* **25,** 5011–28 (2013).

8. Wilson, W. C. & Boland, T. Cell and organ printing 1: protein and cell printers. *Anat Rec. Part A* **272,** 491–6 (2003).

9. Derby, B. Bioprinting: inkjet printing proteins and hybrid cell-containing materials and structures. *J. Mat. Chem.* **18,** 5717–21 (2008).

10. Binder, K. W., Allen, A. J., Yoo, J. J. & Atala, A. Drop-on-demand ink-jet bioprinting: a primer. *Gene Ther. Reg.* **06,** 33–49 (2011).

11. Guillemot, F. *et al.* High-throughput laser printing of cells and biomaterials for tissue engineering. *Acta Biomater.* **6,** 2494–500 (2010).

12. Moon, S. *et al.* Layer by layer three-dimensional tissue epitaxy by cell-laden hydrogel droplets. *Tissue Eng. Pt. C-Meth.* **16,** 157–66 (2010).

13. Faulkner-Jones, A. *et al.* Development of a valve-based cell printer for the formation of human embryonic stem cell spheroid aggregates. *Biofabrication* **5,** 015013 (2013).

14. Grossin, L. *et al.* Step-by-Step Build-Up of Biologically Active Cell-Containing Stratified Films Aimed at Tissue Engineering. *Adv. Mat.* **21,** 650–655 (2009).

15. Tritz, J. *et al.* Designing a three-dimensional alginate hydrogel by spraying method for cartilage tissue engineering. *Soft Matter* **6,** 5165 (2010).

16. Fredriksson, C., Kratz, G. & Huss, F. Transplantation of cultured human keratinocytes in single cell suspension: a comparative *in vitro* study of different application techniques. *Burns* **34,** 212–9 (2008).

17. Nahmias, Y., Arneja, A., Tower, T. T., Renn, M. J. & Odde, D. J. Cell patterning on biological gels via cell spraying through a mask. *Tissue Eng.* **11,** 701–8 (2005).

18. Di Risio, S. & Yan, N. Piezoelectric Ink-Jet Printing of Horseradish Peroxidase: Effect of Ink Viscosity Modifiers on Activity. *Macromol. Rapid Commun.* **28,** 1934–1940 (2007).

19. Nishiyama, Y. *et al.* Development of a three-dimensional bioprinter: construction of cell supporting structures using hydrogel and state-of-the-art inkjet technology. *J. Biomech. Eng.* **131,** 035001 (2009).

20. Ferris, C. J., Gilmore, K. G., Wallace, G. G. & In het Panhuis, M. Biofabrication: an overview of the approaches used for printing of living cells. *Appl. Microbiol. and Biot.* **97,** 4243–58 (2013).

21. Yamaguchi, S., Ueno, A., Akiyama, Y. & Morishima, K. Cell patterning through inkjet printing of one cell per droplet. *Biofabrication* **4,** 045005 (2012).

22. Saunders, R. E., Gough, J. E. & Derby, B. Delivery of human fibroblast cells by piezoelectric drop-on-demand inkjet printing. *Biomaterials* **29,** 193–203 (2008).

23. Li, E. Q., Tan, E. K. & Thoroddsen, S. T. Piezoelectric Drop-on-Demand Inkjet Printing of Rat Fibroblast Cells: Survivability Study and Pattern Printing. *ArXiv* (2013).1310.0656.

24. Tirella, A. & Ahluwalia, A. The impact of fabrication parameters and substrate stiffness in direct writing of living constructs. *Biotechnol. Prog.* **28,** 1315–20 (2012).

25. Tasoglu, S., Kaynak, G., Szeri, A. J., Demirci, U. & Muradoglu, M. Impact of a compound droplet on a flat surface: A model for single cell epitaxy. *Phys. Fluids* **22,** 1–15 (2010).

26. Barbee, K. A. Mechanical cell injury. *Ann. N. Y. Acad. Sci.* **1066,** 67–84 (2005).

27. Takamatsu, H. & Rubinsky, B. Viability of deformed cells. *Cryobiology* **39,** 243–51 (1999).

28. Groulx, N., Boudreault, F., Orlov, S. N. & Grygorczyk, R. Membrane reserves and hypotonic cell swelling. *J. Membr. Biol.* **214,** 43–56 (2006).

29. Clanet, C., Béguin, C., Richard, D. & Quéré, D. Maximal deformation of an impacting drop. *J. Fluid Mech.* **517,** 199–208 (2004).

30. Visser, C. W., Tagawa, Y., Sun, C. & Lohse, D. Microdroplet impact at very high velocity. *Soft Matter* **8,** 10732 (2012). 1206.1574.

31. Visser, C. W. *et al.* Dynamics of high-speed micro-drop impact: Numerical simulations and experiments at frame-to-frame times below 100ns. *Soft Matter* **11,** 1708–22 (2015).

32. Chen, Y., Liu, X., Zhang, C. & Zhao, Y. Enhancing and suppressing effects of an inner droplet on deformation of a double emulsion droplet under shear. *Lab Chip* **15,** 1255–61 (2015).

33. Tran, T., de Maleprade, H., Sun, C. & Lohse, D. Air entrainment during impact of droplets on liquid surfaces. *J. of Fluid Mech.* **726,** R3 (2013).

34. Mangili, S., Antonini, C., Marengo, M. & Amirfazli, A. Understanding the drop impact phenomenon on soft PDMS substrates. *Soft Matter* **8,** 10045 (2012).

35. Jussila, J. Preparing ballistic gelatine-review and proposal for a standard method. *Forensic Sci. Int.* **141,** 91–8 (2004).

36. Meyers, M. A., Chen, P.-Y., Lin, A. Y.-M. & Seki, Y. Biological materials: Structure and mechanical properties. *Prog. in Mater. Sci.* **53,** 1–206 (2008).

37. Lim, C. T., Zhou, E. H. & Quek, S. T. Mechanical models for living cells-a review. *J. Biomech.* **39,** 195–216 (2006).

38. Tsai, M. A., Frank, R. S. & Waugh, R. E. Passive mechanical behavior of human neutrophils: power-law fluid. *Biophys. J* **65,** 2078–88 (1993).

39. Allouni, A., Papini, R. & Lewis, D. Spray-on-skin cells in burns: a common practice with no agreed protocol. *Burns* **39,** 1391–4 (2013).

40. Boland, T., Xu, T., Damon, B. & Cui, X. Application of inkjet printing to tissue engineering. *Biotechnol. J* **1,** 910–7 (2006).

41. Derby, B. Printing and prototyping of tissues and scaffolds. *Science* **338,** 921–6 (2012).

42. Khatiwala, C., Law, R., Shepherd, B., Dorfman, S. & Csete, M. 3D Cell Bioprinting for Regenerative Medicine Research and Therapies. *Gene Ther. Reg.* **07,** 1230004 (2012).

43. Melchels, F. P. *et al.* Additive manufacturing of tissues and organs. *Prog. Polym. Sci.* **37,** 1079–1104 (2012).

44. Xu, T. *et al.* Viability and electrophysiology of neural cell structures generated by the inkjet printing method. *Biomaterials* **27,** 3580–8 (2006).

45. Gruene, M. *et al.* Laser Printing of Stem Cells for Biofabrication of Scaffold-Free Autologous Grafts. *Tissue Eng. Pt. C-Methods* **17,** 79–87 (2011).

46. Guillotin, B. & Guillemot, F. Cell patterning technologies for organotypic tissue fabrication. *Trends Biotechnol.* **29,** 183–90 (2011).

47. Lin, Y., Huang, G., Huang, Y., Tzeng, T.-R. J. & Chrisey, D. Effect of laser fluence in laser-assisted direct writing of human colon cancer cell. *Rapid Prototyping J* **16,** 202–208 (2010).

48. Catros, S., Guillotin, B., Bačáková, M., Fricain, J.-C. & Guillemot, F. Effect of laser energy, substrate film thickness and bioink viscosity on viability of endothelial cells printed by Laser-Assisted Bioprinting. *Appl. Surf. Sci.* **257,** 5142–5147 (2011).

49. Ringeisen, B. R. *et al.* Laser printing of pluripotent embryonal carcinoma cells. *Tissue Eng.* **10,** 483–91 (2004).

50. Li, F., Chan, C. U. & Ohl, C. D. Yield strength of human erythrocyte membranes to impulsive stretching. *Biophys. J* **105,** 872–9 (2013).

51. Pharmacosmos, "http://www.dextran.net/about-dextran/dextranchemistry/physical-properties.aspx," 2014.

“Hot off the press! What’s the hype – bioprinting parameters tailored to cell type?! Read the exclusive inside story in chapter 6“

6

Cell type determines viability in bioprinting: altering cellular properties results in improved survival

Bioprinting has a large potential to revolutionize healthcare. Present technology is limited however by a fundamental trade-off between printing parameters, such as printability, throughput and resolution on one hand and the cell viability on the other. To print complex structures with multiple cell types, a better understanding of printing process parameters on cell viability is required. Here, we assessed the effect of droplet-based cell deposition technology using cell spraying on the viability of eight different cell types. Our results showed that printing parameters have a cell type dependent impact on cell viability ranging from 30% in susceptible cells such as Myoblasts to 90% in resistant cells such as primary chondrocytes at high pressure. Subsequently, by applying a previously developed analytical cell survival model we identified three parameters that could be responsible for this difference: cell size, cell viscosity and membrane strength. We then altered each of these parameters by adjusting osmolarity, temperature and cholesterol content, respectively, and assessed the impact on cell survival using 3T3 cells. We showed that especially shrinking the cell by increasing the osmolarity, and depletion of cholesterol content improved the resilience of the cells to deformation in the printing process. Our data show that bioprinting applications should be carefully tailored for individual cell types to maximize cell survival. Decreasing cell size and adjusting cholesterol content in the

---

Jan Hendriks[1], Claas Willem Visser[2], Daniël B.F. Saris[3,4] & Marcel Karperien[1]

1 Department of Developmental BioEngineering, TechMed institute, University of Twente, The Netherlands.

2 Physics of Fluids Group, TechMed institute, Faculty of Science and Technology, University of Twente, The Netherlands.

3 Department of Orthopedics, UMC Utrecht, The Netherlands.

4 Department of Reconstructive Medicine, TechMed institute, Faculty of Science and Technology, University of Twente, The Netherlands.

Manuscript in preparation

plasma membrane are two simple methods to increase the parameter space available for printing vulnerable cells. These insights could break the deadlock holding back bioprinting of living cells and could help unleash its full potential.

6.1 Introduction

Bioprinting is a highly versatile research field combining printers, biomaterials and cells and has large potential for application in disease modelling, drug development and tissue engineering. The ultimate goal of bioprinting is the creation of mature functional tissues and / or organs, significantly impacting donor shortage problems.

The technology should optimally combine printers with high resolution and throughput and biomaterials with high shape fidelity and bioactivity while simultaneously maintaining the viability of the printed cells [1]. The most popular printing technologies are based on droplet deposition or on extrusion methods, also known as bioplotting. The most used droplet deposition methods originate from inkjet printing and have several advantages. They are highly versatile, relatively inexpensive and can create structures with a high resolution [2]. However, the throughput is limited, only low viscosity solutions can be used and cell number is restrained through clogging issues. The desirable increase in throughput and viscosity, however, leads to increased shear rate and therefore poses a challenge to cell viability [3]. Bioplotting has a higher throughput, larger variety in available bioinks and is relatively cheap. However, the resolution is limited and the shear rate during printing is higher than in droplet based methods leading to reduced cell viability. Furthermore, the desirable high shape fidelity of bioinks to increase printing resolution leads to further increased shear rate and an additional strain on cell survival [3, 4]. Therefore, there is a trade-off between the most important printing parameters: resolution, throughput and shape fidelity at one hand and cell viability at the other that poses a serious limitation in bioprinting development [2, 5].

To overcome these limitations a better understanding of the parameters governing cell survival is essential. Several studies have tried to assess the influence of the printing parameters on the viability of the cells [6]. In these papers, a strong relationship was found between shear stress and cell viability [4, 7]. In previous work, we developed an analytical model predicting the cell viability depending on printing parameters in droplet based printing methods [8]. We showed there is a strong relationship between droplet size, velocity and viscosity, and printing distance on the cell viability. These studies have improved our knowledge on the effect of process parameters on cell survival. While this work can be very useful in optimizing the printing parameters for a specific cell type, little work has been performed comparing the cell survival between different cell types with distinct mechanical properties [9]. As the ultimate goal is to print organs containing many different cell types, it is likely that no single process parameter will be optimal for all cell types printed. It is therefore essential to gain more knowledge in the effect of the printing process on different cell types and to elucidate the underlying mechanisms.

When cells enter the printing process, they are subjected to shear stresses for a specific (often short) duration particularly in the nozzle and during impact. These stresses will lead to cell deformation the extent of which critically depends on specific cell characteristics. In a simplified model, a cell can be seen as a visco-elastic bag with a

certain resistance to deformation based on its stiffness, governed in large part by the cytoskeleton [10]. The deformation results in a strain on the cell and a stretch on its membrane. The membrane can survive this dilation to a certain threshold, depending on membrane contents and cortical cytoskeleton, after which it ruptures. This hole in the membrane leads to the influx of Ca^{2+} triggering repair mechanisms [11]. Small holes can be repaired within seconds, but larger holes require longer recovery time and are energy intensive to close [12]. In principle three deformation regimes can be defined [13]: Small deformations leading to no damage. Intermediate deformations, leading to small or medium holes in the membrane. When these deformations are sustained, the cells will eventually undergo apoptosis, but when the deformation is restored timely the cells can recover [14]. In contrast, large deformations result in large scale rupture and cell death by necrosis.

Cells normally reside in tissues and are exposed to a wide range in physiological mechanical loading rates in a tissue dependent manner. For example muscle cells are loaded with very large strains, while neurons are generally protected from mechanical loads [14]. It is therefore likely that specific cell types have developed adaptations to cope with mechanical stress and strain. Indeed, it has been shown that there is a large difference in the stiffness of various cell types, resulting from distinctive cytoskeleton organization [15]. This leads to differences in the extent of deformation at similar shear stress. In addition, the composition of the cell membrane is cell type dependent particularly in cholesterol content and the organization of the underlying cortical cytoskeleton [10]. This leads to differences in rupture thresholds [14]. Furthermore, the cells differ in size leading to variable deformations. Finally, the reparative capacity differs largely between cell types. For example, it was shown with the uptake of fluorescent dextran that muscle cell membranes rupture frequently during physiological loading, but are repaired without indications of harm to the cells [11]. In contrast, damage to neurons can often not be repaired or only at a very low rate.

In this study we set out to better understand the effect of the cell type on the cell survival in bioprinting. To achieve this, we compared the cell survival after cell spraying between 8 distinct cell lines originating from different tissues. Using a previously described experimental set-up, we were able to measure the survival of cells after impact of a single droplet layer on a glass slide. A large intercellular variability in cell survival was observed which ranged from 20% in susceptible cells to almost 90% in resistant cells at harsh printing conditions. We subsequently applied our analytical model to predict the cell survival. Using this approach we identified three cell type dependent parameters that are important in cell survival: Cell diameter, cell viscosity/stiffness and the critical membrane expansion before rupture. To further investigate these parameters, we attempted to alter the cell size, viscosity/stiffness and membrane fluidity in 3T3 fibroblasts by adjusting the osmolarity of the medium which impacts cell size and viscosity, temperature with main impact on viscosity and the cholesterol content with a main impact on membrane fluidity. We demonstrate that by relatively simple

adjustments in osmolarity of the printing medium and/or by varying the cholesterol content of the cell membrane cell survival can be increased.

6.2 Materials and Methods

6.2.1 Cell culture

Eight cell lines from different tissues were compared to assess the influence of cell spraying on their viability: mouse embryonic fibroblasts (3T3), mouse myoblasts (C2C12), human breast cancer (MCF-7), human prostate cancer (PC3), human chondrocytes (C20A4), human pancreatic beta cells (Min6), human embryonic kidney cells (Hek293T) and mouse lung endothelial cells (MLEC).

The cells were cultured in Dulbecco's modified eagle medium (DMEM, Gibco, Ref: 41965-039) with 10% Fetal bovine serum (FBS, Sigma, Ref: F7524) and 1% pen/strep (Gibco, Ref: 15140122) at 37 °C and 5% CO_2. For the 3T3 and Min6 cell lines β-mercaptoethanol (Gibco, 50mM, Cat: 31350010, also known as 2-mercaptoethanol) was freshly added at 1.4µL/mL when refreshing the medium to reduce the level of oxygen radicals. To harvest the cells, they were washed with PBS (Lonza, Reference:17-516F) and incubated with trypsin (Gibco, 0.25% Trypsin-EDTA, Reference: 25200072) for 4 minutes at 37 °C. The trypsin EDTA was inactivated by adding DMEM with 10% FBS (ratio 5:1). For each spray experiment, the cells were used at 80% confluency.

6.2.2 Cell spray experiment

The cell spray experiments were performed using a previously described custom set-up [8]. In this set up shear stress experienced by the cells is mainly dependent on droplet impact since the shear stress at the nozzle is neglectable. This set-up ensures the impact of a single cell layer on a dry substrate. This ensures that the measured viability is the result of the impact of a droplet on the surface and not drop on drop, therefore providing a clear parameter space that determines the cell viability. A schematic representation of the spray set-up is shown in figure 1. More detailed photos are depicted in supplementary figure 1.

A typical cell spray experiment is performed as follows. The cells are harvested as described above and are resuspended in DMEM with 1% pen/strep (impact medium) at 1.5 million cells/ml. FBS is known to reduce the surface tension of the droplet, which influences the cell viability and was therefore not added to the medium. Cells were added in equal volume to two 5 ml syringes (BD Plastipak) and placed in the Harvard Apparatus PHD2000 pump to achieve an homogeneous cell spray in the duplojet nozzle (Flow rate = 1.2 ml/min). The air pressure for the spray was controlled by a pressure regulator (ControlAir, type 100LR) and a pressure monitor (Wika). During a spray impact measurement a linear motor (Zaber T-LSQ150B) was used to move a microscope slide under the nozzle (distance nozzle-slide = 30 mm) to collect a single cell layer. The microscope slide is partially coated with superhydrophobic coating to create a reproducible impact zone size (20 by 15 mm). The microscope slide is subsequently

weighted to verify that only a single cell layer is collected, after which the suspension is washed with 300 µl impact medium and collected in 12 ml tubes. As a control a single droplet is collected from the nozzle on a microscope slide without applying external air pressure. Each control and impact measurement is performed in triplicates and each experiment is performed at least at three separate days.

6.2.3 Cell viability model

To analyse what potential cell characteristics could be responsible for the observed differences between the cell types, we applied our previously developed analytical model [8]. Briefly, this model describes the effect of droplet impact on the viability of cells. It combines three sub-models: the deformation of a bare cell impact, the influence of the outer droplet and the relationship between deformation and viability. This model was shown to accurately predict cell viability in cell sprays, when considering the influence of pressure, distance, viscosity and surface stiffness. The model includes three main parameters that are specific for the cell type: the cell size, cell viscosity and membrane strength. These parameters were investigated and the influence of viability was assessed.

6.2.4 Influence of temperature on cell viability

The influence of the temperature on the cell viability during bioprinting was assessed with a slightly adjusted version of the standard cell spray experiment using 3T3 fibroblasts. Three temperatures were compared 4 °C, 21 °C and 37 °C. The viability at room temperature (21 °C) was determined as described above. To assess the viability at 4 °C, the set-up was placed in a cold room at 4 °C. Set-up and cell suspensions were allowed to equilibrate for 30 minutes before a standard cell spray experiment was performed. To assess the viability at 37 °C the set-up was placed inside a standard cell culture incubator, without applying CO_2 injections. The set-up and cell suspension were allowed to equilibrate for 30 minutes before a standard cell spray experiment was performed.

6.2.5 Influence of osmolarity on cell viability

The influence of the cell size and cell viscosity on viability after spraying was assessed by incubating 3T3 fibroblasts in buffers with a range of osmolarities. The buffers used were based on 10 mM HEPES, contained 5.63 mM glucose, 1 mM $CaCl_2$ and 0.4 mM $MgCl_2$ at pH 7.4. The osmolarity was determined by the NaCl and KCL concentration with was increased in fixed ratio to obtain five osmolarities: 60.6 mM NaCl / 4.49 KCl (150 mOsm/ml), 95.5 mM NaCl / 7.08 mM KCl (225 mOsm/ml), 130.4 mM NaCl / 9.66 mM KCl (300 mOsm/ml), 200.3 mM NaCl / 14.8 mM KCl (450 mOsm/ml) and 270.1 mM NaCl / 20 mM KCl (600 mOsm/ml).

To determine the effect of these buffers on cell size, the cells were incubated in the buffers for a total of 2 hours. After 10 min, 30 min, 60 min, 90 min and 120 min photos were taken with a brightfield microscope. Cell size was determined using ImageJ and was based on measuring at least 40 cells per image. After 120 minutes cell viability was determined using a Live Dead assay.

During cell spray experiments, the cells were incubated for 30 minutes in the respective osmolarity, since the largest change in cell size occurs before this time point. Spray experiments were performed in the same buffers using the procedure explained above, with minor alteration: washing was performed not with the Impact medium, but with the respective osmolarity buffers.

6.2.6 Influence of the cholesterol content on cell viability

The influence of membrane strength and cell stiffness on viability post bioprinting was assessed by adjusting the cholesterol content of 3T3 fibroblasts. The cholesterol content can be effectively altered by incubating the cells with cyclodextrins as described before [16]. The most effective cyclodextrin for cholesterol depletion or enhancement is methyl-β-cyclodextrin (MβCD). When added pure it can deplete cholesterol from the membrane, when pre-loaded with cholesterol it can enhance the membrane cholesterol content.

Freshly made 5mM and 10mM solutions of methyl-β-cyclodextrin (Sigma Aldrich, Reference: C4555) were made in serum free medium to deplete the cells from cholesterol. To enrich the cells with cholesterol 5mM and 10mM solutions of MβCD containing 1 mM cholesterol (Sigma Aldrich, Reference: C3045) were made. Dissolving cholesterol in the cyclodextrin was achieved by stirring and heating the solution on a magnetic stirrer at 40°C for 90 minutes. The solutions were sterilized using a 0.2 µm filter. To change the cholesterol content of the membrane, the cells were suspended in the cholesterol depletion or enrichment solution and incubated for 45 minutes at 37°C. After incubation the cells were washed by centrifuging and the pellet was resuspended serum free medium.

The effect of cholesterol alteration on the cytoskeleton was assessed by phalloidin staining. To achieve this the fibroblasts were transferred to a 96 well plate at a seeding density of 8000 cells/cm² and incubated untill the cells were adhered. The cells were washed three times with PBS and fixed with a 10 % formalin solution (Sigma Aldrich, Reference: HT501128) for 10 minutes. After incubation, the cells were again washed three times with PBS. The cells were permeabilized with Triton X-100 0,1 % diluted in PBS for 5 minutes. After 5 minutes the cells were washed two times with PBS. A phalloidin staining (ThermoFisher, Reference: A12379, Excitation: 495 nm, Emission: 518 nm) was prepared in PBS to stain F-actin (1:40 v/v). The cell nuclei were counterstained with a DAPI staining (ThermoFisher, Reference: P36962, Excitation: 358 nm, Emission: 461 nm) diluted in PBS (1:100 v/v). The cells were incubated for 20 minutes at room temperature with the phalloidin staining and washed three times with PBS. The cell nuclei were stained by incubating the cells for 5 minutes with the DAPI staining. Images were captured using the EVOS microscope. Images of F-actin were made with the GFP-cube and the cell nuclei were imaged with the DAPI-cube (Excitation: 357/44 nm, Emission 447/60 nm). The pictures were analysed by two blinded individuals to avoid an observer bias. Two properties of the cells were evaluated: formation/reorganisation of stress fibres

and morphological changes. The magnitude of these properties were classified in three categories; no change (1), medium (2) and large (3).

Cell spray experiments were performed as described above with minor alterations. For cholesterol depletion cells were incubated in 10 mM MβCD and for enrichment they were incubated in 10:1mM MβCD:CHOL.

6.2.7 Live dead assay

A live dead assay was performed to determine the viability after the cell spray experiments. In this assay Calcein AM (Sigma, Ref: 17783) is reduced by live cells to Calcein which stains brightly green and Ethidium Homodimer (Sigma, Ref: 46043) only penetrates damaged membranes to stain the nuclei. In this assay cells can be stained only green (Live), red (Dead) or a combination of both (Live, but with previously damaged membrane). As previous results have shown that damaged cells can recover, we count damaged cells as alive [8]. To stain the cells, 100 µl 10X live dead solution was added to the collected cell suspension (900 µl). The resulting cell suspensions with 2 µM Calcein AM and 4 µM Ethidium Homodimer were transferred to a 48 wells plate and incubated at 37 °C and 5% CO_2 for 30 min. Images were taken with the EVOS FL Color Imaging System using the GFP (Excitation: 470/22 nm, Emission 510/42 nm) and the Texas red (Excitation: 585/29 nm, Emission: 624/40 nm) filter cubes. In each well six photos were taken in both GFP and Texas red at 4x objective to gain a good overview. The conditions were imaged in randomized order to avoid time bias in the experiments. The last images were taken within two hours after incubation. The stained cells in the images were counted with a home-made Matlab script. Briefly, this script automatically enhances the contrast of the image, counts circles and determines double stained cells. The contrast thresholds are equal over all conditions to avoid observer bias. The scripts are available upon request.

6.2.8 Statistical analysis

Statistical analysis was performed using IBM SPSS statistics 22. The difference in sample size (more cells counted in control vs. conditions) was corrected by adjusting all counts to the smallest sample in the respective measurement. In this way statistical misinterpretation can be avoided and the type I error is reduced [17]. The data collected is categorical (binary: live or dead), while the predictors are also categorical, therefore assumptions of normality are per definition not met. For this reason the Pearson chi-square test was used to determine the overall significance of the results. The significance between the conditions is assessed using a z-test, which is corrected for the family-wise error with the Bonferroni method.

6.3 Results

6.3.1 The set-up to measure cell survival

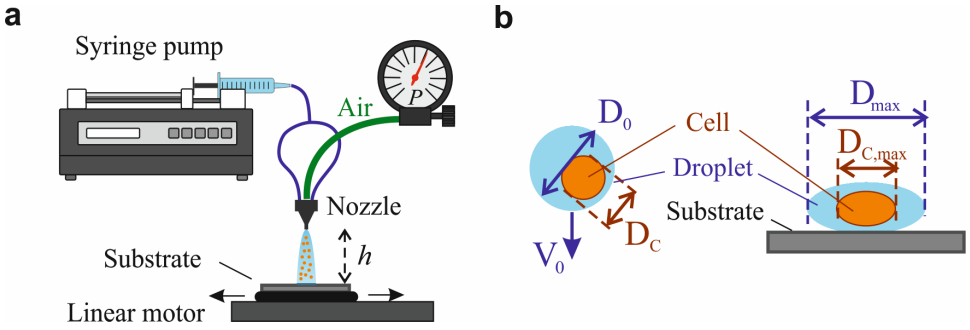

Figure 1: A) the set-up used for cell spray experiments. A syringe pump allows for steady fluid flow to a cell spray nozzle (duploject). Pressure is regulated to ensure reproducible spray. The substrate is moved under the nozzle and back for single cell layer impact. B) Impact on substrate leads to spreading of cells ($D_{c,max}$ / D_c) inside the droplets (D_{max} / D_o) depending on the impact velocity (V_o). The resulting membrane dilation can lead to rupture and cell death.

Cell viability after bioprinting was assessed using a custom cell spray set-up that was described extensively before [8]. In this set-up the air pressure and liquid flow rate can be controlled. A linear motor is used to move a glass substrate under the nozzle and back to achieve impact of droplets. This ensures a clean impact of a single layer of droplets. Therefore only droplets impacting on glass and not on water are measured. This enables the determination of the effect of droplet characteristics on cell viability as described in Hendriks et al., but also allows for the determination of effect of cell characteristics on cell viability.

6.3.2 The influence of the cell type on viability post impact

Using this set-up we looked at the effect of cell spraying on the viability of eight different cell lines sprayed at 0.4 and 0.8 bar, respectively. The results are shown in figure 2.

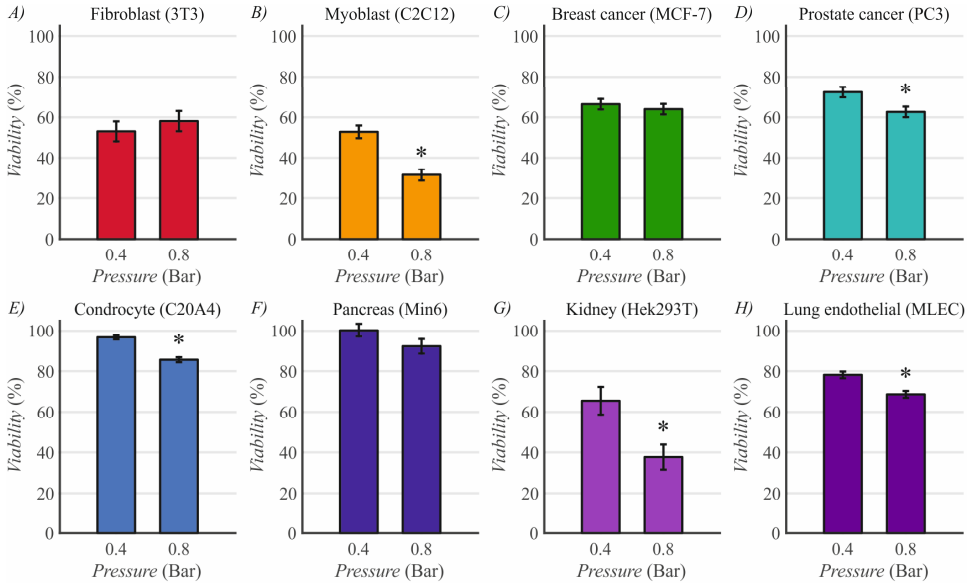

Figure 2: Cell viability after impact dependent on cell line. A-H) the viability after impact at 0.4 and 0.8 Bar air pressure is shown for the cell lines 3T3 (A), C2C12 (B), MCF-7 (C), PC3 (D), C20A4 (E), Min6 (F), Hek293T (G) and MLEC (H). Error bars depict the standard error of the mean. Asterisks show significance ($p<0.01$).

From figure 2 it can be seen that the viability after spraying varies between 50% and 90% between the different cell lines at low pressures and even further significantly deteriorates when the pressure is increased up to 0.8bar. Viability at 0.8 bar is only 30% in C2C12 cells, 60% in 3T3s and over 90% in Min6 cells. This is a very large variation that will have significant impact on designing bioprinting applications for a specific cell type or a mixture of cell types. In addition, this indicates there are cell specific characteristics that govern the cell survival after cell spraying.

6.3.3 How cell characteristics influence cell survival

We have previously developed an analytical model to predict cell survival after droplet impact. This model describes the deformation of the outer droplets, the resulting deformation of the inner cell and predicts the resulting viability (for a detailed explanation, please refer to Hendriks et al.). The model predictions are based on the spray characteristics, but also on the cell characteristics. Three cellular characteristics were found to be of importance: cell size, cellular viscosity/stiffness and membrane strength. We hypothesize that these cellular properties are responsible for the observed differences in viability between the cell lines. To assess this, we first simulated the effect

of changing the cell characteristics for the 3T3 fibroblasts as a model system. The results are shown in figure 3.

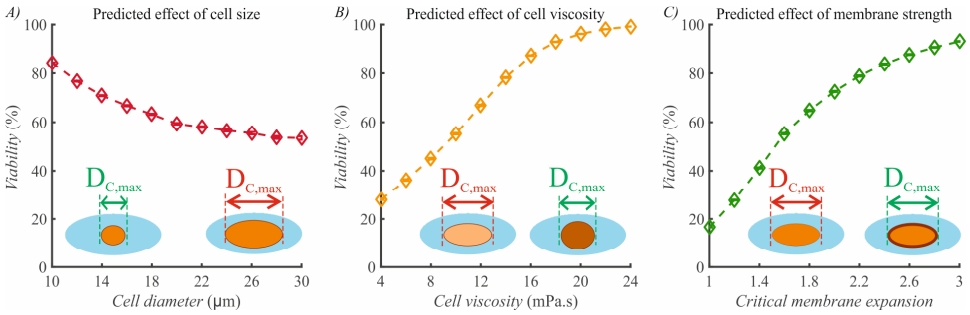

Figure 3: Model predictions for the effect of cell size (A), cell viscosity (B) and membrane strength on cell viability (C). Inserts show expected effect on cell deformation. Dc,max is the maximum deformation experienced by the cell. When Dc,max is shown in red, the deformation is harmful to the cells. 3T3 were used as a model system with standard model parameters: Size 18 µm, viscosity 12 mPa.s and critical membrane expansion of 1.6. Droplet input parameters were based on a spray with air pressure 0.4 bar: mean droplet size 22.5 µm, mean velocity 8.65 m/s.

The predictions from figure 3 demonstrate there can be a clear and significant effect of the cellular properties on the cell survival. By decreasing the size of 3T3 cells with unchanged droplet size, cell survival increases to 80%. In contrast cell enlargement decreased cell survival to below 60%. The increase in viability can be explained by a relatively larger cushioning effect of the external droplet. Adjusting cell viscosity/stiffness or membrane strength gives even larger possible variations from 20% to 100% survival. Higher cell viscosity/stiffness is protective as this results in reduced deformation relative to the outer droplet. By increasing membrane strength also 100% cell survival can be achieved in the model. The larger membrane strength is protective by increasing the maximal deformation before rupture occurs. These large predicted effects inspired us to see if we could achieve these improvements in viability after spraying by actively adjusting the cellular properties. We therefore proceeded to alter the cell size, cell stiffness and membrane strength of our 3T3 model system and assessed the influence of cell viability.

6.3.4 Influence of cell size on cell viability post impact

The cell size of 3T3 fibroblasts was altered by incubation cells in buffers with different osmolarities to assess the influence of the cell size on the viability after impact (figure 4).

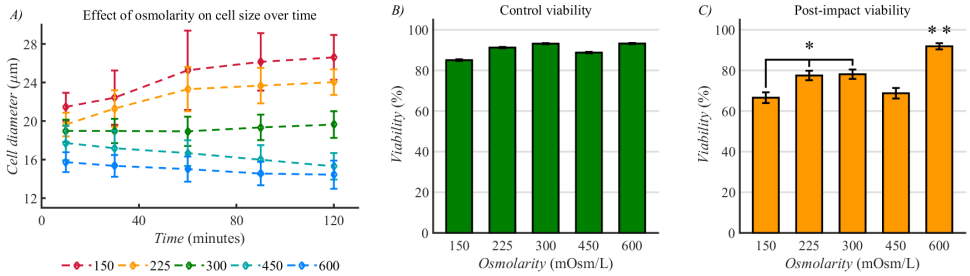

Figure 4: The influence of cell size on cell viability post-impact. A) 3T3 fibroblasts were incubated in buffers with different osmolarities (150, 225, 300, 450 and 600 mOsm/L) and the effect on cell size was measured. B) The viability of 3T3 fibroblasts after incubation with the osmolarity buffers in the impact experiment without external applied air pressure. Error bars depict standard error. C) The viability post-impact after incubation with the osmolarity buffers. The viabilities were corrected for their respective controls. The spray experiments were performed with a flow rate of 2.4 ml/min and a pressure of 0.4 Bar. Asterisks depict significance (* $p<0.05$, ** $p<0.001$)

Figure 4 shows the effect of the size cell on the cell viability. It can be seen in figure 4A that the incubation in buffers with different osmolarities leads to a broad range of cell sizes. The 3T3 are 18 μm in diameter under isotonic conditions (300 mOsm/L), swell to 28 μm under hypotonic conditions (150 mOsm/L) and shrink to 14 μm in hypertonic conditions (600 mOsm/L). The majority of swelling/shrinkage occurs within the first 10 minutes, but continues for at least one hour. The swelling and shrinkage at all osmolarity buffers is well tolerated with viabilities above 80% and no general trend visible (Figure 4b). When the cells are sprayed in their osmolarity buffers there seems to be a trend towards a higher viability at increasing osmolarity and thus decreasing cell size (Figure 4C). This difference is especially clear when comparing the highest osmolarity (92% viable) and the lowest osmolarity (67% viable). The data show a significant difference between 150 mOsm/L and both 225 and 300 mOsm/L and a strong significant differences between 600 mOsm/L and the other conditions. Remarkably, although cell size also shrinks using a hypertonic buffer of 450 mOsm/L, this did not have a significantly positive impact on cell survival. When we compare these results with the model prediction, we can see that the same trend is followed. However the effect at highest osmolarity is stronger than expected from cell size alone. Furthermore, the absence of a positive effect using the intermediate hypertonic buffer might indicate that additional factors than cell size play a role in the protective effect. Substantiating this, we found no correlation when we compared cell size from figure 2 to survival (supplemental figure 2). It is possible that the increased viscosity upon cell shrinkage might be responsible for the beneficial effect.

6.3.5 Influence of cellular stiffness and membrane strength on cell viability post-impact

We subsequently looked at the effect of the cell stiffness and membrane strength on the cell viability post impact. To achieve this, we adjusted the cholesterol content of the membrane by depletion or enrichment experiments It is expected from literature that a depletion of cholesterol from the membrane will improve the attachment of the cell membrane to the cytoskeleton and thereby improve the cell stiffness [18]. An enhancement of the cholesterol content however is not expected to influence the cell stiffness, but is expected to increase the strength of the cell membrane itself. The results for the cholesterol depletion and enhancement are shown in figure 5.

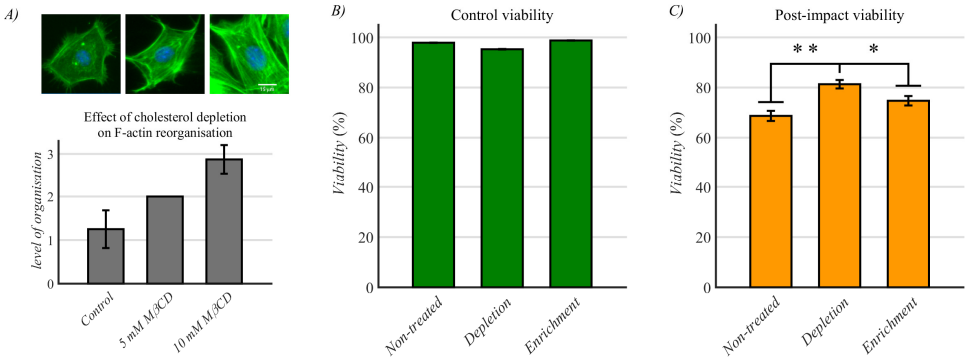

Figure 5: Effect of cholesterol depletion or enhancement on the post-impact viability. A) The depletion of cholesterol by methyl-β-cyclodextrin (MβCD) leads to a more organized F-actin cytoskeleton depending on the MβCD concentration (green: phaloidin, blue: DAPI). B) The effect of incubation with MβCD on F-actin organization was scored by two blinded observers. 1 = weak organization, 2 = medium organization, 3 = strong organization. C) The effect of cholesterol depletion or enhancement on cell viability in the impact experiment without external applied pressure is depicted. D) The viability after spray impact is shown, control corrected, for cells that were untreated, depleted from cholesterol or enriched with cholesterol. The spray experiments were performed with a flow rate of 2.4 ml/min and a pressure of 0.4 Bar. Asterisks depict significance (* $p<0.05$, ** $p<0.001$)

It can be seen from figure 5A that the depletion of cholesterol has a clear effect on the F-actin organization and thus on the cell stiffness as was expected from literature. The effect was scored by two blinded observers (figure 5B) which shows that the level of organization increased from weak (1.3) to strong (2.9). Depletion or enrichment of the cell membrane with cholesterol had only a minor effect on the viability of the incubated cells (figure 5C: viability untreated 98%, depletion 95% and enrichment 99%). The post-impact viability did show an influence of the treatments. The viability of both membrane depletion of as enrichment with cholesterol showed an improved viability compared to the control. The improvement of cell viability by depletion of cholesterol (+13%) is significant ($p<0.001$) and larger than the improvement by enrichment (+6%) which is not significant ($p=0.09$). This could indicate that for this cell type it is more beneficial to improve the cell stiffness than the membrane strength. This is in part confirmed by experiments in which the temperature at which the cell spraying was performed was varied. Temperature has an established effect on membrane strength. This had no effect

on cell survival (supplemental figure 3). Interestingly, we performed similar experiments with C20A4 chondrocytes by depleting and enriching the cholesterol content. These cells showed no benefit from cholesterol depletion, but did show a marked increase in viability after cholesterol enrichment (supplemental figure 4). This indicates that the effect of cholesterol alteration on post-impact viability is likely dependent on the cell type. The effect may possibly depend on the amount of physiological cholesterol in the membrane or the normal cell stiffness.

6.4 Discussion

Bioprinting of cells is complicated by a trade-off between printability, resolution and throughput on one hand and the cell viability on the other. This trade-off significantly limits the further development of the bioprinting field. For a successful print, this trade-off should be optimized to achieve good printing parameters and cell viability. When more complex tissues are printed, especially with a view on organ printing, multiple cell types are involved. It is unlikely that a single parameter set will result in optimal viability for all cell types that can be used. The response of different cell types to the bioprinting process is, however, relatively unexplored.

We have used a droplet based printing method (cell spraying) to evaluate the influence of the printing process on the cell viability of eight different cell lines. In the experiments we were able to collect a single layer of droplets on a glass surface. This enabled us to purely evaluate the effect of droplet impact on a surface. Previously we have shown that in this set up shear stress in the nozzle is neglectable [8]. The velocity of the droplets could be controlled via the air pressure, thereby influencing deformation and thus cell damage.

We show there is a strong difference in cell viability between various cell lines at both low and high pressure. The viability at high pressure ranged between 31 % for myoblasts (C2C12) up to 85 % for the chondrocytes (C20A4). This difference observed in cell lines should be repeated using primary cells, but it indicates that there is a strong difference in resilience to deformation damage depending on the cell type.

The high viability of the chondrocytes after printing was expected, since chondrocytes normally reside in a highly challenging mechanical environment and consequently have developed adaptive mechanisms to cope with these forces. This is confirmed in other literature [19]. Similar high tolerance for impact was shown for the pancreatic epithelial cells (Min6) with 92% viability at high pressure. This confirms the findings by Roberts et al. that epithelial cells and chondrocytes have similar viabilities after cell deposition [20]. The lung endothelial cells also show a good resilience to the cell spray process with 70% viability at 0.8 Bar. This can potentially be explained by the high shear stresses that these cells have to endure in their natural mechanical environment.

The two organ cancer cells lines show similar viabilities at 0.8 bar (64% for breast cancer MCF-7 and 63% in prostate cancer PC3), but higher viabilities than the cells

derived from embryonic tissue such as Hek293T cells (38% survival). This is interesting as it is shown in several cancer cell lines [21], including MCF-7 [22], that stiffness reduces with progression of malignancy. This would result in increased susceptibility for cell deformation and consequently a reduced viability with increasing shear stress during impact. It is possible however that the embryonic kidney cells are not fully matured and therefore also more vulnerable.

The fibroblast cell line shows average resilience to deformation by achieving a 60% viability at low pressure, but also at high pressure. It is unclear why the overall viability of the 3T3 cells did not decrease with increased droplet velocity in these experiments (although the number of damaged cells does increase), but the viabilities measured here at low pressure closely resemble those of earlier spray experiments [8].

The low viability of the myoblasts is more surprising at first glance considering the mechanical environment in muscle tissue. However, this result might be explained by the undifferentiated state of these muscle precursor cells, likely increasing their vulnerability. This is substantiated by the low viability of mesenchymal stem cells after cell spraying [19] and especially the vulnerability of embryonic stem cells . Therefore it would be interesting to test mature muscle cells in future experiments.

The differences in viability between the cell-types could potentially be caused by many cell specific parameters. Of these the cell stiffness, the cell size, membrane strength and the the cell's intrinsic capacity to repair membrane damage could play an important role.

In previous work, we have developed an analytical model predicting the cell viability after impact. This model combined three processes: pure cell deformation, effect of the outer droplet and the translation between deformation and viability. In this model we identified three parameters that are governed by the cells: Cell size, cell viscosity and membrane strength.

The cell size is important, as the cell to droplet ratio determines the cushioning effect. A larger outer droplet compared to the cell provides more cushioning and therefore results in higher viabilities. Similarly, a smaller cell in the same droplet experiences more cushioning and is therefore expected to have a larger viability. However, when we compared the native cell size of the 8 different cell lines to the cell viability, we found no significant correlation. When the cell size was strongly reduced using a hypertonic buffer cell survival somewhat improved. However a clear dose-relationship was lacking suggesting that additional parameters might play a role. For example, decreasing cell size by extracting water using hypertonic buffers will increase the viscosity of the cytoplasm.

The cell viscosity is the second cell specific parameter. The higher the viscosity of the cell, compared to the droplet, the smaller the deformation and the larger its resistance to shear stress. As, the cell is not a Newtonian fluid, this viscosity is a measure for the cell deformability. In reality, this parameter is governed by a complex interplay of both the cell viscosity and the cytoskeleton.

The third parameter is the membrane strength. The membrane strength determines the strain at which the membrane ruptures. And thus when the cells undergo injury. This parameter is dependent on the components of the cell membrane (the lipid content and protein content), the underlying cortical cytoskeleton and their interaction.

We wanted to test further whether these parameters governed the differences in cell viability between the cell types. Therefore, we adjusted these parameters in a single cell type (3T3 fibroblasts) and assessed the influence. We used three approaches to achieve this: Adjust the osmolarity, change the temperature or alter the cholesterol content.

We adjusted the osmolarity of the cell spray buffers to change the size of the fibroblasts. By incubating the cells in buffers ranging from 150 to 600 mOsm/L, we could acquire a range of cell sizes from 14 µm in hyper-osmolarity to 28 µm in hypo-osmolarity, while the original cell size was 18 µm. This indicates that the cells could swell two-fold in size and eight-fold in volume from smallest to largest state. These reactions to the osmolarity had no effect on the cell viability up to at least four hours after incubation. However, after cell impact there seemed to be a trend in increasing viability with increasing osmolarity. This trend is similar to what was expected from the model and indicates that smaller cells are more resilient to strain. The effect is especially clear between the two extremes, the hyper-osmolarity (93%) and hypo-osmolarity (66%). Shrinking 3T3 cell size using pre-treatment with a hyperosmotic buffer can thus increase the resilience to shear stress up to levels seen in chondrocytes which are adapted to deal with higher shear stress. The viability after cell shrinkage is even higher than expected from the cell size alone. It is possible that the increase in viscosity resulting from cell shrinkage results in reduced deformation which may contribute to the cell's resilience [23].

In general, changing the osmolarity is an easy method to reduce the cell size. This allows for smaller droplets, potentially increasing printing resolution and especially at larger osmolarities results in improved resilience to shear stress with higher cell survival.

We subsequently altered the temperature of the spraying experiments to assess the influence of the membrane fluidity on the cell viability. The membrane fluidity is known to be dependent on the temperature [24]. A lower temperature increases membrane viscosity and is therefore expected to result in higher cell survival after spraying. However, both the decrease in temperature (4 °C) and an increase in temperature (37 °C) had no observable effect on cell survival. This result correlates well with the findings from Takamatsu et al [25] . They showed that there was no difference in cell survival after deformation at 0 °C, or 23 °C. This might indicate that the fluidity of the membrane is not a highly influential parameter in determining the cell's resilience to shear stress [25]. This is substantiated by work from Tan et al. where they describe that protein content of the membrane and their interaction with the cytoskeleton are the dominant factors determining the cell's resilience to injury [15].

Finally, we both depleted and enhanced the cholesterol content of the 3T3 fibroblasts. According to literature the depletion of cholesterol results in a reduction of lipid rafts

and leads to increase in attachment to the cytoskeleton [18, 26]. This results in a reorganization of f-actin and in an overall improvement of the cell stiffness [18]. This was tested in fibroblasts and it was shown that the bending modulus improved from 0.18 to 0.25 pN.μM [27]. Enrichment with cholesterol on the other hand is expected to have minor effects on the cell stiffness, but can improve the membrane strength [15, 18] and reparative capacity [10]. Therefore both depletion and enrichment could potentially be beneficial for cell survival.

We depleted or enhanced cholesterol using MβCD, which is shown to be most effective for this purpose [27]. After cholesterol depletion, we observed a reorganization of F-actin as expected. This effect was dependent on the concentration of MβCD and thus the amount of depleted cholesterol, which is roughly 80% depletion at 5 mM and 85% depletion at 10 mM MβCD [27, 28]. Both the depletion and enrichment of cholesterol had no marked effect on the cell viability of the 3T3 cells. However, after cell spraying both depletion and enrichment showed an improvement in cell survival. The largest effect was demonstrated by the depletion of cholesterol. This increased the viability significantly from 69% to 81%, effectively improving the viability of 3T3s to the level of lung endothelial cells. This indicates that the reorganization of F-actin resulted in a stronger resilience of the fibroblast to the deformation caused by droplet impact. This effect is likely mediated via the increased cell stiffness as was predicted in our model. The enrichment with cholesterol also increased the cell viability, albeit slightly smaller (69% to 74%) and not significantly. This could indicate that the improved stiffness of the membrane, in combination with the increased reparative capacity additionally has a beneficial effect on the cell survival.

Interestingly, where the depletion of cholesterol resulted in improved cell viability in fibroblasts, it reduced the cell viability in chondrocytes. In contrast the enrichment did improve the cell viability in both cell types. This indicates that the role of cholesterol in cell stiffness might be cell type dependent. This is substantiated by the work of Taglieri et al., where they describe a differential role of cholesterol in cell stiffness depending on cell type. While some cell types, such as fibroblast and β-cells, increase the attachment to the cytoskeleton upon cholesterol depletion, other cells such as the HEK293 cell increase cytoskeletal attachment upon cholesterol enrichment [29]. These observations suggest that cell survival after droplet based cell deposition can be tuned by adapting the cholesterol content of the plasma membrane in a cell type dependent manner.

The cholesterol alteration of 3T3 resulted in improved cell viability after cell impact and therefore provides evidence that improving cell stiffness or membrane strength might be a good strategy to increase cell survival in bioprinting. However, as the cholesterol content is important in cell function and in cell signalling [28], altering this content might have serious side effects. In our experiments, we did not focus on these effects as we were interested primarily in what determines the cell viability. Nonetheless, this should be carefully considered before applying this strategy in bioprinting applications. For example, the cholesterol content could be restored after printing to avoid unfavourable effects [28].

Our results show that cell survival in bioprinting is largely cell type dependent. Therefore, it is essential the bioprinting parameters are optimized for each cell type individually. When vulnerable cell types are applied, this places serious constrains on the printing parameters, such as printability, throughput and resolution. Improving the resilience of vulnerable cells could be a potent strategy to reduce the difference between cell types and increase the available printing parameter space. From our results, especially applying hyper-osmolarity buffers seems an easy method to acquire larger resilience in otherwise fragile cells. The effect is reversible and can be resolved by placing the cells in an isotonic buffer after printing restoring cell volume to normal. Depletion or supplementation of cholesterol can also improve the resilience, but this might have more side effects. Alternative methods for improving the cell stiffness or membrane strength should be considered. Additionally, improving the reparative capacity of the cells might be an as of yet unexplored strategy for increasing the resilience. Furthermore combining these approaches might provide synergistic effects that could allow cells to survive the harshest conditions. These strategies could break the deadlock holding back the bioprinting world and could help unleash its full potential.

6.5 Conclusion

The potential of bioprinting is limited by the trade-off between printing parameters and cell viability. Moreover, when printing complex tissues, such as organs, multiple cell types are required with a range of mechanical properties. However, the effect of the printing process on different cell types is not well understood. In this work we showed cell survival after impact is largely cell type dependent. We subsequently applied our analytical cell survival model and identified three cell specific parameter that could govern this difference and which are open for easy manipulation: the cell size, cell viscosity and membrane strength. We assessed this further by adjusting the osmolarity, temperature and cholesterol content with 3T3 fibroblasts. This showed that especially cell shrinkage and increase in cell stiffness could improve the cell viability after printing. These strategies could improve the resilience of especially vulnerable cells thereby increasing the parameter space available in bioprinting. Therefore, improving the cell specific survival could be a potent strategy to bring the bioprinting field one step further.

6.6 Supplementary information

6.6.1 Cell spray set-up

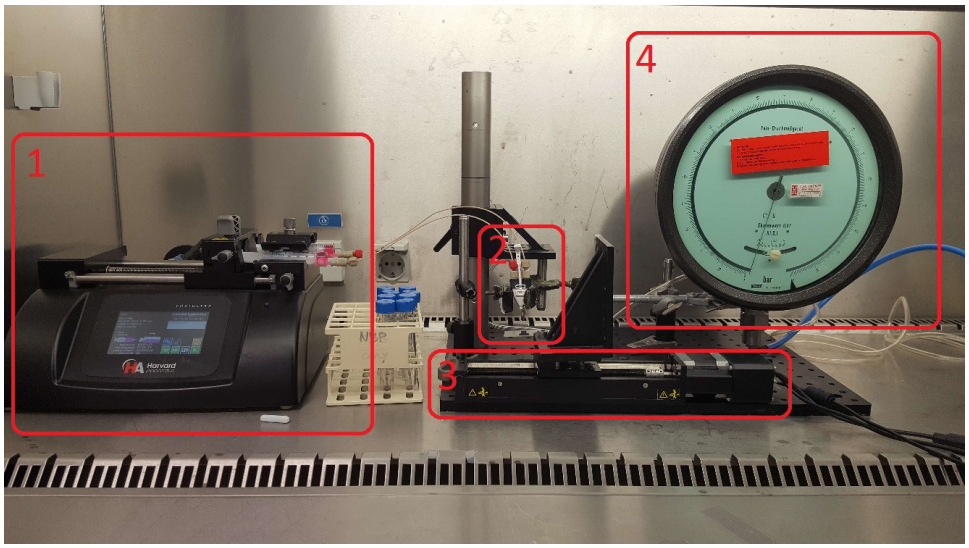

Figure S1: Spray impact set-up. The boxes with numbers indicate different compartments of the spray set up. 1: the pump with the syringes, 2: the nozzle with the microscope slide positioned under it, 3: the linear motor, 4: the pressure gauge.

6.6.2 Correlation between cell size and survival

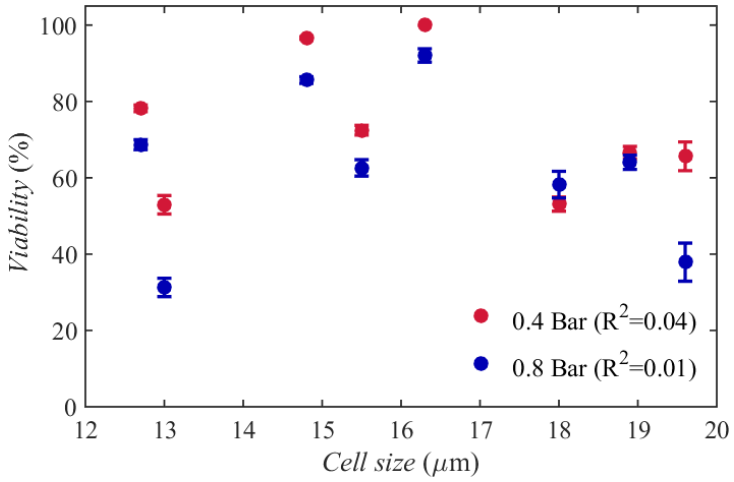

Figure S2: Correlation between cell size and survival. The figure shows the cell viability at 0.4 and 0.8 bar versus the cell size from the 8 different cell types. No correlation was found at both 0.4 bar (R^2=0.01) and 0.8 bar (R^2=0.04). This indicates that other cellular properties are more important than size to explain the observed difference in viability.

6.6.3 Influence of temperature on cell survival in cell spraying

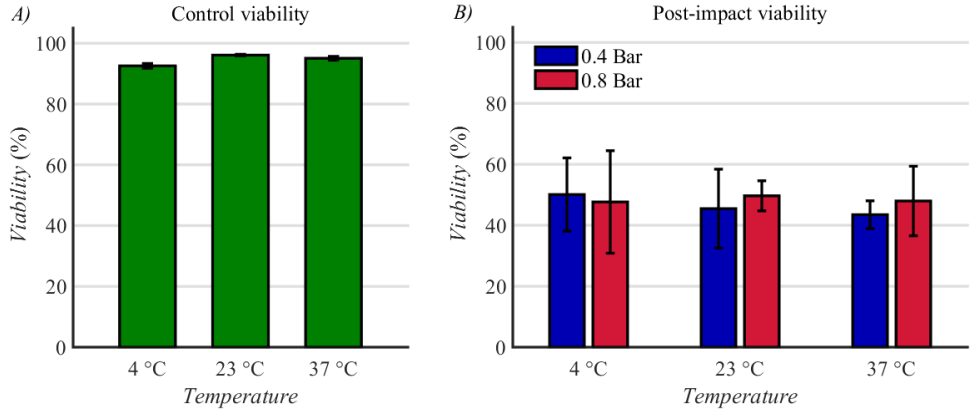

Figure S3: Influence of temperature on cell spraying with 3T3 fibroblasts. A) The influence of temperature on the cell viability of cells that were ejected without external pressure. The cell viability was generally high (>90%) and no influence of the temperature was observed. B) The cells were sprayed at 4 °C, 23 °C and 37 °C at 0.4 and 0.8 bar air pressure and the effect on viability was assessed. The results demonstrate there is no marked effect of temperature on viability at both low and high pressure, indicating a marginal role of membrane fluidity on cell survival.

6.6.4 Influence of cholesterol content on cell viability of C20A4

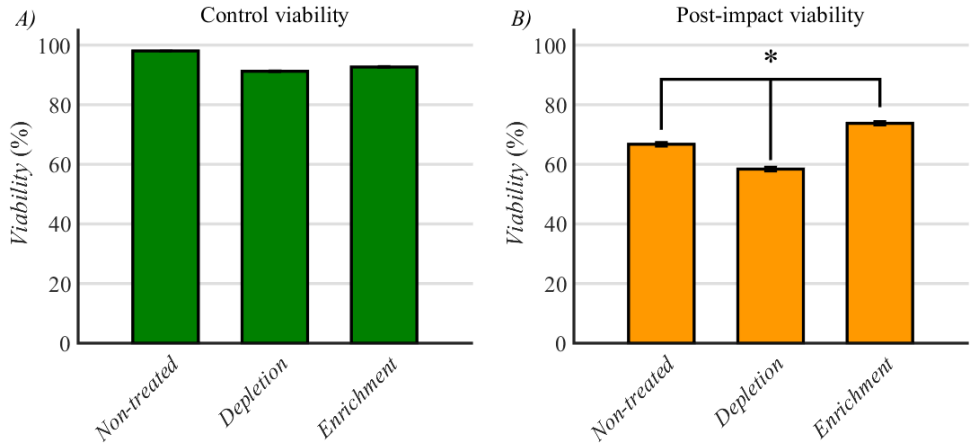

Figure S4: Influence of cholesterol content on cell viability of C20A4 cells. The cholesterol content of C20A4 cells was depleted or enriched with MβCD treatment and the effect of cell survival was assessed. A) The cholesterol depletion and enrichment had a slight, but significant influence of the cell viability when cell were ejected without external pressure. The viability of the cells decreased from 98% in untreated cells to 91% in the depleted cells. Error bars depict standard error. B) The control corrected post-impact viability is shown. The cholesterol treatment seemed to have a small influence on the cell viability after spraying. In contrast to 3T3 fibroblasts, the depletion of cholesterol seemed to negatively affect the viability (-8%), but similarly to 3T3s the enrichment improved the resilience of the cells (+7%). Both differences where significant ($p<0.001$). This indicates that the cholesterol treatment has a cell type specific effect.

References

1. Williams, D., et al., *A perspective on the physical, mechanical and biological specifications of bioinks and the development of functional tissues in 3D bioprinting.* Bioprinting, 2018. **9**: p. 19-36.
2. Murphy, S.V. and A. Atala, *3D bioprinting of tissues and organs.* Nature biotechnology, 2014. **32**(8): p. 773.
3. Haitao, C., et al., *3D Bioprinting for Organ Regeneration.* Advanced Healthcare Materials, 2017. **6**(1): p. 1601118.
4. Liliang, O., et al., *Effect of bioink properties on printability and cell viability for 3D bioplotting of embryonic stem cells.* Biofabrication, 2016. **8**(3): p. 035020.
5. Lepowsky, E., M. Muradoglu, and S. Tasoglu, *Towards preserving post-printing cell viability and improving the resolution: Past, present, and future of 3D bioprinting theory.* Bioprinting, 2018. **11**: p. e00034.
6. Kalyani, N.; Milind, G.; Saif, K.; Chang, Y. K.; Michele, M.; Kenneth, B.; Wei, S. Biotechnology Journal 2009, 4, 1168-1177.
7. Kalyani, N., et al., *Characterization of cell viability during bioprinting processes.* Biotechnology Journal, 2009. **4**(8): p. 1168-1177.
8. Hendriks, J., et al., *Optimizing cell viability in droplet-based cell deposition.* Scientific Reports, 2015. **5**: p. 11304.
9. Thiebes, A. L.; Albers, S.; Klopsch, C.; Jockenhoevel, S.; Cornelissen, C. G. BioResearch Open Access 2015, 4, 278-287.
10. Jimenez, A.J. and F. Perez, *Physico-chemical and biological considerations for membrane wound evolution and repair in animal cells.* Seminars in Cell & Developmental Biology, 2015. **45**: p. 2-9.
11. McNeil, P.L. and R.A. Steinhardt, *Loss, Restoration, and Maintenance of Plasma Membrane Integrity.* The Journal of Cell Biology, 1997. **137**(1): p. 1-4.
12. Abreu-Blanco, M.T., J.M. Verboon, and S.M. Parkhurst, *Single cell wound repair.* BioArchitecture, 2011. **1**(3): p. 114-121.
13. Gefen, A. and D. Weihs, *Cytoskeleton and plasma-membrane damage resulting from exposure to sustained deformations: A review of the mechanobiology of chronic wounds.* Medical Engineering & Physics, 2016. **38**(9): p. 828-833.
14. Barbee, K.A., *Mechanical Cell Injury.* Annals of the New York Academy of Sciences, 2006. **1066**(1): p. 67-84.
15. Tan, S.C.W., et al., *Rupture of plasma membrane under tension.* Journal of Biomechanics, 2011. **44**(7): p. 1361-1366.
16. Ayee, M.A. and I. Levitan, *Paradoxical impact of cholesterol on lipid packing and cell stiffness.* Front Biosci (Landmark Ed), 2016. **21**: p. 1245-1259.
17. Field, A., *Discovering Statistics Using IBM SPSS Statistics*. 4th Revised edition ed. 2013: Sage Publications Ltd. . 952.
18. Ayee, M.A. and I. Levitan *Paradoxical impact of cholesterol on lipid packing and cell stiffness*. Frontiers in bioscience (Landmark edition), 2016. **21**, 1245-1259 DOI: 10.2741/4454.
19. Dijkstra, K., et al., *Arthroscopic Airbrush-Assisted Cell Spraying for Cartilage Repair: Design, Development, and Characterization of Custom-Made Arthroscopic Spray Nozzles.* Tissue Engineering Part C: Methods, 2017. **23**(9): p. 505-515.
20. Andrew, R., W.B. E., and B. Lawrence, *Aerosol delivery of mammalian cells for tissue engineering.* Biotechnology and Bioengineering, 2005. **91**(7): p. 801-807.
21. Xu, W., et al., *Cell Stiffness Is a Biomarker of the Metastatic Potential of Ovarian Cancer Cells.* PLOS ONE, 2012. **7**(10): p. e46609.
22. Li, Q.S., et al., *AFM indentation study of breast cancer cells.* Biochemical and Biophysical Research Communications, 2008. **374**(4): p. 609-613.
23. Effros, R.M., R. Chang, and P. Silverman, *Effect of osmolality on red blood cell viscosity and transit through the lung.* Journal of Applied Physiology, 1977. **42**(6): p. 941-945.
24. Los, D.A. and N. Murata, *Membrane fluidity and its roles in the perception of environmental signals.* Biochimica et Biophysica Acta (BBA) - Biomembranes, 2004. **1666**(1): p. 142-157.
25. Takamatsu, H., et al., *On the mechanism of cell lysis by deformation.* Journal of Biomechanics, 2005. **38**(1): p. 117-124.

26. Sun, M., et al., *The effect of cellular cholesterol on membrane-cytoskeleton adhesion.* Journal of Cell Science, 2007. **120**(13): p. 2223-2231.
27. Hissa, B., et al., *Membrane Cholesterol Removal Changes Mechanical Properties of Cells and Induces Secretion of a Specific Pool of Lysosomes.* PLOS ONE, 2013. **8**(12): p. e82988.
28. Gimpl, G., K. Burger, and F. Fahrenholz, *Cholesterol as Modulator of Receptor Function.* Biochemistry, 1997. **36**(36): p. 10959-10974.
29. Taglieri, D., D. Delfín, and M. Monasky, *Cholesterol regulation of PIP2: why cell type is so important.* Frontiers in Physiology, 2013. **3**(492).

6

“A droplet of wisdom can cause a ripple in the sea”

“I may not have gone where I intended to go, but I think I have ended up where I needed to be.”

7

Cell viability in bioprinting depends on the droplet: A new model predicts influence of size and velocity

The large potential of bioprinting is frustrated by the trade-off between optimal printing properties and cell viability. However, the exact influence of these printing properties on cell viability remains to be elucidated. In previous work, we have developed an analytical model to predict the viability in droplet based cell deposition based on droplet parameters and printing surface. This model accurately predicts cell viability in cell deposition using a polydisperse spray. However whether this model holds with monodisperse bigger droplets such as commonly used in inkjet printing remains unknown. In this work, we have developed a new set-up to create monodisperse droplets of custom size that can impact on a surface at well-defined velocity. Using this set-up we have investigated the effect of droplet parameters on cell viability post-impact. We have shown that the droplet velocity at impact is a major contributor to cell death. Unexpectedly increasing droplet size without altering droplet impact velocity decreased cell viability. Our data show a strong relationship between the droplet weber number and cell viability post-impact. This relationship holds when we compare our data with cell-spray data from the field. We subsequently updated our analytical model to better capture the influence of the droplet size. This improved model can help to further optimize bioprinting properties, while retaining high cell viabilities.

Jan Hendriks[1], Claas Willem Visser[2], Daniël B.F. Saris[3,4] & Marcel Karperien[1]

1 Department of Developmental BioEngineering, TechMed institute, University of Twente, The Netherlands.

2 Physics of Fluids Group, TechMed institute, Faculty of Science and Technology, University of Twente, The Netherlands.

3 Department of Orthopedics, UMC Utrecht, The Netherlands.

4 Department of Reconstructive Medicine, TechMed institute, Faculty of Science and Technology, University of Twente, The Netherlands.

Manuscript in preparation

7.1 Introduction

Bioprinting is a rapidly growing field of research that combines cells, materials and biofabrication technologies to create functional tissue. The technology can be used for disease modelling, tissue engineering and potentially for fully mature organs. While there is undoubtedly a large potential to the technology, the trade-offs between optimal cell survival and printing parameters still pose a significant challenge [1]. An optimal bioprinting technology should combine high resolution and high throughput printers with biomaterials with large shape fidelity and bioactivity, while additionally maintaining a high viability of the printed cells [2].

There are many biofrabrication technologies available for bioprinting, of which bioplotting and droplet based deposition methods are most popular. Bioplotting is based on extrusion of fibre filaments of biomaterials containing cells to create three dimensional structures. The method has a high throughput, a large variety in bioinks and is relatively cheap. However, the resolution is limited and the high shear rate rapidly leads to a reduced cell viability[3]. Additionally, while the resolution can be improved with biomaterials of higher shape fidelity, the resulting increased shear stress possess an additional strain on cell survival [4, 5]. The droplet based deposition method originates from inkjet printing and has many advantages. It is relatively inexpensive, highly versatile and can print tissues with high resolution. However, the throughput is limited, only low viscosity bioinks can be used and clogging issues put a restrain on cell concentrations. Unfortunately, the desired increase in throughput and viscosity results in higher shear stress that leads to a reduced cell viability [4].

This underscores a significant challenge in improving biofrabrication technologies, while retaining sufficient cell survival. To achieve this a better understanding of the parameters in bioprinting that govern cell survival is essential. Several studies evaluated the relationship between printing parameters and cell viability [6]. Most papers evaluated bioplotting technologies and generally found a strong link between shear stress and cell viability [3, 5, 7]. Less work has focussed on the effect of droplet parameters on cell viability in droplet deposition methods. In our previous work, we analysed cell survival in cell spraying and assessed the influence of the droplet impact on the viability [8]. We developed and validated an analytical model that revealed a strong relationship between droplet size, velocity and viscosity, and printing distance on the cell viability. While this work has improved insight into how bioprinting processes influence cell viability, the model still possessed several limitations. Particularly the predictions of our model with respect of relationship between shear stress and cell viability deviated from reported data in literature. Additionally, the relationship between droplet size and velocity and cell viability was experimentally determined using a polydisperse spray which has several drawbacks. This could be improved by using cell laden monodisperse droplet trains.

In this work we have developed a new method to measure the effect of droplet based cell deposition on cell viability in a controlled and reproducible manner. We achieve this by evaluating the impact of cell containing droplets on a surface with fully controlled

droplet size, impact velocity and viscosity. Our set-up creates monodisperse droplets at high throughput, with a size that can be fully controlled. The impact velocity is decoupled from the droplet velocity to be able to specifically study the effect of shear stresses at impact. This is achieved by using a rotating motor to impact a surface to the droplet train with specified velocity. By applying this method we investigated the relationship between droplet size and velocity with cell viability. Subsequently, we improved our analytical model to better predict cell survival during bioprinting. This improved understanding of cell viability in printing processes can help to further optimize biofabrication technology and bring the field one step further.

7.2 Materials and Methods

7.2.1 Cell culture

NIH 3T3 fibroblasts were used as model cells to assess the influence of droplet parameters on cell viability and allow for comparisons with our previous work involving fibroblasts survival in droplet based deposition using a polydisperse spray [8]. The cells were cultured in DMEM (Gibco REF: 41965039), supplemented with 10% FBS (Gibco REF 10279-106) and 1% pen/strep (Gibco cat 15140) at 37 °C and 5% CO_2. The cells were seeded at a density of 2000 cells / cm^2 and 1.4 µl/ml β-mercaptoethanol was added freshly to newly seeded flasks. This allows for the scavenging of free radicals and ensured better cell survival.

To determine the influence of droplet parameters on cell viability, the cells were harvested at 60-90% confluence using 0.25% trypsin-EDTA (Gibco ref 25200-072). The resulting suspension was counted, centrifuged for 3 min at 300G, washed twice with PBS (Lonza, ref: 17-516F) and resuspended in impact medium. Impact medium consisted of DMEM with 1% pen/strep, but lacked FBS. This mitigated the influence of FBS on surface tension and created a well-defined droplet impact. The cells were used at a concentration of 100.000 cells/ml in both the experiments for the 50 µm and the 100 µm nozzle. Before each impact experiment the cells were filtered through a 40 µm cell strainer to obtain single cell suspensions.

7.2.2 Set-up

To investigate the influence of droplet parameters on cell viability in bioprinting, we developed a custom set-up that enables highly controllable impact (figure 1). The set-up has two main components: a monodisperse droplet train generator and a controllable impact stage. To produce the droplet train, a syringe pump (PhD 2000 ultra) was used to achieve constant fluid flow through a micrometer nozzle (Smans) creating a jet. The flow rate was dependent on the nozzle size and was set to 0.6 ml/min for 50 µm nozzle and 1.8 ml/min for 100 µm nozzle. These flow rates enabled relatively similar flow velocities (5.8 m/s for 50 µm and 4.8 m/s for 100 µm), while maintaining capacity for monodispersity. The nozzles were placed in a custom-made aluminium holder containing four piezo elements (6,3 kHz Farnell ref 7BB-20-6L0). The piezo elements

were actuated with a function generator (HP 3310B) to create sinusoidal perturbations in the droplet train. These perturbations led to a controlled break-up resulting in a monodisperse droplet train. The size of the droplets was dependent on the nozzle size, flow velocity and the actuation wavelength and can be calculated using eq. 1 [9].

$$r_{droplet} = \left(\frac{3r_{jet}^2 v_{jet}\lambda}{4}\right)^{1/3} \quad (1)$$

In this equation $r_{droplet}$ is the radius of the droplet, r_{jet} is the radius of the jet, v_{jet} is the fluid velocity, and λ is the wavelength of the acoustic actuation.

Altering the droplet velocity of the jet led to a change in droplet size, at same actuation frequency, and to an increase in shear stress at the nozzle. Therefore v_{jet} was not a suitable parameter to investigate the effect of droplet velocity on viability after impact on a surface. We therefore decoupled the impact velocity from the droplet velocity to independently control the droplet size and impact velocity. We achieved this by attaching our impact surfaces (microscope slides) on a rotation motor with freely adjustable angular velocity. The rotating motor (sm34165dtde, ve: 5.03.40) was controlled with a Smart Motor Interface (version 3.3.11.152, 12-3-2010). Using this motor, the microscope slides were rotated unto a monodisperse droplet train with chosen velocity to create a well-defined impact event. The impact velocity can be freely chosen and can reach up-to 20 m/s.

In this experimental set up, the impact event has a horizontal (v_{jet}) and a vertical component (v_{motor}). To reduce the horizontal component by half, the jet is placed at a 45 ° angle. This ensured that the majority of impact velocity was determined by the rotating motor and that impact was perpendicular to the surface. Additionally, this reduced rolling of droplets that was observed in initial experiments. This rolling resulted in reduced cell count and therefore reduced reliability. To further reduce the rolling of cells, we coated the collecting microscope slides with poly-lysine.

To enable multiple lines of impact with the same droplet train, the nozzle was placed on a linear motor (Zaber TLSQ150B), controlled by ZaberConsole (version 25-10-17), that was synched to the rotation motor. In this way, the monodisperse droplet train moved parallel to the microscope slides in between each impact line. This enabled clean impact events of droplets on dry glass in multiple lines in the length of the microscope slide. This increased the amount of cells that were measured and improved the reliability of the cell viability measurements.

7.2.3 Characterization of monodisperse droplet train

The droplet size in the droplet train can be manipulated by varying the nozzle size and by altering the actuation frequency. The effect on droplet size and monodispersity was evaluated using water and impact medium. To achieve this, the droplet train was illuminated with a schott light source and imaged with a high speed camera (Photron APX-RS) with a frame rate of 5000 fps. The droplet train was imaged at the same distance from nozzle as the impact event (3 cm). In these experiments two nozzles were tested

(50 µm or 100 µm) and an actuation frequency of 3 to 8 kHz was applied. The resulting images were analysed with a custom made Matlab script that automatically detected the droplets. The script determined droplet size, distribution and inter-droplet distance.

Subsequently cells were added at 100.000 cells/ml or 800.000 cells/ml and the effect on droplet size, monodispersity and inter-droplet distance was evaluated.

7.2.4 Influence of droplet size and velocity on cell viability

The effect of droplet parameters on cell viability after impact on a surface was analysed. In these experiments 50 µm and 100 µm nozzles were used with actuation frequencies of 6.4 kHz and 7 kHz respectively, resulting in droplet sizes of 156 and 204 µm in diameter. When cells at a concentration of 100.000cells/ml were added, these frequencies resulted in the most stable monodisperse droplet trains.

The impact velocity is determined in part by the velocity of the jet and by the velocity of the rotation motor and can calculated by equation 2.

$$V_{impact} = V_{rotation} + V_{jet} * \cos(45) \quad (2)$$

In these experiments V_{impact} was kept constant by adjusting $V_{rotation}$. This enabled direct comparison of both nozzles with different v_{jet}.

A typical impact experiment was performed as follows. The cell suspension in the nozzle was homogenized using a magnetic stirrer. The jet was initiated and after it was stabilized the function generator was activated to actuate the droplet train and create a monodisperse droplet train. Subsequently, both the linear motor and the rotation motors were activated at their respective velocities to create impact events on the microscope slides. On these microscope slides an impact zone of 30 by 15 mm was created of which the circumference was defined by a superhydrophobic coating applied with a swab to create a reproducible impact area. After the impact events 300 µl of impact medium was added to these impact zones to avoid dehydration of the freshly impacted droplets.

As a control, the jet was collected in a 50 ml greiner tube containing a layer of impact medium. These droplets have passed through the nozzle and thus underwent the shear stresses at the nozzle, but did not undergo an impact event.

7.2.5 Live dead measurements

A live dead assay was performed to determine the viability after the impact experiments. In this assay Calcein AM (Sigma) is reduced by live cells to Calcein which stains brightly green while Ethidium Homodimer (Sigma) can only enter cells and stain nuclei after membrane damage. In this assay cells can be stained only green (Live), red (Dead) or a combination of both (Live, but with damaged membrane). As previous results have shown that the latter cells can recover, these damaged cells were counted as alive [8]. To stain the cells, 30 µl 10X live dead solution was added to the microscope slides. The slides with 2 µM Calcein AM and 4 µM Ethidium Homodimer were incubated

at 37 °C and 5% CO_2 for 30 min. Images were taken with the EVOS FL Color Imaging System using the GFP (Excitation: 470/22 nm, Emission 510/42 nm) and the Texas red (Excitation: 585/29 nm, Emission: 624/40 nm) filter cubes. The conditions were imaged in randomized order to avoid time bias in the experiments. The last images were taken within two hours after incubation. The stained cells in the images were counted with a home-made Matlab script. Briefly, this script automatically enhanced the contrast of the image, counts circles and determines double stained cells. The contrast thresholds are equal over all conditions to avoid observer bias. The scripts are available upon request.

7.3 Results

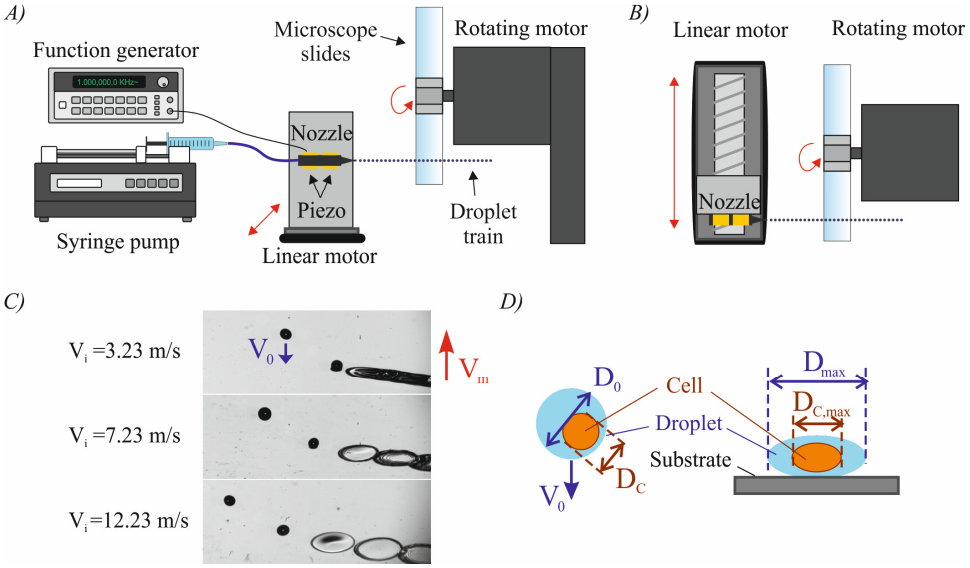

Figure 1: controlled droplet impact set-up. A) side-view of the droplet impact set-up. A syringe pump creates a jet through a micrometre nozzle. This nozzle is actuated via piezo elements to create a monodisperse droplet train. These droplets can impact on a microscope slide with an impact velocity determined by a rotating motor. B) Top view of the moving parts of the impact set-up. A linear motor can move the nozzle parallel to the rotating motor to create multiple lines of impact droplets on dry glass. C) The droplet train is place under 45 ° angle to reduce the horizontal velocity component of the jet. High-speed camera images are shown of micro droplet impact (204 µm in diameter) at three velocities of the rotating motor (V_i = combined velocity of motor (V_m) and droplet (V_o)). D) Schematic representation of compound impact of a cell in a droplet. The cell deforms depending on D_o and V_i resulting in a $D_{c,max}/D_c$. The magnitude of deformation determines the cell viability.

The set-up for controllable impact of droplets is shown in figure 1. Using this set-up we were able to create well defined monodisperse droplets and created impact events with freely chosen velocities. This enabled us to directly and reproducibly study the effect of droplet parameters on the viability of cells after impact.

The set-up consists of two main components, a monodisperse droplet train and an independently controlled impact stage. We first characterized the monodisperse droplet train via high speed camera analysis(figure 2).

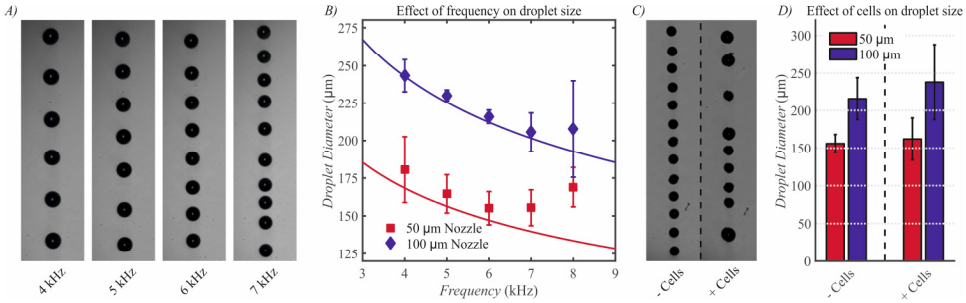

Figure 2: Characterization of monodisperse droplet train. A) High speed camera images of the droplet train at 4, 5 ,6 and 7 kHz actuation frequency with a 100 µm nozzle. B) The effect of the actuation frequency on droplet diameter is shown for a 50 and 100 µm orifice nozzle. The lines show the expected droplet sizes for theory. C) High speed camera image showing the effect of adding cells at 100.000 cells/ml to the droplet train. D) Influence of adding cells to the average droplet size and variation.

Figure 2A demonstrates the monodispersity of the droplet train, when actuated via piezo elements. It can be seen that the droplet size and inter-droplet distance was dependent on the actuation frequency, with a higher frequency leading to smaller and more closely packed droplets. This was quantified in figure 2B where both a 50 µm and a 100 µm nozzle were actuated at a range of frequencies. The increase in frequency resulted in a reduction in droplet size and followed the theoretical predictions. With our actuation system there was a maximum stable frequency of 7 kHz. With these two nozzles this provided a freedom to create monodisperse droplets with a diameter between 260 and 150 µm. Smaller or larger nozzles could increase this range. We subsequently added cells to the actuated solutions and assessed the influence on the droplet train. Figure 3C shows that adding cells led to the creation of a subset of droplets with larger diameter. Analysis of droplet volume showed that these droplets are created by a fusion of two standard monodisperse droplets in mid-air (Figure S1 and S2). Quantification of the droplets however showed that this had no significant effect on the average droplet size (Figure 2D), nor on droplet distribution (Figure S1 and S2) at low cell concentrations. This showed that we were able to create cell laden monodisperse droplet trains with freely controlled droplet size, which remained stable in the presence of cells. We subsequently assessed droplet impact of the droplet train on microscope slides and semi-quantitatively determined droplet spreading versus droplet velocity. The results are shown in Figure S3 and confirmed that the droplet spreading follows a scaling with weber number $(we)^{1/4}$ as described by Clanet et al. [10].

We next used the set up to assess the role of distinct droplet parameters on cell viability post-impact. To this end, stable droplet trains with droplet sizes of 144 µm and 204 µm containing 100.000 cells/ml were created using the 50µm and the 100µm nozzles. Impact events were created with at velocities ranging from 3 to 10 m/s and post impact cell viability was assessed. The results are depicted in figure 3.

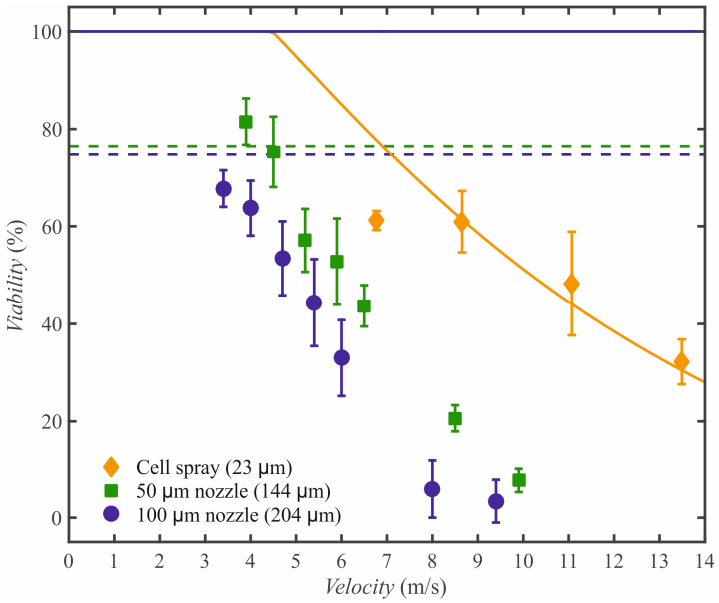

Figure 3: Effect of droplet parameters on cell viability post-impact. The effect of droplet velocity and droplet size on cell viability is shown for experiments with a 50 and 100 µm nozzle which resulted in droplets of 144µm and 204µm, respectively. The dashed lines indicate control viability of non-impacted jet droplets. To compare these results with literature, old cell spray data with fibroblasts with an average droplet size of 23µm is depicted in yellow diamonds [8]. Our previous model accurately predicted cell viability of the cell spray as expected (solid yellow line) but failed in predicting cell viability when droplet size was increased (solid blue and green lines overlapping at 100%).

The data showed a strong relationship between the impact velocity and the cell viability post impact. Increasing the velocity resulted in reduced viability and almost zero survival at velocities above 10 m/s in our set-up. These results compared well with old data which showed a similar negative relationship with the impact velocity. The data also revealed a strong relationship between the droplet size and the cell viability. Unexpectedly, a larger droplet size led to a lower viability at a specific velocity as demonstrated by the left shift of the curves. Highest cell survival was obtained at given velocities using cell spraying with the smallest droplet size of 23µm on average. We subsequently applied our previously developed cell survival model to the new and old data. For a detailed explanation of this model we would like to point the reader to our previous publication [8]. Briefly, the model predicts the spreading of a cell with a certain size after impacting at a specific velocity according to micro-droplet spreading relationship devised by Clanet et al [10]. The resulting deformation is then corrected for the presence of the outer droplet according to Tasoglu et al. [11]. The size of the outer droplet is expected to cushion the impact (i.e. a larger droplet results in higher viabilities), the viscosity of the droplet is expected to have an opposite effect. The corrected deformation is finally related to cell viability according to the model from Takamatsu et al. [12]. Figure 3 shows that our model accurately predicted the cell viability depending on the velocity for the small cell spray droplets as expected. In contrast, the

model predicted 100% cell survival in droplets obtained using the 50 and 100µm nozzles with an average diameter of 144µm and 204µm, respectively, at all tested impact velocities. However, experimentally the increase in droplet size decreased cell survival.

Clearly the previously developed model wrongly predicted a cushioning effect of the outer droplet. This inspired us to revaluate the basis under our model. In the current model, the inner cell was leading to determine the spreading of the micro-droplet. This can be accurate for relatively small droplets, but might deviate strongly when droplet size gets much bigger than the cell size. We therefore developed a new model in which the outer droplet was leading to determine droplet spreading. This can be achieved by applying Clanet's scaling law ($We^{1/4}$). However, this did not take the relationship between outer and inner droplet into account. Tasoglu et al. have numerically predicted the effect of outer droplet weber number on inner droplet cell spreading. Fitting this relationship resulted in a scaling of $We^{0.18}$ and therefore a slightly cushioned effect on cell deformation (Equation 3).

$$\frac{D_{c,max}}{D_c} = C_1 * We^{0.18} \quad (3)$$

In this equation $D_{c,max}/D_c$ is the maximal spreading of the cell, C_1 is the scaling factor and *We* is the weber number. We complemented our old model with these new insights. In figure 4, the relationship between velocity and viability is shown with predictions using the new model in which the relationship between weber number and viability is taken into account.

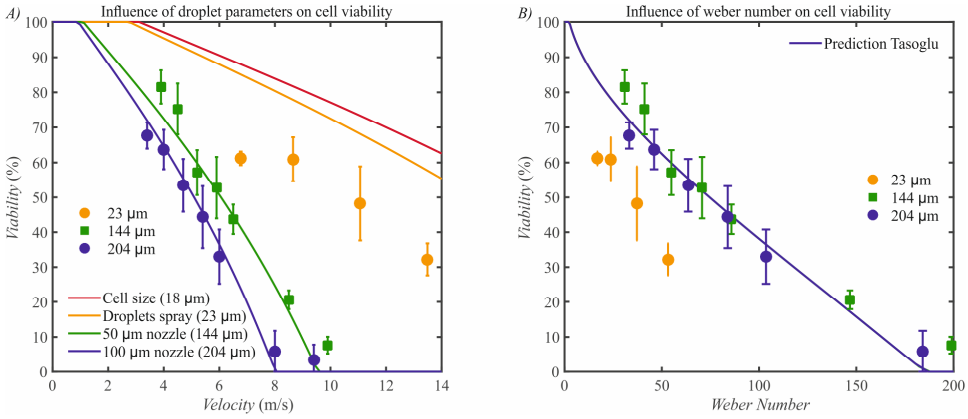

Figure 4: Predictions of cell viability post-impact. A) The influence of droplet parameters on cell viability is plotted. The solid lines depict the new model predictions for droplets of cell size (red), spray size (yellow), from 50 µm nozzle (green) and from 100 µm nozzle (blue). The adjusted model accurately predicted cell survival in the larger droplet sizes but was less accurate in predicting cell survival in the cell spray. B) The relationship between weber number and cell viability. The solid line depicts the new model prediction (C1=0.289).

Figure 4A shows that the new model was capable of accurately predicting the cell viability post-impact in our controlled droplet experiments. Additionally, it predicted correctly the trend between droplet size and cell viability at a certain velocity with larger

droplets leading to lower viability. This trend was also true for the old cell spray data, however the cell viability was overestimated. This either indicated that the new model was only valid for larger droplets, or could indicate an underestimation of droplet size in the spray experiments. Figure 4B shows the relationship between the outer droplet weber number and the cell viability. The data clearly showed a strong relationship between weber number and cell viability following $We^{0.18}$ for the controlled droplet impact experiments. The cell spray data was also strongly dependent on the outer droplet weber number, but was again overestimated.

7.4 Discussion

The large potential of bioprinting is hampered by the trade-off between optimal printing parameters and viability of printed cells. A better understanding of what governs cell viability in bioprinting is therefore highly desired and could lead to improved outcomes [13]. Furthermore, accurate models predicting cell survival could provide handles to rationally optimize the printing process. In this work, we have specifically focused on the effect of droplet parameters on cell viability in droplet-based deposition applications. Using the experimental data, we subsequently updated our analytical model to accurately predict the cell survival.

In a previous study we have developed an analytical model that accurately predicted cell viability in cell spraying of fibroblasts based on droplet parameters and surface properties. While this work has provided interestingly new insights in what governs cell viability after droplet impact, several questions remained. The experiments were performed with a cell spray that contains droplets not much bigger than individual cells at relatively high velocities. This is difficult to compare with ink-jet bioprinting were droplets are much bigger and generally impact at lower velocities. Moreover, while the velocity of the droplets could be easily tuned by adjusting air-pressure, the droplet size remained relatively stable. Additionally, the spray contained droplets with a large polydispersity which meant that only the result of averages could be determined. Therefore, it remains undecided what the role of droplet size is on the viability of cells after impact and how this is related to the velocity.

To solve this, we have developed a new set-up by which we can fully control droplet size and impact velocity. We have shown that using this set-up, we are capable of creating monodisperse droplets much larger than in cell spray, within a broad size range. This range can easily be expanded by applying smaller or larger nozzles. The addition of cells to these droplet trains creates small disturbances depending on the concentration. This poses a limitation to using high cell concentrations. For our intended use to study cell survival the throughput is still considerable and therefore not a main concern. At several frequencies the cell containing droplet trains are stable and monodisperse and average droplet size is slightly larger to pure liquids. Using this set up we can create reproducible cell containing monodisperse droplets of various sizes with controlled impact.

To study the impact of micro-droplets we decoupled the droplet velocity from the impact velocity. This is important as the velocity of the droplet is directly related to the shear stress experienced at the nozzle orifice. As the nozzle is of similar or even smaller size than the droplet, this shear will be similar to the shear experienced at impact. Therefore, it would remain unclear whether cell damage occurs in the nozzle or at the impact surface. By impacting the droplet train from the side we are able to freely adjusting impact velocity without changing droplet shear stress at the nozzle and therefore purely study impact phenomena. To further reduce the effect of droplet velocity, we placed the nozzle at a 45 degrees angle to half the horizontal component and ensure almost complete directed impact.

With this set-up we performed experiments to determine the effect of droplet parameters on cell viability post-impact. We showed that especially the droplet velocity has a large influence on cell survival after impact. This dependency is similar to the cell spray results from our previous study (insert ref). We additionally showed that the droplet size influences the cell viability, with a larger droplet leading to lower viabilities at similar velocities. This trend continues when we enter the cell spray data, where the smaller droplets have even larger viabilities. However, when we applied our previously developed analytical model, we showed that the cell spray data was accurately predicted, but a completely opposite trend for droplet size was expected. Indeed our old model, based on the numerical simulations of Tasoglu et al., predicted that a larger droplet should provide a stronger cushioning effect and therefore results in reduced cell damage and better cell survival [11]. Our new data however clearly shows that larger droplets with diameters > 5-fold higher than the cell diameter were damaging for cells when they impact at similar velocities.

To tackle this discrepancy, we updated our analytical model. In the updated model the deformation of the outer droplet determines, with a scaling factor, the deformation of the inner cell. This is opposite to the old model in which the deformation of the inner cell was calculated and was only corrected for the outer droplet. While the old model accurately predicted the cell viability, this was true for droplets of roughly cell size. The effect of droplet size was therefore never properly investigated. The droplet deformation in the new model could be determined by the scaling laws for Clanet, but could also be explained by the model from Roisman et al. [14]. However, these models only predicted the spreading of a single and not a compound droplet. Models determining the spreading of compound droplets are sparse in literature. Goa et al determined several morphological outcomes for compound droplet spreading, but no simple spreading laws [15]. We previously applied the numerical model of Tasoglu et al to correct for the effect of the outer droplet [11]. Other outcome parameters from the Tasoglu's model, however allowed us to both predict the spreading of the outer and the inner droplet. This is achieved by a scaling to the weber number with a scaling factor which is likely dependent on the cell type. Applying this model showed us that we can accurately predict the viability depending on velocity for both droplet sizes tested with our set-up. Moreover, we were able to predict the correct trend for the cell spray data. We show that the

viability was strongly dependent on the weber number. However, the viability for the cell spray data was systematically under predicted. This could indicate that the model is mainly valid for larger outer droplets, but it is also possible that the droplet size in cell spray experiments is underestimated. Calculations showed that cell spray data would be accurately predicted by the new model if droplet size would be double. The droplet size in the cell spray experiments was determined using high speed camera of droplets without cells [8]. An assumption was made that only droplets with cell size or larger could contain cells and smaller droplets were not included in the droplet population. The average droplet size of the remaining population was slightly larger than cell size and this was assumed to be the droplets in the cell spray. However, as the droplet are roughly similar to cell size it is highly likely that actual cells would increase the size of the droplets which contain them. Therefore it is highly likely that actual cell containing droplet population was larger than estimated and therefore might still be accurately predicted by our new model. An alternative explanation would be that in the relative importance of the cell compared to the droplet is larger in smaller droplet through the higher cell to droplet volume ratio. As the viscosity of the cell is higher than that of the outer droplet, a more viscous regime dependent on Reynolds number could be followed. To investigate this, it is essential to further measure the effect of droplet size in our set-up with smaller micro droplets, preferably only several cells in size.

In most bioprinting applications, cell are encapsulated in a viscous hydrogel precursor, or in a gelating visco-elastic hydrogel. Therefore, further experiments should investigate the effect of the viscosity on the viability after impact. In the previous version of the model the viscosity was assumed to have a negative effect on the viability post impact, as the viscosity increases the transmission of shear stress from the outer to the inner droplet. This trend was validated with cell spray experiments. However, in our new model the outer droplet mainly determines the spreading of the inner cell which was shown to be accurate for larger droplets. In this situation, a higher viscosity might actually reduce the spreading of the outer droplet and thereby protect the inner cell. This dual role of viscosity, depending on droplet size should be investigated in future experiments. Furthermore, the effect of viscoelasticity of both cell [16-18] and droplet [18, 19] should be included in future models.

7.5 Conclusion

Bioprinting would benefit greatly from a better understanding of the effect of parameters on cell viability. We have developed a new set-up to accurately evaluate the effect of droplet parameters on the cell viability post impact. With this set-up we have shown that droplet size and velocity both have a negative effect on the cell viability. This has resulted in a new model to predict cell viability post-impact. This model predicts that smaller and slower droplets will result in higher viabilities. Additionally, a beneficial effect of viscosity is expected, which is part of ongoing work. Further development of this model will help in providing guidelines for optimal parameter space to rationally improve bioprinting applications.

7.6 Supplementary information

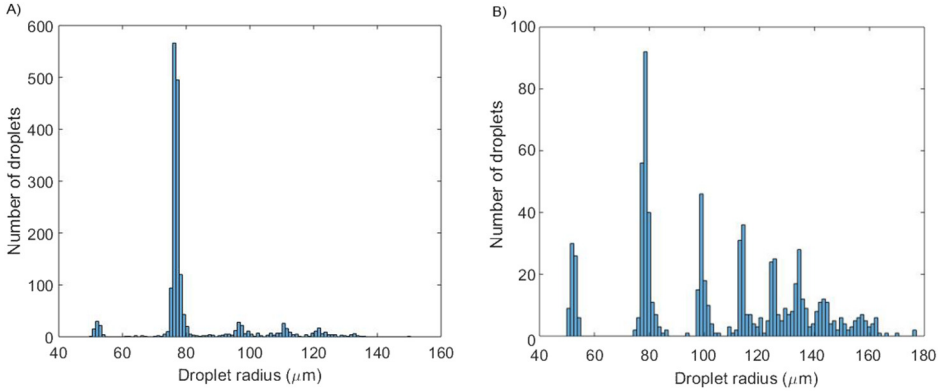

Figure S1: Influence of cells on droplet distribution. A) Droplet distribution of 50 µm nozzle with 100.000 cells/ml. It can be seen there is one major peak at a droplet radius of 76 µm. Small subpeaks exist at a 96 µm and 110 µm and 120 µm. These peaks represent droplets with 2, 3 and 4 times the volume of a single droplet. This indicates that a small portion of the droplets coalesce in air. The smaller peak at 52 µm (roughly ¼ volume of single droplet) shows that satellite droplets are shed during this process. B) When the cell concentration is increased to 800.000 cells/ml the distribution becomes much broader. There is still one major peak at 80 µm, but there are several significant peaks at 100, 115, 130, 137 and 145 µm. These peaks represent 2, 3, 4, 5 and 6 times single droplet volume. This indicates that droplets rapidly coalesce in air at high cell concentrations.

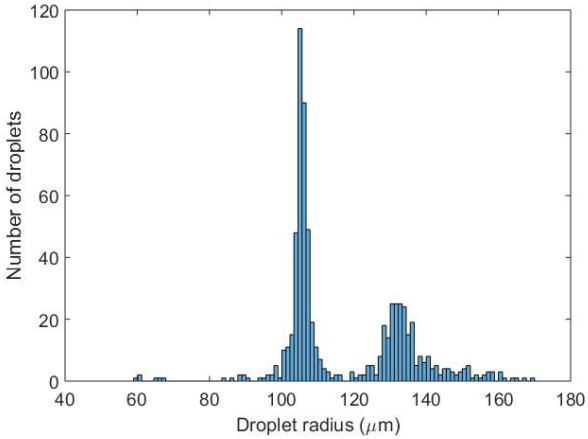

Figure S2: Influence of cells on droplet distribution of 100 µm nozzle with 100.000 cells/ml. The figure shows there is one major peak at 105 µm and one smaller subpeak at 132 µm. This subpeak is roughly twice the volume of the major peak and indicates minor coalescence of droplets in air.

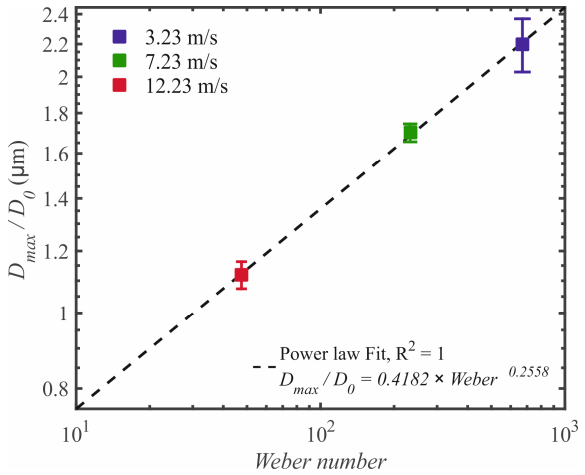

Figure S3: The relationship between weber number and droplet spreading in our controlled impact set-up. We performed three impact experiments at total impact velocities of 3.23, 7.23 and 12.23 m/s with a 100 µm nozzle at 2.9 kHz actuation resulting in a droplet size of 320 µm. We subsequently measured the size of the puddle after impact to calculate D_{max} / D_o and plotted this against the weber number. We fitted the results with a power law function and show that the droplet spreading scales with weber to the power 0.2558, which is very close to the 0.25 predicted by Clanet et al. [10]. This demonstrated that the microdroplet spreading we encountered in our experiments could be modelled using Clanet et al.

References

1. Murphy, S.V. and A. Atala, *3D bioprinting of tissues and organs.* Nature biotechnology, 2014. **32**(8): p. 773.
2. Williams, D., et al., *A perspective on the physical, mechanical and biological specifications of bioinks and the development of functional tissues in 3D bioprinting.* Bioprinting, 2018. **9**: p. 19-36.
3. Kalyani, N., et al., *Characterization of cell viability during bioprinting processes.* Biotechnology Journal, 2009. **4**(8): p. 1168-1177.
4. Haitao, C., et al., *3D Bioprinting for Organ Regeneration.* Advanced Healthcare Materials, 2017. **6**(1): p. 1601118.
5. Liliang, O., et al., *Effect of bioink properties on printability and cell viability for 3D bioplotting of embryonic stem cells.* Biofabrication, 2016. **8**(3): p. 035020.
6. !!! INVALID CITATION !!! [3, 5-7].
7. Blaeser, A., et al., *Controlling shear stress in 3D bioprinting is a key factor to balance printing resolution and stem cell integrity.* Advanced healthcare materials, 2016. **5**(3): p. 326-333.
8. Hendriks, J., et al., *Optimizing cell viability in droplet-based cell deposition.* Scientific Reports, 2015. **5**: p. 11304.
9. Rayleigh, L., Philosophical Magazine Series 5, 1882: p. 184-186.
10. Christophe Clanet, C.B., Denis Richard, David Quere, *Maximal deformation of an impacting drop.* Journal of Fluid Mechanics, 2004. **517**: p. 199-208.
11. Tasoglu, S., et al., *Impact of a compound droplet on a flat surface: A model for single cell epitaxy.* Physics of Fluids (1994-present), 2010. **22**(8): p. -.
12. Takamatsu, H. and B. Rubinsky, *Viability of Deformed Cells.* Cryobiology, 1999. **39**(3): p. 243-251.
13. Lepowsky, E., M. Muradoglu, and S. Tasoglu, *Towards preserving post-printing cell viability and improving the resolution: Past, present, and future of 3D bioprinting theory.* Bioprinting, 2018. **11**: p. e00034.
14. Roisman, I.V., *Inertia dominated drop collisions. II. An analytical solution of the Navier–Stokes equations for a spreading viscous film.* Physics of Fluids, 2009. **21**(5): p. 052104.
15. Gao, P. and J.J. Feng, *Spreading and breakup of a compound drop on a partially wetting substrate.* Journal of Fluid Mechanics, 2011. **682**: p. 415-433.
16. Khismatullin, D.B. and G.A. Truskey, *Three-dimensional numerical simulation of receptor-mediated leukocyte adhesion to surfaces: Effects of cell deformability and viscoelasticity.* Physics of Fluids, 2005. **17**(3): p. 031505.
17. Luo, Z.Y., et al., *Two-dimensional numerical study of flow dynamics of a nucleated cell tethered under shear flow.* Chemical Engineering Science, 2014. **119**: p. 236-244.
18. Chung, C., et al., *Effect of viscoelasticity on drop dynamics in 5:1:5 contraction/expansion microchannel flow.* Chemical Engineering Science, 2009. **64**(22): p. 4515-4524.
19. Izbassarov, D., et al., *Effects of viscoelasticity on droplet-based bioprinting.* Bulletin of the American Physical Society, 2018.

“At the heart of difficulties are possibilities”

8

Gelatin-tyramine improves cell attachment, migration and metabolic activity of multiple cell types in enzymatically crosslinkable dextran-hyaluronic acid hydrogels

Hydrogels are receiving increasing attention for use in 3D cell culture, tissue engineering and bioprinting applications. Each application places specific mechanical and biological demands on these hydrogels. For example, cell culture with organoids requires soft hydrogels, whereas bioprinting demands for high shape fidelity and thus stiffness. Currently, most synthetic and natural hydrogels lack the versatility to meet these demands. Here, we describe the development of a hydrogel toolbox based on enzymatically crosslinkable components via tyramine moieties. The hydrogel backbone is based on tyramine conjugates of the polysaccharides Dextran and Hyaluronic acid and allows for rapid and tuneable crosslinking with well-defined stiffness and high cell viability. We modified gelatin with tyramine (TA) moieties and combined this in low concentrations with the polysaccharide hydrogels to improve the biological properties. We show that 3T3 fibroblasts and HUVECs attached to and proliferated on the enriched hydrogels at minute gelatin-TA concentrations, in contrast to bare or unmodified gelatin enriched hydrogels. Moreover, we were able to switch HUVECs for quiescent to migratory phenotype simply by altering the ligand concentration. Thereby demonstrating the potential to easily control cell fate. In encapsulation studies, we showed that gelatin – TA greatly improved the metabolic activity of 3T3 fibroblasts in soft 2,5% wt/v hydrogels. Furthermore, we showed rapid

Jan Hendriks[1], Bram Zoetebier [1], Daniël B.F. Saris[3,4] & Marcel Karperien[1]

1 Department of Developmental BioEngineering, TechMed institute, University of Twente, The Netherlands.

3 Department of Orthopedics, UMC Utrecht, The Netherlands.

4 Department of Reconstructive Medicine, TechMed institute, Faculty of Science and Technology, University of Twente, The Netherlands.

Manuscript in preparation

migration and network formation in gelatin-TA enriched hydrogels even at low concentrations in contrast to a non-migratory behaviour in non-enriched polysaccharide gels based on the rounded cell morphology. We intent to further develop this by adding other ECM proteins, peptides and growth factor adhesion sites. This will lead to a toolbox that allows researchers to create the hydrogel optimal for their desired application

8.1 Introduction

Hydrogels are receiving increasing attention in cell culture, tissue engineering and bioprinting applications for their 3D nature, versatility and their recapitulation of native tissue [1]. While there has been good progress in the hydrogel field, the large variety of applications demands for a large versatility in the used hydrogels [2]. For example, bioprinting applications require hydrogels with large shape fidelity and thus stiffness [3], while cell culture systems often prefer soft hydrogels for optimal migration and differentiation [4]. Beside tuneable mechanical properties, there is a large demand for tuneable biological properties [2]. While some cell types thrive in non-adhesive hydrogels, others demand for adhesion factors [5]. When culturing stem cells or organoids and specific differentiation is desired, the type of biological interaction with the hydrogel is also of importance. For example, organoids could be formed in PEG-fibronectin hydrogels, but efficiency was much higher when laminin was added [4]. Therefore, a toolbox is desired for developing hydrogels with tuneable mechanical and biological properties to recapitulate to native ECM.

Previously, our group has developed polysaccharide hydrogels based on crosslinking via horse radish peroxidase (HRP) of polymer-tyramine conjugates [6]. This crosslinking process is highly biocompatible with viabilities over 95%. Moreover, the crosslinking speed can be easily tuned by altering the HRP concentration. Therefore, these hydrogels have great potential for use in bioprinting applications. The hydrogels are liquid when extracted from the nozzle, and therefore ensure high cell viability, but crosslink during printing, and therefore ensuring high shape fidelity. The stiffness of the hydrogels can be modified by multiple strategies: altering molecular weight of the polymers, the degree of substitution of tyramine and enzyme or H_2O_2 concentrations as means to control cross linking density and by simply reducing gel concentration. We have additionally shown that the stiffness of these hydrogels can be temporally controlled, resulting in time dependent matrix stiffening. Specifically, we have developed a hydrogel based on a combination of dextran – tyramine (Dex-TA) and hyaluronic acid – tyramine (HA-TA). The Dex-TA component is highly biocompatible, non-degradable and provides long term stability to the gel, while the HA-TA is degradable and highly bioactive [7].

We have shown that these hydrogels are highly suitable for culture of chondrocytes and mesenchymal stromal cells (MSCs) where they promote extensive matrix production [8]. However, while these hydrogels possess excellent mechanical properties, they lack the biological attachments factors required for most cells types. Moreover, to be able to efficiently mimic the native ECM, other factors are desired. These factors include proteins such as collagen and fibronectin or peptides such as RGD to stimulate cell attachment or growth factor adhesion sites such as heparin and potentially growth factors themselves to increase bioactivity.

Here, we demonstrate the development of a strategy to easily and efficiently add any desired biological component to our tyramine based hydrogels. We show a proof of concept in which we modified gelatin with tyramine moieties to enable covalent

crosslinking into the polysaccharide hydrogels. We show that the addition of small concentrations tyramine modified gelatin but not gelatin only already results in stable cell attachment and proliferation in contrast to adding unmodified gelatin. In addition, we show a large increase in metabolic activity and migration in 3D. This demonstrates the potential of modifying ECM proteins with tyramine moieties for the addition in polysaccharide hydrogels. This will lead to a freely tuneable hydrogel to create the artificial ECM needed for any specific tissue.

8.2 Materials and Methods

8.2.1 Materials

Chemical components: Dextran (40 kDa, pharmaceutical grade) was purchased from Pharmacosmos, Denmark. Sodium hyaluronate (27 kDa, pharmaceutical grade) was purchased from Contipro Pharma, Czech Republic. Gelatin from porcine skin (BioReagent, gel strength ~300 g Bloom, Type A), tyramine (99%), DMF (anhydrous, 99.8%), LiCl (99.0%), p-nitrophenyl chloroformate (96%), pyridine (anhydrous, 99.8%), DMSO-d6 (99.9%), NaCl (≥99.0%), D2O (99.9 atom % D), horseradish peroxidase (HRP, 325 units/mg solid), hydrogen peroxide (30%) were purchased from Sigma-Aldrich. Tyramine·HCl salt (99%) was obtained from Acros Organics. 4-(4,6-Dimethoxy-1,3,5-triazin-2-yl)-4-methylmorpholinium Chloride (DMTMM, 97%) was purchased from Fluorochem Ltd. UK. Ethanol (P.A., ≥99.9%) and Diethyl ether were purchased from Merck. Milli-Q water was used from Milli-Q Advantage A10 system equipped with an 0.22 µm Millipak®-40 Express filter.

Cell culture components: DMEM (Ref:41965039), FBS (Ref: 10279-106), pen/strep (Ref:15140) and 0.25% trypsin/EDTA (Ref:25200-072) were purchased from Gibco. PBS (Ref:17-516F), EBM2 (Ref: 00190860) and EGM2 (Ref: CC-4176) were purchased from Lonza.

8.2.2 Procedure synthesis Dex-PNC

LiCl (4.0 g, dried at 115 °C) and dextran (5.00 g, 30.8 mmol r.u.) are weighed into a 500 mL three necked round bottom flask equipped with a stirrer bar. The flask is evacuated and refilled with nitrogen for 3 times after which it is left under vacuum at 95 °C for 1.5h. After thoroughly drying, the flask was filled with nitrogen and 200 mL of anhydrous DMF was added via a cannula while stirring. The flask was then equipped with a thermometer and heated to 95 °C while stirring the solution. Once the dextran was completely dissolved, the solution was cooled to 0 °C and anhydrous pyridine (2.0 ml, 25.8 mmol) was added. Subsequently, freshly sublimed para-nitrophenyl chloroformate (2.5 g, 12.4 mmol) was added in small portions, keeping the temperature below 2 °C. After 1 hour, the reaction mixture was poured into 1 L of ice-cold ethanol. The precipitate was filtered off (Por 4) and washed with copious amounts of cold ethanol and diethyl ether. After drying under vacuum, the product was obtained as a white powder (6.00 g, 30.7 mmol r.u., 99 % yield, DS20%). 1H-NMR (400 MHz, DMSO-d6): δ(ppm) = 3.0-4.0 (saccharide

ring protons, m, 6H); 4.2-5.8 (anomeric and hydroxyl protons, m, 4H); 7.58 (Ar o-CH, d, 2H); 8.34 (Ar m-CH, d, 2H).

8.2.3 Procedure synthesis Dex-TA

Dextran-PNC (6.00 g, 30.7 mmol r.u., 6.15 mmol p-nitrophenyl carbonate) was weighed into a 250 mL three necked round bottom flask equipped with a stirrer bar. The flask was evacuated and refilled with nitrogen for 3 times after which the flask was filled with nitrogen and 100 mL of anhydrous DMF was added via a cannula while stirring. Once the dextran was completely dissolved, tyramine (1.69 g, 12.3 mmol) was added. After 1 hour, the reaction mixture was poured into 1 L of ice-cold ethanol. The precipitate was filtered off (Por 4) and washed with copious amounts of cold ethanol and diethyl ether. After drying under vacuum, the crude product was obtained as a white powder. The crude product was dissolved in water and dialysed against Milli-Q water for 3 days (MWCO 3500 Da), followed by filter sterilization and freeze-drying yielding the product as a white foam (5.04 g, 28.0 mmol, 92 % yield, DS10%). 1H-NMR (400 MHz, DMSO-d6): δ(ppm) = 3.0-4.0 (saccharide ring protons, m, 6H); 4.2-5.8 (anomeric and hydroxyl protons, m, 4H); 6.67 (Ar m-CH, d, 2H); 6.99 (Ar o-CH, d, 2H).

The calculation of the DS of dextran-TA and dextran-PNC is based on the integrals of 4.2-5.8 ppm (corresponding to the 4 anomeric protons from dextran), compared with the integral of the aromatic protons of tyramine (6.60-6.75 and 6.90-7.07) or para-nitrophenyl (7.40-7.65 and 8.20-8.40). The DS of dextan is given as the percentage of saccharide units modified in dextran.

8.2.4 Procedure synthesis HA-TA

Sodium hyaluronate (5.00 g, 12.5 mmol r.u.) was dissolved in 500 mL Milli-Q water in an 1 L round bottom flask equipped with a stirrer bar. While stirring at room temperature, 4-(4,6-dimethoxy-1,3,5-triazin-2-yl)-4-methylmorpholinium chloride (DMTMM, 3.46 g, 12.5 mmol, 1eq) and tyramine hydrochloride (TA·HCl, 2.17 g, 12.5 mmol, 1eq) were added subsequently. The addition of DMTMM and TA·HCl was repeated after 24 and 48 hours. After 72 hours, 40 mL NaCl (sat) was added to the reaction mixture and the reaction mixture was poured into 2.5 L cold ethanol. The crude product was isolated by centrifugation at 5000 rpm followed by drying in vacuo. The crude product was dissolved in 75 mL Milli-Q water and dialysed against Milli-Q water for 3 days (MWCO 1000 Da). Filter sterilization and lyophilization yielded the product as a white foam (5.10 g, 12.4 mmol, 99 % yield, DS10%). 1H-NMR (400 MHz, D2O): δ(ppm) = 1,93 (acetyl-CH3, s, 3H); 2,75 (2-CH2, s, 2H); 2,90 (1-CH2, s, 2H); 3.2-4.2 (saccharide ring, m, 10H); 4,34 (s, 1H); 4,43 (d, 1H); 6,77 (Ar m-CH, d, 2H); 7,16 (Ar o-CH, d, 2H).

The degree of substitution (DS) was calculated based on the integral of the methyl group at 1.93 ppm is compared to the integral of the tyramine signal at 6,77ppm. The DS of hyaluronic acid is given as the percentage of COOH groups modified in hyaluronic acid (i.e. per disaccharide).

8.2.5 Procedure synthesis Gel-TA

Gelatin from porcine skin (5.00 g, type A) was dissolved in 500 mL Milli-Q water at 40 °C in an 1 L round bottom flask equipped with a stirrer bar. After cooling down to 35 °C, the gelatin was chemically modified and purified as described for HA-TA. The product was obtained as a white foam (3.9 g, 75% yield, DS5%). The degree of substitution (DS) was calculated based on the increase of aromatic protons (6.6-7.5 ppm) in the 1H-NMR of Gel-TA vs gelatin, with the amino acid composition measured by Raja Mohd Hafidz, R. N. et al. The DS of gelatin is given as the percentage of amino acids modified in gelatin.

8.2.6 Cell culture

NIH 3T3 fibroblast were cultured in DMEM, supplemented with 10% FBS and 1% P/S at 37 °C and 5% CO_2. 1.4 µl β-mercapto-ethanol was added freshly per ml of medium to reduce free radical formation. The cells were cultured from passage 3 to x and were harvested at 80% confluence for each experiment. Human umbilical vein endothelial cells (HUVECs) were cultured in endothelial growth medium (EGM-2™). This medium was obtained by adding the EGM-2™ bullet kit to EBM-2 medium. The HUVECs were seeded at p0-1 and were used before p3.

8.2.7 Influence of (tyramine functionalized)-gelatin on cell attachment to Dex/HA – TA hydrogels

12.5% Dex-TA, 12.5% HA-TA and 1.25% Gel-TA w/v precursor solutions were prepared by dissolving sterile lyophilized Dex-TA, HA-TA and Gel-TA in PBS. 1.25% gelatin precursor was prepared by dissolving sterile gelatin in PBS at 37 °C. Subsequently, Dex-TA and HA-TA precursors were combined in 50:50 ratio to obtain a final concentration of 10% w/v and depending on the experimental condition buffer, gelatin or Gel-TA were added to a final concentration of 500 µg/ml. To this HRP was added to a final concentration of 1 u/ml and the resulting solutions were left overnight at 4°C to homogenize. To start the gelation process H_2O_2 was added to reach a final concentration of 0.03%. The gelling precursors were quickly transferred to a 48 wells-plate with 150 µl/well in triplicates and were centrifuged at 300G for 10 min to reduce meniscus formation and create a flat gel surface. As a control matrigel wells were prepared by adding 150 µl/well in triplicate and incubating at 37 °C for 30 minutes. As an additional control cells were added to culture treated well plates

After the gels were completely gelated, 3T3 fibroblasts and HUVECs were harvested using trypsin/EDTA. The cells were subsequently added to the wells at a concentration of 35000 cells/cm2. Cell morphology, attachment and proliferation were assessed at 4h, 24h and 7d.

8.2.8 Influence of Gel-TA concentration on cell behaviour seeded on Dex/HA –TA hydrogels

Flat hydrogels were prepared as explained above. Gel-TA concentration was varied in increments of factor 2. Concentrations used were 31.25 µg/ml, 62.5 µg/ml, 125 µg/ml and

500 µg/ml. As a control Dex/HA – TA gels were used without Gel-TA. After flat gels were prepared, 3T3 and HUVECs were seeded at 35000 cells/cm2. Cell morphology, attachment and proliferation were assessed at 4h, 24h and 7d.

8.2.9 Influence of addition of (tyramine functionalized)-gelatin to Dex/HA – TA hydrogels on cellular metabolism and migration in 3D

12.5% Dex-TA, 12.5% HA-TA and 1.25% Gel-TA w/v precursor solutions were prepared by dissolving sterile lyophilized Dex-TA, HA-TA and Gel-TA in PBS. 1.25% gelatin precursor was prepared dissolving sterile gelatin in PBS at 37 °C. Subsequently, Dex-TA and HA-TA precursors were combined in 50:50 ratio to obtain final concentrations of 2.5%, 5% and 10% w/v and depending on the experimental condition buffer, gelatin or Gel-TA were added to a final concentration of 500 µg/ml. To this HRP was added to a final concentration of 3 u/ml and the resulting solutions were left overnight at 4°C to homogenize. Subsequently, 3T3 cells were harvested with trypsin/EDTA. The cells were centrifuged at 300G for 4 min and resuspended in the respective gel-precursor solutions at 1 million cells / ml. To the precursor solutions H_2O_2 was added to a final concentration of 0.03% and 100 µl was transferred per well in triplicate to a flat 96 wells plate. To each well 200 µl cell culture medium was added, which was refreshed every 3 days. After t=0, 3d, 7d, 14d, 21d and 24d morphology was assessed and after 3d, 7d, 14d and 21d metabolic activity was measured. Metabolic activity was measured using presto blue. Briefly 20 µl presto blue was added to each well. The samples were incubated for 30 minutes and fluorescence was measured (ex: 535 nm, em: 615 nm). Results were processed by subtracting the background at each time point.

8.2.10 Influence of hydrogel density on migration in gelatin enriched hydrogels

To further demonstrate the influence of gel concentration on cell spreading and migration, hydrogels of low density were prepared. The hydrogels were prepared as explained above. The hydrogel concentrations used were 1.25% and 2.5% w/v and depending on the experimental condition buffer, gelatin or Gel-TA were added to a final concentration of 500 µg/ml. Again 100 µl gel per well was added to a 96 wells plate in triplicate with a cell concentration of 1 million cells/ml. Morphology and migration was assessed at 3d and 7d.

8.3 Results

8.3.1 Conjugation of dextran, hyaluronic acid and gelatin with tyramine moieties

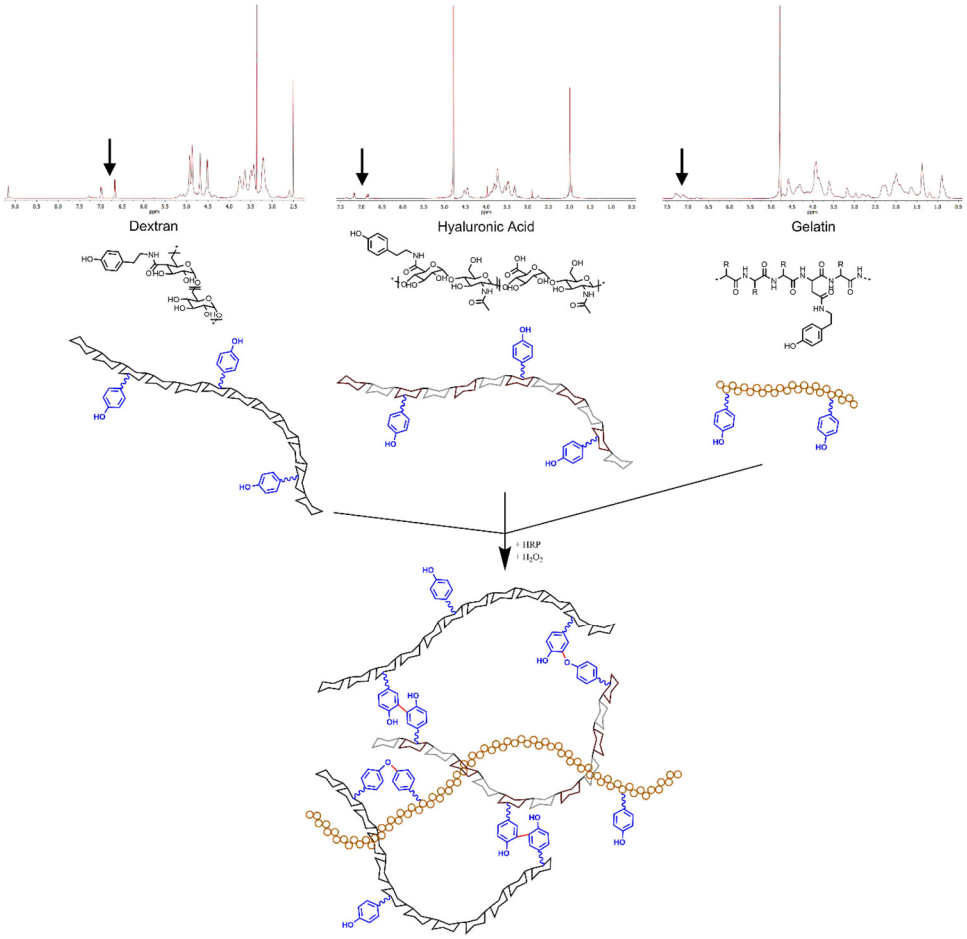

Figure 1. Conjugation of tyramine moieties. A-C) The NMR and structure of Dextran - Tyramine (Dex-TA), Hyaluronic Acid - Tyramine (HA-TA) and Gelatin – tyramine (Gel-TA) is shown. Arrows indicate tyramine peaks D) Schematic representation of combined crosslinking of Dex-TA, HA-TA and Gel-TA.

Figure 1 shows the result of the conjugation of dextran, hyaluronic acid and gelatin with tyramine moieties. Dextran (MW=44000) was conjugated with tyramine moieties with a yield of 92 % and a degree of substitution of 10 (e.g. number of tyramine groups per monosaccharide unit). Hyaluronic acid was conjugated with tyramine moieties with a yield of 99 % and a degree of substitution of 10 (e.g. number of tyramine moieties per disaccharide repeat). Finally, gelatin was conjugated with tyramine moieties with a yield of 75 % and a degree of substitution of 5. These components can be combined in any desired ratio to obtain hydrogels optimal for a specific application.

8.3.2 Influence of (tyramine functionalized)-gelatin on cell attachment to Dex-HA – TA hydrogels

We assessed the beneficial effect of addition of gelatin or Gel-TA to Dex-TA and HA-TA hydrogels on the behaviour of cells seeded on these gels. Specifically, we seeded 3T3 fibroblasts and HUVECs on 10% w/v Dex-HA-TA combined hydrogels that were enriched with a low concentration (500 µg/ml) of either gelatin or Gel-TA. This small addition of gelatin or Gel-TA did not influence the mechanical properties of the gels (supplemental figure 1). We subsequently assessed cell attachment, morphology and proliferation after 4h, 24h and 7d. The results are depicted in figure 2.

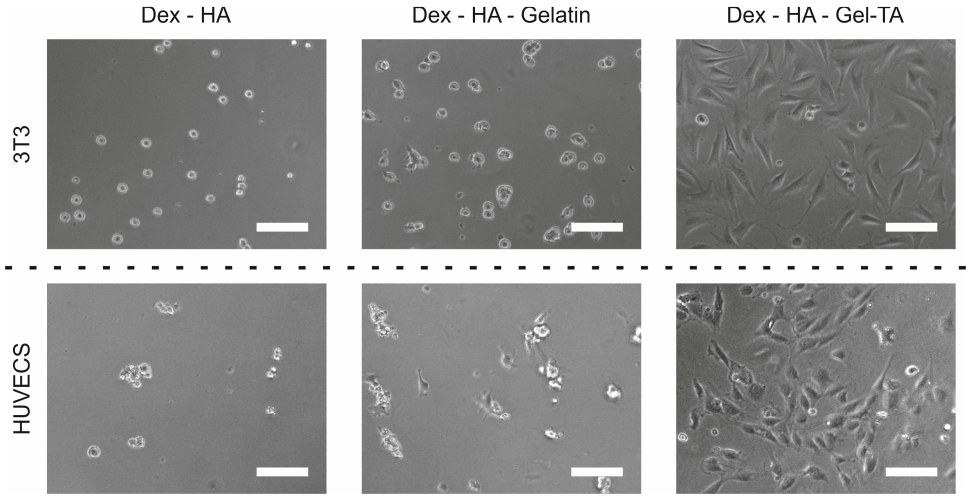

Figure 2: Influence of gelatin or Gel-TA (500µg/ml) on cell behaviour on 10% w/v Dex-HA-TA hydrogels. The photos depict a 200x magnification of cells seeded upon the hydrogels at 4h after seeding. Scale bar indicates 100 µm.

The figure shows that both the 3T3 fibroblasts and HUVECs are unable to attach to the Dex-HA – TA hydrogels. They remain rounded and start to form one big aggregate after 24h (supplemental figure 1) on the edge of the gel. On Dex-HA-TA - Gelatin the cells show signs of attachments, but do not completely stretch. After 24h the cells form multiple small aggregates at fixed positions, indicating some, but inadequate attachment. On Dex-HA – Gel-TA hydrogels, the cells attach well and completely stretch. The behaviour is very similar to that on culture plastic controls. After 24h the cells remain attached and have proliferated to confluency. They continue to remain attached and proliferate for at least 7 days (supplemental figure 2).

8.3.3 Influence of Gel-TA concentration on cell behaviour seeded on Dex-HA –TA hydrogels

We concluded that a low concentration of Gel-TA in Dex-HA –TA hydrogels allows for sustained cell attachment, spreading and proliferation of multiple cell types. This in contrast to the same concentration of natural gelatin. Moreover, morphology of the cells

was similar to that on cell culture plastic. As the morphology of HUVECs was cuboidal on the hydrogels in contrast to the spindle shape seen on matrigel controls, we were curious whether the Gel-TA concentration might play a role. It is known from literature that ligand concentration and resulting strength of attachment can determine whether cells will attain a migratory or quiescent phenotype [9]. We therefore tested a concentration series of Gel-TA in 10% w/v Dex-HA – TA hydrogels to investigate this and to assess the lower limit of ligand concentration for these cell types. None of these concentrations significantly influences the mechanical properties of the hydrogels (supplemental figure 1). The results are depicted in figure 3.

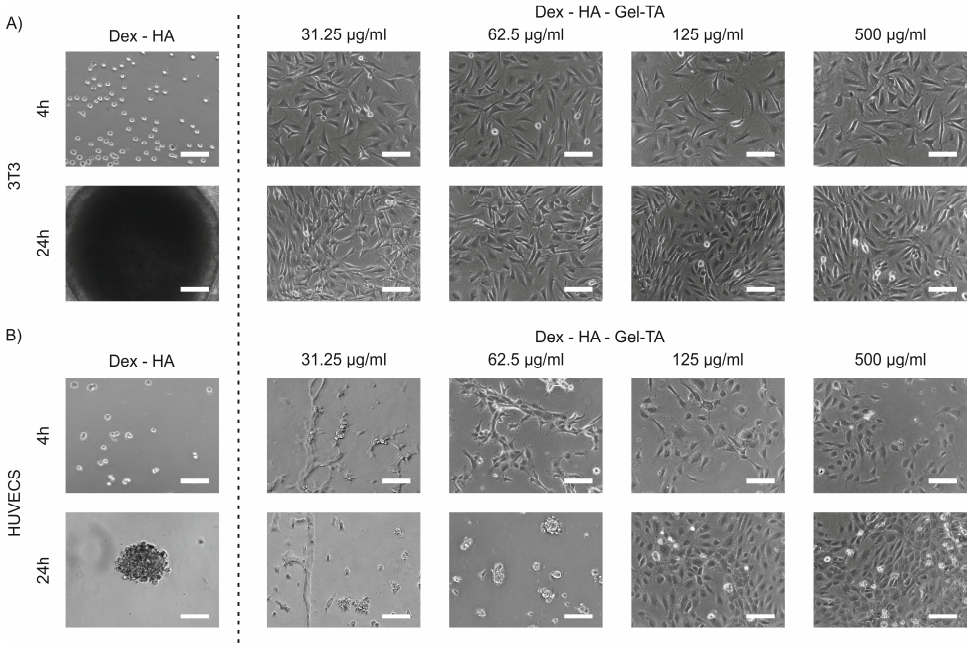

Figure 3: The influence of Gel-TA concentration on cell behaviour on 10% w/v Dex-HA –TA hydrogels. The photos show cell morphology of 3T3s and HUVECs after 4h and 24h on Dex-HA – TA hydrogels (left) and on gels enriched with increasing concentration of Gel-TA (right). Scale bars indicate 100 µm.

Figure 3A shows the effect of Gel-TA concentration on the behaviour of 3T3 fibroblasts seeded upon 10% Dex-HA – Gel-TA hydrogels. It can be seen that after 4h the cells are fully attached and obtained characteristic fibroblast morphology already at lowest Gel-TA concentration, in contrast to natural Dex-HA – TA gels. This concentration is 0.003% w/v in a 10% w/v gel, indicating that very low ligand densities are needed for cell attachment of 3T3 fibroblasts. After 24h the cells have proliferated to near confluency independent on ligand concentration, and continued to grow for 7d (supplemental figure 2). Cell morphology appeared independent of Gel-TA concentration. Figure 3B shows the same experiment for HUVECs. Again no cell attachment is seen on the bare Dex-HA – TA gels, however here a clear effect of Gel-TA concentration on cell behaviour can be observed. At low Gel-TA concentration (31.25 µg/ml and 62.5 µg/ml) the endothelial cells obtained a primarily spindle shape and migrated into tubular like

structures, highly similar to behaviour on matrigel. The cells subsequently release after 24h, an effect also regularly seen in angiogenesis assays upon matrigel [10, 11]. On higher Gel-TA concentrations (125 µg/ml and 500 µg/ml), the cells obtained a cuboidal morphology and attached to the gel similarly as on cell culture plastic. After 24h, the cells on these gels have proliferated to near confluency. However, after 7 days the cells have formed sprouts and organized into a network, with local proliferation, contrasting behaviour on culture plastic (supplemental figure 3).

8.3.4 Cellular metabolism and migration is influenced by addition of (tyramine functionalized)-gelatin to Dex-HA – TA hydrogels.

We subsequently went further to investigate the effect of gelatin and Gel-TA on cell behaviour in 3D. In this experiment we were interested in the combination of the gels micro- and macro-properties and the Gel-TA concentration. We therefore encapsulated 3T3 hydrogels in 2.5%, 5% and 10% w/v Dex-HA – TA hydrogels with or without gelatin or Gel-TA at 500 µg/ml. This allowed us to investigate whether the mechanical properties plays a role in cell-ligand interaction in these hydrogels (more details on mechanical properties in supplementary figure 1). We assessed the metabolic activity of the cells and focussed on cell spreading and migration after 3d, 7d, 14d and 21d. The results are depicted in figure 4.

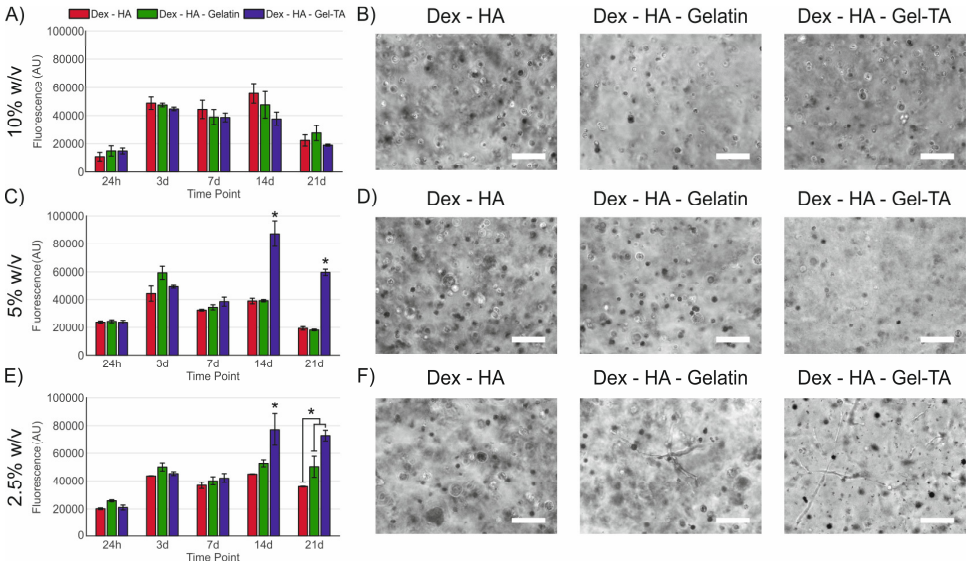

Figure 4: the effect of gelatin and Gel-TA in Dex-HA – TA hydrogels on 3T3 behaviour in 3D. A, C, E) The metabolic activity of the fibroblasts after 24h, 3d, 7d, 14d and 21d in 10%, 5% and 2.5% w/v hydrogels, respectively. B, D, F) photos of cell morphology after 21d of culture in 10%, 5% and 2.5% w/v hydrogels, respectively. Scale bars represent 100 µm. Asterisks show significance ($p<0.05$).

Figure 4A shows that metabolic activity of 3T3 fibroblasts in 10% w/v Dex-HA – TA gels reached a peak at day 3, remained stable for 14 days and then slowly decreased again. However, neither gelatin, nor Gel-TA had a significant effect on metabolic activity in

these gels at the measured time points. When we assessed morphology at day 21 (Figure 4B), only rounded cells were seen with no sign of spreading, migration or significant proliferation. In 5% hydrogels a similar general trend in metabolic activity was observed in Dex-HA – TA or Dex-HA – TA hydrogels with gelatin, with an initial increase at day 3 and a drop at day 21 (Figure 4C). However, Gel-TA is significantly increased metabolic activity at day 14 which continued until at least day 21. Morphological images at day 21 however showed no signs of cell spreading or migration as only rounded cells were observed (Figure 4D). In 2.5% hydrogels there was a similar peak in metabolic activity at day 3. At day 14 and day 21 there is a clear significant increase in metabolic activity in Gel-TA enriched cells compared to gelatin enriched and basic gels and in gelatin enriched gels compared to basic gels (Figure 4E). When we look at morphologic images, we can see that the cells remained rounded in Dex-HA – TA gels. In Dex-HA – Gelatin gels there were some spreading cells and there were signs of cell migration. In Dex-HA – Gel-TA hydrogels this observation was more pronounced, with clear cell spreading and migration throughout the gels.

8.3.5 Low density hydrogels functionalized with Gel-TA allow for rapid cell migration

This indicates that both the presented ligand and the gel mechanical properties are of importance in cell metabolic activity, spreading and migration. To investigate this further, we performed a 3D experiment in which we encapsulated 3T3 fibroblasts in low density hydrogels of 2.5% and 1.25% w/v and assessed cell behaviour at an early time point (7 days). The results are shown in figure 5.

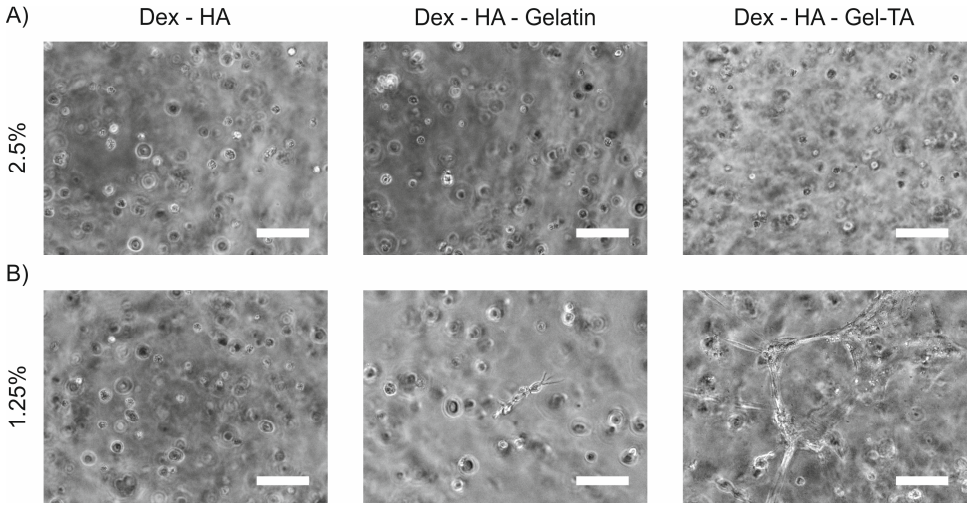

Figure 5: Cell migration in low density hydrogels enriched with gelatin or Gel-TA. Images represent cell morphology at 7 days in 2.5% (A) and 1.25% (B) w/v Dex-HA – TA hydrogels. Scale bars indicate 100 µm.

Figure 5A shows that the cells remained rounded after 7 days in Dex-HA, Dex –HA – Gelatin and Dex-HA – Gel-TA hydrogels. In 1.25% hydrogels, however, there were already

clear differences in this early time point. In Dex-HA –TA hydrogels the cells remained rounded, with no signs of attachment or migration. In Dex-HA – Gelatin hydrogels there were clearly cells that were spreading and attaching, but also a large number of cells that remained rounded. In addition, limited cell migration is seen. However, in Dex-HA – Gel-TA hydrogels there was a large network formation throughout the hydrogel. The majority of cells appeared to be involved in cell spreading and migrating through the gel to create large networks. This further substantiates the importance of both the cell attachment and the mechanical properties of the hydrogel to achieve specific behaviour.

8.4 Discussion

Hydrogels are gaining increasing attention for use in cell culture, tissue engineering and in bioprinting for their 3D environment. However, current hydrogel systems often lack optimal mechanical and biological properties for specific applications. Here, we have described a hydrogel system based on crosslinking of tyramine conjugated polysaccharides that have previously demonstrated great flexibility in mechanical properties and crosslinking settings [6]. We have developed a strategy to extent the biological properties of these hydrogels. To achieve this we created a proof of concept in which we show the potential of adding tyramine modified gelatin, as a model protein.

We show in 2D attachment experiments that Gel-TA enables attachment of both 3T3 fibroblast and HUVECs within 4 hours. This in strong contrast to bare Dex-HA – TA hydrogels, as expected [12], and hydrogels enriched with unmodified gelatin. It is likely that the covalent coupling of Gel-TA in the hydrogel enables a stronger attachment of the cells to the hydrogel than on unmodified gelatin [13]. Moreover, it is likely that the unmodified gelatin diffuses from the gel caused by the hydrophilic and polyanionic properties of HA-TA [12], resulting in lower local ligand concentrations. Additionally, it is possible that the proteins are actively pulled from the gels by the traction forces generated by the cells during attachment and migration [14, 15]. We subsequently showed that the attachment on Gel-TA enriched hydrogels is sustainable for over 7 days and that the cells proliferate similarly as on culture plastic. This makes our hydrogels useful as a 2D culture system, with much lower and tunable stiffness than culture plastic (between 0.1 and 10 kPa vs 10 MPa). This can have a beneficial effect on differentiation of stem cells [16, 17] and can avoid de-differentiation of primary cells [18].

We assessed the effect on ligand concentration on the behaviour on the hydrogels. We showed that 3T3 fibroblast can attach from the lowest Gel-TA concentration (31.25 μg/ml) and no significant effect of ligand concentration was seen. This indicates that these cell types have large number of integrins available to bind on the enriched hydrogels. Furthermore, it shows that minute concentrations are required for robust attachment, in this case 0.003% w/v in a 10% w/v hydrogel. This makes our approach highly cost-effective. It also cast a doubt on the ligand concentrations available in pure Gel-MA or collagen gels, which are of completely different order. As it is known that ligand concentration plays a significant role in cell behaviour this is an interesting point

for further studies [9]. The same experiment in HUVECs showed a ligand concentration dependent effect on cell behaviour. At low ligand concentrations the cells presented a spindle shaped migratory phenotype, similarly as on matrigel. Moreover, sprouting was observed. This in contrast to the cuboidal phenotype seen on higher ligand concentrations. It is known that the strength of attachment has an influence on the migration properties of cells in 2D [9]. Here, we show that we can influence these properties simply by changing the ligand concentration. This allows for tuneable hydrogel properties tailored towards migration or to proliferation.

We subsequently assessed the effect of enriching the hydrogel in 3D. We showed that cells in low density (2.5% and 5% w/v) hydrogels enriched with Gel-TA showed higher metabolic activity after 14 and 21 days, compared to bare or unmodified gelatin enriched gels. However, this effect was not visible in high density hydrogels (10% w/v). It is possible that the cells in these high density hydrogels are trapped by the small mesh size and cannot properly remodel their environment in the experimental time [19]. This would reduce their interaction with the ligands and therefore minizes their effect. This difficulty to remodel the hydrogels is also seen in hydrogels of middle density (5%). While the metabolic activity is high in Gel-TA enriched hydrogels, the cells remain rounded, cannot spread and do not migrate. In the low density hydrogels however, the cells do spread and migrate after 21 days. The amount of cells attaching and migrating is also higher in Gel-TA enriched gels versus gelatin enriched gels. This indicates that both a low gel density and sufficient attachment properties, as well as covalent cross linking of the ECM proteins in the matrix are required for migration behaviour in these hydrogels [14].

To further test this, we assessed cell behaviour in very low density hydrogels after 1 week of culture. We showed that cells in 1.25% w/v gels attached, migrated and created extensive networks after only week of culture in Gel-TA hydrogels. In stark contrast to bare and gelatin enriched hydrogels or to hydrogels with larger density (2.5%). This further substantiates the claim that a hydrogel of sufficiently low density is needed for cells to actively migrate through the gel. It is likely that the increased mesh size is responsible for the faster migration of cells in lower density hydrogels. While this migration is beneficial for many 3D applications, the trade-off is the weaker mechanical strength of low density hydrogels. This is not a major problem for cell culture applications, but could become problematic in bioprinting. Therefore it might be useful to extent the toolbox to complement the polysaccharide gels with ECM proteins or peptide sequences that can be remodeled by proteases like Matrix Metalloproteinases (MMPs). This can increase the local degradability of the hydrogel and improve migration without significantly sacrificing mechanical strength. We will further build on this toolbox by incorporating other ECM proteins, peptides, growth factor adhesion sites, and potentially growth factors themselves. This will finally lead to an extensive toolbox to create the hydrogel of desire for the application of choice.

8.5 Conclusion

We have shown the development of a polysacharide hydrogel system based on enzymatically crosslinking of polymer tyramine conjugates that is easily tuneable in mechanical properties and highly biocompatible. To improve the biological properties we have modified gelatin with tyramine and enriched the hydrogels. We showed improved cell attachment, migration and proliferation for sustained periods. Furthermore, we demonstrated control over cell fate simply by altering ligand concentration. In encapsulation studies we showed that enrichment with Gel-TA increases metabolic activity, and leads to rapid migration and network formation in low density, but not in high density hydrogels. This shows that the simple toolbox already results in tuneable and desirable mechanical and biological properties to control cell behaviour. We intent to further develop this by adding other ECM proteins, peptides and growth factor adhesions sites. This will lead to an extensive toolbox to create the hydrogel of desire for any specific application.

8.6 Supplementary information

8.6.1 Influence of hydrogel density and (tyramine functionalized)-gelatin on mechanical properties

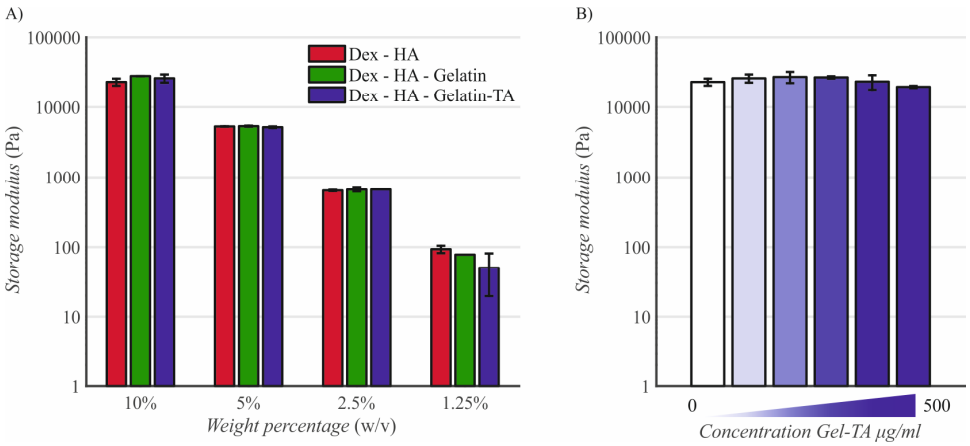

Supplemental figure 1: A) The effect of hydrogel concentration and addition of (tyramine functionalized)-gelatin on mechanical properties was assessed. It can be seen that the storage modulus can be tuned by weigth percentage of hydrogel. From 10000 Pa at 10% w/v down to 100 Pa at 1.25% w/v. Gelatin (-TA) had no effect on the mechanical properties. B) The addition of gelatin-TA had no effect on mechanical properties at the concentrations tested.

8.6.2 Influence of (tyramine functionalized)-gelatin on cell attachment to Dex-HA – TA hydrogels

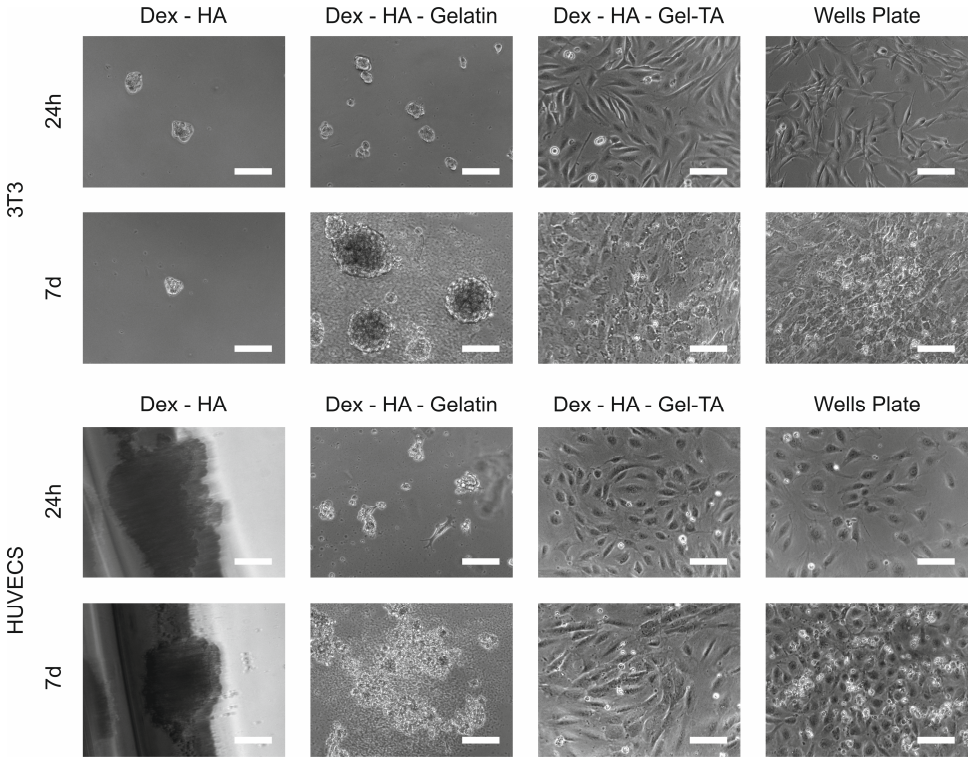

Supplemental figure 2: The figure shows the effect of addition of gelatin or Gel-Ta to Dex-HA – TA hydrogels after 24h and 7 days for both 3T3 fibroblasts and HUVECs. It can be seen the 3T3 fibroblasts do not adhere to Dex-HA – TA hydrogels and start to aggregate. Larger aggregates are formed on the edges of the wells, likely by rolling of smaller aggregates by gravity (not shown). On Dex-HA – Gelatin gels the cells also start to form aggregates, but these remain in place and grow bigger, indicating that some cell attachment does occur. On Dex-HA - Gel-TA gels, cells attach and proliferate to confluency after 7 days, similarly as on a wells plate. In HUVECs similar behaviour is observed. On Dex-HA – TA gels, no cell attachment is observed and most cells end in large aggregates at the edge of the wells. On Dex-HA – Gelatin the cells remain at the spot and form small aggregates, but do not spread. On Dex-HA – Gel-TA the cells spread and proliferate to confluency, as on the wells plate. The morphology of the confluent cells on the gels in different from that on the wells plate. On the gels, the cells remain more spindle like, in contrast to the cuboidal shape on the wells plate.

8.6.3 Influence of Gel-TA concentration on cell behaviour seeded on Dex-HA –TA hydrogels

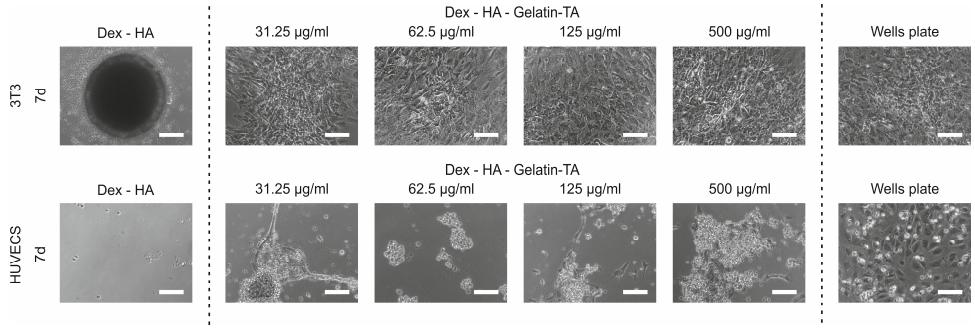

Supplemental figure 3: The effect of Gel-TA concentration on Dex-HA – Gel-TA hydrogels after 7 days of culture with 3T3 fibroblasts and HUVECs. It can be seen the fibroblasts on Dex-HA – TA gels remain in one large aggregate after 7 days. On all the Gel-TA concentration applied here, the cells are grown to full confluence, with morphology similar to on a wells plate. The HUVECs remain on Dex-HA – TA gels in single rounded cells and in a large aggregate at the edge of the gel. At the lower Dex-HA – Gel-TA concentrations it can be seen that remains of structures seen after 4h and 24h are still visible, yet part of the cells have retracted and started to aggregate. At higher Gel-TA concentrations (125 µg/ml and 500 µg/ml) the confluent cell layer seen after 24h has started to organize and form sprouts and networks, with local proliferation. This is in contrast to the wells plate, where the cells have grown to near confluence, with no apparent organization.

References

1. Caliari, S.R. and J.A. Burdick, *A practical guide to hydrogels for cell culture.* Nature Methods, 2016. **13**: p. 405.
2. Huang, G., et al., *Functional and Biomimetic Materials for Engineering of the Three-Dimensional Cell Microenvironment.* Chemical Reviews, 2017. **117**(20): p. 12764-12850.
3. Li, H., C. Tan, and L. Li, *Review of 3D printable hydrogels and constructs.* Materials & Design, 2018. **159**: p. 20-38.
4. Gjorevski, N., et al., *Designer matrices for intestinal stem cell and organoid culture.* Nature, 2016. **539**: p. 560.
5. Walters, N.J. and E. Gentleman, *Evolving insights in cell–matrix interactions: Elucidating how non-soluble properties of the extracellular niche direct stem cell fate.* Acta Biomaterialia, 2015. **11**: p. 3-16.
6. Jin, R., et al., *Enzyme-mediated fast in situ formation of hydrogels from dextran–tyramine conjugates.* Biomaterials, 2007. **28**(18): p. 2791-2800.
7. Darr, A. and A. Calabro, *Synthesis and characterization of tyramine-based hyaluronan hydrogels.* Journal of Materials Science: Materials in Medicine, 2009. **20**(1): p. 33-44.
8. Jin, R., et al., *Enzymatically Crosslinked Dextran-Tyramine Hydrogels as Injectable Scaffolds for Cartilage Tissue Engineering.* Tissue Engineering Part A, 2010. **16**(8): p. 2429-2440.
9. Ayres-Sander, C.E. and A.L. Gonzalez, *Approaches in extracellular matrix engineering for determination of adhesion molecule mediated single cell function.* Frontiers in Biology, 2013. **8**(1): p. 32-49.
10. Nicosia, R. and A. Ottinetti, *Modulation of microvascular growth and morphogenesis by reconstituted basement membrane gel in three-dimensional cultures of rat aorta: A comparative study of angiogenesis in Matrigel, collagen, fibrin, and plasma clot.* In Vitro Cellular & Developmental Biology - Plant, 1990. **26**(2): p. 119-128.
11. Arnaoutova, I., et al., *The endothelial cell tube formation assay on basement membrane turns 20: state of the science and the art.* Angiogenesis, 2009. **12**(3): p. 267-274.
12. Shu, X.Z., et al., *Attachment and spreading of fibroblasts on an RGD peptide–modified injectable hyaluronan hydrogel.* Journal of Biomedical Materials Research Part A, 2004. **68A**(2): p. 365-375.
13. Seidlits, S.K., et al., *Fibronectin–hyaluronic acid composite hydrogels for three-dimensional endothelial cell culture.* Acta Biomaterialia, 2011. **7**(6): p. 2401-2409.
14. Lee, J., et al., *Traction forces generated by locomoting keratocytes.* The Journal of cell biology, 1994. **127**(6 Pt 2): p. 1957-1964.
15. Maskarinec, S.A., et al., *Quantifying cellular traction forces in three dimensions.* Proceedings of the National Academy of Sciences of the United States of America, 2009. **106**(52): p. 22108-22113.
16. Sun, M., et al., *Effects of Matrix Stiffness on the Morphology, Adhesion, Proliferation and Osteogenic Differentiation of Mesenchymal Stem Cells.* International journal of medical sciences, 2018. **15**(3): p. 257-268.
17. Park, J.S., et al., *The effect of matrix stiffness on the differentiation of mesenchymal stem cells in response to TGF-β.* Biomaterials, 2011. **32**(16): p. 3921-3930.
18. Cozzolino, A.M., et al., *Modulating the Substrate Stiffness to Manipulate Differentiation of Resident Liver Stem Cells and to Improve the Differentiation State of Hepatocytes.* Stem cells international, 2016. **2016**: p. 5481493-5481493.
19. Liu, Y. and M.B. Chan-Park, *Hydrogel based on interpenetrating polymer networks of dextran and gelatin for vascular tissue engineering.* Biomaterials, 2009. **30**(2): p. 196-207.

"A long stretch of road will teach you more about yourself than a hundred years of quiet introspection."

“Try not to become a man of success, but rather try to become a man of value”

9

Discussion and outlook

9 Discussion and outlook

The main goal of this thesis was to develop strategies that could save the joint from unavoidable progression into osteoarthritis. We have focussed on two main subjects to achieve this: new methods for early diagnosis and early treatment. In this chapter we will recapitulate on the successes, limitations and potential improvements of our approach.

In chapters 3 and 4 we focussed on developing a new method for the early diagnosis of osteoarthritis. These methods are highly desired to prevent progression, evaluate treatment efficacy and to aid in the development of new drugs. We aimed to develop a biomarker detection assay with stringent requirements. The assay needed to be able to detect minute concentrations of biomarkers in small volumes of synovial fluid, a highly challenging complex fluid. Moreover, multiple classes of biomarkers needed to be detected simultaneously requiring a broad dynamic detection range and the potential for multiplex measurements of biomarkers. To date no assay existed that could meet these requirements.

We demonstrated in chapter 3 the development of such a biomarker assay based on surface plasmon resonance imaging (SPRi). We applied a new enhancement cascade based on biotinylated nanoparticles to increase the SPRi signal. Using this approach we reached sub fM sensitivity, a dynamic range of 7 logarithms and high specificity measuring four cytokines simultaneously. We subsequently showed good recovery after spiking in synovial fluid, indicating a large potential for the assay.

Subsequently, we continued the development of this system in chapter 4. We focussed on improving the applicability for clinical practice. In this setting, especially a good quality control system is essential. The SPRi technology is highly suited by its real time measurements. We kinetically characterized the assay and showed the potential of this approach. We were able to fully predict the enhancement cascade, which allows for identification of cross-reactivity, heterophilic antibodies and spotting irregularities. Furthermore, we showed this enables calibration free measurements that saves valuable resources and time. Finally, we demonstrated that this toolbox allows for simple further optimization of the assay.

The data from chapters 3 and 4 have led to the development of a powerful biomarker assay with characteristics that are highly suitable for clinical translation. This assay could be applied in several interesting applications.

The first application is the early diagnosis of osteoarthritis. As this disease is still only diagnosed after symptoms are present, often decades after disease onset, there is a high demand for such a system. For this purpose, two situations could be imagined.

In the first situation, the assay is used as an early screening for patients with high risk of developing OA. These patients include the elderly, the obese and patients with a history of joint injury and /or osteoarthritis in family members In a very early stage the

biomarkers in the joint of these patients can measured, enabling an early and highly specific diagnosis. This could result in a reduced progression by early treatment and possibly altogether prevention of osteoarthritis. A limitation to this approach is that it might be difficult to obtain sufficient synovial fluid from relatively healthy patients. Additionally, patient approval for synovial fluid aspiration might be challenging. Therefore, it is recommended to further develop the assay for urine and plasma biomarker measurements.

In the second setting, the assay will be used to improve the current diagnostic setting. A patient comes the hospital with complaints. Instead of only an X-Ray, the patients' biomarkers will additionally be measured. This results in a much more specific diagnosis, could provide clear prognosis and could lead to a better defined treatment plan. For example, if a specific biomarker or class of biomarkers is pathologically elevated, drugs can be applied that target the underlying pathways. The effect of these drugs can be assessed over time and treatments can altered accordingly, long before structural changes to the joint are visible.

Biomarkers also have a significant role in drug development. In the current setting, it is notoriously difficult to develop disease modifying drugs for osteoarthritis. This is partly due to the lack of sensitive outcome measures. Most clinical trials rely on subjective surveys and on insensitive and low specific X-Ray measurements. Therefore, subtle but important differences to the joint are missed and drugs can be incorrectly labelled ineffective. Secondly, the heterogeneous nature of OA means that the pathways leading to the disease can differ significantly in different patient populations and so can the effectiveness of drugs. The biomarker assay we have developed, can be applied to improve both major hurdles. It can potentially provide a highly sensitive clinical end point to supplement the clinical or X-Ray end points. It can provide a much clearer overview of the joint status and progression. Moreover, patients' biomarker status can be measured before entering the trial to stratify the patient population. This can enable inclusion criteria for specific drug and help elucidate reasons for none responders.

Despite the large potential of the assay, there remain some limitations to our approach. An important one is the time it takes to acquire a single measurement. Together with sample collection and machine preparation, approximately 4 hours are required for a full assay. This is reasonable for screening purposes and diagnosis in the hospital. However, if point of care applications or treatment guidance during surgery are desired, this time is too long. Preferably, an assay time of maximally 30 minutes would be acceptable for these applications.

Reducing the time in the current assay would result in unacceptable loss in sensitivity for several biomarkers. This sensitivity is dependent on the specific antibodies and on the nanoparticle enhancement. To address this issue we are working from two sides. On the one hand we are looking at alternative ligands to bind the biomarkers apart from the traditional antibodies. Promising in this respect is the work performed with cameloid nanobodies (VHH), which show generally higher affinities and better stability. On the

other hand, we are looking to improve the enhancement of the signal by the application of different nanoparticles. We will look in more detail to larger or smaller particles, different materials or a combination of materials, and to particle shape. Together this should lead to an improvement of the sensitivity of biomarker detection and could result in shorter assay times.

In addition to this, point of care applications would benefit from automation and miniaturization of the SPRi machine. In current setting a bulky, expensive machine is required for the measurements. The machine enables extensive customization and control and is suitable for application in clinical laboratories, as was confirmed by clinical chemists. However, when applications at general practitioner level are desired, more fool proof and less expensive machinery is needed. This issue is known to the suppliers of SPRi devices and new machines are being developed to address this. For example, IBIS technologies is currently developing a table top model of their machine that is significantly more automated at an estimated 5 times reduced cost. This machine and others in pipeline at competitors could bring the technology to the desired level for point of care applications.

In the current assay we have shown promising data on the measurement of 4 cytokines implicated in osteoarthritis. These cytokines could provide crucial information on the activity of multiple inflammatory pathways. However, the disease is notoriously complex and several other pathways are implicated. A more expanded, but not exclusive list, would at least include the FGF, TGF-beta and Wnt pathways [1-3]. Therefore, biomarkers for these and other pathways should be included to gain a broader picture of the disease state as was explained in more detail in chapter 2. Moreover, biomarkers describing the rate of anabolism or catabolism should be included. Interesting in this respect are markers for cartilage degradation, such as COMP and CTX-II which have been widely investigated in OA and shown to have some clinical usefulness [4, 5].

Currently we have already made first steps in expanding our panel to other promising biomarkers. We have been working on developing the assay for inflammatory makers associated with macrophage polarisation (IL-4 and IL-8) and recruitment (CCL-2), and for the anti-inflammatory marker IL-10. We have selected the desired antibodies for these markers and have already shown promising results for IL-8 and CCL-2. In addition, we have made progress in expanding the assay for markers of the WNT pathway. We have developed VHH nanobodies for the Wnt antagonists DKK1 and FRZB which show good affinities in SPR and potential for multiplexing.

In collaboration with Bristol University we have been working on a highly promising biomarker for early diagnosis. In a study of 284 participants, the group of Mo Shariff found a fragment of Complement 3 (C3F) via mass spectometry in serum, that could distinguish between OA, RA and healthy knees from K&L score 0 [6]. It is unique that a single biomarker has such power in detecting the disease. However, the subsequently developed ELISA assay was not sensitive enough to measure this marker in the same samples. Therefore, we have been working on developing an assay for this biomarker

based on SPRi. We have already characterized the antibodies and shown the feasibility of our enhancement cascade. Preliminary results show a very high sensitivity in clean buffers. We are working on further characterizations and will perform spiking experiments in serum. Finally, the assay will be validated via samples provided from Bristol University.

Next to biomarkers from human patients, we have also been working on developing the biomarker assay for patients from other animals. In collaboration with the veterinary department at the University of Utrecht, we have been developing a biomarker assay for inflammatory markers that could be applied in the equine species. We have already developed an assay for the markers IL-1β, TNF-α and CCl-2. We are currently planning to measure these markers in a study that evaluates the effect of exercise on the development of OA in horses. This could eventually result in broadening the application of our assay to horse patients. As osteoarthritis is a highly prevalent disease in these animals, there is a large potential for such assay.

In collaboration with the University of Utrecht we are also planning to expand our technology for the use in dogs. Our collaborators are currently performing experiments with joint distraction as a therapy for OA in dogs and are in search for adequate biomarker assays for the read-out. We are evaluating the options to develop biomarker assays to aid in these experiments. Eventually, this can result in the application of our technology in dogs, which has again a major OA prevalence.

We have developed an enhancement cascade for SPRi to primarily measure proteins as biomarkers. However, the application could be broadened to other classes of promising OA biomarkers such as micro RNAs (miRNA) that are implicated in disease progression. As the enhancement cascade is general for biotinylated species, it can be potentially be applied to detect miRNAs in a sandwich format with SPRi. To this end, we started a collaboration with Majid Nasiriboroumand in which we are attempting to measure micro RNAs important in OA. When successful, this could enable a simple sensitive assay for miRNAs in OA, and could eventually result in a unique hybrid assay for measurement of protein and RNA biomarkers in one single assay.

Considerable work has been performed and is ongoing in the development of the biomarker assay for early OA diagnosis. However, a major hurdle to overcome is the validation of the assay in patient samples. We are already working on this in collaboration with the University of Bristol and are starting a collaboration with Saxion University and the MST hospital to further this goal. Work on validation of the assay will lead to further improvement and bring it one step closer to clinical application.

In summary, we have developed a highly sensitive biomarker assay with many potential applications. We have discussed the major limitations and demonstrated possible solutions and our progress towards them. We consider that overall, we have made major steps in the development of a new method for the early diagnosis of osteoarthritis. This will have a large benefit for new and existing patients, by improving

existing treatments and reducing progression, and is the essential start for saving the joint.

In the second half of the thesis, we mainly focussed on new treatments to prevent the progression of OA. In current situation no preventive or disease modifying treatments exist is clinical practice. We have made an attempt to help in filling this gap. As the disease is highly heterogeneic and complex, several avenues exist for potential treatments. Highly promising are new specific drugs targeting implicated pathways, such as WNT antagonists [7]. Other procedures target risk factors and help modulate the disease by exercise and diets. While these treatments are potentially helpful, they are unlikely to be effective when significant cartilage damage has already occurred. We therefore focussed on treatments targeting cartilage repair in an early stages of trauma, to prevent progression into osteoarthritis. Inspiration for this are chondrocyte implantations and the impact trail that have large promise for the repair of cartilage defects [8]. Here, we worked on effective methods to apply cells with potent biomaterials to relatively large defects to enable an optimal regeneration response.

In chapter 5, we developed an analytical model to predict cell viability post impact in spray applications. This model can predict the deformation of a cell in a compound droplet, depending on droplet volume, velocity and viscosity. We fully characterized the cell spray droplets at specific flow rates, air pressures and distance from the nozzle. These droplet populations were then used as input to the model. We subsequently showed this model accurately predicts the cell viability depending on the applied air pressure, distance, viscosity and surface tension. We showed that a larger pressure, shorter distance, higher viscosity and higher surface tension result in a marked decrease in cell viability.

This information is useful to optimize spray applications in clinical practice. When cells are sprayed to treat (osteo-) chondral defects, they are applied on a stiff surface at short distance. It is therefore essential that cell spray pressure and viscosity are minimized to obtain optimal results. This places restraints on materials in which the cell are sprayed and is important to consider. In addition, it could be an interesting strategy to first apply a thin layer of soft hydrogel before spraying the cells. This results in reduced surface stiffness and increased viability.

An additional strategy to improve cell viability based on this data is to improve the cell spray device. In collaboration with Koen Dijkstra at the University of Utrecht, we have developed new arthroscopic spray devices that applies the insights gained by our model. This spray device creates droplet that have a lower velocity resulting in improved viabilities [9], highly suitable for clinical application.

In chapter 6 we set out to expand our model to include the effect of cellular properties. We evaluated 8 cell lines from different tissues and looked at cell viability post-impact. We discovered that there were large differences between the viability depending on the cell type, with viabilities ranging from 30% to 95% at the same condition. Subsequently, we applied our model to determine which cellular properties could be responsible for

this large difference. We identified three main parameters: Cell size, cell viscosity and membrane strength. We then altered these properties one by one in 3T3 fibroblasts and C20A4 chondrocytes to determine whether we could improve the cell viability. We showed that altering the cell size and viscosity by osmolarity of medium could significantly improve the viability with the same cell type. In addition, both lowering and increasing the cholesterol content to either improve cell stiffness or membrane strength led to an improved cell viability.

This can be used in a clinical setting to improve the cell spray viability. A simple procedure is to increase the osmolarity of the spraying buffer. This will result in smaller, more viscous cells that are better capable of surviving the droplet impact. This is an inexpensive, easy to apply approach with limited side effects that can have major benefits. In addition, or as an alternative, the cholesterol content could be adjusted (either increased, or decreased depending on the cell type) to improve cell viability. However, this approach may lead to detrimental side effects since the cholesterol content is important in cell function.

In chapter 7 we continued to improve our analytical cell viability model. We designed a custom set-up that enabled us to investigate cell viability post impact with controlled droplet size and independently controlled impact velocity. We performed experiments in which the effect of droplet size and impact velocity on cell viability was assessed. This resulted in an improved cell impact viability model. This model confirms the relationship between the impact velocity and viability that was previously discovered in chapter 5. However, an inverse relationship between the outer droplet size and viability was found. In the previous model it was expected that a larger droplet results in more cushioning and therefore a reduced cell deformation. The current results and model shows that in fact the outer droplet is the main factor governing the deformation. A larger droplet at same velocity has more kinetic energy, resulting in larger deformation. The results indicate that this larger deformation is equally transferred to the inner droplet (the cell) and therefore results in increased cell damage. Interestingly, the results from the cell spray experiments performed previously did follow the same trend, providing confirmation for the new model.

Despite these interesting results, it is clear that further validation of the model is required. We have performed experiments with relatively large droplets often used in bioprinting applications. Experiments should be performed with smaller droplets to expand the reach of the model. Furthermore, experiments should be performed in which the viscosity is altered. This will result in a cell viability model that is not only suitable to improve cell spraying, but is predictive for the majority of bioprinting applications. This will vastly improve the reach and usability of our model. In the majority of bioprinting applications there is a delicate balance between printability and cell viability. An intricate understanding of the processes governing the cell viability can result in targeted rational improvements of bioprinting applications.

In future work we aim to further improve our understanding of cell viability during deformation processes. In collaboration with Alvaro Marin of the Physics of Fluids group at the University of Twente, we are working towards this goal. We have developed a microfluidics set-up in which we can controllably deform compound droplets containing cells. We can monitor the deformation in real time and simultaneously determine the influence on the viability of the affected cells. This can result in further improvements and validation of our model. Furthermore, the real-time monitoring can provide new fundamental insights in cell damage during deformation events.

These cell spray and bioprinting applications can be used to treat cartilage defects and thereby help in preventing osteoarthritis. In these treatments, a combination of cells and biomaterials is used to achieve this goal. However, the biomaterials that are currently used in cell spraying of chondral defects are often weak or have suboptimal biological properties. In chapter 8 we developed a toolbox to improve in situ crosslinkable polysaccharide hydrogels with bioactive moieties to create a highly versatile biomaterial. Specifically, we showed a proof of concept by modifying gelatin with tyramine that can be added to dextran- and hyaluronic acid - tyramine hydrogels. We showed that adding gelatin-TA at minor concentrations already resulted in cell attachment and proliferation. Moreover, we showed that we could control cell behaviour by adjusting the gelatin concentration. In 3D, we demonstrated that adding gelatin tyramine resulted in increased metabolic activity and in extensive network formation at low hydrogel densities.

This developed hydrogel is highly suitable to be used in combination with cell friendly spray applications to treat chondral defects. The material can be tuned such that cell migration is possible, while retaining excellent mechanical properties and simultaneously eliciting large metabolic activities. This combination is ideal for tissue remodelling and therefore optimal for the regeneration of tissue. In addition, the dextran – hyaluronic acid gels have shown to crosslink directly to damaged cartilage, enabling good integration with surrounding tissue [10]. This makes the material also highly interesting for cell free therapies. The tight integration with surrounding tissue in combination with the openness to migration can enable rapid ingrowth of cells from the surrounding cartilage. This can enable a simple one step operation to treat early cartilage defects. This is confirmed by subsequent work, not included in this thesis, in which we have performed an in vivo study comparing the gelatin enhanced hydrogels versus basic hydrogels at several gel densities, when implanted subcutaneously. Here, we showed considerably improved integration and increased cell migration into the hydrogels when gelatin – TA was added.

A major limitation is that the gelatin enhanced hydrogels were only tested by using fibroblasts and endothelial cells as models. Ideally, the behaviour of chondrocytes in and on these hydrogels should be tested before further applications can be considered. Promising in this respect is the work that has been performed with basic dextran-hyaluronic acid – tyramine hydrogels in combination with chondrocytes. Excellent biocompatibility, large metabolic activity and good cartilage production was shown [10].

It is likely that addition of gelatin TA will only further improve these properties. Despite this expectation, it is important to further develop the biomaterial toolbox to include bioactive moieties such as other Extra Cellular Matrix (ECM) proteins, peptides and growth factor binding sites. Interesting for cartilage is the addition of fibronectin, found in developing cartilage, but also polysaccharides such as chondroitin sulphate. Currently we are working on a project to further develop these materials.

In summary, we have undertaken extensive work on the modelling and improvement of cell spray and bioprinting applications that can be highly useful for treating cartilage defects in an early stages of OA. We subsequently developed improved biomaterials with optimal properties to facilitate optimal tissue regeneration response. However, it remains important that the cell spray applications in combination with the improved hydrogels should be tested ex vivo and in vivo on cartilage defects to demonstrate their potential. This provides ample room for future researchers to bring our work to the next level

In conclusion we have developed new methods for both the early diagnosis and treatment of osteoarthritis. These strategies have shown great promise and represent a significant step towards saving the joint.

References

1. Weng, T., et al., *Genetic Inhibition of Fibroblast Growth Factor Receptor 1 in Knee Cartilage Attenuates the Degeneration of Articular Cartilage in Adult Mice.* Arthritis and rheumatism, 2012. **64**(12): p. 3982-3992.
2. Xie, L., et al., *Systemic neutralization of TGF-β attenuates osteoarthritis.* Annals of the New York Academy of Sciences, 2016. **1376**(1): p. 53-64.
3. Zhu, M., et al., *Activation of β-Catenin Signaling in Articular Chondrocytes Leads to Osteoarthritis-Like Phenotype in Adult β-Catenin Conditional Activation Mice.* Journal of Bone and Mineral Research, 2009. **24**(1): p. 12-21.
4. Kraus, V.B., et al., *OARSI Clinical Trials Recommendations: Soluble biomarker assessments in clinical trials in osteoarthritis.* Osteoarthritis and Cartilage. **23**(5): p. 686-697.
5. Mobasheri, A., et al., *Osteoarthritis Year in Review 2016: biomarkers (biochemical markers).* Osteoarthritis and Cartilage, 2017. **25**(2): p. 199-208.
6. de Seny, D., et al., *Discovery and biochemical characterisation of four novel biomarkers for osteoarthritis.* Annals of the rheumatic diseases, 2011. **70**(6): p. 1144-1152.
7. Yazici, Y., et al., *A novel Wnt pathway inhibitor, SM04690, for the treatment of moderate to severe osteoarthritis of the knee: results of a 24-week, randomized, controlled, phase 1 study.* Osteoarthritis and Cartilage, 2017. **25**(10): p. 1598-1606.
8. de Windt, T.S., et al., *Allogeneic MSCs and recycled autologous chondrons mixed in a one-stage cartilage cell transplantion: a first-in-man trial in 35 patients.* Stem Cells, 2017. **35**(8): p. 1984-1993.
9. Dijkstra, K., et al., *Arthroscopic Airbrush-Assisted Cell Spraying for Cartilage Repair: Design, Development, and Characterization of Custom-Made Arthroscopic Spray Nozzles.* Tissue Engineering Part C: Methods, 2017. **23**(9): p. 505-515.
10. Jin, R., et al., *Enzymatically Crosslinked Dextran-Tyramine Hydrogels as Injectable Scaffolds for Cartilage Tissue Engineering.* Tissue Engineering Part A, 2010. **16**(8): p. 2429-2440.

Acknowledgements for quotes

I would like to thank my friends and family for the creativity in searching for appropriate quotes in front of each chapter, either by choosing an existing one or even by constructing a new one. I will give a short list of the quotes used, the original author and who picked the quote.

- Chapter 1: “If we knew what we were doing, it wouldn’t be called research” – Albert Einstein (Joost)
- Chapter 2: “One may miss the (bio)mark by aiming too high as well as too low” - Thomas Fuller (Hanneke)
- Chapter 3
    - “The cool thing about this enhancement cascade is, that together it is more than the sum of its parts. Each element is crucial and contributes in its own way to the success of the system. This technique mimics the complex interaction cascades of biology on a small scale” - Lisanne
    - “60 percent of the time, it works all the time” - Anchorman (Joost)
- Chapter 4: “It would be so nice if something made sense for a change.” - Alice in Wonderland (Jelmer)
- Chapter 5
    - “Don’t let your printer know you are in a hurry, it smells fear” - Iris
    - “As with his beer, the author ensures with his research that not a single drop is wasted.” – Stefan
- Chapter 6: Hot off the press! What’s the hype – bioprinting parameters tailored to cell type?! Read the exclusive inside story in chapter 6 – Maartje
- Chapter 7
    - “A droplet of wisdom can cause a ripple in the sea” – Cornelia
    - “I may not have gone where I intended to go, but I think I have ended up where I needed to be.” - Douglas Adams (Vincent)
- Chapter 8: “At the heart of difficulties are possibilities” -Harry
- Chapter 9
    - "A long stretch of road will teach you more about yourself than a hundred years of quiet introspection." Patrick Rothfuss (Lisanne)
    - “Try not to become a man of success, but rather try to become a man of value” Albert Einstein (Harry)

I will end this section with a poem that my parents chose and fits well with this thesis and our work in general. Zomaar…

De bondgenoot

de suggestie van leven is het leven zelf

de verwachting van leven is wat je er aan geeft

je lichaam is het voertuig dat bewogen wordt door de geest

de richting die het gaat wordt bepaald door de taal

die je met de ander spreekt

de ander ben jezelf van je tenen tot aan je kruin

van je innerlijk tot aan de sterren

zijn we kosmisch één geheel

misbruik dit lichaam niet

maar heb het lief

Acknowledgements

I would like to take the time to thank everybody involved directly or indirectly during my PhD project and in creating this thesis.

I would like to start by thanking Marcel Karperien for the supervision during the project. I have been working together with Marcel since my internship in Liverpool in 2012. It has always been very pleasant and relaxed to work with him as a supervisor. He is easy to approach, I could always walk into his office and I did, and he always has useful advice if you're struggling with something. At the same time he has always given me the freedom and trust to approach my work and the experiments in the way I deemed fit. Of course, I hit a few bumps, but it has helped me improve my independence and take responsibility. Therefore I'm happy that I will be working with him for the coming years in my post-doc research.

Secondly, I would like to thank my second supervisor Daniel Saris. As a surgeon, Daniel has constantly kept me sharp in thinking on the practical implications and possible translation of my work. It has given an extra dimension to my thesis and my thinking that I really appreciate. On a personal level, Daniel's more direct style provided a nice balance to Marcel's. It has kept me alert on improving, among other things, my time management skills. Something that I'm continuing to this day. In general he has taught me a lot and I hope we can continue to collaborate in the future.

I also would like to thank my supervisors from my master assignment, which in part has continued in this thesis. I would like to thank Sieger Henke, who has helped me with the cell work in my masters and has helped me getting started during the PhD as my office mate. I really enjoyed working together and the talks in the office. I would also like to thank Claas Willem Visser. As my second supervisor he has helped me with the cell spray work, which we have continued during the thesis. I always enjoyed and still enjoy working together with him. He is still teaching me a lot about science and is a great example to me.

I want to thank my colleagues who helped me through the hard times and with the fun times. First I'd like to thank my office mates. Rong and Leilei, I had great talks with you and learned a lot about Chinese culture. Leilei, I'm honoured to have been your paranymph and of course to be 'godfather' to Meinan! Hopefully, we can meet again someday at your place in China. Lisanne, I'm happy you came to our office, when it had gotten pretty empty. You livened up the place with positive spirit, good conversations and discussions about both personal and work stuff, and of course thanks for being my paranymph!

Michelle and Maik came later to the office, but completed it. Michelle became my SPR buddy and my bear/hot springs 'hunting' partner in Canada, and Maik always provided good stories, also about Asian culture, and is just a funny guy.

During the PhD I had many collaborations with my colleagues in formal and informal settings that I'm thankful for. They enriched my thesis, my output and my working life. I'd like to thank Tom for his help with my thesis and for the collaborations we have had. A great guy to work with, scientifically keeps you sharp and good to have at the borrels. I'd also like to thank Bram for the collaboration. Together, we have continued the work on the hydrogel/protein combinations, which we are still successfully improving. Furthermore, I'd like to thank Kannan for the collaboration on FRAP and Koen for the work on improved spray nozzles.

Then I have to thank Jacqueline for her part in our work. She has been essential in keeping the lab running and has been doing an excellent job in this. And I'm thankful that she sort of accepted my 'free interpretation' of some lab rules and allowed me to do my work.

I'd specially like to mention some colleagues. Brenda and I, started our PhD at roughly the same time. We therefore became PhD-buddies with similar issues and progress which was helpful and fun. Rolf from the AST group and me started to give combined and ever growing borrels. They were always fun, sometimes legendary and actually also provided some of the best inspirations. I'd also like to thank Bas who I still consider as prodigy for borrel organization, for his good stories, indoor football matches and general good fun. And I'd like to thank Carlo, who provided a good boost to the group spirit with the weekly coffee breaks and his enthusiastic Italian character.

Finally, I want to thank all other colleagues who made my PhD a fun time! I won't be able to name you all, but I'd like to thank Yao, Joâo, Melvin, Malin, Jin, Sakshi, Julia, Bastien, Simone, Yusuf, Jean-Baptiste and Barbara.

Without you, it would not have been the same.

I also have a lot to thank my students for. Without them I would never have been able to deliver the thesis as it is now.

First I want to thank my first bachelor- and later also master students Jorke and David. The bachelor assignment was often hard work with long days and sometime evenings, but you persevered without much complain. Therefore, I'm thankful you decided to return for a master assignment adventure after the hard work during the bachelor one. A special thanks to Jorke, who became my partner in crime in stimulating nice active borrels. Although we are still waiting on him organizing a work karaoke night.

Directly after my first bachelor students I received an international master student from Portugal, Taciana Goncalves. I know the assignment didn't always go as we hoped, to the large frustration of us both. It has taught me a lot about the more difficult parts of research, but I think has made us both stronger. Besides the work, it was a really great pleasure of having you as my student. We had great talks, good borrels and parties and in general you were very pleasant to work with. In addition, I'm happy that your time here inspired you to stay in the northern region!

I additionally would like to thank my bachelor students who performed a lot of work on cell spray and impact modelling experiments. I would like to thank Iris and Jan who, among other things, characterized the viability between cell types after spraying, and Sophie, Emiel and Ceri-Anne who looked at the effect of cellular properties of the viability. I would like to thank Floor, Wendy, Danique and again also Jan and Iris for the work on the 'windmill' set-up to study impact viability in more detail. I know the set-up was challenging and could be intimidating at times, but it gave really interesting results. Together, you are largely responsible for two chapters in this thesis, for which I am very grateful. But in addition to this, I learned a lot from supervising you and had a great time doing it.

Considering the importance of my students for my PhD and my thesis I want to specially thank Janneke. She has been very successful in choosing the right students for my projects and therefore had an essential role.

The project had its hard times and its good times. My friends were essential in the process and deserve acknowledgements.

First I'd like to thank Stefan, who has been my closest friend since high school. He has always supported me, with help, but also with a beer, a boardgame or just some old-school age of empires. On the workplace, I appreciate the coffee breaks, walks and indoor football. I'd also like to thank the rest of the GD-unit! Vincent, Bas, Robbert, Marco and Rob. You have been great friends for a long time and I'm happy we're keeping it up.

I like thank the Prague/Krakow/Lisbon/Budapest/Riga group! Ramon, Joost, Jelmer and Berend, you have made the years more fun with festivals, parties, beers and of course the city trips. Hopefully many will follow. I'd also like to Han for still keeping in touch and playing pool and a pubquiz every now and then. And Iris. Our regular 'dates' and long phone calls were fun and helped to get stuff of the chest. I really appreciate this.

And finally my housemates. You have been there supporting me with food, a 'clean' house and good parties. It definitely provided the necessary distraction from the tough times in the research. I have had many nice roommates over the years, but I'd like to specially mention the 'core' group: Jelmer, Joost, Henk, Martijn, Floor and Mark. Thanks!

Finally, but importantly, I want to thank my awesome family. Mum and Dad, Joke and Jan, have raised me to who I am, have taught me a lot and are always there for me. Besides, they are fun to hang with, play football games with, and are just the best parents to have. Additionally, I want to thank my brother and sisters.

Maartje is my sweet little sister and is my festival buddy, concert buddy and just buddy. You're awesome. Hanneke, my big, almost professor, sister has taught me a lot in life, protected me when necessary and will do so again as my paranymph! Harry is my big brother who inspired me to love music, games and football. And although he hardly ever wins anymore, playing football games with him still provided nice distractions. And my oldest sister Cornelia is always supportive, in for good beers and conversations and introduced me to concerts, which is awesome. Of course I should also thank the spouses,

Sander, Sander, Nicole and Stephan, and of course the supercool ever-growing army of small ones Glenn, Dean, Yuna, Tavi and Mila. You are a great family! You are always there when I need you, have really helped me becoming who I am and helped me make it through the PhD process and towards this thesis.

As I'm writing this, I'm seeing how many people I am thankful for! It shows how many people are involved in many different ways in completing a large project like this. Everyone played a different part, some professional, some personal, but each one contributed in his or her way to this work. Therefore, I'm really thankful to all of you for making my PhD project and this thesis as it is today.

- Jan Hendriks -

Biography

Jan Hendriks was born on the 18th of June 1989 in Goor, The Netherlands. In 2007 he finished his pre-university education (VWO) with a dual specialization diploma (Nature & Technology and Nature & Health) from the Waerdenborch in Holten, The Netherlands. In 2007, he started his study Biomedical Engineering at the University of Twente. Three years later he finished his Bachelor with an assignment on the improvement of DNA transfection with interacting poly-amido-amines at the controlled drug delivery group. In 2010 he started his master in the direction of Molecular, Cellular and tissue Engineering. In 2012 he performed a case study for the Medical Cell Biophysics group on the quantification of the metastatic cascade preceding his study tour to Malaysia and Singapore. For his internship he worked with the group of John Hunt at the University of Liverpool in collaboration with the Developmental BioEngineering group at the University of Twente. Here, an in vivo study was performed on enzymatically crosslinkable hydrogels for the application in adipose tissue engineering. In his master thesis the angiogenic properties of the same hydrogels were improved and the application for cell-spray skin tissue engineering was evaluated. In 2013 he graduated on this topic at the group of Marcel Karperien, where he started his PhD in 2014. In his PhD he continued to perform work on cell-spray applications and associated cell survival. Additional, the biomaterials involved were further developed. A separate project was started on the early diagnosis of osteoarthritis with the use of SPRi technology. The diagnosis, cell-spray and biomaterial projects were ultimately combined to achieve new methods for early diagnosis and treatment of osteoarthritis.

Scientific Output

Peer-reviewed Papers

1. **Jan Hendriks**, Claas Willem Visser, Sieger Henke, Jeroen Leijten, Daniël B.F. Saris, Chao Sun, Detlef Lohse, Marcel Karperien. Optimizing cell viability in droplet-based cell deposition. *Published in Nature Scientific Reports, 2015.*

2. **Jan Hendriks**, Ivan Stojanovic, Richard B.M. Schasfoort, Daniël B.F. Saris, Marcel Karperien. A nanoparticle enhancement cascade for sensitive multiplex measurements of biomarkers in complex fluids with SPRi. *Published in Analytical Chemistry, 2018.*

3. Koen Dijkstra, **Jan Hendriks**, Marcel Karperien, Lucienne A. Vonk, Daniël B.F. Saris. Arthroscopic Airbrush-Assisted Cell Spraying for Cartilage Repair: Design, Development, and Characterization of Custom-Made Arthroscopic Spray Nozzles. *Published in Tissue Engineering Part C Methods, 2017.*

4. Kannan Govindaraj, **Jan Hendriks**, D.S. Lidke, Marcel Karperien, Janine N. Post. Changes in Fluorescence Recovery After Photobleaching (FRAP) as an indicator of SOX9 transcription factor activity. *Published in Biochim Biophys Acta Gene Regul Mech., 2018.*

5. Xiaobin Huang, Leilei Zhong, **Jan Hendriks**, Janine N. Post, Marcel Karperien. The Effects of the WNT-Signaling Modulators BIO and PKF118-310 on the Chondrogenic Differentiation of Human Mesenchymal Stem Cells. *Published in International Journal of Molecular Sciences, 2018.*

6. Xiaobin Huang, Leilei Zhong, **Jan Hendriks**, Janine N. Post, Marcel Karperien. Different response of human chondrocytes from healthy looking areas and damaged regions to IL1β stimulation under different oxygen tension. *Published in Journal of Orthopaedic Research, 2018.*

7. Xiaobin Huang, Leilei Zhong, Eefje van Helvoort, Floris Lafeber, Simon Mastbergen, **Jan Hendriks**, Janine N. Post, Marcel Karperien. The expression of DKK1 and FRZB in serum and synovial fluid are negatively correlated to local inflammation and OA severity. *Published in Cartilage, 2019.*

8. Tom Kamperman, Michelle Koerselman, Cindy Kelder, **Jan Hendriks**, João Crispim, Xandra de Peuter, Piet Dijkstra, Marcel Karperien, J Leijten. Spatiotemporal Material Functionalization via Competitive Supramolecular Complexation of Avidin and Biotin Analogs. *Published in Nature Communications, 2019.*

--- In progress ---

1. **Jan Hendriks**, Daniël B.F. Saris, Marcel Karperien. Joint Homeostasis – Implications for diagnosis and treatment. *Manuscript in preparation.*

2. **Jan Hendriks**, Richard B.M. Schasfoort, Daniël B.F. Saris, Marcel Karperien. Kinetic characterization of SPRi-based biomarker assays enables quality control, calibration free measurements and robust optimization for clinical application. *Manuscript in preparation.*
3. **Jan Hendriks**, Claas Willem Visser, Daniël B.F. Saris, Marcel Karperien. Cell type determines viability in bioprinting: altering cellular properties results in improved survival. *Manuscript in preparation.*
4. **Jan Hendriks**, Claas Willem Visser, Daniël B.F. Saris, Marcel Karperien. Cell viability in bioprinting depends on the droplet: A new model predicts influence of size and velocity. *Manuscript in preparation.*
5. **Jan Hendriks**, Bram Zoetebier, Daniël B.F. Saris, Marcel Karperien. Gelatin-tyramine improves cell attachment, migration and metabolic activity of multiple cell types in enzymatically crosslinkable dextran-hyaluronic acid hydrogels. *Manuscript in preparation.*

Conference Abstracts

1. **Jan Hendriks**, C.W. Visser, Sieger Henke, Jeroen Leijten, D.B.F. Saris, Chao Sun, Detlef Lohse, Marcel Karperien. Cell Viability in Bioprinting with Spray Deposition: Influence of the Cell Type. *NBTE 2015, Lunteren, Netherlands.*
2. **Jan Hendriks**, C.W. Visser, Tommy S. de Windt, D.B.F. Saris, Marcel Karperien. Resurfacing of damaged articular cartilage surfaces using arthroscopic bio airbrush. *OARSI 2016, Amsterdam, the Netherlands.*
3. **Jan Hendriks**, C.W. Visser, Tommy S. de Windt, D.B.F. Saris, Marcel Karperien. Resurfacing of damaged articular cartilage surfaces using arthroscopic bio airbrush. *ICRS 2016, Sorento, Italy.*
4. **Jan Hendriks**, I. Stojanovic, Marcel Karperien, D.B.F. Saris. Sensitive multiplex biomarker detection system for assessing joint homeostasis. *ICRS 2016, Sorento, Italy.*
5. **Jan Hendriks**, C.W. Visser, Marcel Karperien, D.B.F. Saris. Cell Viability in Bioprinting with Spray Deposition: Influence of the Cell Type. *NBTE 2016, Lunteren, the Netherlands*
6. **Jan Hendriks**, I. Stojanovic, D.B.F. Saris, Marcel Karperien. A new highly sensitive method for multiplex measurements of biomarkers in synovial fluid aspirates. *OARSI 2017, Las Vegas, USA.*
7. **Jan Hendriks**, I. Stojanovic, D.B.F. Saris, Marcel Karperien. A new method for multiplex measurements of biomarkers in synovial fluid aspirates with high sensitivity and extensive quality control. *Abstract OARSI 2018, Liverpool, UK.*

8. **Jan Hendriks**, M. Sharif, I. Stojanovic, D.B.F. Saris, Marcel Karperien. A highly sensitive multiplex biomarker assay for the early diagnosis of osteoarthritis. *Abstract OARSI 2019, Toronto, Canada.*

9. **Jan Hendriks**, M. Sharif, I. Stojanovic, D.B.F. Saris, Marcel Karperien. A highly sensitive multiplex biomarker assay for the early diagnosis of osteoarthritis. *Abstract OERS 2019, Maastricht, the Netherlands.*

Book Chapters

1. R.B.M. Schasfoort. Handbook of Surface Plasmon Resonance, 2nd edition (2017) Royal Society of Chemistry London. Chapter 12: Future Trends in SPR Technology section: 12.6.2 Signal Enhancement Cascade for Boosting the Dynamic Range. pp 437-439

Teaching and Supervision

Courses

2012 – 2013 Teaching assistant 'cell biology'

2014 – 2018 Tutor and practical instructor 'creating biological tissues'

Students

1. Jorke Willemse (B.Sc. University of Twente, July 2014) "The influence of extra cellular matrix proteins in a biocompatible hydrogel on the behavior of mesenchymal stem cells"
2. David Smith (B.Sc. University of Twente, July 2014) "The influence of extra cellular matrix proteins in a biocompatible hydrogel on the behavior of fibroblasts"
3. Joost Blok (M.Sc. University Medical Centre Utrecht, April 2015) "Cell spray influences cell survival of mesenchymal stem cells"
4. Taciana Gonçalves (M.Sc. University of Minho, August 2015) "Enzymatically crosslinked tyramine- modified fibronectin-Dex-HA hydrogels for tissue engineering"
5. Stanislav Paul (M.Sc. University of Twente, January 2016) "Evaluation of various Organ-on-a-chip applications using human Mesenchymal Stem Cells"
6. Iris Voogt (B.Sc. University of Twente, June 2016) "The effect of bioprinting on the viability of cells from different tissues"
7. Jan Gaede (B.Sc. University of Twente, June 2016) "The effect of bioprinting on the viability of cells from different tissues"
8. Jorke Willemse (M.Sc. University of Twente, August 2016) "'Pre-vascularized' hydrogel constructs: Creating vasculature-like networks inside hydrogel constructs using microfluidics in an effort to overcome the 'vascularization hurdle in tissue engineering"
9. David Smith (M.Sc. University of Twente, November 2016) "A biocompatible hydrogel based basement membrane for the blood-brain barrier improved with extracellular matrix proteins"
10. Sophie Gorter de Vries (B.Sc. University of Twente, November 2016) "Fundamental research on the effect of cell impact on cell viability"
11. Emiel Seta (B.Sc. Saxion University, July 2017) "A fundamental investigation into cellular properties that determine cell viability in bioprinting"
12. Floor Couwenberg (B.Sc. University of Twente, July 2017) "The effect of the contact angle, droplet size and impact velocity on cell viability in droplet-based cell deposition"

13. Wendy Schuitmaker (B.Sc. University of Twente, July 2017) "Developing and optimizing a setup for controlling droplet parameters to investigate viability in droplet-based cell deposition"
14. Ceri-Anne Suurmond (B.Sc. University of Twente, January 2018) "Fundamental research on the effect of bioprinting on cell survival by chondrocytes"
15. Danique Kottelenberg (B.Sc. University of Twente, March 2018) "The effect of droplet size, velocity and viscosity on cell viability in droplet-based cell deposition